

INFORMATION TO USERS

This manuscript has been reproduced from the microfilm master. UMI films the text directly from the original or copy submitted. Thus, some thesis and dissertation copies are in typewriter face, while others may be from any type of computer printer.

The quality of this reproduction is dependent upon the quality of the copy submitted. Broken or indistinct print, colored or poor quality illustrations and photographs, print bleedthrough, substandard margins, and improper alignment can adversely affect reproduction.

In the unlikely event that the author did not send UMI a complete manuscript and there are missing pages, these will be noted. Also, if unauthorized copyright material had to be removed, a note will indicate the deletion.

Oversize materials (e.g., maps, drawings, charts) are reproduced by sectioning the original, beginning at the upper left-hand corner and continuing from left to right in equal sections with small overlaps.

ProQuest Information and Learning
300 North Zeeb Road, Ann Arbor, MI 48106-1346 USA
800-521-0600

UMI[®]

University of Alberta

**Microstructural Characterization of Porous Thin Films and Applications
to Electrochemical Capacitors**

By

Barbara Marie Djurfors



A thesis submitted to the Faculty of Graduate Studies and Research in partial fulfillment
of the requirements for the degree of Doctor of Philosophy

in

Materials Engineering

Department of Chemical and Materials Engineering

Edmonton, Alberta

Spring, 2005



Library and
Archives Canada

Bibliothèque et
Archives Canada

0-494-08224-0

Published Heritage
Branch

Direction du
Patrimoine de l'édition

395 Wellington Street
Ottawa ON K1A 0N4
Canada

395, rue Wellington
Ottawa ON K1A 0N4
Canada

Your file *Votre référence*

ISBN:

Our file *Notre référence*

ISBN:

NOTICE:

The author has granted a non-exclusive license allowing Library and Archives Canada to reproduce, publish, archive, preserve, conserve, communicate to the public by telecommunication or on the Internet, loan, distribute and sell theses worldwide, for commercial or non-commercial purposes, in microform, paper, electronic and/or any other formats.

The author retains copyright ownership and moral rights in this thesis. Neither the thesis nor substantial extracts from it may be printed or otherwise reproduced without the author's permission.

AVIS:

L'auteur a accordé une licence non exclusive permettant à la Bibliothèque et Archives Canada de reproduire, publier, archiver, sauvegarder, conserver, transmettre au public par télécommunication ou par l'Internet, prêter, distribuer et vendre des thèses partout dans le monde, à des fins commerciales ou autres, sur support microforme, papier, électronique et/ou autres formats.

L'auteur conserve la propriété du droit d'auteur et des droits moraux qui protègent cette thèse. Ni la thèse ni des extraits substantiels de celle-ci ne doivent être imprimés ou autrement reproduits sans son autorisation.

In compliance with the Canadian Privacy Act some supporting forms may have been removed from this thesis.

Conformément à la loi canadienne sur la protection de la vie privée, quelques formulaires secondaires ont été enlevés de cette thèse.

While these forms may be included in the document page count, their removal does not represent any loss of content from the thesis.

Bien que ces formulaires aient inclus dans la pagination, il n'y aura aucun contenu manquant.


Canada

Abstract

Electrochemical capacitors are used for applications requiring high power output and high cycle capacity. Ruthenium oxide has been used for pseudocapacitors; however, raw material costs are prohibitive to large-scale commercial production and manganese oxides are becoming popular. In general, there are certain requirements necessary in order to develop capacitance from transition metal oxide materials. The films are porous and amorphous to allow for easy movement of protons through the structure and the active sites (sites that develop capacitance) must be hydrated with a 4+ valence (e.g., $\text{MnO}_2 \cdot n\text{H}_2\text{O}$).

A procedure combining physical vapor deposition and electrochemical oxidation was developed to produce a film that has excellent capacitance ($\sim 500\text{F/g}$). The physical vapor deposition step is used to deposit a thin layer of Mn/MnO onto a standard Si substrate with Ti/Pt metallization. In the as-deposited state, the film is crystalline, dense, 0/2+ valence, with no hydration and develops no capacitance. The film is subsequently oxidized in a solution of 1M Na_2SO_4 using a constant current up to a potential of 0.9V vs. Ag/AgCl. During this step in the processing, the manganese near the surface of the film is oxidized to the 4+ valence, develops significant hydration and becomes both porous and amorphous. It is after this oxidation step that the film becomes highly capacitive.

The porous surface layer responsible for the capacitive behavior can be produced on any PVD deposited manganese layer regardless of the starting film morphology (e.g. dense or porous). Since the electrochemical oxidation step is critical to the formation of the

porous layer, adjusting some of the oxidation parameters can have a significant effect on the porous layer and resulting capacitance. Overall, the capacitance of the films increases as the oxidizing current density increases. Increasing the oxidation current density results in a thinner porous layer, but greater hydration content. The thickness of the porous surface layer is also a function of the thickness of the deposited film. As the starting film thickness increases, so does the resulting porous layer thickness. The hydration remains the same and therefore the thicker films produce greater areal capacitance (F/cm^2) but the specific capacitance (F/g) remains constant.

Acknowledgments

I would like to acknowledge the contributions of my two supervisors: Dr. Ivey and Dr. Brett for their superior supervision and guidance during the past years of my degree. In addition, I would like to gratefully acknowledge the many contributions of Dr. J.N. Broughton.

I would also like to acknowledge funding from the Natural Science and Engineering Research Council of Canada, iCORE, Micralyne and the Killam foundation.

I also acknowledge the many technical contributions of George Braybrook (FE-SEM) Earth and Atmospheric Science, Dr. Karpuzov (XPS) and Dr. He (XPS).

Table of Contents

1	Introduction.....	1
2	Literature Survey	3
2.1	GLANCING ANGLE DEPOSITION.....	3
2.1.1	<i>Growth of GLAD films</i>	4
2.2	MANGANESE OXIDE MATERIALS	5
2.2.1	<i>Properties and Phases</i>	5
2.2.2	<i>Electrochemical Behavior of Mn and the oxides</i>	11
2.2.2.1	Mn ions in solution	11
2.2.2.2	Electrochemical behavior of MnO ₂	13
	Neutral and Acidic Solutions	13
	Alkaline Solutions.....	15
2.3	ELECTROCHEMICAL SUPERCAPACITORS.....	19
2.3.1	<i>Electrostatic Capacitors</i>	20
2.3.1.1	Electrostatic Capacitance Theory.....	20
2.3.1.2	Activated Carbon Materials.....	24
2.3.2	<i>Faradic Capacitors</i>	24
2.3.2.1	Faradic Capacitance Theory	24
2.3.2.2	Underpotential deposition pseudocapacitance	26
2.3.2.3	Intercalation pseudocapacitance	27
2.3.2.4	Redox Pseudocapacitance.....	28
2.3.2.4.1	Conducting Polymers.....	28
2.3.2.4.2	Transition Metal Oxides.....	28
	Ruthenium Oxide.....	29
	Manganese Oxide.....	31
	Electrochemical Deposition from chemical bath.....	31
	Powder synthesis from wet chemistry procedures.....	36
	Physical Vapour Deposition Methods	45
3	Experimental Methods	49

3.1	CAPACITOR ELECTRODE FABRICATION	49
3.1.1	<i>Thin Film Fabrication-GLAD Technique</i>	49
3.1.2	<i>Thin Film Fabrication-Dense Films</i>	50
3.1.3	<i>Electrochemical Oxidation</i>	50
3.2	ELECTRODE CHARACTERIZATION	53
3.2.1	<i>Electrochemical Characterization</i>	53
3.2.2	<i>Structural Characterization</i>	53
3.2.2.1	Scanning Electron Microscopy.....	53
3.2.2.2	Conventional TEM.....	54
3.2.2.3	Scanning TEM	54
3.2.2.4	TEM Sample Preparation	54
3.2.2.5	X-ray Diffraction.....	55
3.2.2.6	X-ray Photoelectron Spectroscopy (XPS)	55
3.3	SOLUTION CHARACTERIZATION	57
3.3.1	<i>Atomic Absorption Spectroscopy (AAS)</i>	57
4	Results	58
4.1	GENERAL STRUCTURES	58
4.1.1	<i>Effect of Material</i>	58
4.1.2	<i>Annealing of GLAD structures</i>	62
4.1.3	<i>Effect of Rotation</i>	64
4.2	MANGANESE OXIDE ELECTROCHEMICAL CAPACITOR MATERIALS	65
4.2.1	<i>As-deposited PVD films</i>	66
4.2.2	<i>Thermally Oxidized Films</i>	74
4.2.3	<i>Electrochemical Oxidation</i>	87
4.2.4	<i>Effect of CV cycling</i>	126
4.2.4.1	Microstructure.....	126
4.2.4.2	Capacitance.....	130
4.2.5	<i>Effect of sample orientation on the oxidation process and production of a porous surface layer</i>	135
4.2.6	<i>Effect of current density on porous layer formation</i>	157

4.2.6.1	Zigzag films	158
4.2.6.2	Dense films	166
4.2.6.3	Capacitance.....	174
4.2.7	<i>Effect of starting layer thickness on porous layer formation.....</i>	<i>178</i>
4.2.7.1	Dense Films	178
4.2.7.2	Capacitance.....	188
5	Conclusions.....	194
5.1	GENERAL GLAD STRUCTURE.....	194
5.2	MANGANESE OXIDE ELECTROCHEMICAL CAPACITOR MATERIALS	194
6	Further Recommendations.....	197
6.1	GENERAL GLAD STRUCTURE.....	197
6.2	MANGANESE OXIDE ELECTROCHEMICAL MATERIALS	197
7	References.....	200

List of Tables

Table 1. Structures of manganese dioxides.	8
Table 2. XPS analysis for films deposited using potentiostatic mode, galvanostatic mode, and CV mode.....	34
Table 3. XPS peak analyses of MnO _x films deposited at different potentials.....	35
Table 4. Reduction of 50 mL of 0.1 M KMnO ₄ with varying amounts of 0.25M KBH ₄ at varying pH.	37
Table 5. Synthesis conditions and capacitance of the various samples.....	38
Table 6. Capacitance values in various electrolytes.....	39
Table 7. Average specific capacitance of dip-coated sol-gel and electrodeposited MnO ₂ films.....	43
Table 8. Table of Mn 3s peak splitting values for various manganese oxides.	56
Table 9. Table of O1s deconvolution energies for different bonds.....	57
Table 10. XPS data for zigzag films and dense films.....	108
Table 11. XPS results for zigzag sample cycled 100 times.	130
Table 12. AAS results for complete oxidation for the two different sample orientations. ..	143
Table 13. XPS results from the Mn 3s splitting data and the O1s peak de-convolution for the different geometries. Each sample was oxidized to 0.9V.....	153
Table 14. XPS Mn 3s peak splitting results and O 1s de-convolution results for different solution volumes	156
Table 15. Sample descriptions for oxidation of zigzag films at different oxidizing currents.	158
Table 16 XPS results giving valence of the samples.....	165
Table 17 Sample descriptions for oxidation of dense films at different oxidizing currents.	167
Table 18 XPS Mn 3s splitting width results giving valence of the samples.....	172
Table 19 Sample descriptions for dense films of different deposited thicknesses.....	179
Table 20 XPS Mn 3s peak splitting results giving valence of the samples.	186

List of Figures

Figure 1. Schematic illustrating the geometry of glancing angle deposition.....	4
Figure 2. Partial phase diagram for Mn-O.....	6
Figure 3. Schematic showing the transformations of the different forms of manganese dioxide.....	10
Figure 4. Pourbaix diagram for manganese in water assuming a temperature of 25°C and 10 ⁻⁶ M ion concentration.....	12
Figure 5. Galvanostatic potential-time curves for the reduction of MnO ₂ film in 1 M KOH.....	17
Figure 6. Schematic illustrating the various transitions occurring upon immersing Mn in an alkaline solution. The forward reaction is illustrated with the solid arrows and the reverse reaction is indicated with the dashed arrows. The potential of the transition is indicated below the reaction path, while the gas and soluble products are indicated above the main reaction path.	18
Figure 7. Simplified schematic of a double-layer capacitor.	21
Figure 8. Charging curve for an electrode exhibiting electrostatic or double layer capacitance.....	22
Figure 9. Cyclic voltammogram for an interface having potential-independent capacitance (ideal capacitor).....	23
Figure 10. CV profile for the UPD of Pb adatoms on Au surfaces.....	27
Figure 11. CV scan of a Mn film deposited at 84° using 0.1M Na ₂ SO ₄ and a sweep rate of 50mV/s. Also shown on the right axis is the CV scan of a blank Pt wafer for comparison.....	47
Figure 12. Graph showing the specific capacitance values as a function of the film deposition angle.	48
Figure 13. Oxidation cell with a vertical sample orientation.....	51
Figure 14. Oxidation cell with horizontal sample orientation.	52
Figure 15. TEM BF image of a Cr helix growing in the direction of the arrow with the diffraction pattern inset, b) TEM BF image showing detail of branching in a helix, and c) corresponding dark field (DF) image, from the (110) reflection, of the same area in (b) showing an approximate grain size of 50 nm.....	59
Figure 16. a) TEM BF image of Ti helix growing in the direction of the arrow with inset diffraction pattern, b) TEM BF image showing detail of branching in helix, and c) corresponding DF image, from the (100) reflection, of the same area in (b) showing an approximate grain size of 20 nm.....	60
Figure 17. a) TEM BF image of Cr zigzag growing in direction of arrow with inset diffraction pattern, and b) TEM DF image of the Cr zigzag from the (110) reflection.	61
Figure 18. a) TEM BF image of TiO zigzag growing in direction of arrow with inset diffraction pattern, and b) TEM DF image of TiO zigzag from the (111) reflection.....	62
Figure 19 a) Selected area (SAD) pattern for an as-deposited titanium oxide vertical post, and b) SAD pattern for an annealed titanium oxide vertical post, indexed as the anatase form of TiO ₂	63
Figure 20. a) TEM BF image of the as-deposited TiO ₂ vertical post, and b) TEM BF image of the annealed TiO ₂ vertical post growing in the direction of the arrow.	64
Figure 21. TEM DF image from the (103) reflection for anatase showing the grain size.....	64

Figure 22. a) TEM BF image of aluminum vertical post deposited with a 42 RPM rotation speed growing in the direction of the arrow, with an inset of the single crystal diffraction pattern, and b) TEM BF image of an aluminum vertical post deposited with a 3 RPM rotation speed growing in the direction of the arrow, with an inset of the single crystal diffraction pattern.....	65
Figure 23 a) FE-SEM secondary electron (SE) images of the as-deposited manganese chevron film revealing the surface texture. b) The chevron film in cross-section showing the morphological texture. c) FE-SEM SE image of the sputtered dense film in cross-section.....	68
Figure 24 a) Cross-section TEM BF image of an as-deposited chevron film. b) EDX spectrum from the zigzag layer shown in Figure 15a. c) Indexed SAD pattern from the deposited zigzag layer showing the presence of Mn and MnO. d) TEM DF image of deposited layer from part of the (111), (200) reflections for the MnO and part of the (330) reflection for the Mn.	71
Figure 25 a) Cross-section TEM BF image of an as-deposited dense film. b) EDX spectrum from the dense layer shown in Figure 25a. c) Indexed SAD pattern from the dense layer. d) TEM DF image of the deposited layer from part of the (111), (200) reflections for the MnO and part of the (330) reflection from the Mn.....	73
Figure 26. XRD pattern from as-deposited zigzag and dense films showing Mn and MnO.	74
Figure 27 FE-SEM SE images of the zigzag layer annealed for a) 30 minutes. b) 60 minutes. c) 120 minutes and d) 1920 minutes.	76
Figure 28. Plot of thermal oxide layer thickness versus annealing time.	77
Figure 29 a) TEM BF image of a cross-section sample of the layer annealed at 300°C for 30 minutes. b) TEM DF image of the annealed zigzag layer in (a) using part of the (111) and (200) reflections for MnO and the (330) reflection for Mn. c) TEM BF image of the layer annealed for 60 minutes clearly showing the oxide layer. d) TEM DF image of the annealed zigzag layer in (c) using part of the (111) and (200) reflections for MnO and the (330) reflection for Mn. e) TEM BF image of the layer annealed for 120 minutes with the visible oxide layer on the top. f) TEM DF image of the annealed zigzag layer in (e) using part of the (111) and (200) reflections for MnO and the (330) reflection for Mn. g) TEM BF image of the layer annealed for 1920 minutes. h) TEM DF image of the annealed layer in (g) using part of the (111) and (200) reflections for MnO.....	79
Figure 30 EDX spectrum taken from the oxide layer on top of the manganese zigzag layer that was annealed for 60 minutes.....	80
Figure 31 SAD patterns from the cross-section samples of the layers annealed for a) 30 minutes. b) 60 minutes. c) 120 minutes and d) 1920 minutes.	81
Figure 32 Overlaid XRD spectra from the four annealed samples indexed to show the disappearance of Mn and the growth of tetragonal Mn ₃ O ₄	82
Figure 33. Microdiffraction patterns from three different grains in the surface oxide layer. a), b) and c) are indexed as the cubic form of MnO and d) is indexed as the tetragonal form of Mn ₃ O ₄	83
Figure 34 Schematic illustration of oxide growth. a) The original material composed of Mn and MnO zigzags. b and c) The original zigzag layer slowly transforms to a columnar oxide layer that is both MnO and Mn ₃ O ₄ . d) The final structure where the original oxide layer has been destroyed and replaced by the columnar oxide layer that is primarily Mn ₃ O ₄ with some MnO.....	84
Figure 35 a) TEM BF image of the plan view section of the sample annealed for 60 minutes. b) SAD pattern from the area in the BF image showing the MnO and Mn ₃ O ₄ phases. c)	

TEM BF image of the plan view section of the sample annealed for 1920 minutes. d) SAD pattern from the area in the BF image showing Mn ₃ O ₄	85
Figure 36. Oxidation trace for a dense sample of 50nm Mn nominal starting thickness oxidized at a current density of $1 \times 10^{-4} \text{A/cm}^2$	88
Figure 37. Plot of the potential of the film as a function of oxidation time during the oxidation process. Four oxidations have been done, each stopped during a different stage of oxidation.	89
Figure 38. FE-SEM SE images in cross-section and oblique view of samples oxidized to a) -1.35V, b) -0.8V, c) 0.1V and d) 0.9V.....	91
Figure 39. Graph of thickness of porous film produced during the oxidation process as a function of the final oxidation potential reached.	92
Figure 40. Growth of manganese oxide layer as a function of oxidation time.....	93
Figure 41. Graph of concentration of Mn at the various stages of oxidation in various locations.....	95
Figure 42. Mn 3s spectrum from the sample oxidized at 0.1mA/cm^2 until a potential of 0.9V vs. Ag/AgCl is reached.....	97
Figure 43. XPS results from oxidation of film at various stages showing the splitting width of the films as compared with the standard values given in the literature. These standard values are tabulated in Table 8.....	97
Figure 44. XPS results from oxidation of film at various stages, now including 0.5V, showing the splitting width of the films as compared with the standard values given in literature. These standard values are tabulated in Table 8.....	100
Figure 45. O1s spectrum from the sample oxidized at 0.1mA/cm^2 until a potential of 0.9V vs. Ag/AgCl is reached. The peak has been deconvoluted into its major constituents: H-O-H, Mn-O-Mn, and Mn-O-H.	102
Figure 46. Relative hydration of the film during the oxidation process.....	103
Figure 47. FE-SEM SE images of zigzag films in an oblique view that have been oxidized for a) 1700s, representing 36% of the total oxidation time and b) 4750s, representing 100% of the total oxidation time.....	107
Figure 48. a) TEM BF cross-sectional image of the sample oxidized for 1750 s (36% of total oxidation time) with inset diffraction pattern showing some crystallinity, indexed as single phase Mn ₃ O ₄ . b) Representative EDX spectrum from the porous surface layer. c) TEM BF plan view image of porous surface layer with inset diffraction pattern indexed as a mixture of MnO and Mn ₃ O ₄ . d) TEM DF plan view image taken from boxed area in diffraction pattern in (c) showing partial crystallinity. e) TEM BF cross-sectional image of zigzag layer from sample electrochemically oxidized for 1750s. f) SAD pattern from the dense intermediate layer indexed as a mixture of MnO and Mn ₃ O ₄ . g) SAD pattern from zigzag layer indexed as single phase MnO.	111
Figure 49 a) TEM BF cross-section image of interface showing growth of the porous surface layer. b) TEM BF cross-section image of zigzag layer only with inset diffraction pattern indexed as single phase Mn ₃ O ₄	113
Figure 50. a) TEM BF plan view image of porous surface layer. b) Amorphous SAD pattern from a).	114
Figure 51. Schematic illustration showing the oxidation process of the porous surface film and the underlying sub-layer through the various stages. a) As-deposited state. b) Immersion into solution showing the immediate dissolution of the manganese	

and the formation of the porous amorphous surface film (MnO). c) The film during the first plateau at -1.35 V vs. Ag/AgCl, showing the continued oxidation of the porous surface film from MnO to Mn_3O_4 . The sub-layer continues to oxidize from Mn to MnO. d) The film during the second plateau at -0.8 V showing the oxidation of the surface film from Mn_3O_4 to Mn_2O_3 . The sub-layer begins to oxidize from MnO to Mn_3O_4 . e) The film during the third plateau at 0.1 V showing the start of the oxidation of the porous surface layer from Mn_2O_3 to MnO_2 . The sub-layer continues the oxidation process from MnO to Mn_3O_4 . f) The film in the transition region between 0.1 V and 0.9 V showing the continued oxidation of the porous surface film from Mn_2O_3 to MnO_2 . The sub-layer continues the oxidation process from MnO to Mn_3O_4 . The porous surface film begins to become slightly thinner. f) The film at the final potential of 0.9 V showing the formation of a porous surface layer that is entirely composed of MnO_2 . The sub-layer has converted entirely to Mn_3O_4 . In addition, the porous surface film has been significantly reduced in thickness..... 116

Figure 52. Current vs. potential plots for samples oxidized to various end potentials and then cycled 100 times. The tenth cycle is shown..... 117

Figure 53. Graph of potential as a function of time for samples oxidized using two different current densities ($0.1/0.8$ mA/cm²) compared with a sample oxidized using a single current density (0.1 mA/cm²)..... 120

Figure 54. FE-SEM SE images in oblique and cross-section view from films oxidized at a) a single current density (0.1 mA/cm²) and b) two separate current densities ($0.1/0.8$ mA/cm²)..... 121

Figure 55. Plot of current vs. potential behavior for the tenth CV cycle for a film oxidized at 0.1 mA/cm² and a film oxidized at 0.1 and 0.8 mA/cm²..... 122

Figure 56. Graph showing the difference between the solubility of Mn during a single current deposition and a bi-current deposition..... 123

Figure 57. TEM BF cross-section image of a zigzag film that has been electrochemically oxidized and then cycled one hundred times between 0 and 0.9 V. 127

Figure 58 a) STEM annular DF image of the electrochemically oxidized sample. b) SAD pattern taken from zigzag layer indexed as single phase Mn_3O_4 . c) EDX spectrum taken from the thin layer region marked with an X and d) EDX spectrum taken from the bulk sample region marked with an O. 128

Figure 59. Current vs. Time curves for a dense film oxidized in a horizontal sample orientation at a current density of 0.2 mA/cm²..... 130

Figure 60. CV curves for the first and tenth cycle. 134

Figure 61. CV curves for the first and tenth cycle. 135

Figure 62. Graph of oxidation process stopped during the various stages indicated by the legend for the sample in a vertical orientation..... 136

Figure 63. FE-SEM SE images of the various stages of oxidation in both oblique and cross-section views for samples oxidized with a vertical sample orientation to a final potential of a) -1.35 V, b) -0.8 V, c) 0.1 V and d) 0.9 V. 138

Figure 64. Graph of porous film thickness as a function of oxidation time and sample orientation..... 139

Figure 65. Graph of film mass as a function of oxidation time. 140

Figure 66. Graph showing the amount of total Mn lost during oxidation as a function of the oxidation potential and sample orientation..... 141

Figure 67. Graph of amount of Mn rinsed off the sample during the oxidation process.....	142
Figure 68. a) A schematic of oxidation process with a horizontal sample orientation showing the location of the lost Mn . b) A schematic of the oxidation process with a vertical sample orientation showing the location of the lost Mn.....	143
Figure 69. Plot of Mn 3s splitting width from XPS as a function of oxidation time.	145
Figure 70. Plot of hydration of the porous film as a function of oxidation time.	146
Figure 71. Plot of current vs. time for cyclic voltammetry scans.	147
Figure 72. Graph of oxidation process at a constant current of $0.1\text{mA}/\text{cm}^2$ under different geometrical constraints.....	149
Figure 73. FE-SEM SE oblique and cross-section images of films produced using a) a normal vertical sample orientation and b) a horizontal sample in the vertical sample cell. The oxidation current for both samples was $0.1\text{mA}/\text{cm}^2$	151
Figure 74. AAS results comparing the control sample, with a vertical orientation, to a sample with a horizontal orientation in the vertical oxidation cell to identify the location and amount of Mn lost during the oxidation process.....	152
Figure 75. Oblique and cross-sectional FE-SEM, SE images for a) horizontal test sample and b) horizontal sample with greater solution volume. Both samples were oxidized at $0.1\text{mA}/\text{cm}^2$	154
Figure 76. AAS results comparing the amount and location of Mn lost during the oxidation process for the horizontal control sample and the horizontal sample with greater solution volume.	155
Figure 77. Current vs. time curves for films of differing geometry.....	157
Figure 78. Plot of the oxidation time to 0.9V for the zigzag samples as a function of applied oxidation current density.	158
Figure 79. Plot of the thickness of the porous layer as a function of the applied current density.	159
Figure 80. FE-SEM SE images of the zigzag films oxidized at various current densities a) $0.2\text{mA}/\text{cm}^2$, b) $0.4\text{mA}/\text{cm}^2$, c) $0.8\text{mA}/\text{cm}^2$ and d) $1\text{mA}/\text{cm}^2$	161
Figure 81. a) TEM BF cross-sectional image of a zigzag sample oxidized at $2 \times 10^{-4}\text{A}/\text{cm}^2$ with inset diffraction pattern identifying the phase of the zigzag as Mn_3O_4 . b) TEM BF cross-sectional image of sample oxidized at $2 \times 10^{-4}\text{A}/\text{cm}^2$ showing porous structure. c) TEM BF cross-sectional image of sample oxidized at $1 \times 10^{-3}\text{A}/\text{cm}^2$ with inset diffraction pattern identifying the phase of the zigzag as MnO and Mn_3O_4 . d) TEM BF cross-sectional image of sample oxidized at $1 \times 10^{-3}\text{A}/\text{cm}^2$ showing detail of the porous surface layer.....	164
Figure 82. Graph showing hydration of the film as a function of the oxidizing current density.	166
Figure 83. Oxidation time to 0.9V as a function of current density for the dense films.	168
Figure 84. FE-SEM SE images of the films produced at various oxidizing currents in oblique view and cross-sectional view. a) $0.2\text{mA}/\text{cm}^2$, b) $0.4\text{mA}/\text{cm}^2$, c) $0.8\text{mA}/\text{cm}^2$, and d) $1\text{mA}/\text{cm}^2$	170
Figure 85. Plot of porous layer thickness as a function of oxidizing current density for both dense and zigzag films.....	171
Figure 86. Plot of percent increase in the total layer thickness (porous surface and dense under-layer) as a function of the oxidizing current density for both zigzag and dense films.....	172

Figure 87. Graph showing the hydration of the dense film as a function of the oxidizing current density.....	173
Figure 88. Current-Voltage curves for the dense samples oxidized at various oxidizing current densities.	175
Figure 89. Plot of planar capacitance for the dense samples as a function of the oxidizing current density.....	176
Figure 90. Graph showing the amount of Mn left in solution following an oxidation at a particular current density.	177
Figure 91. Plot of the total oxidation time as a function of the starting film thickness.....	180
Figure 92. Effect of starting layer thickness on the thickness of the final layer.	180
Figure 93. FE-SEM SE images in the oblique and cross-sectional views for samples different starting film thickness. a) 25nm, b) 60nm, c) 110nm, and d) 230nm.	182
Figure 94. Effect of the starting layer thickness on the thickness of the porous surface layer produced.	184
Figure 95. The effect of starting layer thickness on the thickness of the dense under-layer.	185
Figure 96. Graph of relative hydration of films as a function of the starting film thickness.	187
Figure 97. Effect of starting film thickness on the planar capacitance of the films.....	189
Figure 98. Graph of the porous film thickness as a fraction of the original film thickness..	190
Figure 99. Graph of the specific capacitance of the film as a function of the starting film thickness.	191
Figure 100. Schematic illustration of modified post structure.....	198

1 Introduction

Electrochemical supercapacitors are capacitors that make use of electrochemical phenomena in order to store charge. As charge storage devices they are primarily used for applications that require a high power output and a high cycle capacity. They are often used in conjunction with other energy storage devices, such as batteries, in an attempt to improve the overall performance of the system by supplementing the continuous power output of the battery with periodic bursts of high power provided by the electrochemical supercapacitor. Their primary advantage over traditional electrical capacitors is a significantly improved capacitance per unit mass^{44,45}.

Electrochemical supercapacitors can be of two types: double layer and redox. The former type is comparable to a traditional capacitor as it employs the non-Faradic charge separation that occurs naturally across a double layer in an electrochemical cell in order to store charge. Activated carbon materials are predominantly used for this purpose because of their relatively low cost and high surface area (up to 2500m²/g)⁴⁵. The redox capacitor makes use of both reversible redox reactions and double layer charging in order to store charge, thereby giving a significant advantage over purely double layer capacitors. This behavior is typically termed “pseudocapacitance” and tends to resemble a re-chargeable battery more than a traditional capacitor. Traditionally, ruthenium oxide has been the material focused on for pseudocapacitors as it exhibits specific capacitance values of up to 750F/g. However, ruthenium raw material costs are prohibitive to large-scale commercial production⁴⁵.

Manganese and its oxides have enjoyed some interest as replacement materials for the more costly ruthenium oxides in electrochemical supercapacitor applications because of their relatively low cost and low toxicity⁶². Typically, MnO₂ films have been created by chemical reactions and often result in an amorphous hydrated MnO₂ product or a weakly crystalline hydrated MnO₂ product^{61,62,63,64,65,66,67}. Broughton and Brett developed a new procedure making use of physical vapour deposition and an oblique vapour incidence

angle in order to produce a chevron-type porous metallic structure that is then electrochemically oxidized and subsequently used as a capacitor⁷⁴. Prior to this work, the specific capacitance realized by these films, $225 \pm 25 \text{F/g}$, has yet achieved the thin-film levels of Chin et al⁷¹ (720F/g).

What is lacking in the original analysis of Broughton and Brett's method is an understanding of the phases involved and produced during the deposition, thermal annealing, and the electrochemical oxidation of the supercapacitor. A clear understanding of the phases and phase evolution will help in any work to modify and improve the supercapacitive behavior. The purpose of this research is to study the manganese electrochemical supercapacitor films in their as-deposited, electrochemically oxidized, and furnace annealed states in order to conclusively determine which phases are present during each stage and suggest improvements in processing that may help this technique achieve the high capacitance values of Chin et al⁷¹. X-ray diffraction, electron diffraction, transmission electron microscopy and scanning electron microscopy are used to characterize the materials.

2 Literature Survey

There are two sections to the thesis and thus the literature survey. The first section focuses on studying the general growth of films from the glancing angle deposition process. The second section examines manganese oxide electrochemical capacitor material which is the focus of the thesis work.

2.1 Glancing Angle Deposition

The Glancing Angle Deposition (GLAD) technique for producing porous thin films has been studied by the research group of Brett for several years^{1,2,3,4}. Taking advantage of self-shadowing effects, it is possible, through careful control, to produce porous films composed of independent columns of material. Ordinarily, an inclined vapour source will result in a film that has columns inclined toward the direction of the vapour source. However, if an extremely oblique vapour incidence angle ($>80^\circ$) is used, the growing columns on the surface of the substrate will shadow the area directly behind them thereby preventing any material from being deposited in that area (Figure 1). In this manner, it is possible to produce independent, inclined columns. The self-shadowing phenomenon may be exploited in order to produce porous thin films with a variety of different structures: slanted posts, chevrons, helices, and vertical posts. Individual slanted posts are produced when no substrate rotation is used, just an extreme oblique vapour incidence. Discontinuous substrate rotation of 180° at a time will result in a chevron structure, while continuous substrate rotation during deposition will result in a helical structure. When the rotation speed is increased sufficiently, the helical pitch will become so small that the film will resemble a series of vertical posts. The relatively high surface area and porosity of these sculpted films makes them ideally suited for a variety of applications including electrochemical supercapacitors. This type of substrate tilt and rotation can be adapted to virtually any physical vapour deposition system.

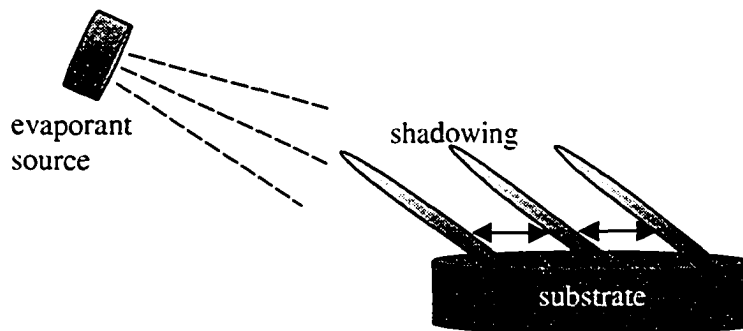


Figure 1. Schematic illustrating the geometry of glancing angle deposition.

2.1.1 Growth of GLAD films

There is a significant body of work studying the parameters that influence the growth of GLAD films on a macroscopic/morphological scale. Of particular relevance and interest is the work done by Malac^{5,6,7} and Dick⁸ that explores the microstructure of the films produced in significantly greater detail.^{1,3,4,9,10,11,12,13} Previous analysis of these films has revealed the importance of adatom surface diffusion on the final microstructure of the film, often described in terms of the dimensionless ratio T_s/T_m where T_s is the substrate temperature and T_m is the melting temperature, both quoted in Kelvin. Materials with low surface adatom diffusion rates (low T_s or high T_m) tend to exhibit branching or bifurcation due primarily to a combination of shadowing and limited diffusion, while those materials with high surface diffusion (high T_s , or low T_m) rates tend not to exhibit these characteristics because bulk and surface diffusion suppress branching^{5,6,7} and reduce the effects of shadowing.

Through studying the microstructure of Si helices, Malac⁶ made the following observations regarding film growth during the GLAD process. The first is that an increase in adatom diffusion length is directly related to an increase in substrate temperature during film growth. Second, during growth there will be an increase in the amount of material that is being deposited onto a growing helix due to a reduction in the number of neighboring helices. The reduction in neighboring helices is related to the random termination of some growing helices through competition. Third, the increase in

substrate temperature that accompanies film growth results in a decrease in the sticking co-efficient of the atom and thus causes an increase in the number of atoms that are scattered between the growing helices. Fourth, bifurcation within a growing helix occurs because of self-shadowing effects within the helix arm. Ultimately, this results in an increased number of fibers growing within each arm. Fifth, the bifurcation within a helix-arm may be assisted by preferential growth of fast-growing crystal planes.

The effect of rotation on the microstructure of the films has been studied by Malac⁶ and to some degree Dick⁸, although his focus was mostly on macrostructure and morphology. Malac concluded that increasing the rate of rotation (transition from helices to posts) results in a suppression of the bifurcation phenomena, resulting in pillars that appear to be formed from a single fiber. Dick found that materials with a low adatom diffusion rate (i.e., Si and SiO₂) showed a typical morphological transition from helix to post, but with little change in the underlying crystal structure of the film and no change in the thickness of the individual column. A similar trend to Si and SiO₂ was also found for higher adatom diffusion materials, such as Bi and Al, where a transition from the helical to post structure occurs with increasing rotation speed. However, it was also noted with respect to Al in particular, that the increase in rotation speed resulted in significantly thinner columns and it was hypothesized that this is because increasing the substrate rotation speed will inhibit the surface diffusion of adatoms. In addition, Al exhibits a faceting of the surface that was suggested to be due to preferred growth along certain crystal planes, though no evidence of crystallinity in the films is presented in this study.

2.2 Manganese Oxide Materials

2.2.1 Properties and Phases

Manganese is a very common metal and has uses in many industries. In the case of the power industry (batteries and capacitors), manganese oxides play a particularly important role. A partial phase diagram is shown in Figure 2 up to 60 at%O. There are four phases of pure Mn metal: α , β , γ , and δ . α -Mn is stable from room temperature to 707°C and has a complex bcc structure with fifty-eight atoms per unit cell. β -Mn is stable up to

1100°C and has a complex cubic structure with twenty atoms per unit cell. γ -Mn is stable up to 1138°C and has a simple fcc structure with four atoms per unit cell. δ -Mn is stable up to 1246°C and has a simple bcc structure with two atoms per unit cell.

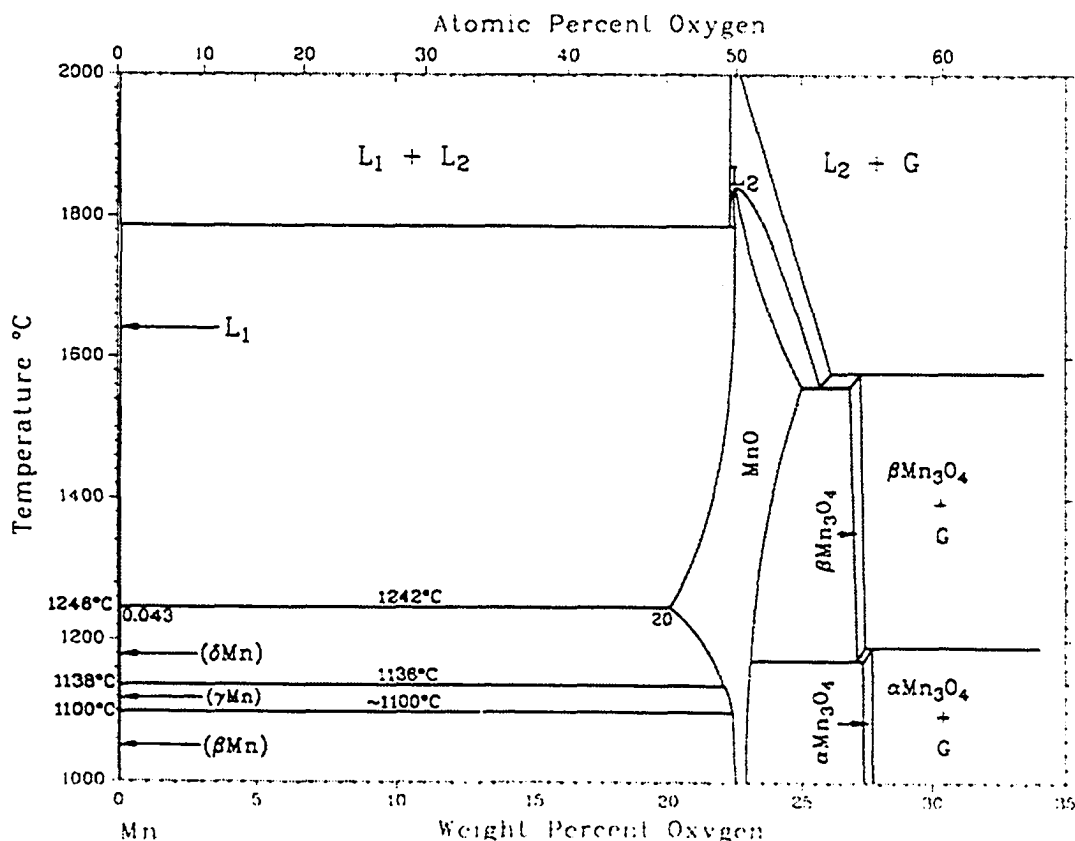


Figure 2. Partial phase diagram for Mn-O¹⁴.

Of note is that the solubility of oxygen in pure Mn, even at high temperatures is minimal, less than 1wt%. Thus, any small amount of oxidation will lead to the formation of an oxide phase since the oxygen will not be accommodated within the Mn lattice. As a transition metal (atomic number 25), manganese has many stable valences (2⁺, 3⁺, 4⁺, and 7⁺) and thus a variety of different oxides are possible (MnO, Mn₃O₄, Mn₂O₃, and MnO₂ are the main forms)¹⁵. The lowest valence oxide that forms is MnO (2+). The most common form of this oxide is manganosite which has a face-centered cubic structure (NaCl type) with 4 MnO molecules per unit cell¹⁶. There are other polymorphs of MnO

(orthorhombic) that can form as well, including a defect structure arising from oxygen vacancies. The next oxide that forms is Mn_3O_4 , commonly called hausmannite. The equilibrium phase has a tetragonal, deformed spinel structure at low temperatures ($T < 1433K$) and a cubic spinel at high temperatures ($T > 1433K$). There are also several polymorphs of this phase, several of which are cubic. The next stable oxide is Mn_2O_3 , commonly called bixbyite, having a body-centered cubic unit cell with 16 formula units per unit cell. As with the other oxides, there are several different polymorphs of Mn_2O_3 with different crystal structures. The final oxide that forms commonly in nature is MnO_2 . Again, there are several polymorphs of this phase each with a different crystal structure and slightly different properties. The most common polymorphs of MnO_2 are the α , β , γ , δ , λ , η , ϵ , and ρ type, each with its own crystal structure and unique properties¹⁵. In addition, there are several other types of oxides that can be formed synthetically, Mn_3O_8 and Mn_5O_8 for example, but they have very limited stability.

Because of the importance of the MnO_2 phase for electrochemical capacitor applications, it will be discussed in more detail. Of all the types of MnO_2 , it is believed that only pyrolusite and ramsdellite (β) are true MnO_2 modifications; the other crystalline forms are considered non-stoichiometric intergrowth structures of the former and are fundamentally also types of β - MnO_2 . The basis for all MnO_2 compounds is the same. It is believed to involve hexagonal close packing of the O^{2-} (with some hydroxyl ion substitutions) with half of the octahedral sites occupied by Mn^{4+} and some Mn^{3+} ions. The result is an octahedral form in which the Mn^{4+} ion is surrounded by six O^{2-} ligands¹⁷. It is the arrangement of the $[MnO_6]$ octahedra that results in the formation of the different MnO_2 polymorphs. A listing of some of the more common polymorphs is shown in Table 1 along with the cell parameters and strong diffracting lines¹⁸.

Table 1. Structures of manganese dioxides¹⁸.

Compound	Crystal System	Unit Cell parameters (nm)			Strongest d-lines (Å)			
		a	b	c	d1	d2	d3	d4
Pyrolusite (βMnO_2)	tetragonal	0.440	0.440	0.287	0.314	0.241	0.163	0.213
Psilomelane (αMnO_2)	monoclinic	0.956	1.385	0.288 $\beta=92^\circ$	0.219	0.346	0.288	0.242
Cryptomelane(αMnO_2)	tetragonal	0.984	0.984	0.286	0.311	0.240	0.154	0.69/ 0.49
Ramsdellite (βMnO_2)	orthorhombic	0.927	0.453	0.287	0.407	0.161	0.136	0.254
$\gamma\text{-MnO}_2$	orthorhombic	0.935	0.444	0.285	0.24	0.14	0.21	0.16

$\alpha\text{-MnO}_2$ itself has two common forms. The first, psilomelane, has a monoclinic unit cell. The lattice is created by cross-linking the double or triple chains of the $[\text{MnO}_6]$ octahedra, which results in two-dimensional tunnels within the structure¹⁷. The structure is often unstable, and is stabilized in nature by incorporating cations into the tunnel portion of the structure. Often these are K^+ , Ba^+ or NH_4^+ . It is thought that without the cations, the tunnel structure would not exist. The simultaneous entry of the cation into the lattice during the crystallization of $\alpha\text{-MnO}_2$ is believed to cause tunnel formation. In order to maintain charge balance, some of the Mn^{4+} is replaced by Mn of a lower valence or cations of a lower valence but with a similar ionic radius. The cations within the $\alpha\text{-MnO}_2$ structure often adversely affect the performance of this material as a battery, which is why it is not often used for such applications¹⁷. The other $\alpha\text{-MnO}_2$ structure has a tetragonal lattice, although it too has the unique tunnel structure caused by the cross-linking of the $[\text{MnO}_6]$ octahedra¹⁸.

One of the most commonly occurring MnO_2 polymorphs is the $\beta\text{-MnO}_2$ phase existing in two forms: pyrolusite and ramsdellite. In this structure the $[\text{MnO}_6]$ octahedra will share edges in order to form single chains that extend along the c-axis¹⁹. Although this

structure is classified as a rutile, the true rutile structure is never met due to the distortion of the $[\text{MnO}_6]$ octahedra resulting in a lattice expansion in the c-axis and a contraction in the a and b axes. Ramsdellite is considered a dimorph of pyrolusite (and also part of the $\beta\text{-MnO}_2$ family) and is made by alternating double chains of linked octahedra, which are further cross-linked to adjacent double chains by sharing oxygen atoms^{17,19}. Because it is a non-equilibrium phase, ramsdellite tends to deviate from the MnO_2 stoichiometry more than pyrolusite¹⁸.

The $\delta\text{-MnO}_2$ or phyllosulfates group has a layer structure, which contains infinite two-dimensional sheets of edge-shared $[\text{MnO}_6]$ octahedra separated by approximately 10Å. There can then be intermediate layers of H_2O molecules that are bonded to the octahedral layers by a cation such as Zn^{2+} , Cd^{2+} , or Mn^{2+} . However, the layer structure indicates that this group of compounds is not a true modification of the MnO_2 structure.

$\gamma\text{-MnO}_2$, or nsutite, is a non-stoichiometric MnO_2 compound with Mn^{3+} replacing Mn^{4+} and OH^- replacing O^{2-} in the lattice¹⁷. In addition, it is common to have only partial substitution of the Mn^{4+} and O^{2-} , producing a wide variety of compositions within this subgroup and a wide variety of x-ray diffraction patterns for this group. As a result, these phases tend to have extensive defects and vacancies throughout the structure. $\gamma\text{-MnO}_2$ is commonly thought to be a hexagonal-type lattice structure. It has been suggested that $\gamma\text{-MnO}_2$ is fashioned from alternating layers of pyrolusite and ramsdellite^{18,20}. As a further note, the sub-group $\eta\text{-MnO}_2$ differs from $\gamma\text{-MnO}_2$ only in crystallite size and the concentration of microdomains of pyrolusite within the ramsdellite matrix; however, they have the same lattice. In addition, the $\eta\text{-MnO}_2$ group seems to have adsorbed water whereas the $\gamma\text{-MnO}_2$ group has chemically bound water. Most researchers consider these two sub-groups to be a single sub-group, $\gamma\text{-MnO}_2$.

Electrolytic MnO_2 (EMD or $\epsilon\text{-MnO}_2$) is often thought to belong to the $\gamma\text{-MnO}_2$ family²¹. However, it has a different structure. There is a hexagonal close-packed lattice of O^{2-} ions in which half the octahedral sites are filled randomly by Mn^{4+} ions, as with $\beta\text{-MnO}_2$.

While this structure is not thought to be based on the $[\text{MnO}_6]$ octahedra, it is thought that there may be some face-shared octahedra in $\epsilon\text{-MnO}_2$ ¹⁷. $\epsilon\text{-MnO}_2$ is considered to be a thermodynamically metastable state and is easily recrystallized to the more stable $\gamma\text{-MnO}_2$ and will form under conditions of high current density, enhanced nucleation or limited growth situations. Like $\gamma\text{-MnO}_2$, $\epsilon\text{-MnO}_2$ also has significant defects and vacancies within the structure. It is these structural imperfections that explain the high water content, porosity and specific surface areas of these two compounds¹⁷.

The thermal transformations that most likely occur between the different forms of manganese dioxide are shown in Figure 3.

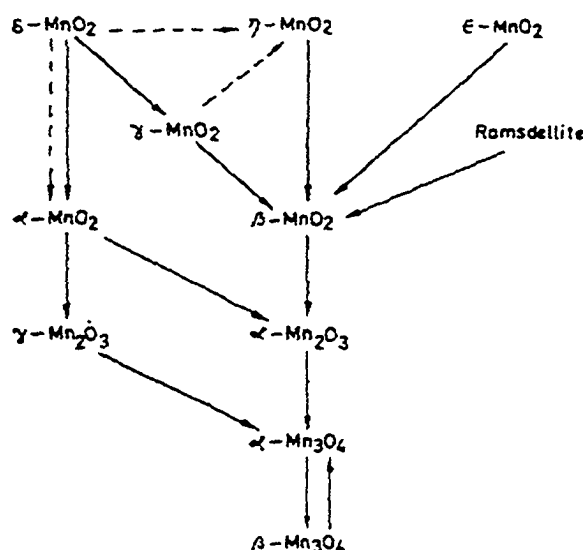


Figure 3. Schematic showing the transformations of the different forms of manganese dioxide¹⁸.

Of particular interest is that the various forms of MnO_2 all tend to form into the $\beta\text{-MnO}_2$ form. It is the most thermodynamically stable of the MnO_2 phases. $\alpha\text{-MnO}_2$ is the only product that does not decompose directly to $\beta\text{-MnO}_2$, but instead breaks down into either $\alpha\text{-}$ or $\gamma\text{-Mn}_2\text{O}_3$. However, it will decompose at a higher temperature than $\beta\text{-MnO}_2$, and thus the $\beta\text{-MnO}_2$ is still considered to be the most thermodynamically stable phase¹⁸.

2.2.2 Electrochemical Behavior of Mn and the oxides

2.2.2.1 Mn ions in solution

The behavior of manganese and its ions in aqueous solutions has been fairly well documented because of the importance of manganese oxide materials in the rechargeable battery industry. A Pourbaix diagram for manganese in aqueous solutions is shown in Figure 4. Through electrochemical oxidation, it is possible to produce manganese ions with oxidation states between +2 and +7 depending upon the particular conditions²². Mn is very unstable in most aqueous solutions. Under most conditions, the Mn^{2+} ion is the most stable oxidation state for the element. The stability is attributed to its unique electronic structure, which contains a half-filled d-band ($3d^5$)²³. The Mn^{2+} salts of strong acids are quite soluble, while the hydroxide salts are relatively insoluble²³.

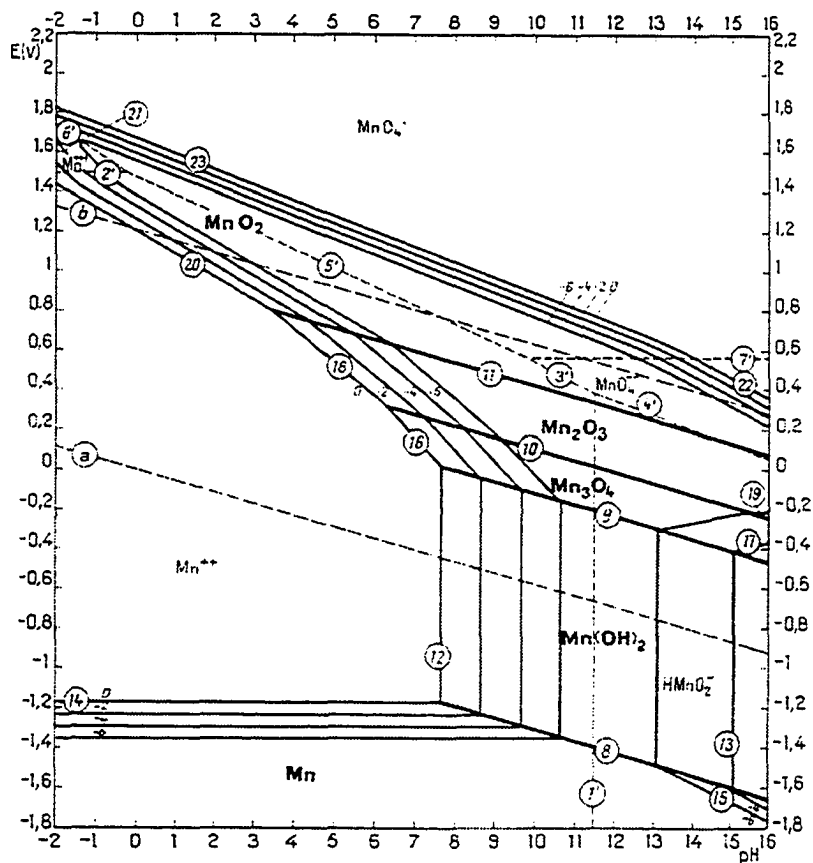


Figure 4. Pourbaix diagram for manganese in water assuming a temperature of 25°C and 10^{-6} M ion concentration²⁴.

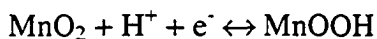
Mn^{3+} is extremely unstable in aqueous solutions because it is a very strong oxidizer and will quickly undergo disproportionation to Mn^{2+} and manganese dioxide²³. In aqueous solutions, the only stable Mn^{3+} exists as a solid of extremely low solubility, e.g., manganic fluoride and manganic oxide. Mn^{4+} is known to be a strong oxidizing agent, and its oxide, MnO_2 , is completely insoluble in aqueous solutions. Higher valences of manganese ions have been identified. The hypomanganate ion (MnO_4^{3-}) containing Mn^{5+} has been observed several times and is fairly stable in strongly alkaline solutions, but not at lower pH²⁵. Mn^{6+} generally exists as the manganate ion MnO_4^{2-} and is also quite stable in alkaline solutions. The permanganate ion (MnO_4^-) is the only important species containing Mn^{7+} . It is also a strong oxidizing agent and will slowly be reduced by the water in an aqueous solution. These higher valences of manganese are not generally found as solid oxides in nature²³.

2.2.2.2 Electrochemical behavior of MnO₂

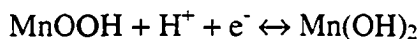
Of all of the oxides, MnO₂ is the most studied because of its use in batteries and electrochemical capacitors. As mentioned earlier, there are many different types of MnO₂ and the electrochemical behavior of each type is different. In view of the fact that γ -MnO₂ can be discharged more efficiently than the other types of MnO₂ and is, therefore, widely used for batteries and other cathode materials, the bulk of the literature, and hence my discussion, focuses on this particular form of MnO₂.

Neutral and Acidic Solutions

Based on investigations done in NH₄Cl at various pH values^{26,27} a reduction mechanism for MnO₂ in neutral and acidic solutions has been proposed. The first step in the primary cathodic reaction is the reduction of MnO₂ directly to aqueous Mn²⁺. The Mn²⁺ then reacts with the remaining MnO₂ on the electrode to give MnOOH. There is the possibility that MnOOH is formed from an intermediate product, Mn(OH)₂, but that has not been verified. More extensive studies done by Vosburgh et al^{28,29} identified a slightly different mechanism in which the initial product of the cathode reaction is actually MnOOH according to the reaction:



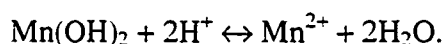
The formation of the MnOOH phase is considered to be due to the diffusion of protons and electrons into the MnO₂ lattice²⁸. When the current is applied to the electrode, electrons from the electrode and protons from the electrolyte will meet at the surface of the MnO₂ that is exposed to the electrolyte and also beneath the surface of the electrode where the protons have penetrated into the lattice. The electrons are used by the Mn⁴⁺ to form Mn³⁺ and the protons attach themselves to O²⁻ ions to form the OH⁻ ions, thus making the MnOOH phase³⁰. As the surface composition changes from largely MnO₂ to largely MnOOH, the electrode potential decreases. When enough MnOOH has formed on the surface of the MnO₂, a further reduction to Mn(OH)₂ occurs according to:



The next step is the appearance of Mn^{2+} in the electrolyte as the surface continues to reduce and the potential of the electrode continues to fall. However, this subsequent reaction is dependent on the pH of the electrolyte. At a pH of 5, the following reaction will occur:

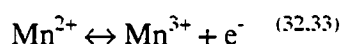


If the pH is increased into the neutral range, then the following reaction will occur instead:



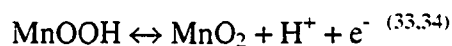
Technically, this final reaction involves two steps with the MnOOH that accumulates on the surface of the electrode being reduced to $\text{Mn}(\text{OH})_2$ and then the $\text{Mn}(\text{OH})_2$ is dissolved back into the electrolyte as Mn^{2+} .

More recent work on the oxidation and reduction of MnO_2 in an acidic environment was carried out by Nijjer³¹ et al in 2000. The reactions given are more specific and perhaps, more useful for subsequent analysis. Their analysis confirmed that the oxidation of Mn^{2+} to MnO_2 occurs in two steps. This first is an oxidation to Mn^{3+} as shown below.



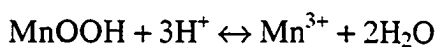
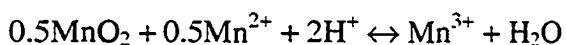
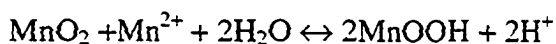
with the Mn^{3+} immediately hydrolyzing to form MnOOH and 3H^+ (33.34)

The second step is the production of MnO_2 according to:



The oxidation step to Mn^{3+} was found to be diffusion controlled, while the final reaction to form MnO_2 was controlled by the rate of the chemical reaction³¹. Thus, higher temperatures and convection enhance the oxidation rate of Mn^{2+} to MnO_2 .

The subsequent reduction of MnO_2 to Mn^{2+} was proposed by many researchers to occur by the reactions proposed for the oxidation of the Mn^{2+} (32,33,35). Other researchers have complicated the issue by suggesting various other reactions that are assumed to be occurring simultaneously^{34,36,37} and are listed below.

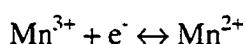


Alkaline Solutions

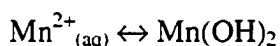
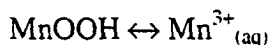
The reactions of the MnO_2 electrode in alkaline solutions were studied in depth by Bell and Huber³⁸. They suggest that the reduction of MnO_2 proceeds in three main steps. The first is the conversion of MnO_2 to $\text{MnO}_{1.7}$ occurs in a homogeneous phase reduction. Homogeneous reactions are chemical reactions that occur in the solution independently of the electrode³⁹. The second step is a further reduction to $\text{MnO}_{1.47}$ in a heterogeneous reduction (at the electrode/electrolyte interface) and then finally a reduction below $\text{MnO}_{1.47}$ in another heterogeneous reduction. It was also observed that under low current densities, the recrystallization of some of the lower manganese oxides would occur (Mn_2O_3 in some cases). It has also been suggested that the reduction of MnO_2 in alkaline solutions may produce MnOOH through an H^+ and electron diffusion into the crystal lattice, as seen in the acidic solutions, rather than forming Mn_2O_3 ²³.

Other studies by Kozawa et al^{40,41} in very concentrated alkaline electrolytes showed two distinct steps in the reduction process. The first is a reduction from MnO_2 to $\text{MnO}_{1.5}$ in which the potential was continually decreasing during the transformation. The electrons are introduced into the lattice and reduce the Mn^{4+} to Mn^{3+} . Simultaneously, H_2O

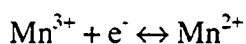
decomposes at the electrode/electrolyte interface and the protons are inserted into the lattice and form OH⁻. The second step is the reduction of the MnO_{1.5} to MnO by a reaction in which the potential does not change during this process indicating a two-phase region. This particular reduction step was found to occur entirely in the solution phase³¹, as the Mn³⁺ and Mn²⁺ oxides were both quite soluble in the very concentrated alkaline solution. Kozawa et al assume that the two solid phases involved are MnOOH (or MnO_{1.5}) and Mn(OH)₂ (or MnO) and that both are in solubility equilibrium with their ions, Mn³⁺ and Mn²⁺. The potential of the electrode can then be expressed as a function of the dissolved species Mn³⁺ and Mn²⁺ according to the overall reaction:



Under conditions where the two solid phases are in equilibrium with their respective ions, the concentration of ions in the solution will not change, and therefore, the potential, according to the Nernst equation, does not change. In other words, the dissolution of the MnOOH into solution to form Mn³⁺ and the precipitation of the Mn(OH)₂ phase from Mn²⁺ according to:



must occur faster or at the same rate as the overall reduction (in the solution) of Mn³⁺ to Mn²⁺ according to:



If this is the case, then the potential of the electrode does not change during the reduction reaction.

Cha and Park proposed a slightly different method for the oxidation/reduction²². In the first step, the Mn metal oxidizes to form a Mn(II) hydroxide which will passivate the

metal surface. The process continues through the production of manganese hydroxides of higher valence. The MnO_2 phase is finally produced through the simultaneous oxidation of $\text{Mn}(\text{OH})_2$ and MnOOH .

Gosztola and Weaver⁴² (in 1989) have identified a similar type of reduction mechanism shown in Figure 5.

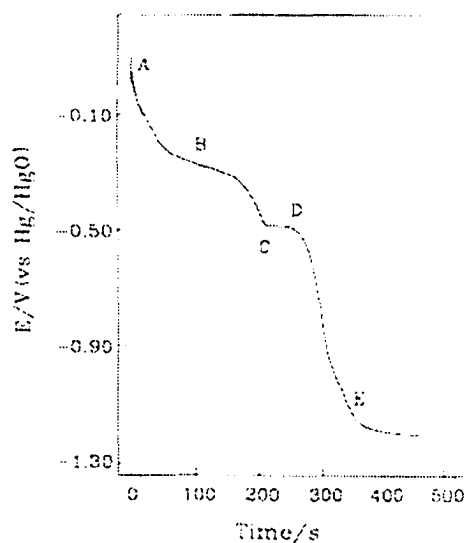
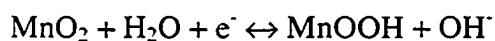
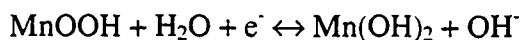


Figure 5. Galvanostatic potential-time curves for the reduction of MnO_2 film in 1 M KOH ⁴².

The region in Figure 5 labeled A-C is considered to correspond to the reduction of the γ - MnO_2 to the α - MnOOH according to:



The region of constant potential labeled C-D is considered to refer to the formation of the $\text{Mn}(\text{OH})_2$ phase by a heterogeneous (at the electrode/electrolyte interface) phase reaction^{40,42} according to:



Both of these reactions have been proposed in various forms by several other researchers^{22,23}. The region from D-E is considered to be the further reduction of the $\text{Mn}(\text{OH})_2$ to the metal Mn, though details of this process were not given.

Reactions based on a metallic Mn starting material in an alkaline medium were studied by Messaoudi et al in 2001⁴³. The transitions identified by the research are summarized in the schematic shown in Figure 6.

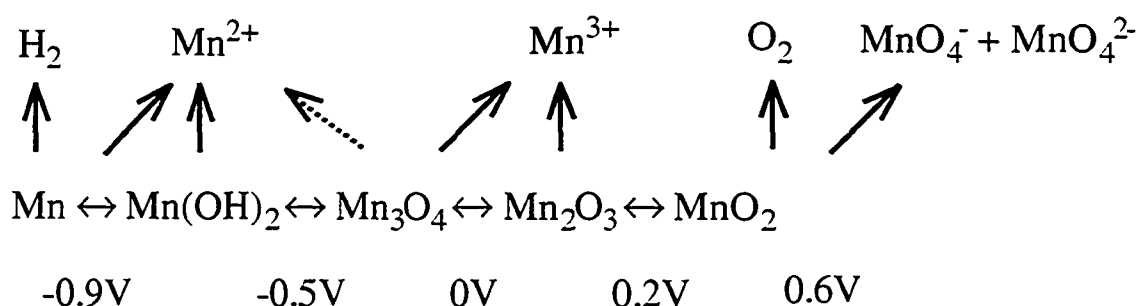


Figure 6. Schematic illustrating the various transitions occurring upon immersing Mn in an alkaline solution⁴³. The forward reaction is illustrated with the solid arrows and the reverse reaction is indicated with the dashed arrows. The potential of the transition is indicated below the reaction path, while the gas and soluble products are indicated above the main reaction path.

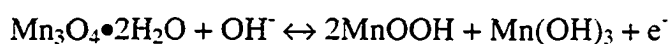
It was determined experimentally that metallic manganese, when immersed in a strong alkaline solution (1M NaOH), will immediately passivate. This reaction takes place at -0.9V vs. Hg/HgO, and involves the oxidation of Mn to $\text{Mn}(\text{OH})_2$ as illustrated in the first part of the schematic (Figure 6). This oxidation from Mn to $\text{Mn}(\text{OH})_2$ occurs with the elimination of H_3O^+ . At the same time, Mn is also directly ionizing into $\text{Mn}^{2+}_{(\text{aq})}$, and the $\text{Mn}(\text{OH})_2$ that forms is also producing $\text{Mn}^{2+}_{(\text{aq})}$ through a chemical dissolution process (Figure 6). This reaction can be best represented by:



There is a second passivation process that occurs at -0.5V vs. Hg/HgO where the $\text{Mn}(\text{OH})_2$ is transformed into Mn_3O_4 according to:



The third passivation process takes place at 0V vs. Hg/HgO and results in the formation of Mn_2O_3 during which Mn^{3+} is dissolved chemically from both the Mn_3O_4 and the Mn_2O_3 . The suggested reaction is:



where MnOOH is often considered the hydrated form of $\text{MnO}_{1.5}$ (Mn_2O_3)

On the other hand, reducing from Mn_2O_3 to Mn_3O_4 will result in the formation of a soluble Mn^{2+} species (Figure 6), which is either a hydroxide or a hydrated structure. Above 0.2V vs. Hg/HgO, Mn_2O_3 transforms to MnO_2 according to:



Above 0.6V vs. Hg/HgO, the MnO_2 converts to MnO_4^- (aq) and MnO_4^{2-} (aq) at the same time as the oxygen evolution reaction is occurring.

2.3 Electrochemical Supercapacitors

Electrochemical supercapacitors, or electrochemical capacitors, are charge storage devices that make use of electrochemical phenomena in order to store charge. Like all electrochemical systems, they require two electrodes (anode and cathode), an electrolyte, and a conducting charge path in order to operate. These four components are then packaged together and can be used, as a conventional capacitor would be. The capacitance can be defined as follows:

$$C = \Delta q / \Delta V \quad \text{where } q \text{ is charge and } V \text{ is the voltage} \quad (1)$$

However, because the system is electrochemical, the amount of charge, Δq , is defined by the current, i , according to:

$$\Delta q = \int i \cdot dt \quad (2)$$

and thus, the capacitance is defined as:

$$C = \int i \cdot dt / \Delta V = i \Delta t / \Delta V \quad (3)$$

There are two major types of electrochemical capacitors: those that exhibit a true capacitance (electrostatic), and those that exhibit a pseudocapacitance (Faradic). The electrostatic capacitors store charge directly across the electrical double layer, while the Faradic capacitors store the charge indirectly using a redox reaction.

2.3.1 Electrostatic Capacitors

2.3.1.1 Electrostatic Capacitance Theory

Electrostatic capacitors store the electric charge directly across the double layer of the electrode. Because there is no charge transfer across the interface, this is a true capacitance effect. Figure 7 is a very simplified schematic of the electrical double layer. The capacitance arises from the two array layers of opposing charges that are separated by a small distance (x), directly analogous to a parallel plate capacitor. As an excess or deficiency of charge builds up on the electrode surface, ions of the opposite charge build up in the electrolyte near the electrode/electrolyte interface in order to provide charge balance. In this manner, the amount of charge stored is proportional to the voltage

applied to the electrode as described by $C = \Delta q / \Delta V$ and the charge can be stored electrostatically, and released by simply reversing the polarity of the system.

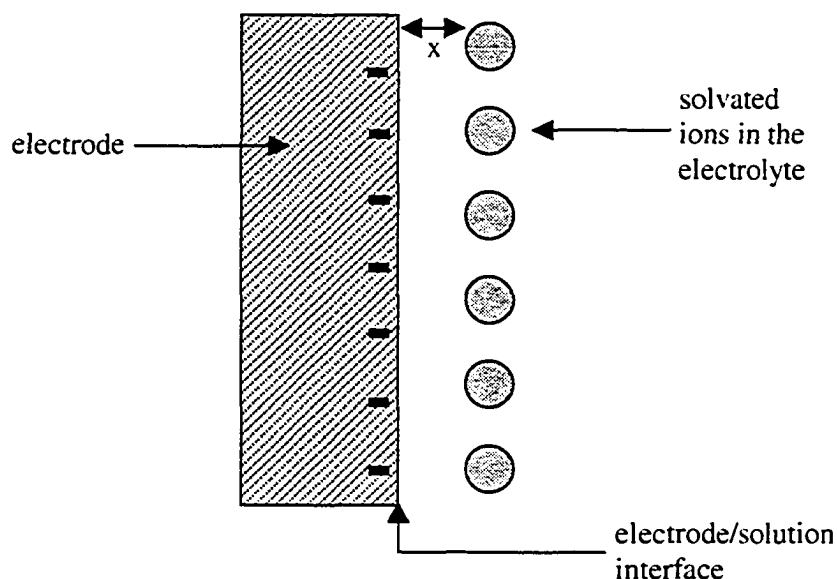


Figure 7. Simplified schematic of a double-layer capacitor.

If the current is held constant, and the electrode is truly electrostatic, then the capacitance does not change with changing potential. Thus, C can be calculated as the reciprocal of the slope of the relation between potential and time⁴⁴ as shown in Figure 8. This relation is only valid in a certain voltage range (particular to the system) until the Faradic decomposition of the solution begins and then there is a non-linear deviation from the original charging curve⁴⁴. Once this non-linear deviation occurs, the system is no longer considered electrostatic, and the capacitance cannot be calculated in this manner.

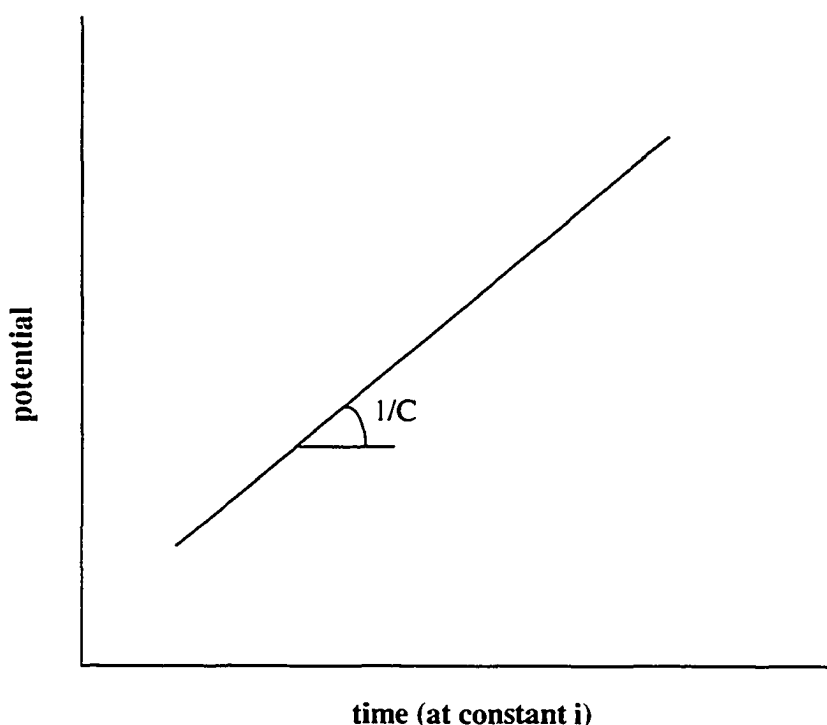


Figure 8. Charging curve for an electrode exhibiting electrostatic or double layer capacitance⁴⁴.

The CV (cyclic voltammogram) scans for an electrostatic electrode (Figure 9) exhibit a rectangular shape that is typical of an ideal capacitor with potential independent capacitance. With this type of testing, the applied potential is varied linearly with time and the resulting time-dependent current is measured, allowing for the construction of a potential/current graph. The anodic current corresponds to the discharging of the capacitor while the cathodic current corresponds to the charging of the capacitor. Because the capacitor is ideal and the capacitance is independent of potential, the anodic and cathodic currents are constant and equal in magnitude, although opposite in sign. In an ideal system, once the polarity of the system is reversed, the direction of current reverses immediately and results in the rectangular CV scan. As a result, the CV scan is very useful in determining the nature of the capacitor, whether it is electrostatic or otherwise. It can also provide a simple means of calculating the capacitance. From $C = i \cdot \Delta t / \Delta V$, the capacitance is defined as a function of the current and the $\Delta t / \Delta V$ term. In the case of

an ideal (electrostatic) capacitor, the current (i) is constant and the applied potential sweep rate of the scan, v , is simply the inverse of the $\Delta t / \Delta V$ term. Thus, the capacitance can be re-written for this ideal case as

$$C = i/v \quad (4)$$

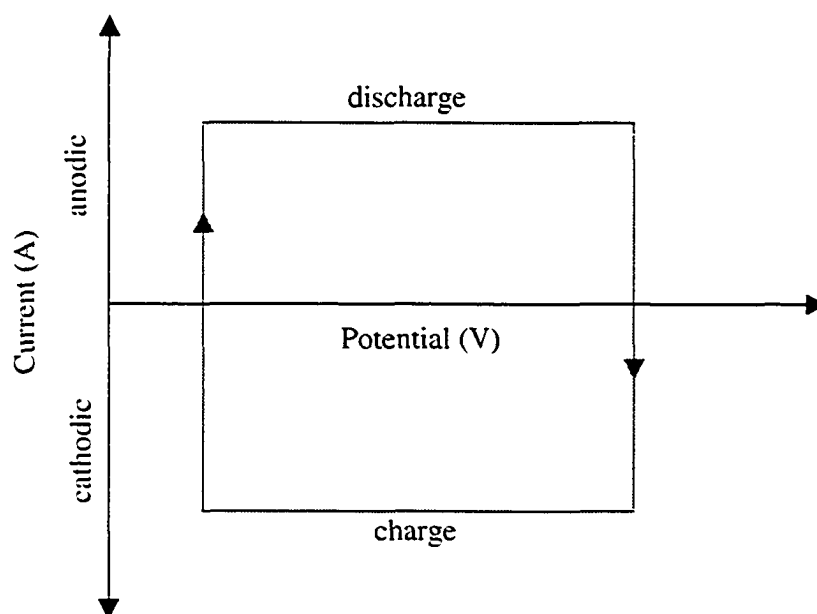


Figure 9. Cyclic voltammogram for an interface having potential-independent capacitance⁴⁴ (ideal capacitor).

Because electrostatic capacitors make use of the double layer in order to “store” the charge, the greater the amount of double-layer area, the greater the amount of charge that can be stored, giving rise to a large current and hence a large capacitance. Thus, very high surface area electrodes are employed for this kind of capacitor.

2.3.1.2 Activated Carbon Materials

Carbon based materials are very popular for these applications because of their low cost, high surface area, availability of material, and because it is already an established electrode production technology. In fact, carbon electrodes can be produced with a specific area of up to 2500 m²/g⁴⁵. Pure electrostatic capacitance is difficult to achieve outside of a parallel plate capacitor; however, activated carbon materials produce electrodes that are the closest to exhibiting true electrostatic capacitance behavior. While the overwhelming bulk of the capacitance is due solely to double-layer charging, it has been found that there is some element of the capacitance that is due to a redox reaction involving the surface functionalities on the surface of the carbon electrode⁴⁵. However, the behavior of these electrodes is very nearly entirely electrostatic.

Theoretically, these double-layer capacitors can reach a specific capacitance of 250 F/g; however, practically, only 20% of the theoretical value is achievable⁴⁴. Even at such seemingly low values, this translates to a greater capacitance per area than a conventional capacitor, accounting for the popularity of the electrochemical capacitor. A small disadvantage of these carbon electrodes is that they can sometimes have stability issues in the electrolyte⁴⁵ resulting in a slow breakdown of the capacitor.

2.3.2 Faradic Capacitors

2.3.2.1 Faradic Capacitance Theory

All Faradic capacitors are considered pseudocapacitors because there is an exchange or passage of charge across the double layer, rather than a static separation of charge across a finite distance as is the case with the electrostatic double layer capacitor. The capacitance originates because certain thermodynamic conditions cause a unique relationship between the extent of charge acceptance (Δq) and the change in electrode potential (ΔV) giving rise to the derivative $\frac{dq}{dV}$, which is defined as a capacitance⁴⁴.

From a thermodynamic perspective, pseudocapacitance originates when a property that is related to the amount of charge being passed, y , is related to potential by an equation taking the form⁴⁴:

$$y/(1-y) = K \exp\left(\frac{VF}{RT}\right) \quad (5)$$

where R is the ideal gas constant, T is the temperature in Kelvin, F is Faraday's constant and V is the potential.

Taking the derivative with respect to V gives the following relationship, dy/dV , which is proportional to the capacitance⁴⁴:

$$dy/dV = \frac{F}{RT} \cdot \frac{K \exp(VF/RT)}{\left[1 + K \exp(VF/RT)\right]^2} \quad (6)$$

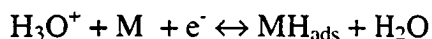
Theoretically, the maximum capacitance occurs at half the value of “ y ”.

If cyclic voltammetry (CV) is used to evaluate the capacitance of the system, the relationship in Equation 4, $C = i/v$, is still valid. However, unlike the electrostatic capacitors where the current is constant, for Faradic capacitors, the current is not always a constant value and may exhibit a current maximum. In this manner, a CV scan may be used to differentiate between systems that exhibit pseudocapacitance behavior and systems that exhibit electrostatic capacitance.

There are three main systems that produce a pseudocapacitive response: underpotential deposition, lattice intercalation, and redox systems. The latter is of primary interest to this thesis and will thus be discussed in greater detail than the first two systems, which will only be discussed very briefly. However, the general equations for pseudocapacitance hold true for each of the three systems.

2.3.2.2 Underpotential deposition pseudocapacitance

Underpotential deposition (UPD) systems are really an electrochemical surface process that gives rise to pseudocapacitive behavior. These types of systems involve the Faradic deposition or desorption of an electroactive species onto the surface of a metal electrode. One of the most common types of UPD systems is the deposition of H onto the surface of a metal, M (most often a noble metal) according to the following reaction where M is the metal electrode.



This type of process is very common for the deposition of hydrogen on catalytic noble metals such as Pt, Rh, Ru, and Ir⁴⁶ and also for base metal adatom deposition processes on Au or Ag⁴⁴. The process is referred to as an underpotential deposition because the potential at which the H ion is adsorbed to the surface is at potentials positive to the reversible hydrogen electrode potential and therefore occurs prior to the formation of hydrogen gas at the electrode surface. Thermodynamically, the Gibbs energy of the hydrogen to metal bond must be lower than the Gibbs energy for the hydrogen to hydrogen bond if adsorption pseudocapacitance is to take place.

The defining property for this process is the fractional surface coverage, θ , which is proportional to the amount of charge passed and hence corresponds to the variable “y” in the equations (5 & 6). The mathematics reveals that the maximum capacitance will be derived in the situation in which $\theta = 0.5$, or half of the sites on the surface are covered by adsorbed hydrogen. Because the passage of Faradic charge is required for the adsorption of the ion onto the surface of the material, the fraction of the electrode surface that is covered is a function of the amount of charge passing and the potential of the system and thus gives rise to a pseudocapacitive behavior. Unlike the electrostatic capacitor, the CV scan for a UPD system is not a true rectangle, but often has several current spikes that are common for pseudocapacitive behavior. Figure 10 shows a typical CV scan for the adsorption of Pb on a single crystal (110) Au electrode surface. The relatively rectangular shape of the scan indicates significant capacitance, but the multiple current

spikes during capacitive charging and discharging differentiate this type of pseudocapacitive scan from the electrostatic capacitor.

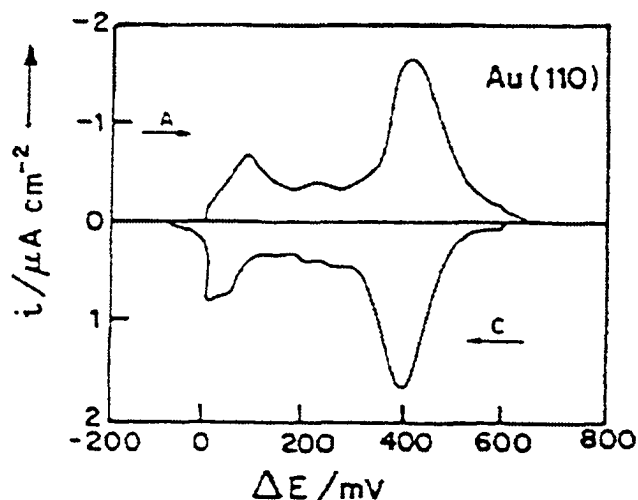


Figure 10. CV profile for the UPD of Pb adatoms on Au surfaces⁴⁷.

2.3.2.3 Intercalation pseudocapacitance

Intercalation systems are often thought of as a transition region between electrochemical capacitors and batteries and are quite similar to the UPD systems. Instead of involving surface adsorption, the ions are intercalated (inserted) into the lattice structure. A very common system is Li^+ intercalation into a layer-lattice host cathode material (MoS_2 , TiS_2 , V_6O_{13} , and CoO_2)⁴⁸. Although these types of intercalation systems are often used as batteries, their cyclic voltammetry profiles are consistent with what is seen in the UPD system and exhibit a similar type of pseudocapacitance behavior.

The defining property for this type of process is X , the occupancy fraction of the layer lattice sites. This then defines the fraction of available layer lattice sites in the host material, e.g., TiS_2 , that are occupied by the intercalated ion, e.g., Li^+ . Thus for this system, the property, y , in the defining equations, becomes X . Since a Faradic charge is required for the deposition of the Li^+ into the cathode host material, the quantity X

depends on the amount of charge that is passed and is thus related to the potential of the electrode, giving rise to a formal pseudocapacitance. Thus, like the UPD systems, maximum capacitance will occur at the half-occupancy of the available lattice sites by the intercalating ion⁴⁴.

2.3.2.4 Redox Pseudocapacitance

In addition to the two surface types of pseudocapacitance mentioned above, redox reactions can also give significant capacitance. There are a few different groups of materials that are capable of producing a redox pseudocapacitive response.

2.3.2.4.1 Conducting Polymers

Some polymeric materials, p- and n-dopable poly(3-arylthiophene), p-doped poly(pyrrole), poly(3-methylthiophene), or poly(1,5-diaminoanthraquinone) for instance, have exhibited pseudocapacitive behavior when used as capacitive electrodes^{49,50}. Because the behavior is pseudocapacitive, the typical CV curve is not rectangular like that of an ideal capacitor, but instead has a well-defined current peak at the redox potential of the polymer⁴⁵, making their performance more like a battery than a capacitor. These polymeric capacitors have comparable capacitance values to the other redox pseudocapacitance systems. However, the electroactive polymers often swell and shrink during cycling, ultimately degrading the quality of the capacitor making them difficult to use for long-term applications⁴⁵.

2.3.2.4.2 Transition Metal Oxides

Transition metal oxides also produce a pseudocapacitive response. Their CV characteristics are rectangular in shape like those for a purely capacitive electrode, but the shape is not due to pure capacitive effects as with electrostatic capacitors. Instead, the transition metal oxide electrodes undergo a sequence of redox reactions, rather than one, that gives rise to a rectangular shaped CV scan. This effect is a result of the many possible valence states for transition metals⁴⁵. Generally, it is thought that in order to provide effective pseudocapacitance, these films must have three characteristics. The first is good electronic conductivity. The second is the ability to exist easily in more than

a single oxidation state in order to accommodate the electron hopping. Finally, it is necessary to allow protons to freely intercalate into and out of the oxide lattice during the reactions according to the reaction $O^{2-} \leftrightarrow 2OH^-$. These electrodes can have very high specific capacitance coupled with very low resistance resulting in a high specific power, which makes them very appealing in commercial applications. The mechanism of pseudocapacitance has been suggested to be proton insertion into the lattice bulk causing a partial valence change in the host material. The most commonly used transition metal oxide for this type of electrode has been ruthenium oxide. However, there have been problems making these electrodes cost-effective and dealing with the toxic nature of the ruthenium, resulting in the pursuit of cheaper and less toxic raw materials, such as manganese oxide.

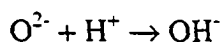
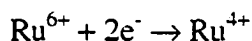
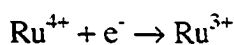
Ruthenium Oxide

Hydrous RuO_2 was studied extensively as an electrode material for electrochemical capacitors. Ultimately, specific capacitance values as high as 750 F/g were reported and the electrodes exhibited excellent cyclability ($\sim 10^5$) with little deterioration. Any degradation that does occur is due to the formation of RuO_4^{2-} at the high potential ends of the CV cycle⁴⁴. Unfortunately, the electrodes were found to be too expensive to pursue as a commercial product; however, the extensive research on this material may help explain the behavior of other transition metal oxide systems.

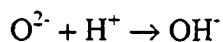
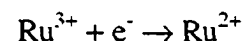
There are two procedures by which RuO_2 films have generally been formed. The first is to electrochemically cycle bulk metallic Ru or a similar ruthenized substrate, between 0.05 and 1.4V in aqueous H_2SO_4 to produce a hydrated RuO_2 product^{51,52,55,53}. Films of up to several microns thickness can be grown. The second method is to paint a suitably stable anodic metal (Ti) with $RuCl_3$ and then fire the deposit in an oxygen environment at 300–400°C^{54,56}. This causes a thermochemical decomposition resulting in RuO_2 . Both of these methods will produce electrochemically active RuO_2 films⁴⁴. However, it has been noted by several researchers that the electrochemically produced films have superior properties (in a capacitive sense) than the thermally produced films⁴⁴. This was postulated to be a result of the fact that thermally produced RuO_2 is only partially

hydrated, resulting in 2-7% of the Ru being involved in the redox reaction. In the electrochemically produced films, 100% of the Ru takes part in the redox reactions⁵⁵. Thus, it is suggested that the electron transfers are localized to sites where water molecules are present. In addition to the redox process that must occur to develop the pseudocapacitance, there must also be an injection or withdrawal of protons in order to electrically balance the conversion of O^{2-} to OH^- ⁵⁴. The increased hydration gives the film both protonic and electron-hopping conductivity as well. In addition, it has been suggested⁴⁴ that the capacitance developed by the thermally produced films is entirely due to double-layer capacitance, while the electrochemically produced films are clearly producing capacitance in excess of what can be developed by double layer charging alone.

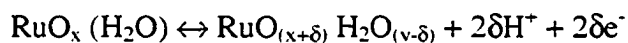
The mechanism for charging and discharging of the ruthenium electrodes is similar to the process used in Ni^{II}/Ni^{III} oxides⁴⁴. Because RuO_2 possesses relatively good conductivity ($10^{-4} \text{ ohm}^{-1} \text{ cm}^{-1}$)⁵⁶, it allows for relatively easy movement of electrons through the bulk electrode. In addition, if the RuO_2 has a hydrous structure, then proton transfer through the bulk is also made possible⁴⁴. No explanation is given as to why that is possible. These two effects allow simultaneous reactions to occur:



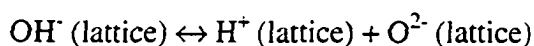
or



Both possibilities ultimately lead to the formation of $Ru(OH)_2$ ⁴⁴. A similar, but more general, redox process was proposed for the electrochemical oxidation of Ru in a hydrated state and is shown below⁵⁵.



Although the insertion of a proton into the lattice structure appears at first to be an intercalation process (as with Li^+ into MnO_2), this is not strictly true. The proton has a localized state (on O^{2-} as OH^-) and thus this charge/discharge mechanism is considered to be a redox mechanism rather than an intercalation mechanism⁴⁴. In addition, it is suggested that interlattice ionization of the hydrate water could provide additional OH^- or O^{2-} according to:



If this is the case, then it is important for the base electrode structure to have significant hydration.

The total specific capacitance exhibited by the film is due to both the redox pseudocapacitance and the double layer capacitance for the electrode⁵⁷⁻⁵⁸, which has been estimated to be as high as $150 \mu\text{F}/\text{cm}^2$ for these electrodes⁵⁹.

Manganese Oxide

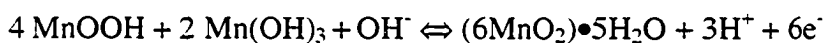
As an alternative material for the ruthenium oxide electrochemical capacitors, manganese oxides are currently being studied. Not only do these materials exhibit supercapacitive behavior, but also the technology of fabricating manganese oxides for battery applications is fairly well advanced making fabrication of an electrochemical capacitor a logical progression.

Several of the techniques currently being employed to produce porous manganese oxide films rely on wet chemistry methods, or wet chemistry in conjunction with electrochemical synthesis.

Electrochemical Deposition from chemical bath

Jiang and Kucernak⁶⁰ have produced an Mn_3O_4 structure containing a moderate amount of carbon to improve the electrical conductivity of the electrode using an

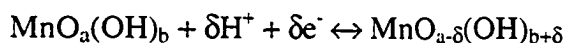
electrodeposition process from a manganese halide complex in water containing an acetonitrile electrolyte at room temperature. The film is deposited onto an indium-doped tin oxide (ITO) glass from the acetonitrile solution by cycling the potential several times between -1.2 and 1.5 V at room temperature. Approximately 800 cycles were used to produce a 12 micron film whose physical and chemical characteristics were studied for supercapacitor application. The films were identified as tetragonal hausmanite Mn_3O_4 with approximately 19wt% C. The capacitance values ranged from 50 to 144 F/g depending upon the cycle rate that was used. A faster CV cycling rate produced a smaller specific capacitance due to kinetic effects limiting the insertion of protons into the structure of the lattice. The charge storage on the film electrode was suggested to be a result of a sequence of redox reactions occurring in the manganese oxide shown below⁴³.



It has been further suggested that the charge storage process may be completed by the combination of chemisorption/desorption of ions from the electrolyte and proton insertion from the water, although no proof is offered⁶⁰. Similarly, there is no indication of the amount of hydration that is present in their structures although it is assumed that the oxide is produced in the hydrated state since it follows a similar procedure to that used for ruthenium oxide, which resulted in a hydrated oxide.

Hu and Tsou⁶⁴ and Hu and Wang⁷⁶ developed a procedure for producing an amorphous, hydrated electrode using a plating process. The $MnO_x \cdot nH_2O$ is electroplated directly onto a graphite substrate. Originally, the plating bath was 0.25M $MnSO_4 \cdot 5H_2O$ and the deposition was done potentiostatically⁶⁴ with a total passed charge of $0.4 C/cm^2$. These anodically deposited films were shown to exhibit fairly substantial capacitance values of

36–43 mF/cm²⁶⁴. Hu and Tsou proposed that the mechanism for developing capacitance was analogous to that for ruthenium oxide.



The original work⁶⁴ by Hu and Tsou further investigated the effect of annealing on the capacitance of the films, as it was previously shown that annealing had the positive effect of stabilizing the ruthenium oxide films. The annealing of the manganese films, however, resulted in a fairly significant loss of capacitance (measured at room temperature), often half the value at the higher annealing temperatures. This loss of capacitance was felt to be a result of the reconstruction of the oxide, where surface Mn oxides that have lower coordination numbers would move into the lattice, effectively reducing the number of non-stoichiometric sites and thus reducing the number of possible sites for redox transition. Perhaps more importantly, their XPS (X-ray photoelectron spectroscopy) O1s deconvolution results show that during the annealing process, the hydrated portion of the film (Mn-O-H) is reduced from 38.80at% to 14.36at%. This is a fairly significant decrease in hydration, and should result in reduced capacity for proton movement within the lattice structure.

In the later work by Hu and Wang⁷⁶, the plating bath was adjusted to 0.16 M MnSO₄·5H₂O with a pH of 5.6⁷⁶. The deposition occurred potentiostatically at 0.8V, galvanostatically at 3.7mA/cm² or using cyclic voltammetry at 10mV/s between potentials of 0.4 and 1.0 for 30 cycles. Morphologically, the galvanostatic and CV films look quite similar exhibiting a three-dimensional nano-structured network, termed nanorods. XPS analysis for these films indicated that they were a mixture of Mn(II), Mn(III) and Mn(IV). Each different method of deposition (potentiostatic, galvanostatic, and CV) resulted in approximately the same quantity of each Mn species, but a more substantial difference in terms of the relative hydration of the film (information from the O1s spectra). The results are summarized below in Table 2.

Table 2. XPS analysis for films deposited using potentiostatic mode, galvanostatic mode, and CV mode.⁷⁶

Deposition Mode	Mn (II) at%	Mn (III) at%	Mn(IV) at%	Mn-O-Mn at%	Mn-O-H at%	H-O-H at%
Potentiostatic	13.86	29.69	56.45	64.21	25.68	10.11
Galvanostatic	16.89	27.90	55.21	60.34	23.07	16.59
CV	17.98	24.30	57.72	71.74	14.82	13.44

Clearly, the CV method of deposition results in films with the smallest quantity of hydration within the oxide structure (Mn-O-H), which may result in poor capacitance. However, that is not the case. The galvanostatic deposition results in the highest capacitance at 230 F/g followed by the CV deposition with 200 F/g. Potentiostatic deposition results in only 150 F/g of capacitance being developed. Although there is no full explanation for this result, the FE-SEM (field emission scanning electron microscope) images of the three different films suggests less porosity for the film deposited under potentiostatic conditions which may therefore account for the poor capacitance.

More recently, Hu and Wu⁶¹ have produced capacitive electrodes from a 0.1 M solution of $\text{Mn}(\text{CH}_3\text{COO})_2 \cdot 4\text{H}_2\text{O}$, again using potentiostatic deposition at 1.0V. It was found that increasing the thickness of electrodeposited material ultimately reduced the capacitive response of the film. This decrease in capacitance was attributed to the increase in the equivalent series resistance for the thicker deposit because of the relatively poor conductivity of amorphous MnO_2 coupled with the significant proton diffusion barrier in these thicker materials⁶¹. No capacitance values were available in the article nor was there any explanation of why potentiostatic deposition was used despite its previously poor result in terms of capacitance.

Similarly, a research group from Japan, Chigane and Ishikawa and Izaki^{75,77} has also been working on a potentiostatic deposition procedure with fairly similar results. The first

procedure involved a substrate of glass coated with conductive tin oxide being immersed in a solution of manganese ammine complex $[\text{Mn}(\text{NH}_3)_x^{2+}]$ with a pH of 8. The film was deposited using a potential of 0.2V vs. Ag/AgCl for 1 h and 1.2V for 1 min at 298K⁷⁵. With the second attempt, the procedure was modified slightly to include an anodic electrolysis at 1.2V for 30 s followed by a chemical deposition for 2 hours at 298K. At potentials below 0.4V, Mn_2O_3 and/or Mn_3O_4 formed during the deposition process. At potentials of 0.4V and above, $\text{Mn}_7\text{O}_{13} \cdot 5\text{H}_2\text{O}$ formed, and is often considered to be a hydrated, non-stoichiometric MnO_2 compound. The extensive XPS work done by this group is summarized in Table 3.

Table 3. XPS peak analyses of MnOx films deposited at different potentials.⁷⁵

Sample	Valence	Mn-O-Mn (at%)	Mn-O-H (at%)	H-O-H (at%)
0.2 V	2.3	41.37	51.80	6.83
0.3V	3	46.84	44.98	8.18
0.4V	3.4	64.97	18.80	16.23
0.6V	3.4	73.07	15.75	11.18
0.8V	3.4	74.62	16.08	9.30
1.2V	3.4	67.86	18.66	13.48
1.7V	3.4	71.91	21.15	6.94

Deposition at the lower potential values (0.2V and 0.3V) resulted in significantly more hydration than deposition at the higher values (>0.4V). No reason was suggested for these data, neither was it postulated as to whether or not the increased hydration was somehow related to the different phase that formed at lower potentials. Additionally, there was no capacitance data to indicate which films exhibited superior capacitance, although it was briefly suggested that the best electrochemical behavior was found in the films produced at the higher potential of 1.2V. Unfortunately, there were no data presented to explain this result.

Further analysis⁷⁵ has suggested a mechanism for charging and discharging based on the releasing and combining of H^+ from a terminal OH group to oxygen within the oxide structure resulting in a valence shift between 2+ and 4+. This reaction is summarized below.



Powder synthesis from wet chemistry procedures

Powder synthesis methods typically result in a hydrated, amorphous MnO_2 product or a weakly crystalline product^{62, 63, 64, 65, 66, 67}. Some of the original work fabricating these types of materials as powders was done by Tsang, Kim and Manthiram⁶⁸. The process involves a reduction reaction between a fixed volume of 0.1M KMnO_4 (50 mL) and varying volumes of 0.25M KBH_4 . The KBH_4 is dissolved into a solution of KOH in order to maintain a high pH (11-12) to prevent the rapid loss of hydrogen before the reduction reaction through the hydrolysis of the borohydrides. Their results are presented in Table 4. Note that the phases for each sample were identified after heating in an evacuated, sealed silica tube at 550°C for 2 days. The valence state of the oxide produced was determined through potentiometric redox titration.

Table 4. Reduction of 50 mL of 0.1 M KMnO_4 with varying amounts of 0.25M KBH_4 at varying pH⁶⁸.

pH	Volume of KBH_4 (mL)	Water Content (nH_2O)	Oxidation state of Mn	Phases
1	3	0.76	3.68	MnO (100%)
1	20	0.79	3.78	Mn_2O_3 (100%)
3	10	1.15	3.97	$\text{K}_{2-x}\text{Mn}_8\text{O}_{16}$ (70%) Mn_2O_3 (30%)
3	30	0.86	3.69	Mn_2O_3 (100%)
6	3	1.27	3.76	MnO (100%)
6	20	0.31	3.05	Mn_3O_4 (100%)
11	3	1.62	3.99	$\text{K}_2\text{Mn}_4\text{O}_8$ (90%) Mn_3O_4 (10%)
11	10	1.74	3.99	$\text{K}_2\text{Mn}_4\text{O}_8$ (95%) Mn_3O_4 (5%)
11	28	0.69	3.58	Mn_2O_3 (40%) Mn_3O_4 (60%)

Initial XRD results from the samples in their as-deposited state indicated that they were amorphous; however, the SAD patterns from these same samples suggested that they were nano-crystalline and not completely amorphous as previously thought. The information contained in Table 4 suggests that any number of phases may be produced through this process making it quite versatile. However, it is important to note that the MnO_2 phase is only produced as a K-based compound. Under acidic conditions ($\text{pH}<3$), the oxidation state is greater than 3.68+, which is consistent with the previously developed solution chemistry in which Mn^{3+} will disproportionate in an acid to give Mn^{4+} in the solid and Mn^{2+} in the solution⁶⁹. At the more neutral conditions, oxidation states of close to 3+ are achieved due to the relative stability of Mn^{3+} in neutral solutions.

Additionally, there is a tendency to produce potassium based products at the higher pH values.

Jeong and Manthriam⁶⁷ continued the previous research to some degree, but with some slight changes to the procedure. 0.1M KMnO_4 was still combined with 0.25M KBH_4 , but with the addition of $\text{Na}_2\text{S}_2\text{O}_4$, $\text{NaH}_2\text{PO}_2\cdot\text{H}_2\text{O}$ or some HCl. Once the powdered material had been produced, it was mixed with 25 wt% carbon and 5 wt% polytetrafluoroethylene. This mixture was then added to a small amount of water to make it more homogeneous, then the entire mixture was rolled out and cut into square pieces with a thickness of 0.1mm. An electrode was made by pressing these squares onto pieces of titanium to give the necessary support. With only these small changes to the procedure (addition of certain other chemicals), the powder phase has been identified as nano-crystalline MnO_2 which is a slight change from the previous results. The major change has been the elimination of the potassium ion in the compound. Samples reduced with just KBH_4 were found to have the best capacitance values. A summary of the results from these investigations is tabulated in Table 5.

Table 5. Synthesis conditions and capacitance of the various samples.⁶⁷

Reducing agent	pH	Capacitance (F/g)	
		After drying at 75°C	After drying at 100°C
KBH_4	1	248	234
KBH_4	3	161	155
KBH_4	6	120	132
KBH_4	11	153	109
HCl	0.5	164	126
$\text{Na}_2\text{S}_2\text{O}_4$	1	191	160
$\text{NaH}_2\text{PO}_2\cdot\text{H}_2\text{O}$	1	175	177

There are some general trends that can be taken from these data. At a constant drying temperature, an increase in the pH of the solution used to produce the powder results in a

decrease in the capacitance of the electrode. At the same pH, KBH_4 is obviously the superior reducing agent followed by $\text{Na}_2\text{S}_2\text{O}_4$ and then $\text{NaH}_2\text{PO}_2 \cdot \text{H}_2\text{O}$. Generally, the films dried at the lower temperature exhibited greater capacitance values; however, this was not always the case (i.e., KBH_4 with a pH of 6). These differences in capacitance are attributed to differences in surface area. Less surface area is produced at higher pH values, while more surface area is produced for KBH_4 -based reactions. It is felt that the differences noted as a function of drying temperature are due to the composition of the final films and the relative hydration.

The effect of electrolyte was also studied with respect to these films. Three different electrolytes were studied, KCl , Na_2SO_4 and LiCl . The results from the tests in different electrolytes are shown in Table 6.

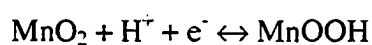
Table 6. Capacitance values in various electrolytes.⁶⁷

Electrolyte	Sample drying temperature (°C)	Capacitance (F/g)
2M NaCl	As-prepared	186
2M NaCl	50	210
2M NaCl	75	248
2M NaCl	100	234
2M NaCl	125	171
2M NaCl	150	177
2M KCl	75	195
2M LiCl	75	180
0.1 M Na_2SO_4	75	188

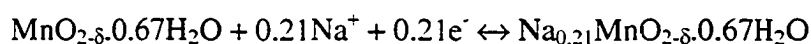
The first result is that an increase in drying temperature causes an initial increase in capacitance, reaching a maximum at 75°C followed by a decrease in capacitance with further temperature increase. This suggests that there is an optimum water content and that the associated microstructure and degree of crystallinity are essential to maximizing

the capacitance. It is suggested that the decrease in water content with increasing drying temperature may increase the degree of crystallinity and thereby the degree of chemisorption and hence the capacitance values. With respect to the different electrolytes, the NaCl electrolyte produces the highest capacitance values, followed by KCl, Na₂SO₄, and finally LiCl. The capacitance values ranged from 248 F/g as the highest value, and 180 F/g as the lowest value. Each of the CV scans exhibited the typical rectangular shape for pseudocapacitance with no redox current spikes apparent for any of the electrolytes. The differences in capacitance for these electrolytes is related to the hydration spheres of the various ions. Although the K ion itself is fairly large, it has a smaller hydration sphere than the Li ion, which leads to faster diffusion and a faster chemisorption rate. Both Na and K have similar hydration characteristics, but because the Na is a smaller ion to begin with, it has slightly better capacitance values. The reason that Na₂SO₄ has a lower capacitance rate than the NaCl is related to the SO₄²⁻ ion, which is thought to decrease the chemisorption rate and therefore decrease the capacitance⁷².

Jeong and Manithram⁶⁷ suggest two alternative reactions that may account for the pseudocapacitance behavior. The first involves just the Mn ions, while the second is based on the intercalation of an ion from the electrolyte into the manganese oxide lattice.



or



The research group Hong, Lee and Kim⁷⁰ and Lee, Kim and Lee⁶⁵ has also worked on a precipitation procedure coupled with a KCl electrolyte. They used a similar type of precipitation process, mixing KMnO₄ with a manganese acetate aqueous solution causing instantaneous precipitation. To fashion an electrode, the powder was mixed with 30wt% conducting carbon. This entire mixture was then homogenized in a mortar with poly(vinylbutral-co-vinyl) in order to make a slurry. This slurry was then dried onto a titanium foil in order to add structure to the electrode. This procedure, then, was very similar to the other procedures, with the exception of using slightly different chemicals.

In the original work⁶⁵ the need for conducting carbon was demonstrated quite clearly as it was shown that films without the carbon did not develop very significant capacitance values. It was suggested that the large capacitance values are a result of the extension of the active site area by the point contacts that develop between carbon and the MnO_x . The researchers suggested that the active sites within the oxide lattice could be extended through contact with the carbon particles since the electrons are expected to flow from the contact point between the carbon and the surface of the oxide a short distance away, thereby extending the overall active area and improving the capacitance behavior. The carbon-mixed electrodes exhibit the typical rectangular cyclic voltammograms, developing specific capacitance values as high as 210 F/g. This value is within the same range as other research that is occurring in this area. However, there was very little microstructural analysis to accompany these results.

A Canadian group is also working with a similar type of precipitation reaction⁶². KMnO_4 was dissolved in de-ionized water and then MnSO_4 was added. Immediately upon the addition of the MnSO_4 , precipitation occurred according to $2\text{Mn}^{7+} + 3\text{Mn}^{2+} \rightarrow 4\text{Mn}^{4+}$, thereby producing the 4+ valence in the manganese. In order to produce an electrode, the precipitated powder was mixed with 7.5wt% of acetylene black, 7.5 wt% graphite, and 5wt% poly(tetrafluoroethylene) to produce a rubber-like paste. This rubber paste was then flattened and pressed onto a stainless steel grid to provide a backing substrate support.

In the as-deposited state, a weakly crystalline MnO_2 product was formed. Upon annealing, the powder samples became more and more crystalline and at 400°C decomposition of MnO_2 to Mn_2O_3 begins. By 600°C, the entire powder had become fully crystallized Mn_2O_3 . FE-SEM images showed a fairly rough surface with significant porosity and surface area. The calculations showed a specific surface area of 180 m^2/g that should give substantial double layer capacitance in addition to the pseudocapacitance. The average manganese valence was 3.85 indicating the presence of both the 4+ cation and the 3+ cation. In terms of the electrochemical behavior, the CV scans exhibit the typical rectangular shape that is associated with pseudocapacitance in

the Na_2SO_4 electrolyte. No capacitance behavior was noted in the H_2SO_4 or NaOH electrolytes. Both of these electrolytes show irreversible redox peaks. At the higher CV sweep rates, the capacitance values developed were fairly low, 100 F/g compared with other research that is being done. However, the authors reported much higher capacitance values at a lower sweep rate (2mV/s), but it is commonly known that a lower sweep rate greatly enhances the capacitance.

Toupin et al⁶² did have some very interesting results regarding the effects of annealing on the capacitance of the films. They noted that the as-precipitated powder showed the highest specific capacitance. After heating for 3 hours between 100 and 200°C, there was a noted decrease in capacitance of 20 F/g. Additionally, as the temperature of the annealing was increased, the capacitance value decreased more and more rapidly. After annealing at 600°C, very little capacitance was measured (40 F/g). It was suggested that the heat treatment between 100 and 200°C removed both the physically and chemically adsorbed water and decreased the surface area of the active material, causing an overall decrease in the capacitance value. Above 400°C, there was a decomposition of the MnO_2 into Mn_2O_3 , which ultimately led to the very significant decrease in capacitance that they noted. These results are only in partial agreement with the previous work done.⁶⁷

The superior results have thus far come from a group at the University of Wisconsin-Madison using a precipitation process. The initial step in this process is a reaction of Mn(VII) (potassium permanganate) with Mn(II) (manganous perchlorate) in an alkaline aqueous medium (~pH 10.5) to produce small particles of manganese oxide^{63,66}. Later, they adjusted the procedure to use a stable colloidal suspension of tetrapropylammonium manganese oxide (TPA-MO) that was produced through reduction of tetrapropylammonium permanganate with 2-butanol in an aqueous solution⁷¹. In each case, a dip-coating process was used, in which a nickel foil was dipped in a solution of the manganese oxide particles produced by either process, until a film of desired thickness was produced. In addition, an electrochemical deposition process was used for comparison to the sol gel process by applying a positive potential of 0.4V vs. SCE to a solution of manganous acetate and sodium sulfate.

With these procedures, the CV curves are rectangular scans indicating the strong pseudocapacitive reaction, although the sol-gel deposited films are slightly more rectangular⁶³. The results for the capacitance that can be developed by these films is tabulated in Table 7.

Table 7. Average specific capacitance of dip-coated sol-gel and electrodeposited MnO₂ films⁶³.

Sample		Average specific capacitance (F/g)
Sol Gel	300°C	678
	200°C	607
Electrodeposition for 300s	25°C	350
	300°C	389
Electrodeposition for 600s	25°C	311
	300°C	359

The tabulated data show that the maximum capacitance values can be reached for the sol-gel films, often with a specific capacitance value over double that of the electrodeposited films. It is thought that this is related to the fact that the films produced by electrodeposition are significantly thicker than the sol-gel coated films⁶³. In addition, the capacitance values increase quite substantially with the annealing or calcining temperature. This effect is attributed to fact that the higher annealing temperature causes the desorption of surface and some structural water, but does not cause decomposition to other manganese oxides. Thus, the increase in capacitance is suggested to be due to the increased electrical conductivity that accompanies the annealing.

The pseudocapacitive reaction proposed by the Wisconsin group is very similar to that proposed by the other groups, just written in a slightly different manner:

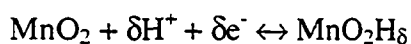


Charging occurs in the left hand direction (production of MnO_2) and discharging occurs in the right-hand direction towards the consumption of MnO_2 . The overall reaction can be split into two reactions at each electrode, the positive and the negative electrode. At the positive electrode, the following reaction will occur.



with charging resulting in the production of MnOOH .

At the negative electrode, the following reaction is occurring:



with charging resulting in the production of MnO_2 .

In a subsequent study⁶⁶, more attention was paid to the microstructural characterization of the films resulting from the sol-gel and electrodeposition procedure. The x-ray diffraction data indicate that even after annealing the film at 300°C, it remains amorphous. This, in fact, is an advantage of their process as an amorphous structure can more easily accommodate the insertion of protons during charging and discharging cycles. From FE-SEM images, both the sol-gel and electrodeposited films are extremely porous with quite large surface areas. XPS analysis was carried out on the films, but no deconvolution data were presented. Instead, it was noted that the peak positions did not vary significantly. These films showed excellent reversibility of the supercapacitor with no permanent phase changes being detected after 1500 cycles for thinner samples. Thicker samples, however, did show more permanent changes upon cycling perhaps accounting for their relatively poor performance.

In the most recent work by this group with the slightly adjusted procedure, the maximum specific capacitance was reached using a structure that was heated to 300°C, but remained amorphous⁷¹. The researchers have attributed the high capacitance to the fact that the amorphous phase allows unhindered movement of the proton into the lattice, enhancing stability and charge capacity. As well, the heat treatment will lower the water

content of the film increasing the electronic conductivity⁷¹, but the film remains amorphous to allow for easy proton movement. These electrodes have produced specific capacitance values of 720 F/g equaling that of ruthenium oxide, which is the state-of-the-art value.

In general, there are two opposing theories concerning the mechanism of pseudocapacitance in the Mn oxide films. Many researchers feel it is an analogous process to ruthenium with the insertion of a proton into the bulk lattice^{63, 66, 71}. However, there are those researchers who feel the mechanism is related to the surface chemisorption of electrolyte ions such as Na⁺ and K⁺^{67, 72}. As yet, there is no clear indication as to which mechanism is correct.

Physical Vapour Deposition Methods

Physical vapour deposition has been studied in the past as a possible way of making electrochemically active devices⁷³. The oxide film was deposited using e-beam evaporation onto a substrate of glass and ITO (indium tin oxide). The deposition took place using a pure Mn target (>99.9%) in an atmosphere of 8×10^{-4} torr of oxygen in order to produce an oxide film. X-ray diffraction did not identify the film as rutile (MnO₂) as expected, but as Mn₃O₄. The films were then immersed into a solution of 1M LiClO₄/γ-butyloactone (an organic electrolyte) in order to measure the CV characteristics of the particular film. The as-deposited film of Mn₃O₄ demonstrated significant electrochemical activity when immersed into the electrolyte, developing fairly significant charge storage. For the Mn₃O₄ films, a charge storage of 35 mC/cm² (17.5mF/cm²) was initially measured, dropping to 3 mC/cm² (1.5mF/cm²) after 2×10^4 cycles. With this system, however, the CV curves were not typical of a pseudocapacitive system with a mirror image, rectangular shape. Instead, the CV scans were asymmetric, exhibiting some current spikes that are indicative of a redox process, which is likely the cause of the significant reduction in charge capacity during long term cycling tests. Nonetheless, this paper provides a significant contribution in terms of developing alternate processing routes for these devices.

More recently a technique was developed to produce the manganese oxide capacitor materials using a combination of physical vapour deposition and electrochemical processes rather than the traditional wet chemistry methods described previously. With this technique, the metal film is deposited (by sputtering or e-beam evaporation) and then electrochemically oxidized separately. The advantage of this particular technique is that thin-film deposition of metal films is considered to be highly scaleable and already well known in the manufacturing industry⁷⁴. In addition, there may be some advantage to depositing the metal film first and then oxidizing the structure as it may provide more flexibility during processing.

Metal chevron films were deposited using e-beam evaporation with the GLAD deposition apparatus that was discussed earlier. The base pressure was typically 5×10^{-7} torr and deposition was done on Si wafers with layers of Si_3N_4 , Ti, and Pt, respectively, to provide a dielectric surface, an adhesion layer, and an innocuous standardized base layer for the experiments. Depositions were conducted using vapour incident angles ranging from 50° to 86° , and also at 0° in order to examine the supercapacitive behavior of the bulk material. All as-deposited manganese films were roughly 500 nm thick.

The oxidized structure that exhibits the supercapacitive behavior must be produced in two separate steps. The first step involves a pre-conditioning of material in which the films are oxidized in the electrolyte for 30 minutes with a current capped at $100 \mu\text{A}$. The pre-oxidation step is not thought to completely oxidize the material, but to stabilize the film prior to completing the oxidation⁷⁴. The oxidation of the film is completed during the first few CV cycles, and is considered to be complete once the CV cycle stabilizes. Porous films ($>60^\circ$) responded quite well to this procedure, although it was found to be more difficult on the denser materials ($<60^\circ$). According to Broughton and Brett, this is possibly due to a lack of electrolyte penetration into the film.

A typical CV scan for a manganese chevron film deposited at 84° is shown in Figure 11. The large rectangular shape of the curve that is seen for the Mn film and not the Pt film is

typical of capacitor materials and confirms that these films have fairly significant capacitance values.

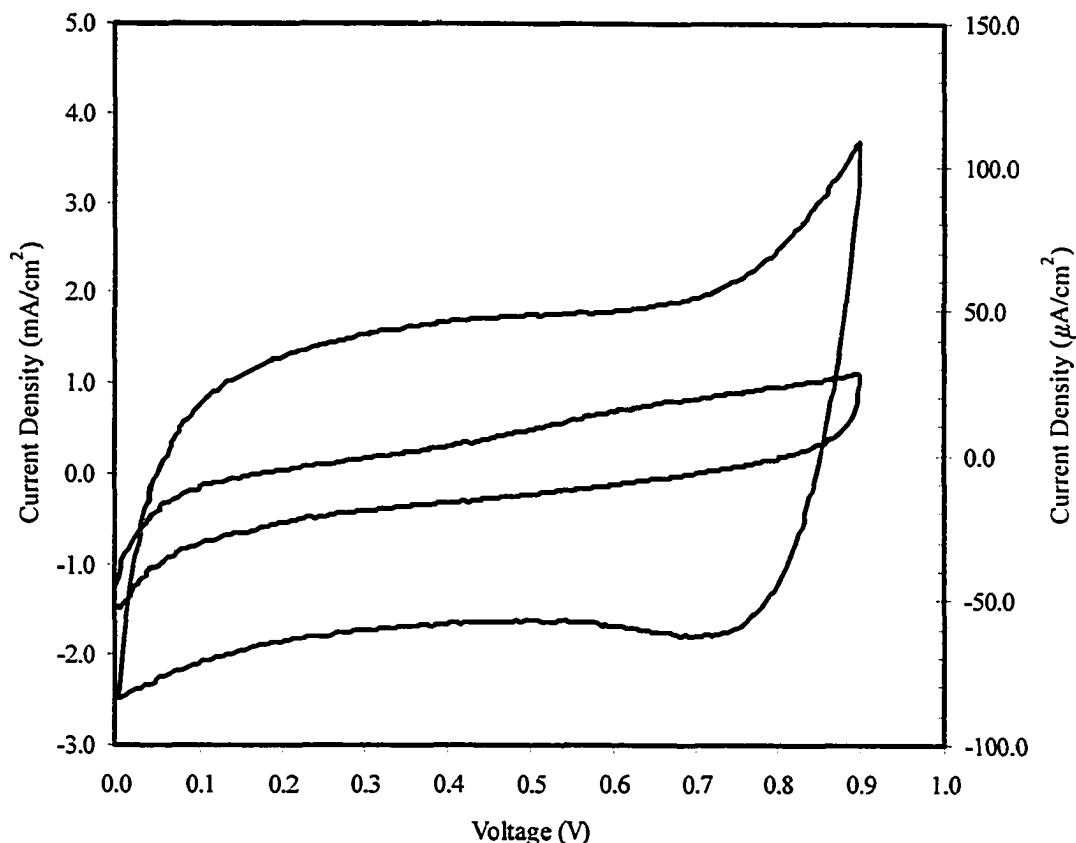


Figure 11. CV scan of a Mn film deposited at 84° using $0.1\text{M Na}_2\text{SO}_4$ and a sweep rate of 50mV/s . Also shown on the right axis is the CV scan of a blank Pt wafer for comparison⁷⁴.

The specific capacitance of these films as a function of the film deposition angle is shown in Figure 12. Dense films (0° up to approximately 65°) exhibit a constant specific capacitance below 150 F/g . However, decreasing the density of these films by increasing the deposition angle ($>65^\circ$) will increase the specific capacitance of the films to approximately 225 F/g ⁷⁴. Although this value has not yet reached the levels of Chin et al⁷¹ at 700 F/g , it is consistent with the results obtained by other groups presented in the previous sections.

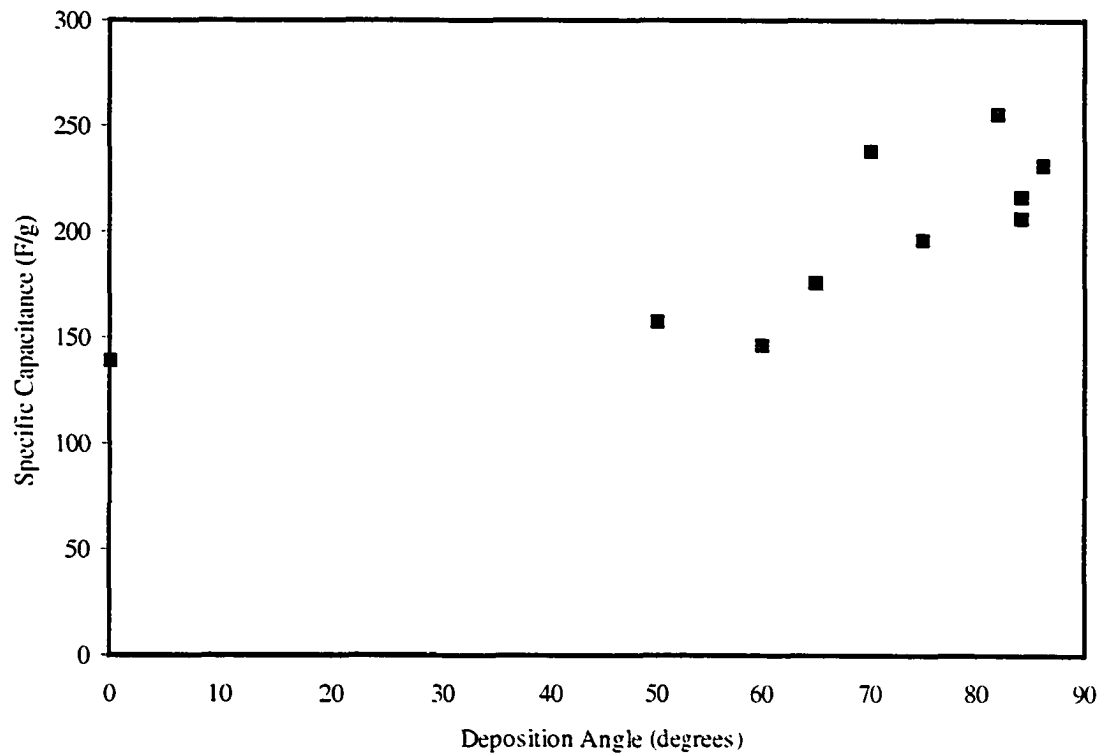


Figure 12. Graph showing the specific capacitance values as a function of the film deposition angle⁷⁴.

3 Experimental Methods

3.1 Capacitor Electrode Fabrication

The procedure for fabricating the capacitor electrodes was developed by Dr. J.N. Broughton while working in Dr. Brett's research laboratory in Electrical and Computer Engineering. All fabrication of electrodes for this project was done in collaboration with Dr. Broughton. The fabrication procedure to produce the capacitor electrodes in this work is a two-step process. The first stage of the process is the deposition of a manganese film on a Si substrate with 25 nm of sputtered Ti to act as an adhesion layer and 250 nm of sputtered Pt to act as a charge collector. In this project, two morphologies of film are studied. The first morphology is a porous nanostructured film that is composed of closely spaced chevrons. The original intention was to use the inherent porosity in the chevron film to achieve a higher surface area. The second morphology is a standard dense thin film. The second step in the fabrication process requires an electrochemical oxidation of the manganese film in order to activate the electrode.

3.1.1 Thin Film Fabrication-GLAD Technique

The GLAD films are all produced using e-beam evaporation of a Mn source in a carbon crucible using a typical physical vapour deposition set up with the exception of a rotating and tilting substrate holder. The crucible to substrate distance was constant at 22 inches. The e-beam power source was run at 7.5 kV with a current of 20-25 mA. The base pressure of the chamber is approximately 5×10^{-7} torr, with a deposition pressure of approximately 2×10^{-5} torr in order to produce an acceptable deposition rate (20 Å/s). Keeping the vapour source inclined obliquely to the substrate surface during the deposition will result in a film of slanted posts. Discontinuous substrate rotation of 180° at a time during the deposition will result in the growth of a chevron structure. The chevron (zigzag) structure was the only GLAD structure investigated during this project.

3.1.2 Thin Film Fabrication-Dense Films

The dense films were all produced in a sputter system using 2 inch Mn target with a standard sputtering set-up (i.e. no substrate tilting). The target to substrate distance was kept constant at 18 inches. The base pressure of the system was 3×10^{-7} torr and the pressure in the chamber during deposition was approximately 6-7 mTorr. The sputtering gas was argon fed in at a rate of 10 sccm. The sputtering was carried out under constant power operation at 200W.

3.1.3 Electrochemical Oxidation

Electrochemical measurements were done in a solution of 1M Na_2SO_4 (pH = 6.3) unless specified otherwise. An Ag/AgCl reference electrode and a Pt counter electrode were used for all of the measurements. The thin films acted as the working electrode in a typical three-electrode system using two different cell set-ups: the electrodeposition cell (Figure 13) and the testing cell (Figure 14). Unless otherwise specified, most of the experimental work was conducted using the testing cell.

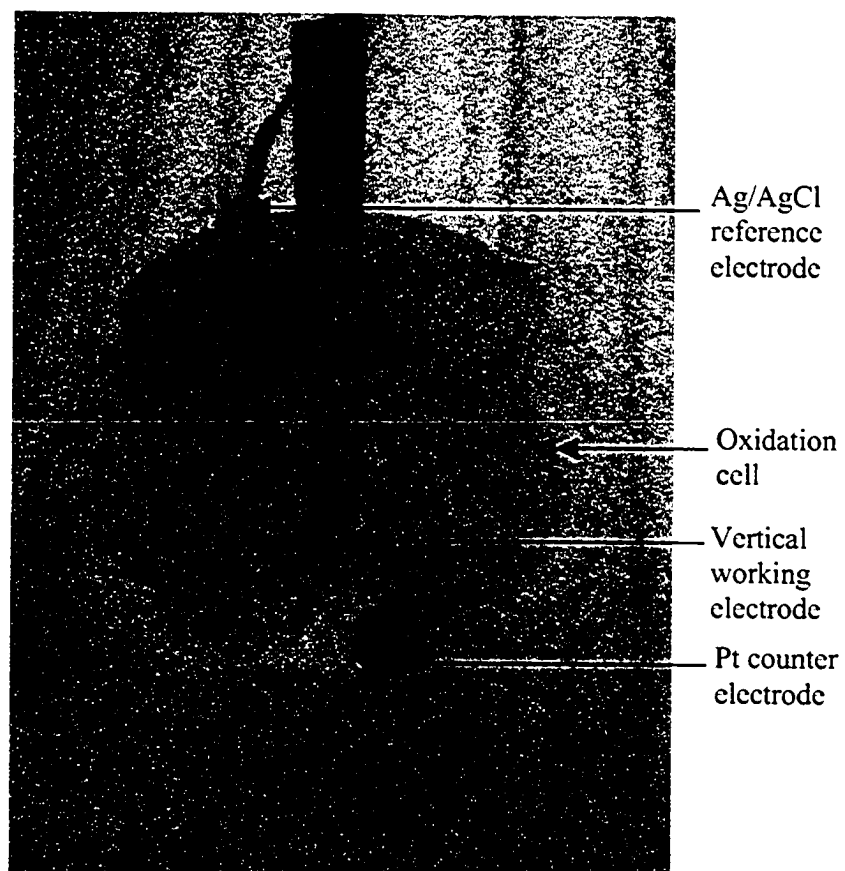


Figure 13. Oxidation cell with a vertical sample orientation.

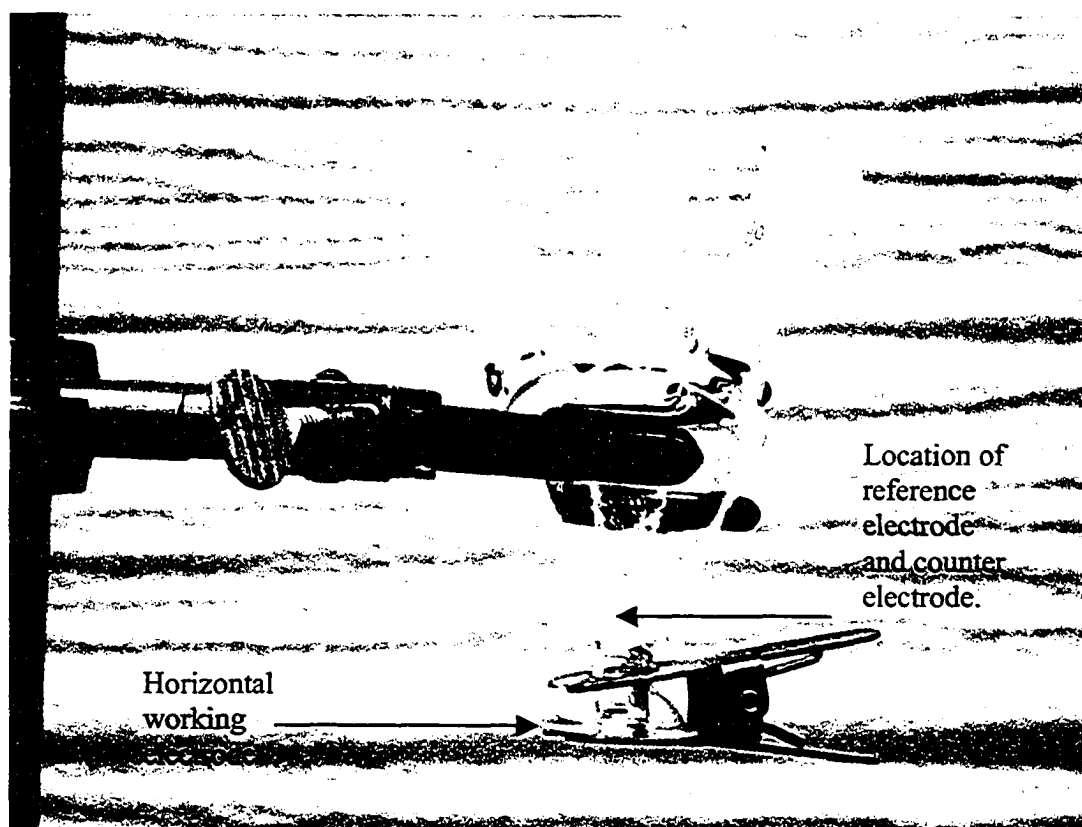


Figure 14. Oxidation cell with horizontal sample orientation.

The major difference between the two cell set-ups is that the electrodeposition cell has a vertical sample orientation and a separate counter electrode and reference electrode. The testing cell has a horizontal sample orientation with the counter electrode wrapped around the reference electrode and the entire assembly placed into the neck of the testing cell near the sample surface.

The second step for fabricating the capacitor electrode is an electrochemical oxidation step. This is done galvanostatically (constant current). A constant current, in the range of 10^{-4} A to 10^{-3} A, is applied using a Gamry 750 potentiostat. The potential vs. time data are collected, and the oxidation process is stopped when the potential reaches 0.9V vs. Ag/AgCl as the film begins to break down if the voltage exceeds 0.9V vs. Ag/AgCl. Once this step is complete, the film is capacitive.

3.2 Electrode Characterization

3.2.1 Electrochemical Characterization

The capacitance is evaluated electrochemically by cyclic voltammetry using a Gamry PC4 750 potentiostat/galvanostat. The cells shown in Figure 13 or Figure 14 are also used for this aspect of the testing. The CV scans are set up to start at 0 V vs. E_{ref} , scan up to a potential of 0.9V vs. E_{ref} and then reverse the scan to 0V. The scan rate used is 50 mV/s for ease of comparison with others working in this area.

Because the CV scans did not always yield a constant current it would be fairly inaccurate to estimate the capacitance using equation 4 and an estimate of the current, i . Instead, the capacitance is estimated from the current vs. time curve that is part of the CV data set. Integrating the area underneath the current vs. time curve between the potentials of 0 and 0.9 V will give an estimate of the total charge capacity of the film. If this is then divided by the change in voltage, 0.9V, an estimate of the capacitance of the film can be obtained.

The areal capacitance is defined as F/cm^2 where the area is the planar area of the electrode that is involved in the capacitive reaction. For the specific capacitance to be calculated, F/g , knowledge of the mass of the active portion of the electrode is required. For this work, the specific capacitance is quoted in terms of total mass of manganese oxide after the electrochemical oxidation process. The film is oxidized and then weighed on a Fisher scientific microbalance. The manganese oxide material is stripped off using a solution of concentrated nitric acid leaving behind the Si wafer with Ti/Pt metallization. This wafer is then weighed again, and the difference is used as the active mass of manganese oxide material. A typical weight for a film is several micrograms.

3.2.2 Structural Characterization

3.2.2.1 Scanning Electron Microscopy

The bulk of the imaging in the scanning electron microscope (SEM) was done on a JEOL 6301F FE-SEM. The samples were imaged first in a JEOL field emission scanning

electron microscope (FE-SEM) at 5 kV without any conductive coating. Some charging was evident producing noise in the images. The primary use of the SEM was to produce an image of the film texture, but not to do any microstructural phase analysis.

3.2.2.2 Conventional TEM

Higher resolution imaging and phase analysis was done using a conventional TEM. A JEOL 2010 transmission electron microscope (TEM) with a Noran ultra-thin window (UTW) x-ray detector for compositional analysis was used. Both plan view and cross-section samples were imaged at 200 kV. Crystal structure analysis was done using electron diffraction patterns. The energy dispersive x-ray (EDX) all contained artifacts of Si and C. The C is often a result of contamination from the pump oils in the microscope. Si was a sputtering artifact as a result of the Si substrate being sputtered away during the ion-milling step and re-deposited on the surface of the film of interest.

3.2.2.3 Scanning TEM

Higher spatial resolution analysis was done on select samples using a Technai F20 field emission gun (FEG) TEM/STEM located at the University of Calgary. Images were obtained in STEM mode using the annular dark field detector, which provided better contrast for thicker samples. This instrument was also used in conventional TEM mode in order to provide a fine enough beam to analyze the structure with convergent beam electron diffraction (CBED).

3.2.2.4 TEM Sample Preparation

Cross-section samples were made using the following procedure. Two pieces of equal size were first cleaved from the sample. The two pieces, with deposit surfaces facing each other, were glued together. Scrap Si pieces were used as supports on either side of the glued samples to build a raft structure. The raft was then ground to a thickness of 200 μm , after which a 3 mm disk was machined from the raft with the sample interface centered in the disk. The disk was dimpled on both sides until optical transparency was reached ($\sim 30 \mu\text{m}$) at the center. The sample was sputtered using a Gagan Model 600 Dual Ion mill from both sides, with a current of 0.5 mA per gun at 5 kV and an incidence angle of 85° , until perforation. At this time, the incident angle was increased to 87° and the current and gun energy lowered to 0.3 mA per gun and 4 kV respectively, to reduce

ion damage. Sputtering was continued for 40 minutes, or until a smooth edge at the hole was formed. All samples were cooled with liquid nitrogen prior to and during sputtering, to reduce preferential sputtering effects.

Plan view samples were made by dimpling from the back side of the material to approximately 10 μm in thickness. Then, the sample was sputtered from the substrate side only using the same conditions as above.

3.2.2.5 X-ray Diffraction

X-ray diffraction (XRD) analysis was done using a Rigaku Rotaflex rotating anode diffractometer with a thin film camera attachment. The filament voltage and current were set at 40 kV and 110 mA, respectively. Samples were scanned between 10° and 90° (2-theta) at a rate of $2^\circ/\text{min}$ using an x-ray incidence angle of 2° to ensure no substrate was sampled. A blank wafer with just the metallization layers, prior to thin-film deposition, was run for background signal comparison and elimination.

3.2.2.6 X-ray Photoelectron Spectroscopy (XPS)

Surface analysis of various films was carried out by x-ray photoelectron spectroscopy (XPS) using a Kratos AXIS 165 x-ray photoelectron spectrometer. A monochromatic Al source was used operating at 210 W giving a pass energy of 20 eV and a step of 0.1 eV. A survey scan was done to identify all elements present in the surface layer and high resolution scanning was done in order to determine the valence and relative hydration of the layer according to a procedure developed by Chigane and Ishikawa^{75,76,77,78}. The C 1s peaks exhibit a low intensity shoulder at a binding energy greater than 285 eV suggesting there is some contamination. This effect has been linked to differential charging in the past and has made it difficult to determine the manganese valence from deconvolution of the Mn 2p peaks⁷⁵. Instead, the Mn 3s peaks were used to approximate the valence using 3s peak splitting widths from Chigane and Ishikawa^{77,75}. These values are tabulated in Table 8.

Table 8. Table of Mn 3s peak splitting values for various manganese oxides.^{75,77}

Sample	Mn 3s splitting width, ΔE (eV)	Valence of Mn
MnO	5.79-5.8	2
Mn ₃ O ₄	5.3-5.50	2.3
Mn ₂ O ₃	5.2-5.41	3
MnO ₂	4.7-4.78	4

When a photoelectron is ejected from the surface of the sample, the result is a final state in which there exists unpaired electrons in the valence band level, often in the d level shells. The exchange interactions between core (or s-level) electrons and those in the incomplete shells (i.e., d-shells) gives rise to multiplet splitting of the s electrons themselves (Mn3s peak splitting). The separation of the peak energies (ΔE) can therefore be described in terms of the exchange interaction energy shown below:

$$\Delta E = (2S + 1) K [3s, 3d]$$

where S is the total spin of the unpaired electrons in the 3s and 3d levels in the final states and $K[3s, 3d]$ is the exchange integral between the 3s and 3d levels. The result is that the lower valences of Mn give rise to wider peak splitting (as seen in the literature values).

The amount of hydration in the samples can be determined from the de-convolution of the O1s spectra into three different spectra representing three different types of bonding: pure oxide bonding (Mn-O-Mn), hydroxide bonding (Mn-O-H), and free water bonding (H-O-H). The area beneath each individual curve gives a semi-quantitative analysis of the amount of that bond present. The hydration of the film is given by the quantity of the Mn-O-H bonds. The standards are tabulated below (Table 9).

Table 9. Table of O1s deconvolution energies for different bonds.⁷⁵

Bond Type	Binding energy (eV)
Mn-O-Mn	529.3-530.0
Mn-O-H	530.5-531.5
H-O-H	531.8-532.8

3.3 Solution Characterization

3.3.1 Atomic Absorption Spectroscopy (AAS)

The solution used for the electrochemical oxidation (1M Na₂SO₄) was characterized using AAS to determine the amount of Mn in the solution during the oxidation processes. The samples were analyzed using a VARIAN FS220 which has a detection limit of 0.04 ppm. No dilution was necessary since the solution samples were within the linear range, which for Mn is up to about 10 ppm. The results are given as mg/L. The total volume of solution is measured for both the bulk solution collected and the amount of solution used to rinse the surface of the sample. In this manner, the amount of Mn (mg) lost during oxidation can be calculated and then divided by the area of the individual sample so that the amount of Mn lost per unit area can be determined.

4 Results

4.1 General Structures

GLAD films offer many different kinds of unique structures with many interesting avenues for study. The following work is a brief look at the effects of some different variables on the ultimate microstructure of these unique films. This work is brief since the focus of the thesis shifted towards the characterization of materials for electrochemical capacitors.

4.1.1 Effect of Material

The effect of the material on the microstructure of the films is mostly a function of surface diffusion. Previously, this value has been evaluated as a ratio, T_s/T_m , (substrate temperature over melting temperature); however, this does not always adequately address the diffusion process. This shortcoming can be seen in the helical films made of Cr (BCC) and Ti (HCP), with melting points of 2148 K and 1941 K, respectively. With a higher melting point (and lower T_s/T_m value), Cr films should exhibit slightly increased bifurcation and a smaller grain size⁵⁻⁶⁻⁷⁻⁸. However, the images (Figure 15, Figure 16) indicate that there is more branching and smaller grains in the Ti helix. This result is presumed due to the difference in material-dependent surface diffusivities. Thus, although Cr has a lower T_s/T_m value, a faster surface diffusion rate than Ti is necessary to account for the surprising result of a larger grain size and less bifurcation than the Ti sample. The reason for this higher surface diffusivity has yet to be determined.

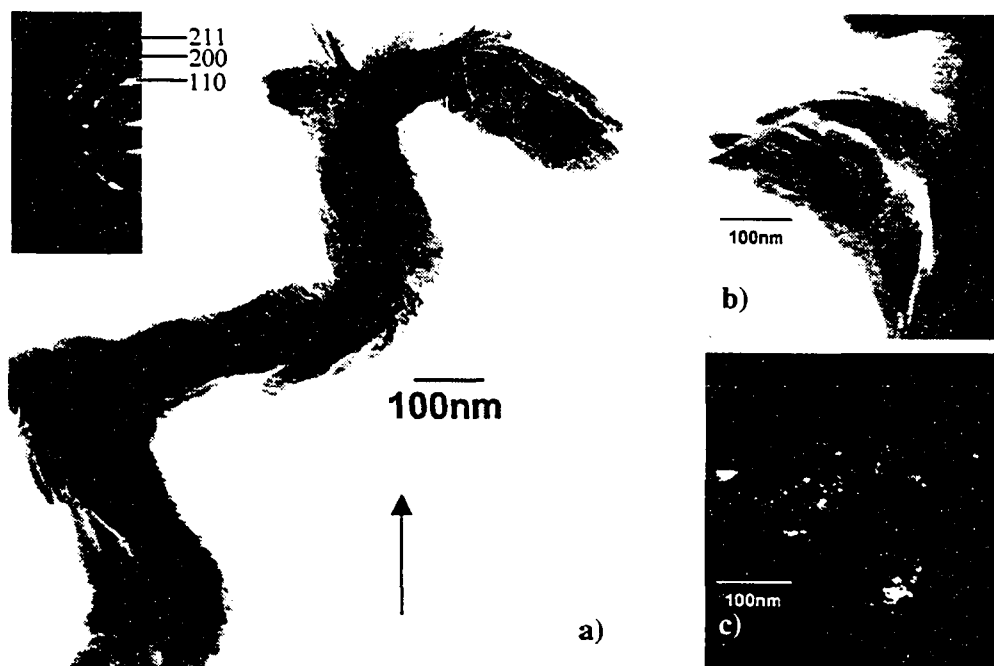


Figure 15. TEM BF image of a Cr helix growing in the direction of the arrow with the diffraction pattern inset, b) TEM BF image showing detail of branching in a helix, and c) corresponding dark field (DF) image, from the (110) reflection, of the same area in (b) showing an approximate grain size of 50 nm.

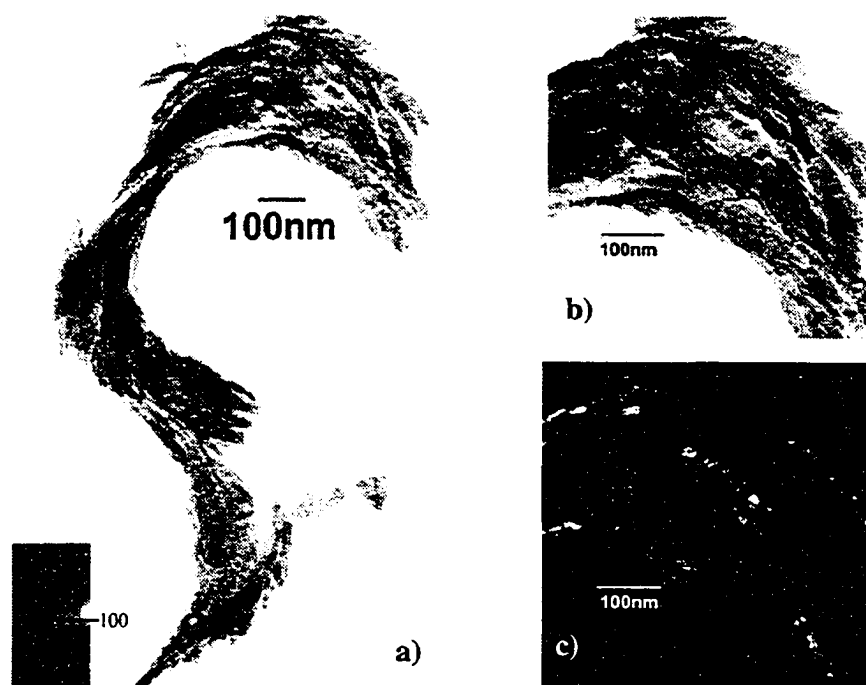


Figure 16. a) TEM BF image of Ti helix growing in the direction of the arrow with inset diffraction pattern. b) TEM BF image showing detail of branching in helix. and c) corresponding DF image, from the (100) reflection, of the same area in (b) showing an approximate grain size of 20 nm.

Crystal structure is also an important factor in microstructure evolution. The effect of crystal structure on growth is illustrated by the zigzag films of Cr and TiO. Both Cr and TiO have fairly similar melting temperatures ($\sim 2100\text{K}$) thus suggesting similar diffusion rates. This would suggest that the two materials would deposit in a fairly similar manner, and their morphology is certainly similar as seen in the TEM bright field (BF) images (Figure 17a and Figure 18a). However, the two structures are actually quite different as revealed by the dark field images (Figure 17b and Figure 18b). The Cr zigzags deposit with a large grain size of 100 nm in width and 500 nm in length. Indeed, each arm of the zigzag comprises an individual grain of chromium growing in the $\langle 100 \rangle$ direction. However, the TiO zigzags have a much finer grain size (50 nm) resulting in polycrystalline arms. The difference in grain size is due to the ordered nature of TiO as compared to the random structure of Cr. Cr is BCC, while TiO is FCC (specifically

NaCl-type). As TiO has a NaCl-type lattice structure, the Ti and O must fill specific positions in the unit cell. More time is required for the atoms to diffuse to suitable Ti and O lattice sites, resulting in a finer grain size than for the Cr structure where the atoms may fill any vacant lattice site. Indeed, a new Cr grain is only formed once the full 180° rotation occurs.

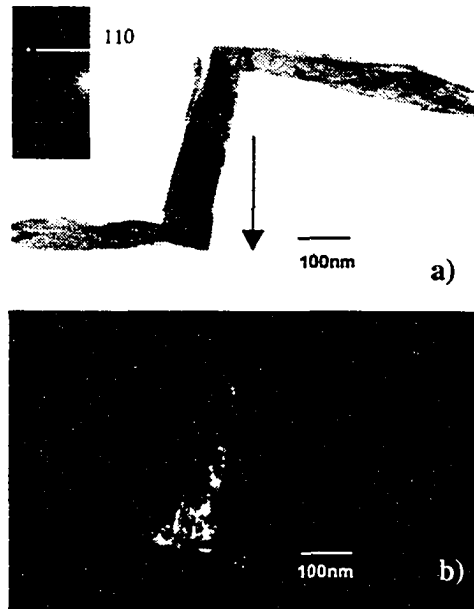


Figure 17. a) TEM BF image of Cr zigzag growing in direction of arrow with inset diffraction pattern, and b) TEM DF image of the Cr zigzag from the (110) reflection.

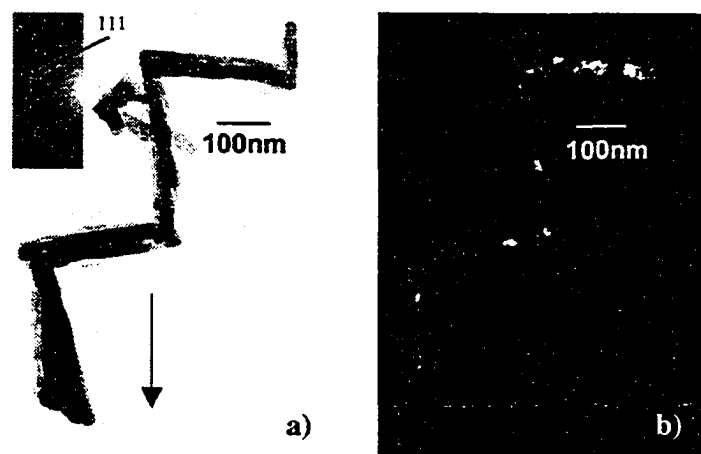


Figure 18. a) TEM BF image of TiO zigzag growing in direction of arrow with inset diffraction pattern, and b) TEM DF image of TiO zigzag from the (111) reflection.

4.1.2 Annealing of GLAD structures

The effects of annealing bulk materials have been extremely well documented. However, these effects have not been studied in GLAD films. Titanium oxide samples (vertical posts) were annealed at 500°C for 5 hours in an inert atmosphere in order to study the effects of annealing on the structure⁷⁹. Vertical posts were amorphous in the as-deposited condition as indicated by the diffuse diffraction pattern shown in Figure 19a. However, after annealing, the diffraction pattern (Figure 19b) indicated a crystalline structure, which was indexed as the anatase phase of TiO₂. Although this is the metastable phase, rather than the equilibrium phase, rutile, it is not unusual for anatase to form.

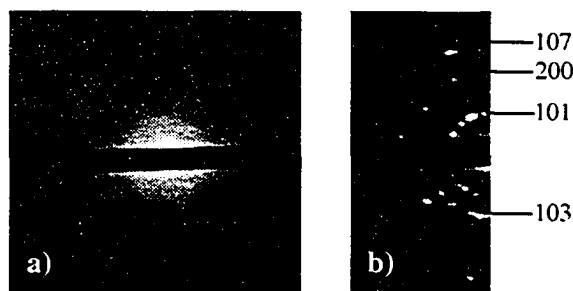


Figure 19 a) Selected area (SAD) pattern for an as-deposited titanium oxide vertical post, and b) SAD pattern for an annealed titanium oxide vertical post, indexed as the anatase form of TiO₂.

Other than crystallizing the material, there is an obvious morphological change (Figure 20a and b). After annealing, the structure of an individual post has become much smoother with a noticeable absence of the branching that was seen prior to annealing. This effect is a result of the diffusion that occurs during the crystallization process. During the amorphous to crystalline transformation, the atoms are undergoing significant diffusion, resulting in a smoothing out of the external surface as new, fairly large, non-equiaxed grains, ~200 nm in length and ~50 nm in width, are formed (Figure 21). Similar results were produced with slanted post structures and helices though the images are not shown. The change in structure that results from annealing has been shown to significantly increase transmission of light across the visible spectrum in TiO₂ films, which is a very useful processing step⁷⁹.

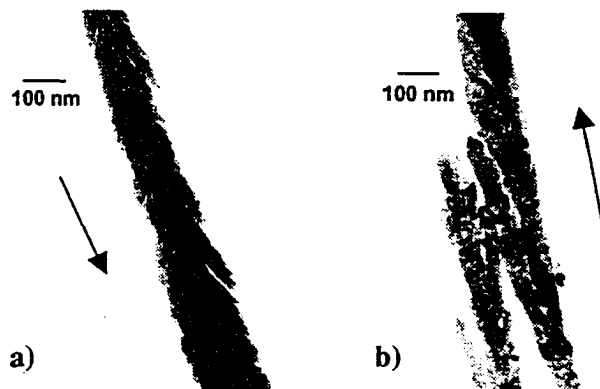


Figure 20. a) TEM BF image of the as-deposited TiO₂ vertical post, and b) TEM BF image of the annealed TiO₂ vertical post growing in the direction of the arrow.

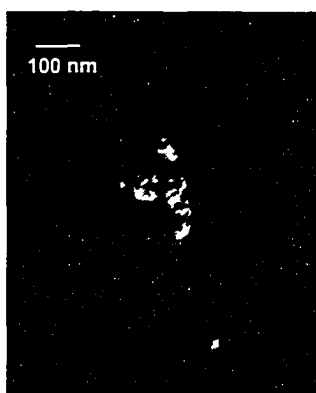


Figure 21. TEM DF image from the (103) reflection for anatase showing the grain size.

4.1.3 Effect of Rotation

Changing the rotation speed of the substrate is one of the easiest methods of changing film morphology. However, the effect is primarily macroscopic rather than microscopic. This is especially the case for materials with very high surface diffusion rates (low melting points). Aluminum vertical post films were made with two different rotation speeds: 42 and 3 RPM. TEM images for the two films are shown in Figure 22, with their corresponding diffraction patterns. The TEM images support previous results^{6,8} in which it was noted that faster than typical rotation (>1RPM) will suppress bifurcation and inhibit surface diffusion and may result in faceting of the structure (Figure 22b).

Although the post broadens at the top as the rotation speed is reduced, each post remains single crystal as indicated by the diffraction patterns, without exhibiting a common growth direction over the entire film. This suggests that the microstructure of the individual films is unaffected by the rotation speed, but determined by the material. It is likely that the faceted structure occurs only at the slower rotation speeds because of the time necessary for surface diffusion. At the faster rotation rates, the faceting is suppressed because the rotation is fast enough to prevent adequate diffusion and diffusion atoms become quickly buried beneath incoming atoms. Further studies of other materials are necessary to confirm these effects.

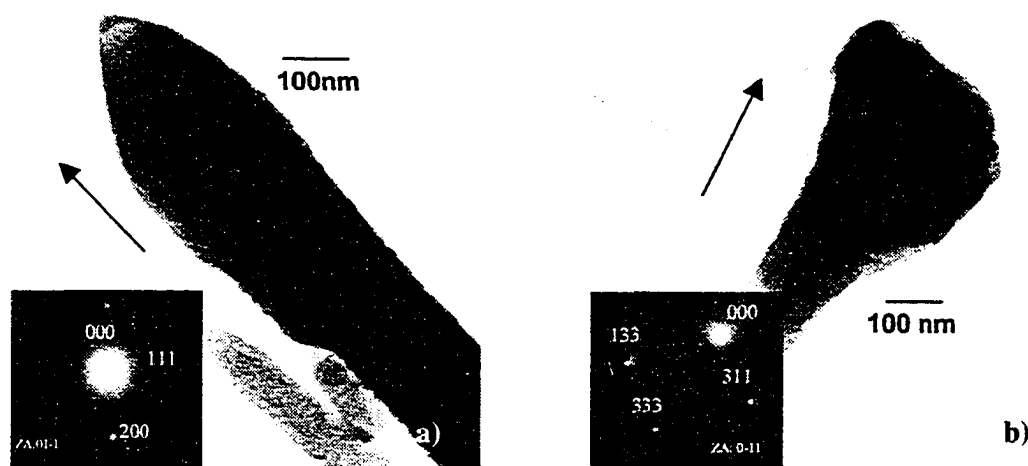


Figure 22. a) TEM BF image of aluminum vertical post deposited with a 42 RPM rotation speed growing in the direction of the arrow, with an inset of the single crystal diffraction pattern, and b) TEM BF image of an aluminum vertical post deposited with a 3 RPM rotation speed growing in the direction of the arrow, with an inset of the single crystal diffraction pattern.

4.2 Manganese oxide electrochemical capacitor materials

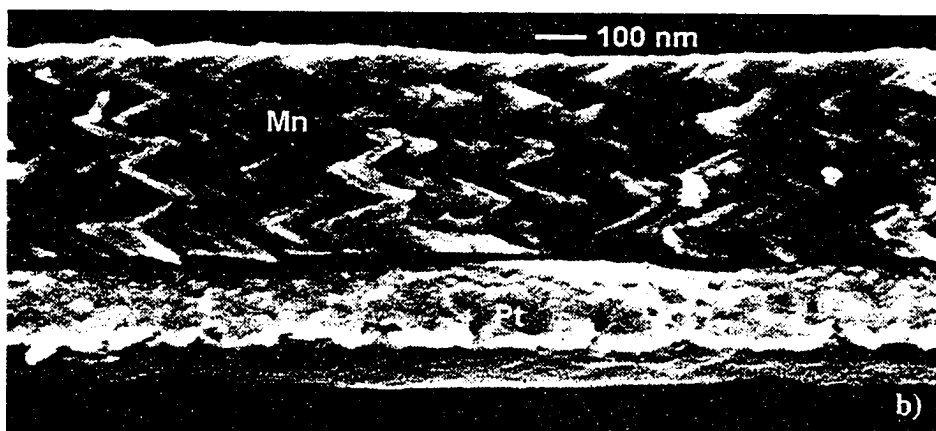
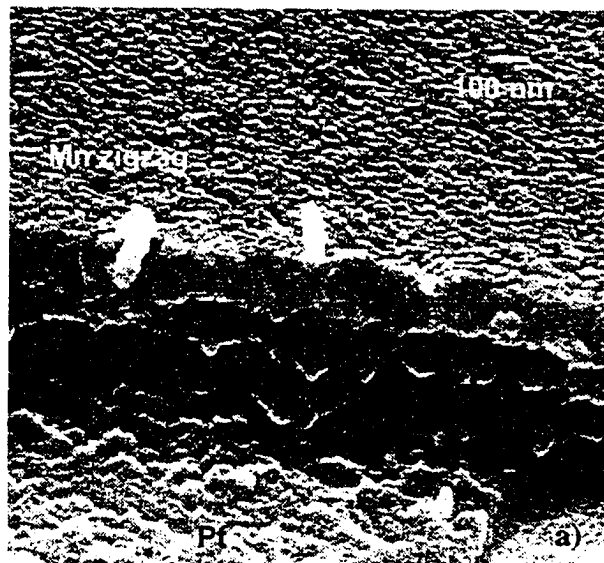
Manganese oxide materials are becoming more and more popular as potential electrochemical pseudocapacitor materials, replacing ruthenium oxide and the more common double layer capacitors. As discussed in the literature survey, there are many

different procedures that can be used to produce a viable electrochemical electrode. In continuation of the study started by Broughton and Brett⁷⁴, the structure of the electrodes produced by their particular process (PVD coupled with electrochemical oxidation) was the focus of this study in order to identify the microstructural features that are critical for developing high capacitance.

4.2.1 As-deposited PVD films

The electrochemical capacitor electrodes were produced from a starting substrate material of a Si wafer with a SiN layer to provide dielectric isolation, followed by a thin (25 nm) Ti layer for adhesion, and a 250 nm Pt layer to act as the charge collector. A manganese layer was sputtered or evaporated onto this base and the entire structure then became the basis for the capacitor electrode. Two different morphologies of the deposited manganese layer were studied: a chevron structure produced through the GLAD technique and a traditional dense sputtered film. The FE-SEM images of these as-deposited structures are shown in Figure 23. The relative porosity of the film surface for the chevron structure is shown in Figure 23a, although the zigzag structure is not visible as the image was taken in plane with the zigzags. Figure 23b does, however, show the typical zigzag structure of the manganese chevron texture produced at a 77° flux incidence angle.

Figure 23b also reveals that the zigzags are quite close together, limiting the overall macroporosity of the structure. The dark areas in the cross-section are not porosity, but missing material that has been removed as a result of cleaving during specimen preparation. If in-plane zigzags are observed, there is very little macroporosity between the individual columns. The dense sputtered film (Figure 23c), as expected, is quite dense with a typical columnar structure.



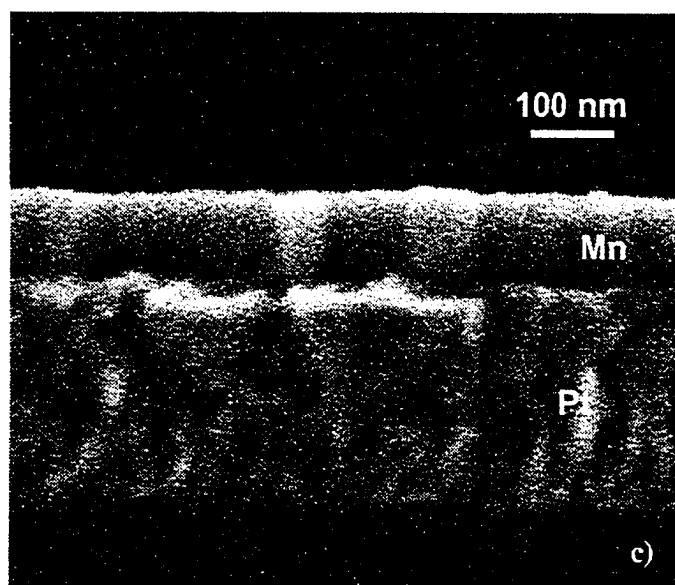


Figure 23 a) FE-SEM secondary electron (SE) images of the as-deposited manganese chevron film revealing the surface texture. b) The chevron film in cross-section showing the morphological texture. c) FE-SEM SE image of the sputtered dense film in cross-section.

The internal structure of the chevron films is revealed in TEM cross-sectional images, both bright field and dark field (Figure 24). The bright field image (Figure 24a) of the as-deposited chevron film reveals that the film, while exhibiting the chevron structure that is visible in Figure 23, is still quite dense. In fact, macroporosity, between the zigs and zags, appears quite limited. Comparison of this image with Figure 23 shows that the only visible porosity appears to be in the final portion of the film that is deposited, i.e., the small visible space between the individual columns near the surface of the film.

An energy dispersive x-ray (EDX) spectrum (Figure 24b), taken from the central region of the zigzag layer indicates that there is a significant amount of oxygen within the manganese zigzag layer. The carbon peak in the spectrum is contamination from the microscope and specimen, while the Si peak is an ion-milling artifact from the Si

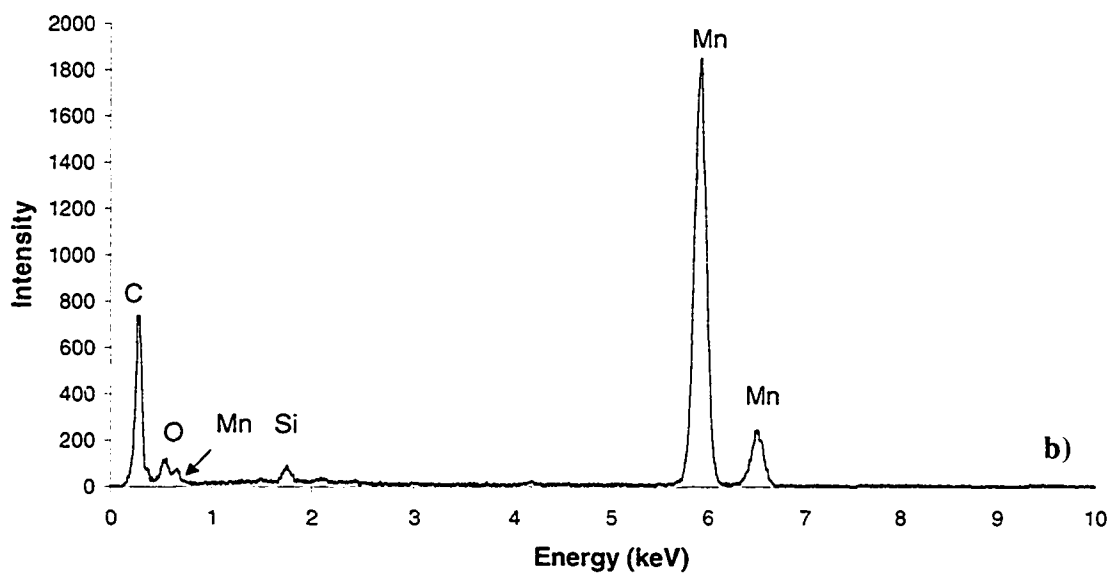
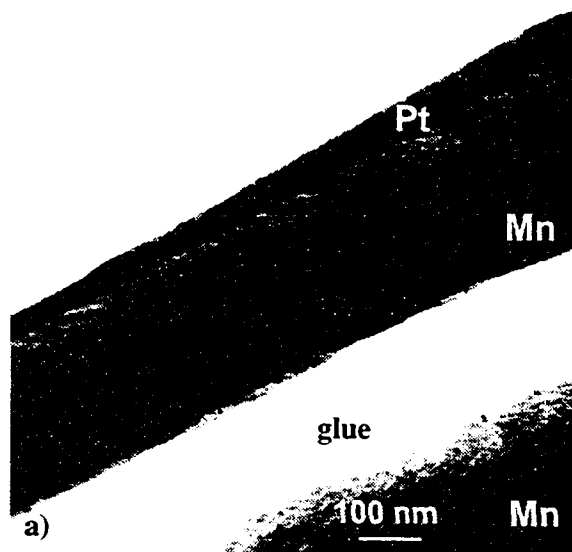
substrate. These types of artifacts are present in each EDX spectrum and will not be commented on henceforth.

Selected area diffraction (SAD) from the zigzag layer resulted in the ring pattern shown in Figure 24c and corroborates the EDX results. The pattern has been indexed as a mixture of cubic manganese, with a cell parameter of 0.8192 nm, and cubic MnO, with a cell parameter of 0.445nm. This is the first major difference between this process and the other processes discussed in the literature survey. Both the electrodeposition and the powder techniques involve the production of an amorphous product immediately. With the GLAD technique, however, a crystalline product is initially produced. In addition, the manganese layer is produced in a relatively low valence (0/2+) instead of the 4+ valence that is produced with the other procedures.

Both the EDX and SAD results indicate that an oxide phase is forming. Although it was expected that only metallic manganese would be deposited, due to the relatively low deposition pressure ($\sim 10^{-5}$ torr), it is not unusual for materials to oxidize during a physical vapour deposition process. The dark field image of the layer (Figure 24d), which is formed from part of the 111 and 200 reflections for MnO and the 330 reflections for Mn, indicates that the oxidation process is occurring during the deposition rather than post-deposition. Grains ~ 20 nm in size appear throughout the layer and since the Mn and MnO grains are indistinguishable it suggests that the MnO grains are throughout the layer. The apparent absence of grains from the central portion of the zigzag layer is an artifact of the specimen preparation process. The Mn/MnO layer sputters more slowly than the Pt, Ti or Si, leaving it thicker in the middle and thus those grains are not visible.

Similar results are produced for the dense sputtered film although the morphology is significantly different (Figure 25a). The EDX spectrum (Figure 25b) shows a fairly significant amount of Pt in the layer and no trace of oxygen. What is likely to have occurred is that, due to the thin nature of the film (38 nm), some Pt was sampled during the EDX collection process and there was insufficient volume of material to produce a substantial oxygen peak. The SAD pattern from this film (Figure 25c) is identical to the

SAD pattern in Figure 24c and confirms that this layer is also a two-phase mixture of Mn and MnO. The dark-field image indicates that the layer is nano-crystalline (Figure 25d).



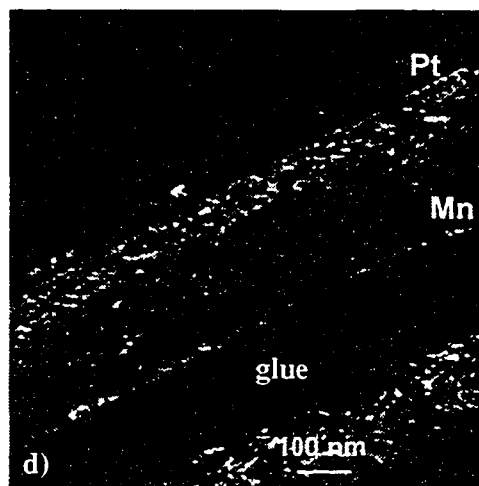
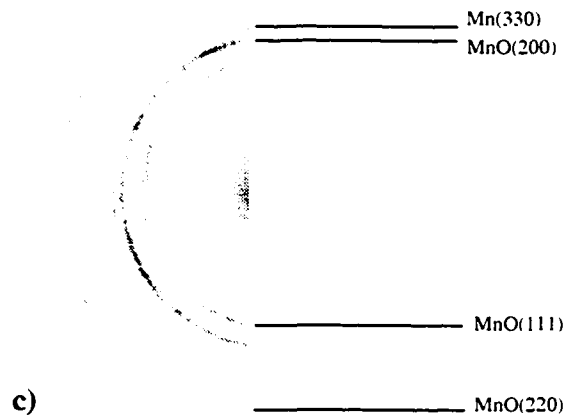
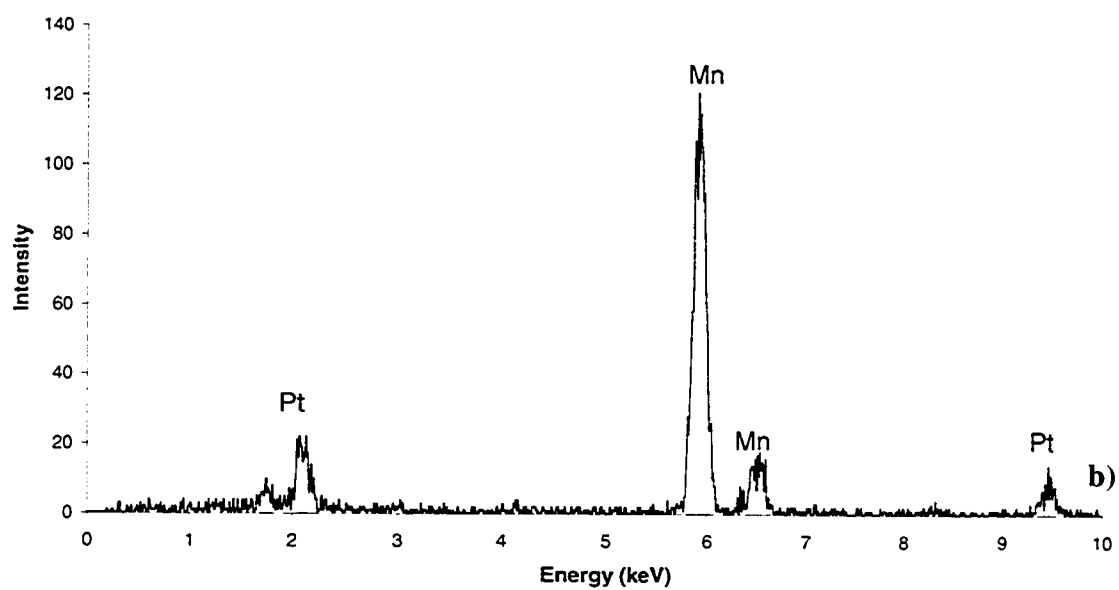
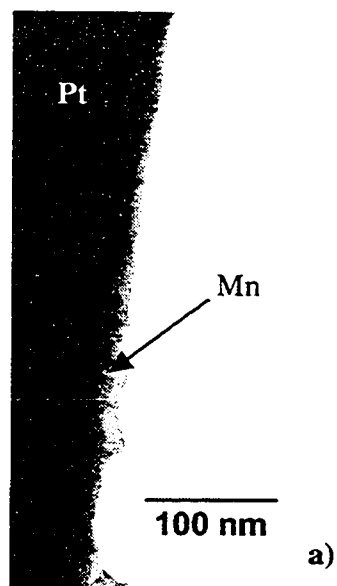
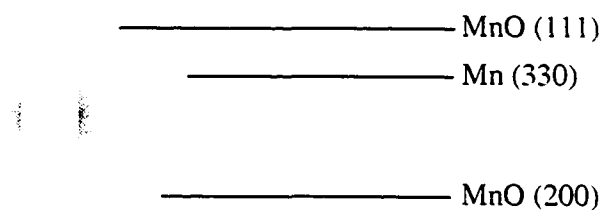


Figure 24 a) Cross-section TEM BF image of an as-deposited chevron film. b) EDX spectrum from the zigzag layer shown in Figure 15a. c) Indexed SAD pattern from the deposited zigzag layer showing the presence of Mn and MnO. d) TEM DF image of deposited layer from part of the (111), (200) reflections for the MnO and part of the (330) reflection for the Mn.





c)

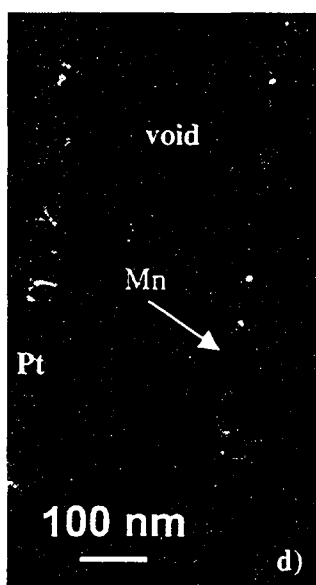


Figure 25 a) Cross-section TEM BF image of an as-deposited dense film. b) EDX spectrum from the dense layer shown in Figure 25a. c) Indexed SAD pattern from the dense layer. d) TEM DF image of the deposited layer from part of the (111), (200) reflections for the MnO and part of the (330) reflection from the Mn.

The x-ray diffraction (Figure 26) data confirms the EDX and electron diffraction results. The major peaks for both Mn and MnO can be indexed, in addition to some of the peaks from the Pt layer.

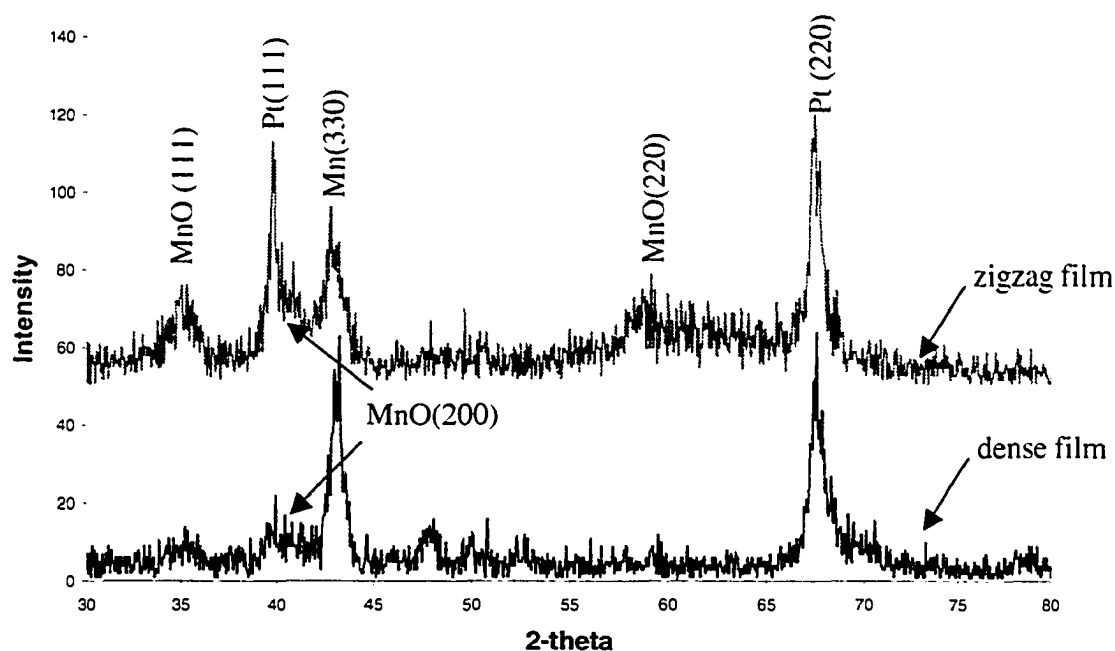
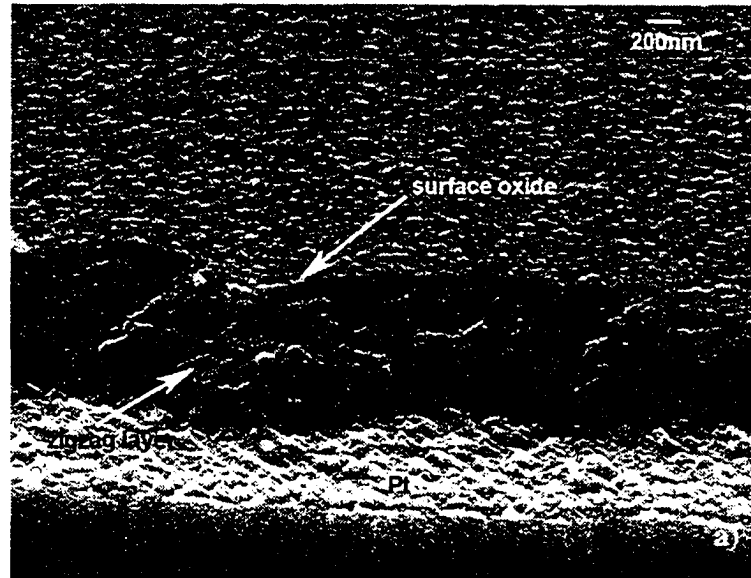


Figure 26. XRD pattern from as-deposited zigzag and dense films showing Mn and MnO.

4.2.2 Thermally Oxidized Films

In the original work by Broughton⁷⁴, the chevron films were thermally oxidized and then electrochemically cycled in order to determine if any increase in capacitance could be produced as reported by other researchers^{63,67,71}. However, the electrochemical oxidation process proved ultimately destructive to the thermally annealed film, making capacitance measurements impossible⁷⁴. In order to determine the physical cause for the poor capacitive performance, the deposited zigzag films were thermally oxidized for 30, 60, 120, and 1920 minutes and then studied using a combination of SEM and TEM imaging.

as well as electron and x-ray diffraction. Figure 27 shows FE-SEM SE images for the four different annealing times. What becomes immediately obvious from these images is that a columnar layer, likely an oxide layer, is formed on the top of the zigzag layer. In fact, even at 30 minutes, the entire zigzag layer is essentially capped, reducing surface porosity. By 1920 minutes, the bulk of the zigzag layer has been replaced by a dense oxide structure with very little zigzag texture remaining.



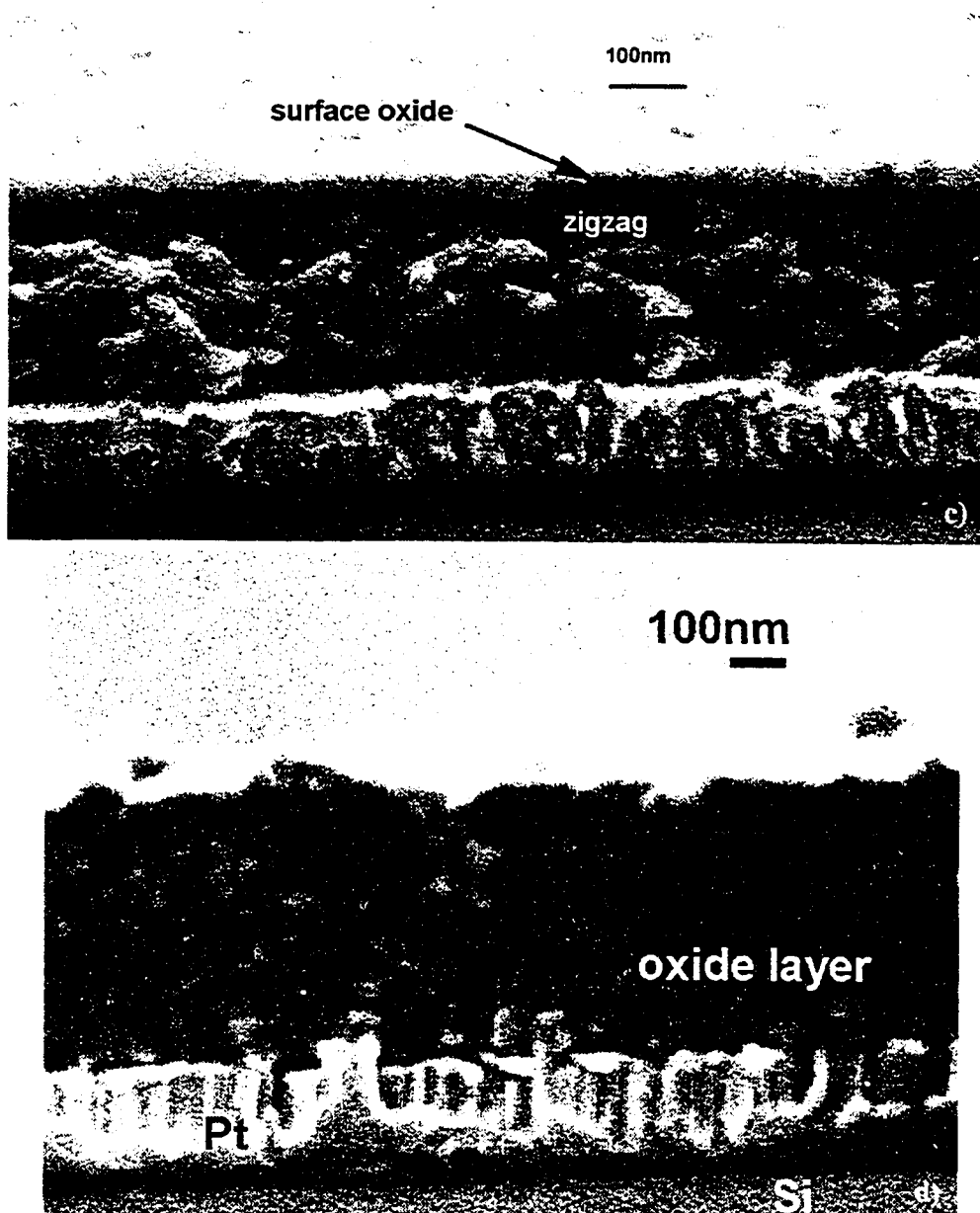


Figure 27 FE-SEM SE images of the zigzag layer annealed for a) 30 minutes, b) 60 minutes, c) 120 minutes and d) 1920 minutes.

If the thickness of the thermally produced oxide film is plotted versus the square root of time (Figure 28) a linear trend is found. This result implies that oxide growth is diffusion

controlled, i.e., $x \propto \sqrt{Dt}$, where x is the thickness of the oxide film, D is the diffusivity and t is the diffusion time. The graph does not extend to a zero intercept because an incubation time is needed for oxide formation.

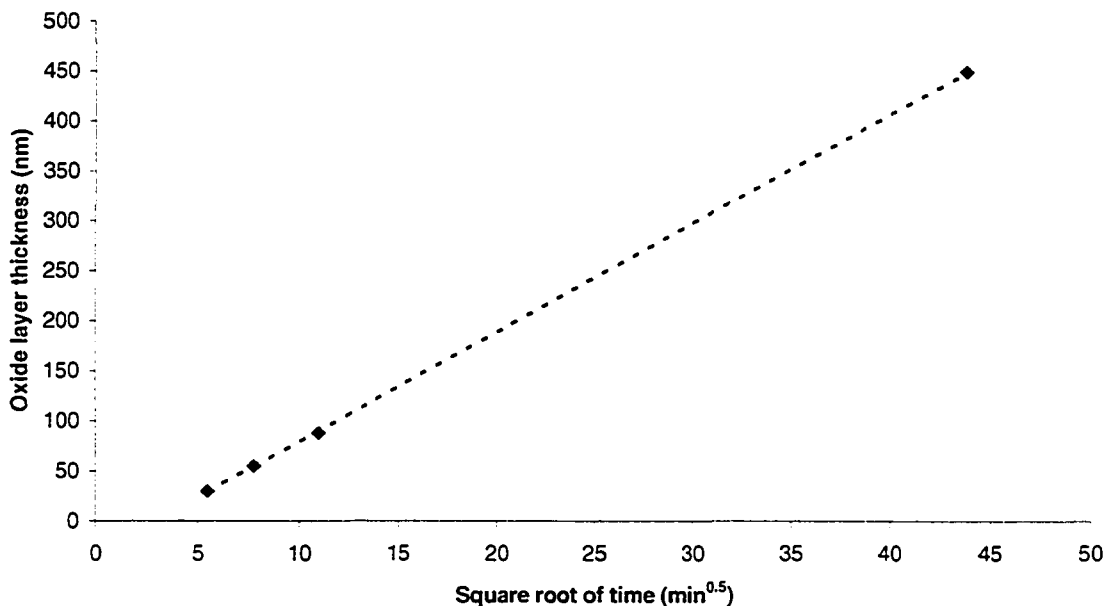
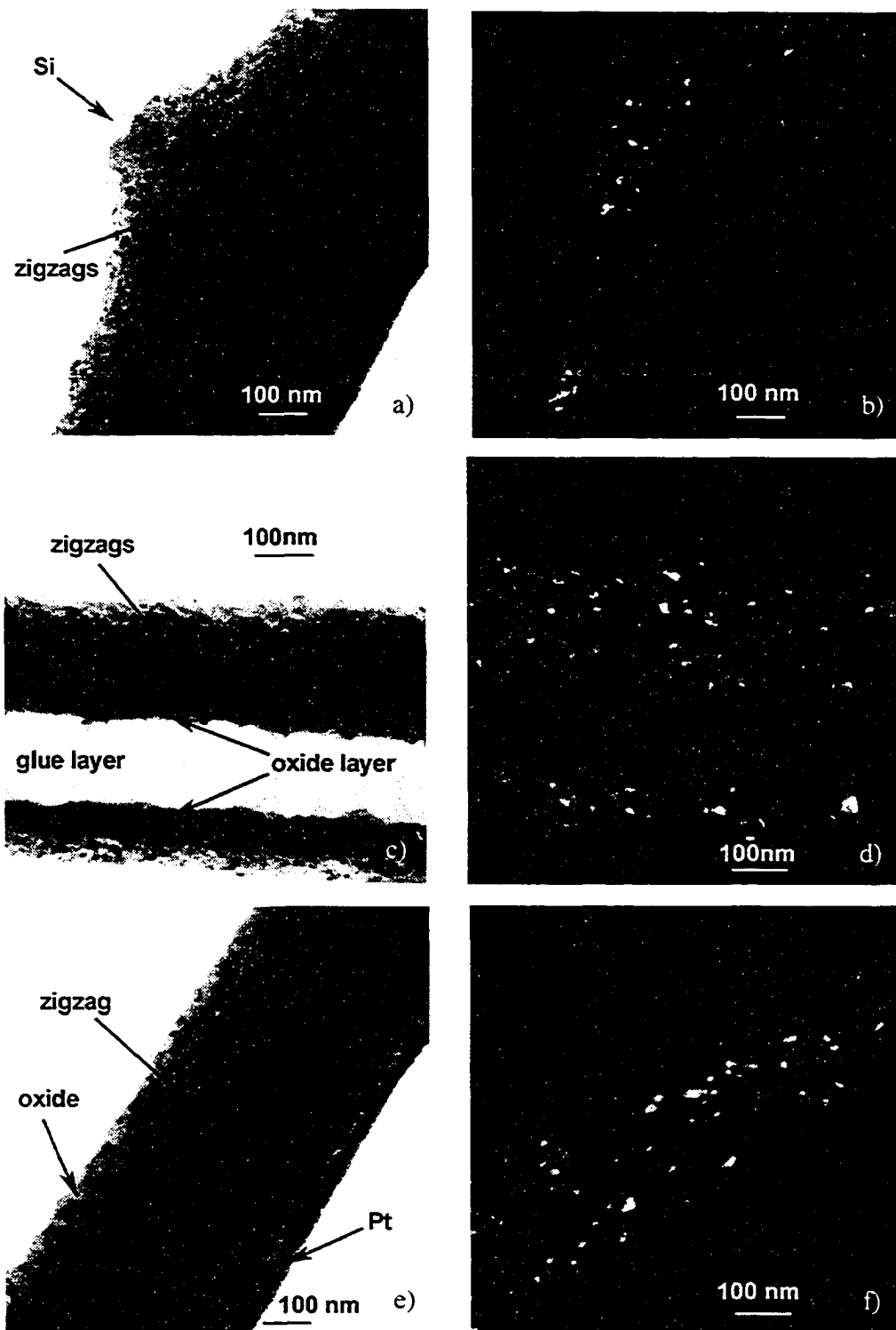


Figure 28. Plot of thermal oxide layer thickness versus annealing time.

The effects of annealing on the internal structure of the zigzag layer were studied using the TEM. Figure 29 shows both bright field and complementary dark field images of the zigzag layer at the various annealing times. Due to sputtering effects, the surface oxide layer is not visible in the sample that was annealed for 30 minutes (it was sputtered away) and the full layer thickness of the sample annealed for 1920 minutes could not be imaged (it too was sputtered away). The surface oxide layer, however, is clearly visible in both the 60-minute and 120-minute samples. Evident in the dark field images is a gradual coarsening of the grains within the zigzag structure from ~25 nm to ~75 nm. EDX spectra taken from the columnar oxide layer in the 60-minute sample confirms that it is a manganese oxide (Figure 30).



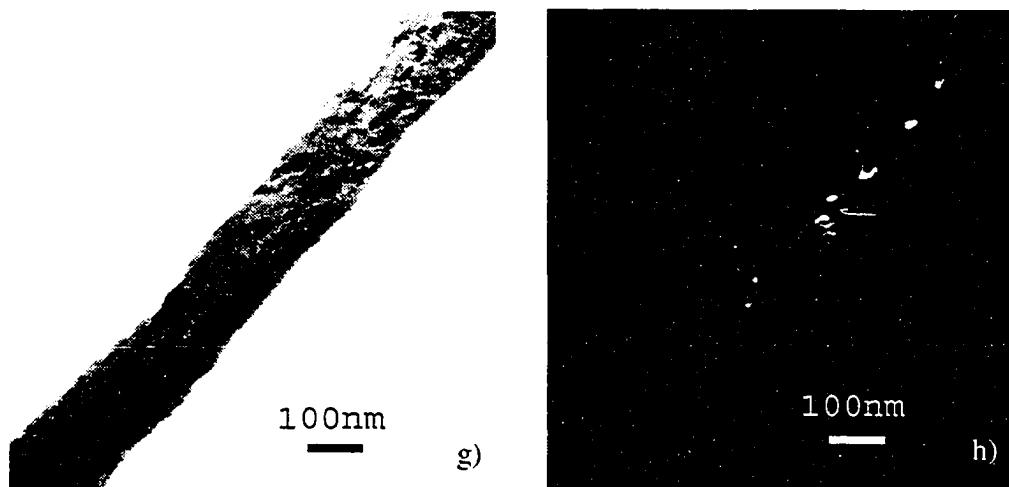


Figure 29 a) TEM BF image of a cross-section sample of the layer annealed at 300°C for 30 minutes. b) TEM DF image of the annealed zigzag layer in (a) using part of the (111) and (200) reflections for MnO and the (330) reflection for Mn. c) TEM BF image of the layer annealed for 60 minutes clearly showing the oxide layer. d) TEM DF image of the annealed zigzag layer in (c) using part of the (111) and (200) reflections for MnO and the (330) reflection for Mn. e) TEM BF image of the layer annealed for 120 minutes with the visible oxide layer on the top. f) TEM DF image of the annealed zigzag layer in (e) using part of the (111) and (200) reflections for MnO and the (330) reflection for Mn. g) TEM BF image of the layer annealed for 1920 minutes. h) TEM DF image of the annealed layer in (g) using part of the (111) and (200) reflections for MnO.

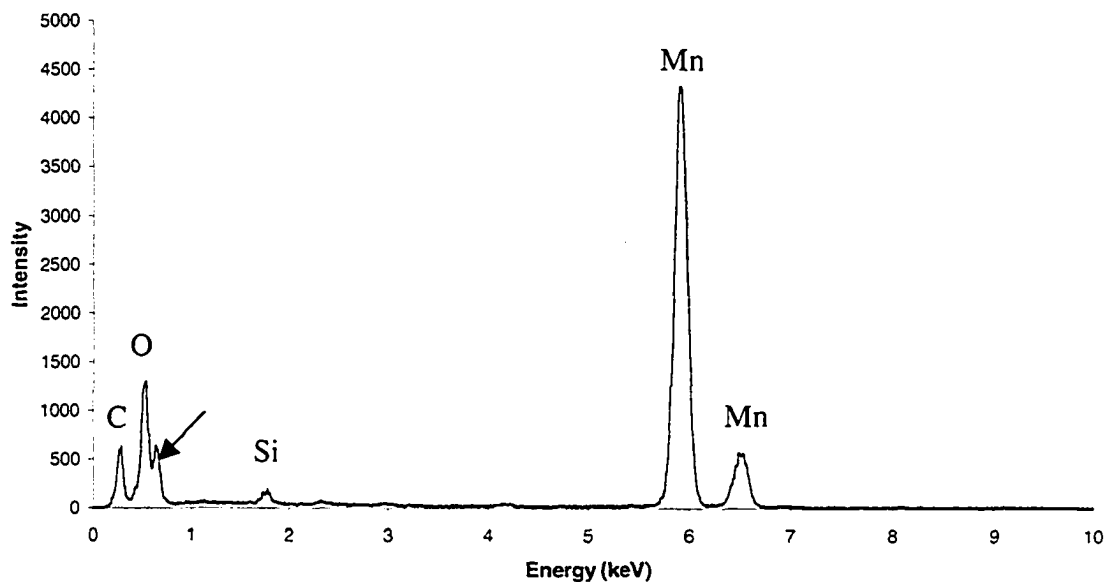


Figure 30 EDX spectrum taken from the oxide layer on top of the manganese zigzag layer that was annealed for 60 minutes.

A comparison of the SAD patterns from the zigzag portion of the layer for the four different annealing times is shown in Figure 31. The first three SAD patterns (Figure 31a-c) are all indexed as a mixture of cubic Mn and cubic MnO and are identical to the as-deposited sample. The diffraction pattern in Figure 31d (1920 minutes) is different from the others and can be indexed to both MnO and Mn_3O_4 . Thus, it appears that the zigzag structure is also slowly oxidizing to Mn_3O_4 . The XRD spectra for the four annealing conditions (Figure 32) corroborate the TEM results. The Mn_3O_4 peaks are significantly more intense in the 1920-minute sample, relative to the other three annealing times. The Mn is consumed during the oxidation process, and completely absent in the 1920-minute sample. The absence of the Mn_3O_4 rings in the SAD patterns of Figure 31a-c may just be a sampling phenomenon of the TEM. The SAD patterns are taken from just a small portion of the sample while XRD samples involve a large area of the sample. Therefore, it is possible that not all areas present in the layer are sampled during SAD analysis.

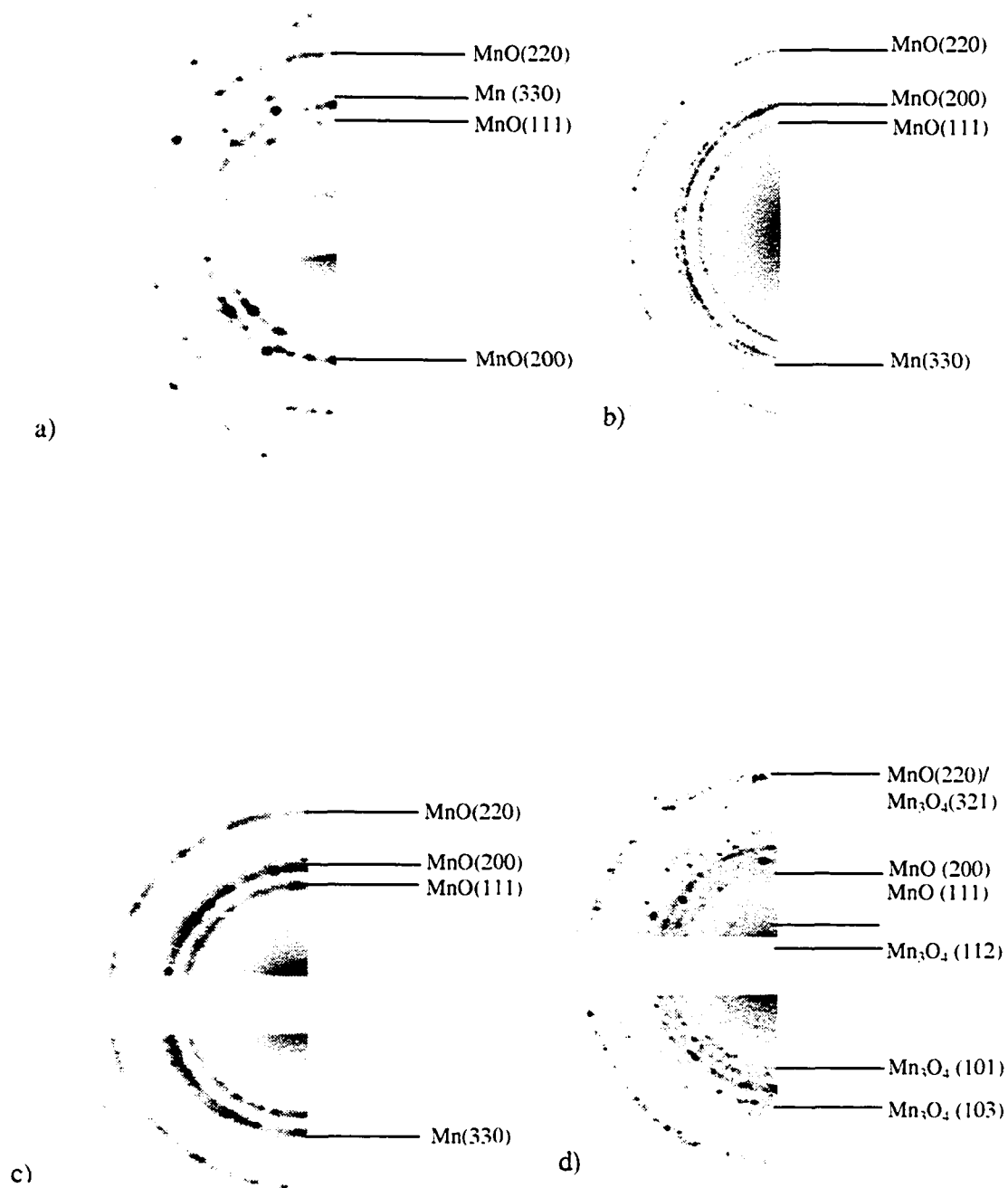


Figure 31 SAD patterns from the cross-section samples of the layers annealed for a) 30 minutes, b) 60 minutes, c) 120 minutes and d) 1920 minutes.

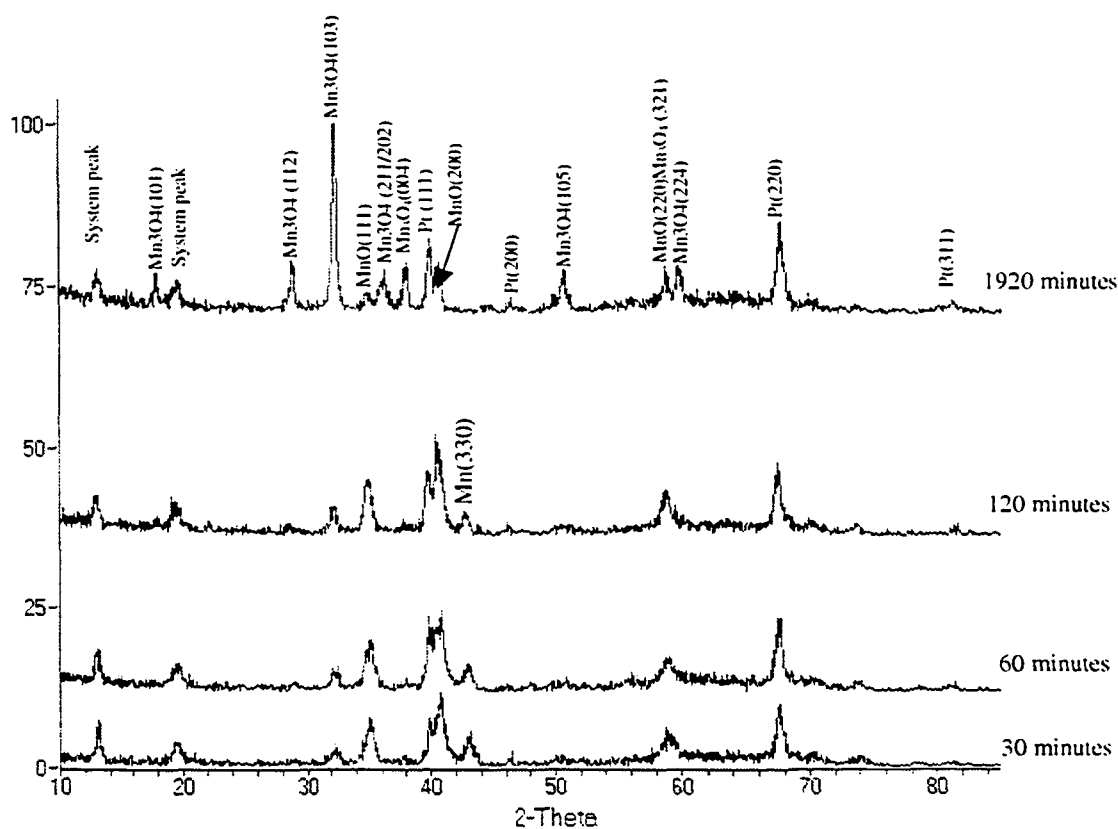


Figure 32 Overlaid XRD spectra from the four annealed samples indexed to show the disappearance of Mn and the growth of tetragonal Mn_3O_4 .

Micro-diffraction of individual grains of the oxide was done for further verification of the above analysis. Four micro-diffraction patterns, taken from grains in the oxide layer of the 120-minute sample, are shown in Figure 33. Micro-diffraction was not attempted on the 30 and 60 minute samples because the oxide layer was too thin, and the grains were too small to provide suitable patterns. XRD results (Figure 32) showed that the same oxide was forming on all samples. The first three micro-diffraction patterns in Figure 33(a-c) are indexed as the cubic form of MnO, while the last micro-diffraction pattern (Figure 33d) is indexed as the tetragonal form of Mn_3O_4 , confirming that there are two different oxides in the columnar layer.

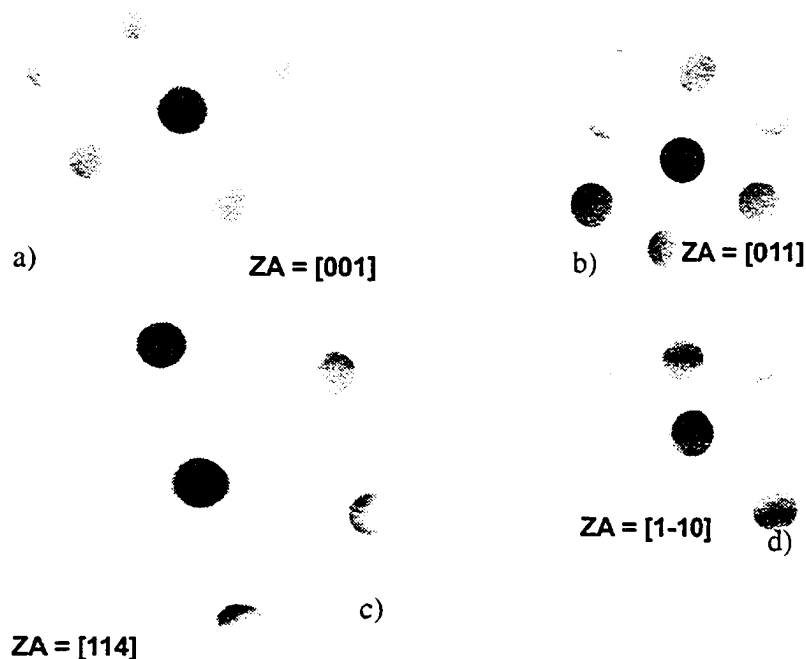


Figure 33. Microdiffraction patterns from three different grains in the surface oxide layer. a), b) and c) are indexed as the cubic form of MnO and d) is indexed as the tetragonal form of Mn_3O_4 .

Based on the above SEM, TEM and XRD results, the following model is proposed, and illustrated schematically in Figure 34, for the thermal oxidation process. The as-deposited sample (Figure 34a) consists of a zigzag structure made up of interspersed grains (~ 20 nm in size) of Mn and MnO. As mentioned previously, some of the Mn is oxidized to MnO during the physical deposition process. During annealing, the remaining Mn is progressively oxidized to MnO (gray) (Figure 34b and c). The zigzag morphology is lost during oxidation, due to the volume increase that accompanies MnO formation since the density of MnO (5.43 g/cm^3) is approximately 75% of that for Mn (7.20 g/cm^3). As the oxidation of Mn proceeds, the MnO begins to oxidize to Mn_3O_4 (black), from the surface inwards (Figure 34b-d). By 1920 minutes, the original zigzag structure is almost completely consumed, leaving a thick Mn_3O_4 layer covering a thin

MnO layer (Figure 34d). Further annealing would result in complete oxidation of the layer to Mn_3O_4 and eventually MnO_2 .

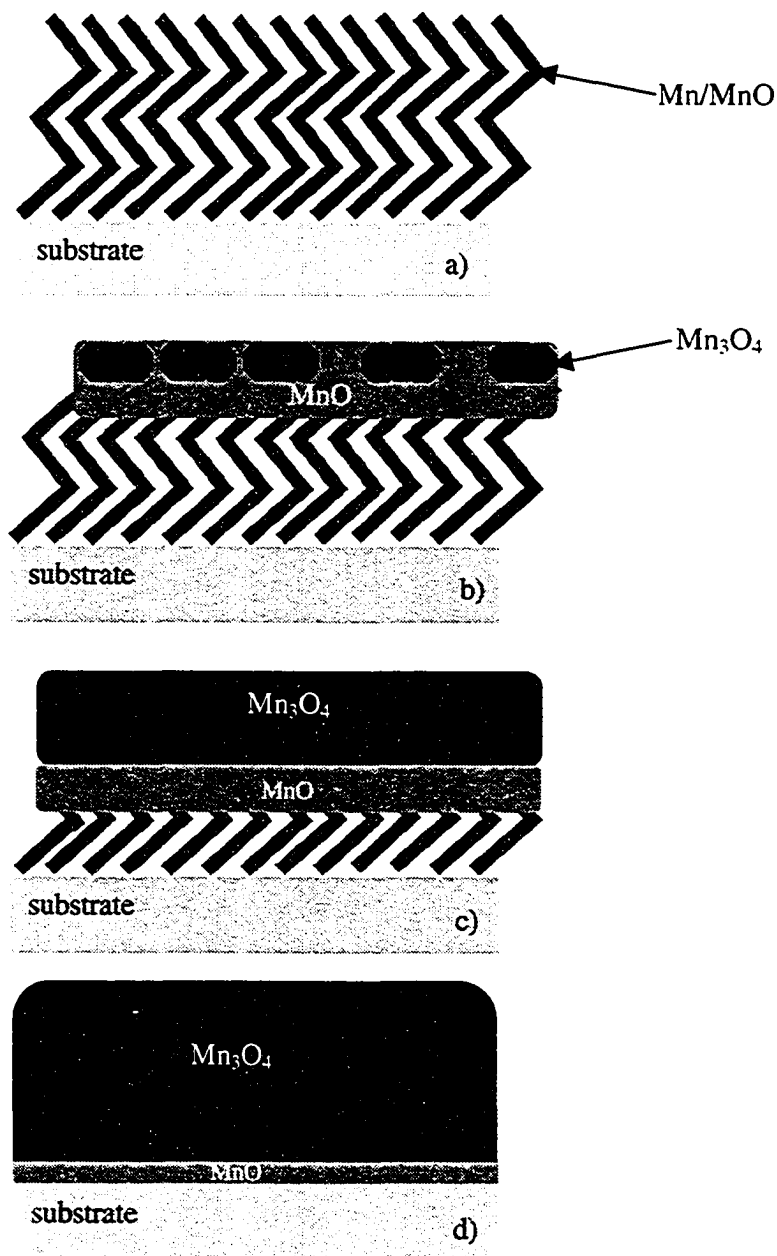


Figure 34 Schematic illustration of oxide growth. a) The original material composed of Mn and MnO zigzags. b and c) The original zigzag layer slowly transforms to a columnar oxide layer that is both MnO and Mn_3O_4 . d) The final structure where the original oxide layer has been destroyed and replaced by the columnar oxide layer that is primarily Mn_3O_4 with some MnO.

Further confirmation for the proposed model was obtained through analysis of plan view specimens. Specimen preparation is such that only the outermost layer is visible in the TEM. The image and diffraction pattern, shown in Figure 35 a and b, are from the 60-minute sample, which has a fairly thin outer oxide layer (<100 nm). The SAD pattern can be indexed as a combination of MnO and Mn₃O₄. However, the sample annealed for 1920 minutes (Figure 35c and d) has a diffraction pattern that can be indexed exclusively as Mn₃O₄, confirming the oxidation mechanism proposed in Figure 34.

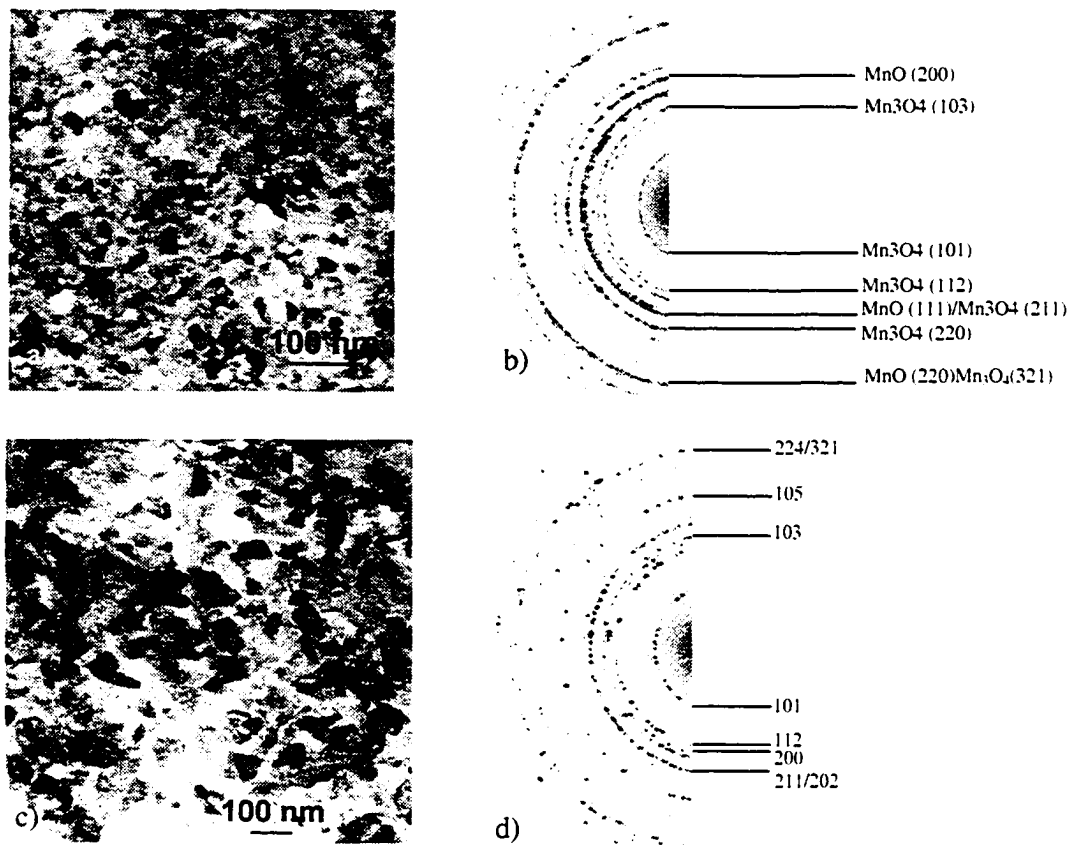
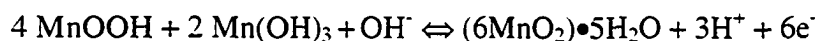
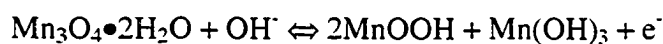


Figure 35 a) TEM BF image of the plan view section of the sample annealed for 60 minutes. b) SAD pattern from the area in the BF image showing the MnO and Mn₃O₄ phases. c) TEM BF image of the plan view section of the sample annealed for 1920 minutes. d) SAD pattern from the area in the BF image showing Mn₃O₄.

The literature indicated that in general the amorphous, hydrated MnO_2 phase produces excellent capacitance, although hydrated Mn_3O_4 has been recently reported as an electrochemical supercapacitor material⁶⁰. The following redox reactions were proposed in an alkaline medium for electrodeposited Mn_3O_4 . While the first two reactions do not necessarily apply to the films in this project, which are metallic Mn and MnO rather than the pure Mn used by Jiang and Kucernak, the final two reactions may give a good starting point for the possible reversible reactions that could occur during the charge/discharge cycle for the samples that have been thermally oxidized.



What is missing in the films produced by the thermal oxidation process in this project is the presence of water in the form of a hydrated compound, $\text{Mn}_3\text{O}_4 \bullet 2\text{H}_2\text{O}$, and the presence of an amorphous structure. The key result of the Jiang and Kucernak⁶⁰ study is the formation of a porous layer that is both hydrated and amorphous. They achieve this result by using an electrochemical deposition method. These qualities (porous, amorphous, and hydrated) are difficult to achieve through the thermal oxidation process and the excess thermal energy tends to crystallize and reduce films to the lowest surface area possible in order to maximize the surface area to volume ratio. Additionally, there is no chance for hydration to occur during a dry thermal oxidation, leaving these films with none of the necessary attributes to develop capacitance. XPS analysis of a film annealed for 1920 minutes confirms that the surface oxide contains no hydrated manganese (Mn-O-H), only anhydrous compounds (50% Mn-O-Mn) and free water (50% H-O-H). There is a significant quantity of free water (~ 50%) in the original scan, but heating the sample to 100°C for a short time in the XPS chamber resulted in a significant reduction in the amount of water present (~30% reduction). The removal of water upon low temperature heating confirms that it is surface adsorbed water from the surrounding environment and

not structural water, and thus does not provide any useful chemical hydration (i.e., Mn-O-H type bonds) to develop capacitance.

Furthermore, it is impossible to electrochemically oxidize the thermally annealed sample in order to obtain the necessary hydration. When a thermally annealed sample is put into the Na_2SO_4 solution and the oxidizing current is applied, the film does not oxidize, but is instead destroyed. It is believed that thermal oxidation of the film prior to electrochemical treatment has altered the surface phases and chemistry such that it is no longer possible to produce a hydrated and amorphous layer upon further electrochemical oxidation. The reason that the thermally annealed layer does not benefit from electrochemical oxidation is likely because the layer is already in an advanced state of oxidation (Mn_3O_4), and therefore the application of an oxidizing current is detrimental to the film as there is very little material remaining to be oxidized. The end result is that any attempt to electrochemically oxidize the sample after thermal annealing results in complete de-lamination of the film from the substrate. Thermal annealing may be more effective if it is applied after the film has been electrochemically oxidized and then the results reported in literature may be observed in this system as well.

4.2.3 Electrochemical Oxidation

The electrochemical oxidation step has proved to be a critical step for the production of a capacitive electrode. The as-deposited film is crystalline, 0/2+ valence, with no hydration. Therefore, the electrochemical oxidation step is thought to be critical to provide the necessary qualities (4+ valence, amorphous, porous, and hydrated) for a capacitive electrode, since thermal oxidation was shown to be unsuccessful in providing hydration and an amorphous structure. The as-deposited zigzag or dense film was oxidized by applying a constant current rather than a constant voltage, as it was desirable to precisely control the reaction rate. A typical trace for the oxidation process of a dense film in the 1M Na_2SO_4 solution is shown in Figure 36. For this portion of the research, dense films were used as they were simpler to produce. The actual oxidation time will vary according to the thickness of the sample or the oxidation current that is applied.

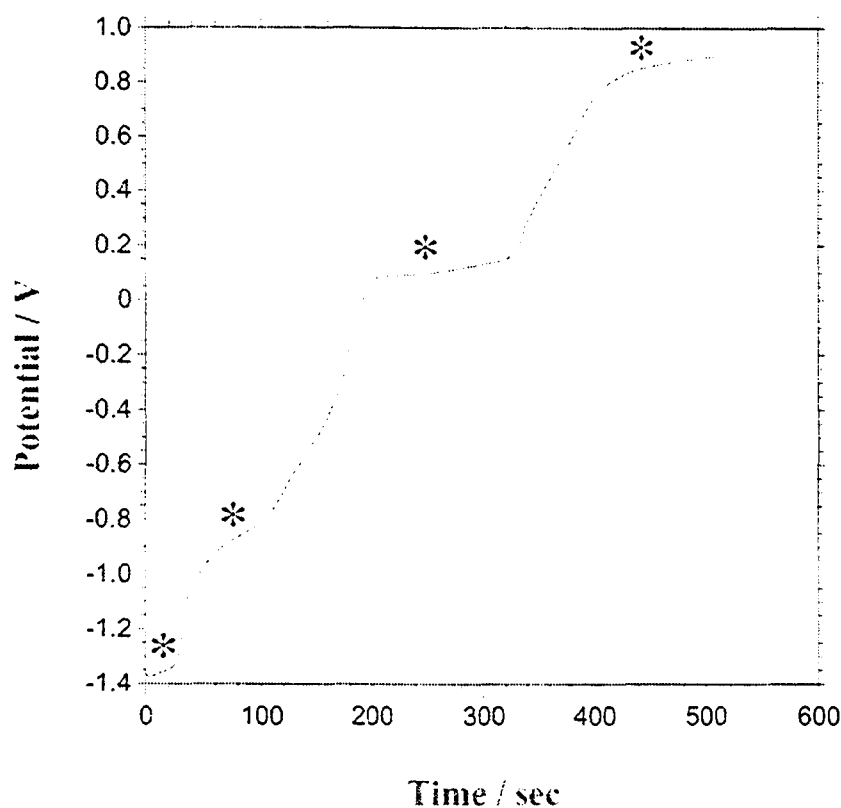


Figure 36. Oxidation trace for a dense sample of 50nm Mn nominal starting thickness oxidized at a current density of $1 \times 10^{-4} \text{ A/cm}^2$.

There are four distinct plateau regions marked in the trace at -1.35V , -0.8V , 0.1V and 0.9V vs. Ag/AgCl. The oxidation was stopped at 0.9V vs. Ag/AgCl after which the film began to delaminate from the substrate.

To identify the reactions occurring during the plateaus, samples oxidized to each of the voltages previously mentioned were studied. The different traces for each stage of oxidation are shown in Figure 37. Although each sample came from the same wafer, it is obvious that there is not perfect reproducibility in the oxidation process. Although the oxidation occurs in the same manner (i.e., the traces are identical in terms of plateau location), the time required for oxidation varies slightly as does the starting potential. There are many possible reasons for this variation. The most important is the variation in the as-deposited Mn film itself. During any sputter process, there is always some

variation in the thickness of the layer (2-30% variation) deposited across the diameter of the wafer, with the thinnest layer being found near the edges. The result is a slightly variable time required for the oxidation process (Section 4.2.7) as shown in Figure 37.

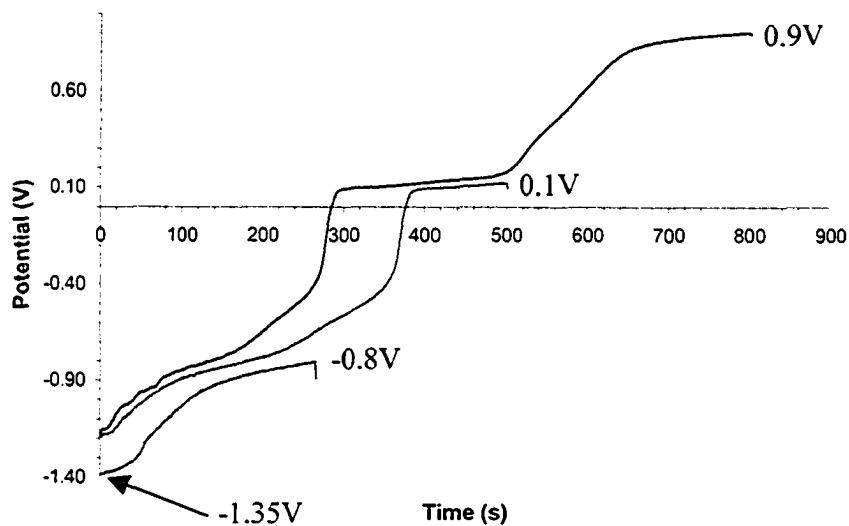
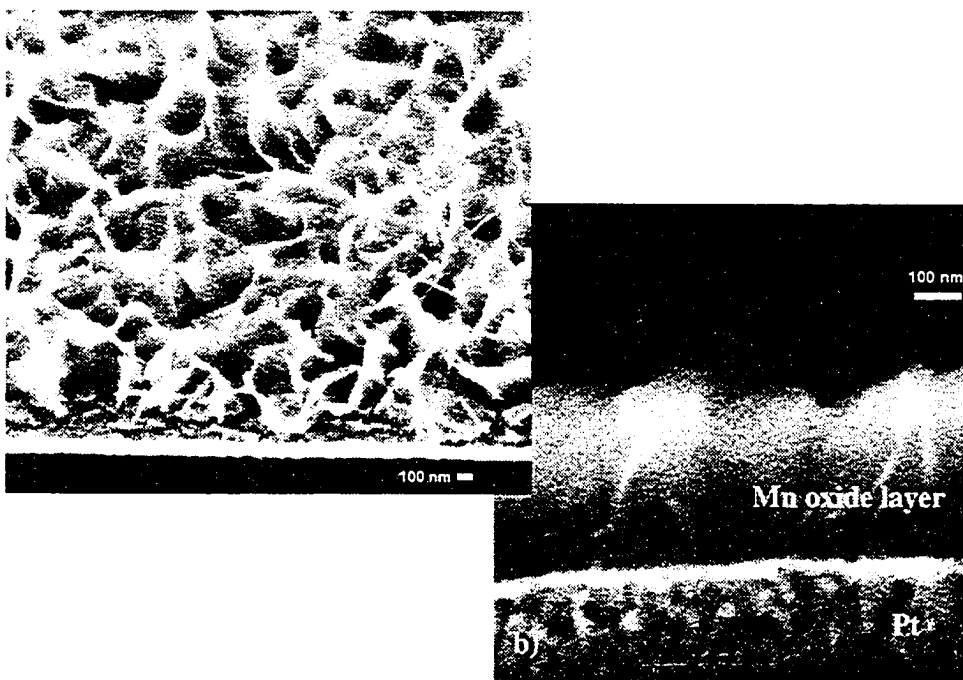
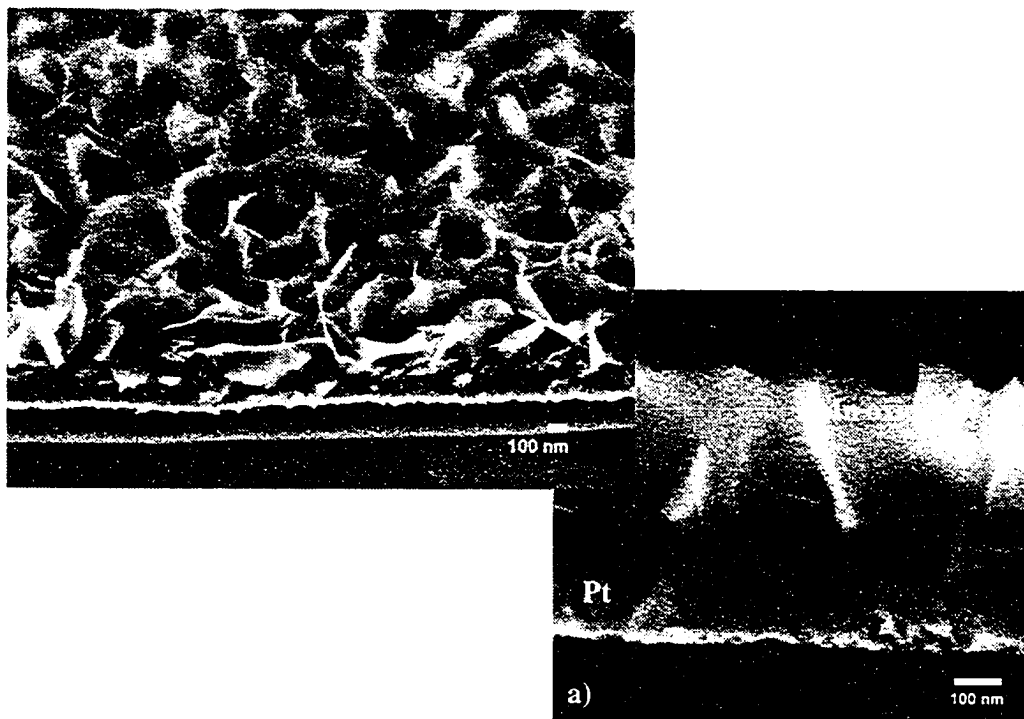


Figure 37. Plot of the potential of the film as a function of oxidation time during the oxidation process. Four oxidations have been done, each stopped during a different stage of oxidation.

The morphology of the layer is seen in the FE-SEM images for each of the four samples at various stages of the oxidation process in Figure 38.



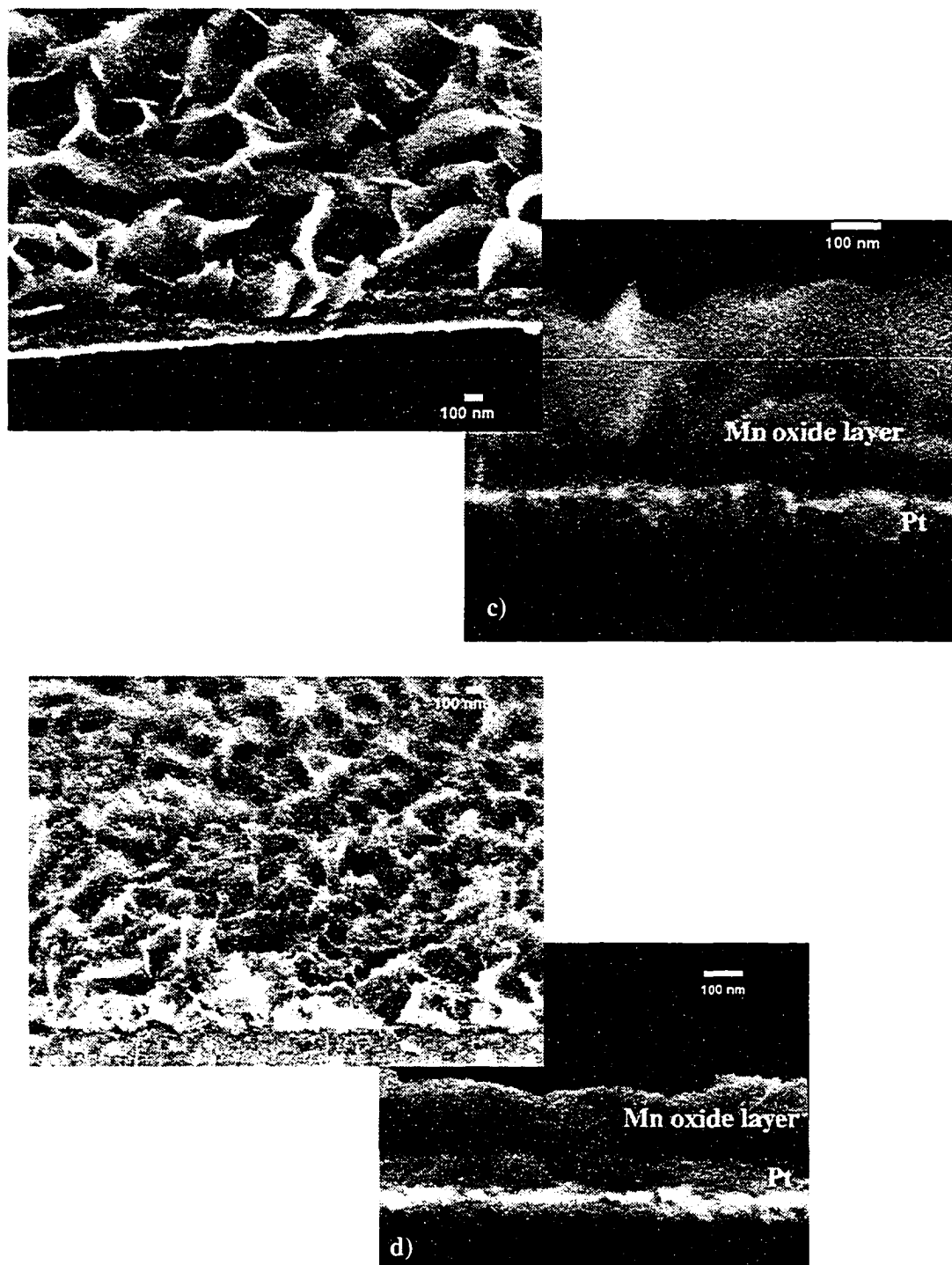


Figure 38. FE-SEM SE images in cross-section and oblique view of samples oxidized to a) -1.35V, b) -0.8V, c) 0.1V and d) 0.9V.

What is immediately apparent, upon comparison to the as-deposited dense structure (Figure 23c), is that the oxidation process drastically changes the film morphology with the formation of an extremely porous surface layer that can be seen in both the oblique and cross-section view. This porous surface layer forms almost immediately during the electrochemical oxidation process, since it is present at a potential of -1.35V vs. Ag/AgCl after only 32s (Figure 38a). During the oxidation process, the film maintains a similar morphology up to and including 0.1V vs. Ag/AgCl . After this potential, the film becomes thinner and produces the somewhat finer porous surface layer seen at the final stage of 0.9V vs. Ag/AgCl (Figure 38d). This trend can be seen in Figure 39 where a sharp decrease in film thickness occurs between 0.1 and 0.9V vs. Ag/AgCl , indicating that the film has become thinner with parts of the film perhaps dissolving into solution, or with the film becoming slightly denser.

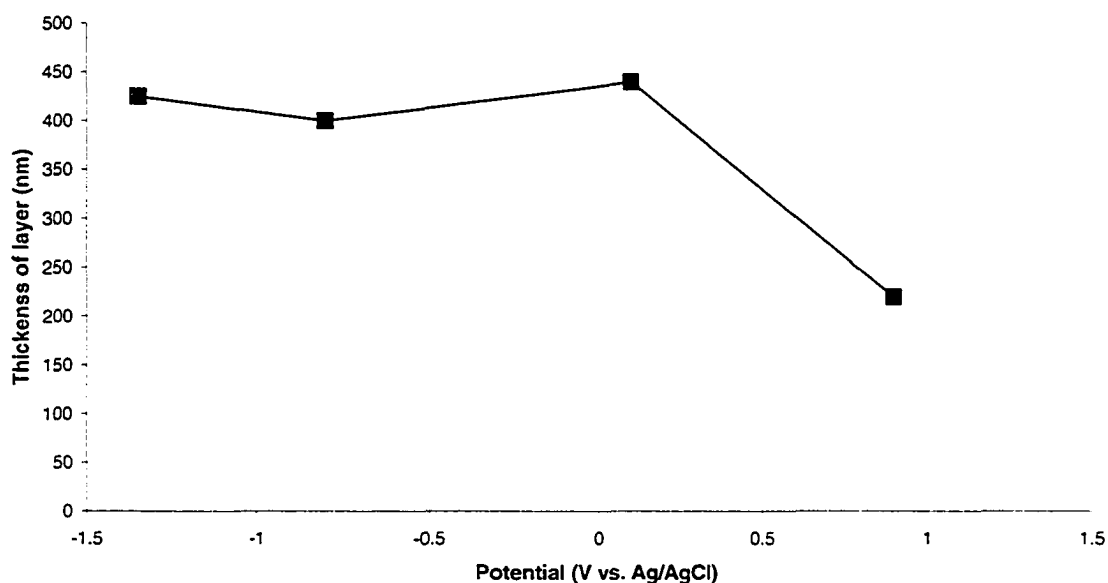


Figure 39. Graph of thickness of porous film produced during the oxidation process as a function of the final oxidation potential reached.

While the film thickness gives a good representation of morphology, it does not give a good indication of the rate of oxidation. For that, the weight change during the oxidation process must be considered, as illustrated in Figure 40.

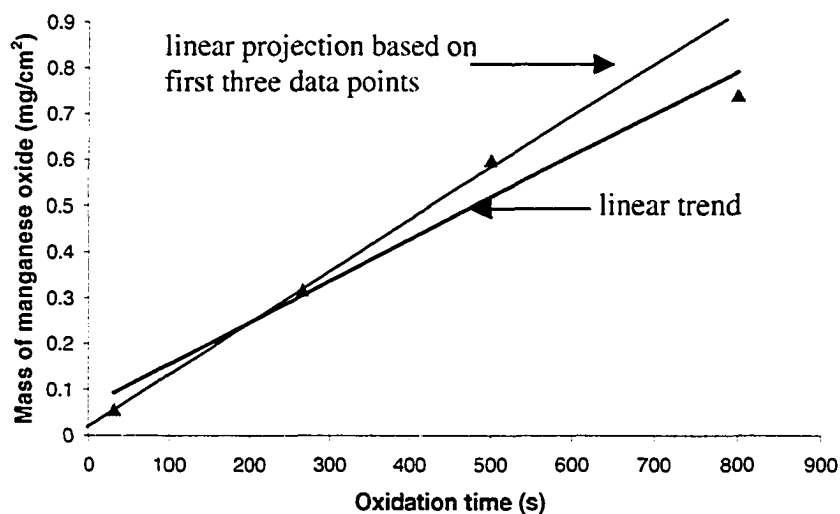


Figure 40. Growth of manganese oxide layer as a function of oxidation time.

The general trend (marked “linear trend”) between weight gain and oxidation time is a linear relationship with the following equation:

$$m = 0.0009t + 0.0645$$

where m is the oxide mass in mg/cm^2 and t is the oxidation time in seconds.

Ordinarily, the rate of oxidation decreases with time due to the increasing oxide thickness, which acts as a progressively stronger diffusion barrier with increasing time and thickness. This type of relationship results in a parabolic growth rate where diffusion of the metal cations becomes the rate-controlling step. However, this type of rate law assumes that a uniform and continuous oxide layer is being produced that is both compact

and non-porous. This is not the case for these films; the layer is far from uniform or continuous (Figure 38). If the SEM images of the films produced are considered in concert with the oxidation data, a linear rate law is very reasonable. The linear rate law typically applies to the formation of a highly porous, poorly adherent or cracked non-protective oxide layer, so the process is often reaction controlled rather than diffusion controlled.

Although the growth rate is linear, and an extremely porous layer is produced, the SEM images (Figure 38) indicate a dramatic thinning between the potentials of 0.1 and 0.9V. This behavior suggests that some portion of the Mn from the original dense layer is lost into solution during the oxidation process. This idea is supported by Figure 40. If the graph is considered more closely, the first three points on the graph form a perfect linear relationship with the final point (800s) lying below the projected linear trend based on the first three data points. The equation for this projected line is given below:

$$m = 0.0012t + 0.0153$$

where m is the mass in mg/cm^2 and t is the time in seconds.

The location of the final data point relative to the projected linear trend suggests that some material is indeed lost during the latter stages, accounting for the difference in the morphology of the film and the slightly lower than expected weight.

The material loss is also corroborated by the atomic absorption spectroscopy (AAS) results (Figure 41) that were used to analyze the amount of Mn that is lost at each stage of the oxidation. The Mn in solution refers to the Mn that is found in the bulk of the electrolyte solution. After oxidation, there is always some portion of the electrolyte that remains on the surface of the sample. The Mn rinsed off the wafer refers to the amount of Mn contained in the solution that remains on the surface of the sample. The total Mn lost during the oxidation process is then the combination of these two values. The Mn lost during oxidation is likely in two forms: ionic (due to disproportionation during

oxidation) and as an oxide (due to small portions of the porous layer being broken off the sample surface). Both of these forms of manganese will be measured by the AAS.

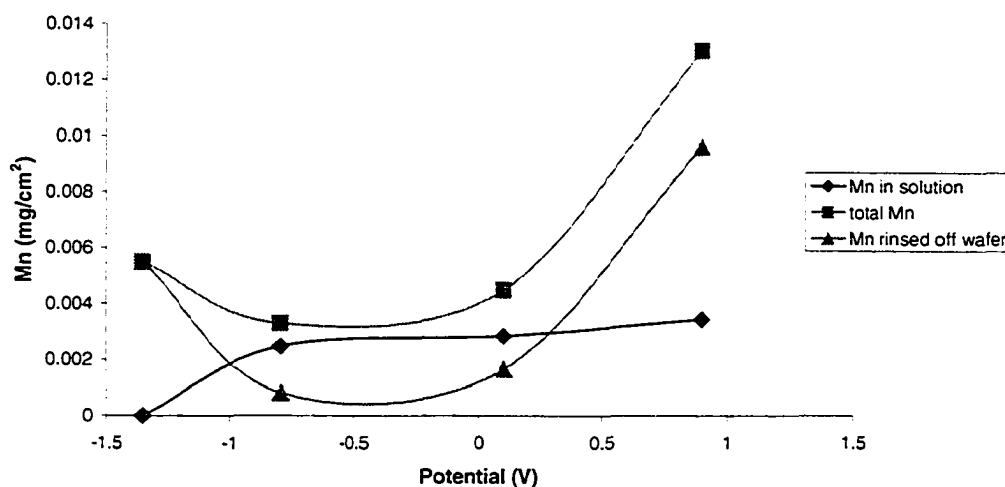


Figure 41. Graph of concentration of Mn at the various stages of oxidation in various locations.

The amount of Mn in solution is slowly increasing during the oxidation process (Mn in solution). However, there is also a significant amount of Mn near the surface of the sample that is readily rinsed off the surface of the wafer (Mn rinsed off wafer). Initially (-1.35V), this value is quite large since the oxidation process has not been occurring for very long and the bulk of the Mn that is lost (in ionic and oxide forms) is still resting on the sample surface. During the next two stages, the amount of Mn still on the surface of the wafer has decreased significantly, but as a consequence, there is more Mn in the bulk solution. After complete oxidation (0.9V), the amount of Mn in the bulk solution does not change significantly from the previous stage; however, there is a very large amount of Mn resting on the surface of the wafer. This indicates that between the potentials of 0.1V and 0.9V, there is a dramatic change resulting in a significant loss of Mn material that remains seated on the surface of the wafer and does not make its way into the bulk

solution. Combining these two trends (Mn in solution and Mn rinsed off wafer), there is an overall trend of increasing Mn loss (total) during the oxidation process, with the most significant change occurring between 0.1V and 0.9V. This result also corroborates the FE-SEM results (Figure 38) and growth results (Figure 40), where there is a dramatic thinning of the film between these two potentials and a corresponding loss of material. Although there is a weight gain during the 400-800s time period (Figure 40) due to the incorporation of additional oxygen, it is less than predicted by the linear trend indicating a loss of some material, which is corroborated by the AAS results.

It is expected that the plateau regions (Figure 36) in the potential-time plots correspond to some type of bulk transformation and are, therefore, expected to be two-phase or multi-valence regions.

The valence of the manganese in the porous film was determined through XPS analysis and measuring the splitting width of the Mn 3s spectra. A representative XPS spectrum is shown in Figure 42.

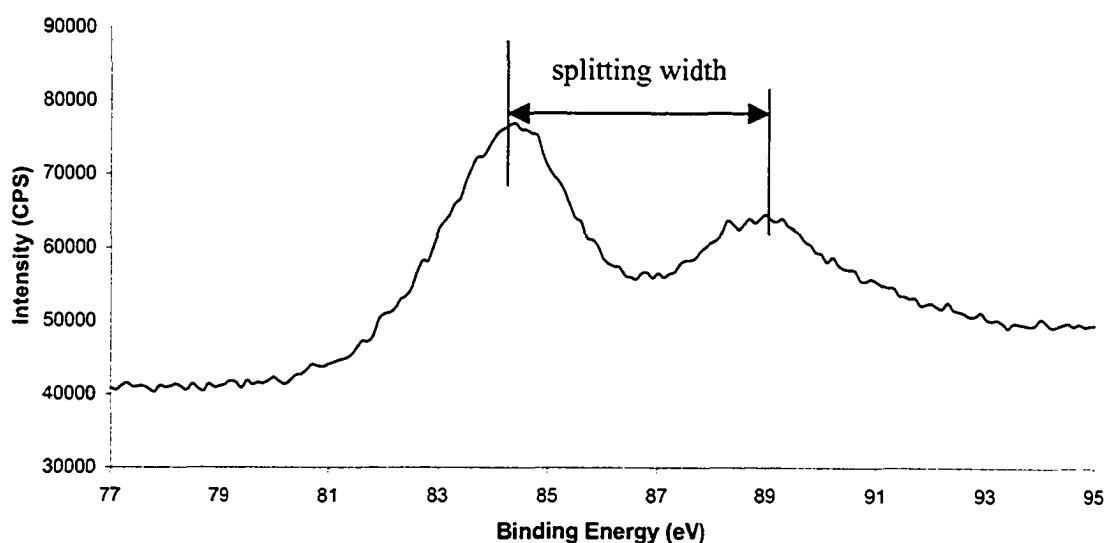


Figure 42. Mn 3s spectrum from the sample oxidized at 0.1 mA/cm^2 until a potential of 0.9 V vs. Ag/AgCl is reached.

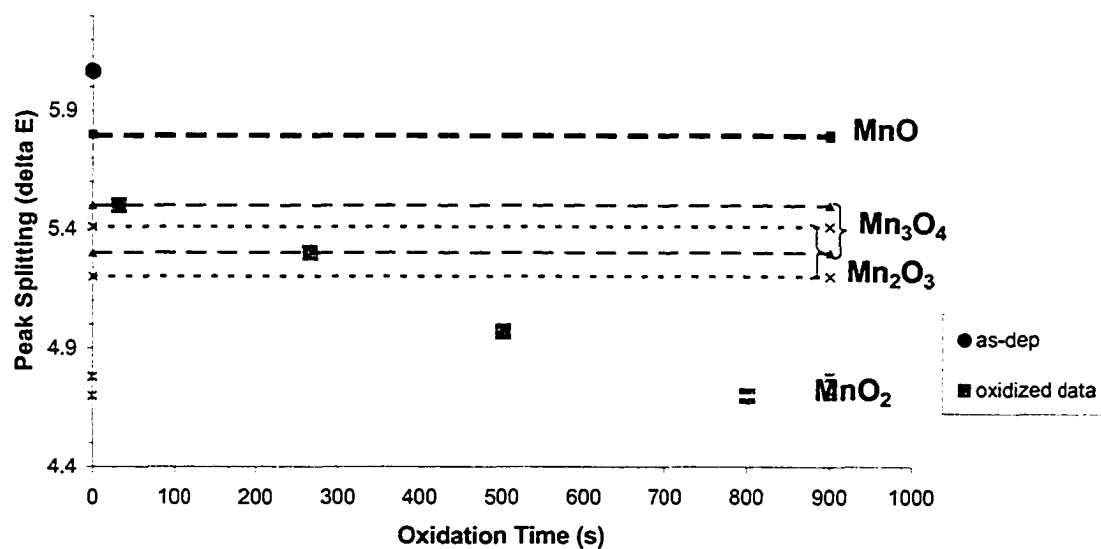


Figure 43. XPS results from oxidation of film at various stages showing the splitting width of the films as compared with the standard values given in the literature. These standard values are tabulated in Table 8.

The initial XPS results (Figure 43) appear to support the hypothesis that the plateau regions are two-phase. Figure 43 also includes the data from the standards found in literature. A range of values is often quoted and, thus, the data from the standards is presented as two lines of the same color between which a particular phase exists. There is some overlap between the ranges of Mn_3O_4 and Mn_2O_3 , but this is to be expected given the similarity in both structure and valence between Mn_3O_4 (2^+ , 3^+) and Mn_2O_3 (3^+), and therefore, some interpretation is required for these XPS results. The as-deposited structure clearly lies above the MnO single-phase region, and thus is considered to be both MnO and Mn as indicated by the TEM results earlier. Unfortunately, there were no data available for the splitting width of pure Mn, so it must be interpreted that since the splitting width of the as-deposited film lies far above the single phase region for MnO that there is some quantity of Mn in the film. The data clearly show that as the oxidation proceeds, the valence of the Mn is continually increasing. During the first plateau (-1.35V) at 33s, the data point lies right on the boundary of Mn_3O_4 , so the sample is not technically two-phase. However, if the oxidation traces in Figure 37 are considered as well, it can be seen that there is some variation in subsequent oxidation processes in addition to some dispute as to the actual start and end potential of the first two plateaus. Because of these uncertainties, it is likely that oxidation to 33s places the film at the very end of the plateau where the bulk transformation would be nearly complete, and the film would be single phase. In this case, the single phase is Mn_3O_4 , which implies that the bulk transformation that is occurring is from MnO to Mn_3O_4 . In addition, there must also be a transition from Mn to Mn_3O_4 (since the starting material is Mn/MnO); however, given the reactive nature of metallic Mn^{24} , it is suggested that the transformation from Mn to MnO occurs almost instantaneously when the film is exposed to the electrolyte and then the bulk transformation from MnO to Mn_3O_4 occurs during the first tens of seconds of oxidation.

The second plateau at -0.8V vs. Ag/AgCl and 266 s results in the production of a two-phase film as expected. Although the data point lies in the confusing transition region between Mn_3O_4 and Mn_2O_3 , it appears that both phases are present in the film. Given the location of the data point, it can be inferred that there is more Mn_2O_3 present in the film

than Mn_3O_4 , but this too can be explained by referring back to Figure 37. When comparing the oxidation trace to -0.8V with the oxidation trace to 0.9V , it is obvious that the oxidation to -0.8V was stopped near the end of the plateau again. This means that the bulk transformation is nearly complete resulting in the bulk of the film being made up of Mn_2O_3 . If the oxidation process were stopped earlier in the plateau, more Mn_3O_4 would be present as compared with the Mn_2O_3 .

The third plateau at 0.1V (500s) is more clearly defined and obviously one of the major transitions to occur during the oxidation. In this case, the data point lies clearly in the two-phase region between Mn_2O_3 and MnO_2 as expected. The final oxidation ends at 0.9V at the end of a smaller plateau and the resulting film is clearly single phase MnO_2 . It is unknown, however, whether the transition to single phase MnO_2 occurs completely within the plateau at 0.1V or after a potential of 0.9V is reached. Since this is the most important transition, a sample was thus produced with a final potential of 0.5V and analyzed in the XPS in order to determine the phases present and identify conclusively when the oxidation to MnO_2 occurs. Using the peak splitting of the Mn 3s peak again, the film at 0.5V was found to be a mixture of two phases: Mn_2O_3 and MnO_2 (Figure 44).

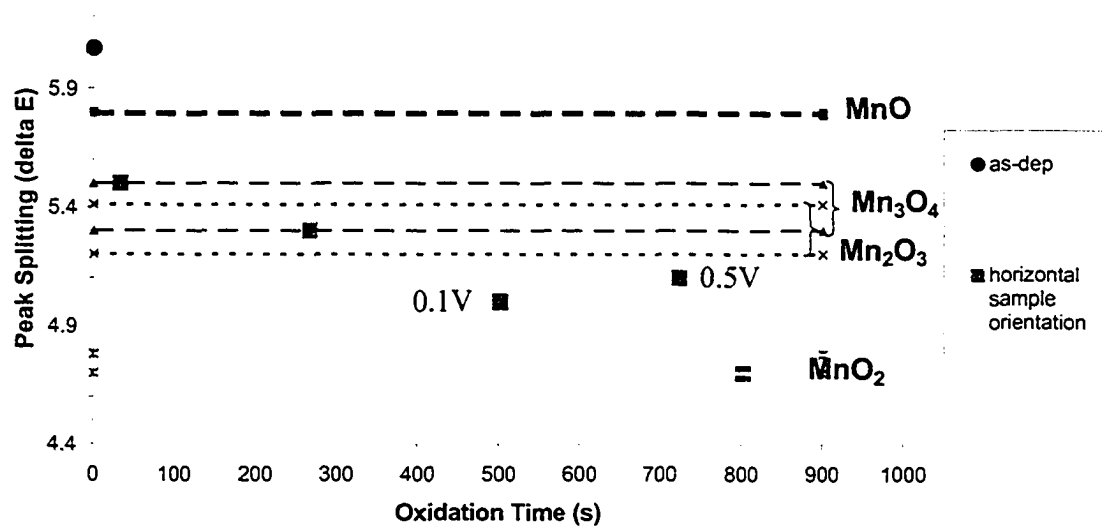


Figure 44. XPS results from oxidation of film at various stages, now including 0.5V, showing the splitting width of the films as compared with the standard values given in literature. These standard values are tabulated in Table 8.

The points for the films produced at a final potential of 0.1V and 0.5V are labeled on the figure. Although they both clearly lie in the two-phase region, the film at 0.5V has a slightly higher peak splitting value indicating slightly more Mn₂O₃ than the film at 0.1V. The opposite effect was expected, i.e., more MnO₂ produced as oxidation proceeds. However, this incongruity may be due to the inherent scatter in this process. As mentioned earlier, although the oxidation process follows the same voltage vs. time curve, the time required for oxidation is quite variable due to differences in the deposited Mn/MnO layer (i.e., thickness, relative oxygen content, etc.). Thus, the film at 0.5V may simply have slower reaction kinetics than the film at 0.1V. The important result, however, is that the film in the transition region between plateaus is also a two-phase structure. This indicates that the full oxidation from Mn₂O₃ to MnO₂ occurs between the potentials of 0.1V and 0.9V. From this result, it can be inferred that the previous oxidation process, MnO to Mn₃O₄, may occur between the potentials of -1.4V and 0.8V and so on. Thus, it can be concluded that the change in phase involves both a region of constant potential and a region of increasing potential. There is no acceptable

explanation of this phenomenon in the literature, although other researchers⁴² have suggested that the constant potential region corresponds to a heterogeneous reaction (at the electrode/electrolyte interface) and the regions of increasing potential correspond to homogeneous reactions (those reactions occurring in the solution). It may be that a combination of these two types of reactions is necessary in order to complete the transformation from one phase to another.

A substantial amount of the MnO_2 phase that is known to give high capacitance values is produced at the end of the plateau at 0.1V (~500s), and therefore, films oxidized just past 0.1V may also exhibit capacitance. This idea will be explored further in a later section.

Another necessary quality for the films is their relative hydration, as hydration plays an important role in developing significant capacitance. The hydration values can be gleaned from deconvoluting the oxygen 1s peaks (O1s) into its three major bond components: Mn-O-Mn, Mn-O-H, and H-O-H (Table 9). A representative de-convoluted O1s spectrum is shown in Figure 45 with complete results shown in Figure 46.

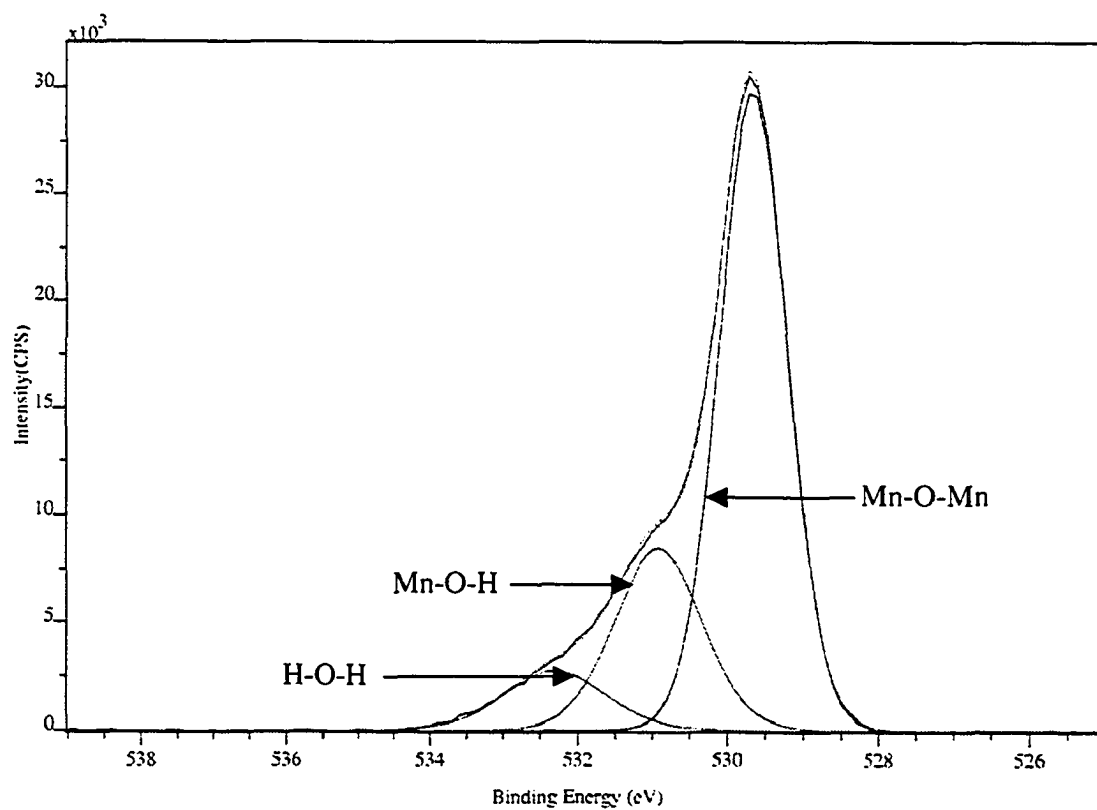


Figure 45. O1s spectrum from the sample oxidized at 0.1 mA/cm^2 until a potential of 0.9V vs. Ag/AgCl is reached. The peak has been deconvoluted into its major constituents: H-O-H, Mn-O-Mn, and Mn-O-H.

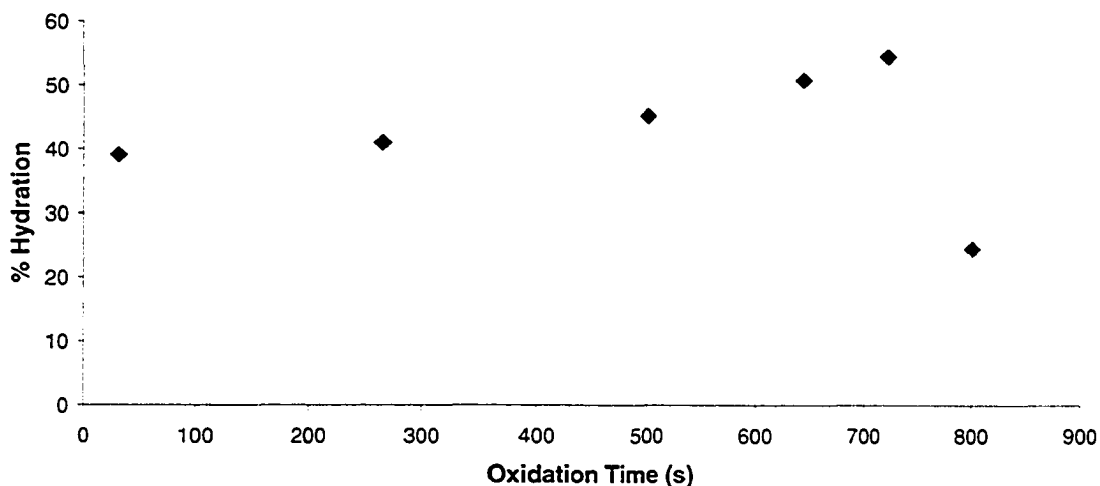


Figure 46. Relative hydration of the film during the oxidation process.

The growing oxide film appears to reach its maximum hydration relatively early in the oxidation process (~33s) and then hydration remains fairly constant to the end of the plateau at 0.1V (~500s). During the transition from 0.1V to 0.9V (~500s-800s), there is first an increase in hydration (measured at 0.3V or 650s and 0.5V or 725s) followed by a significant decrease in the relative hydration of the film to the final value of 25 at% at 0.9V. It should be noted that a hydration value of 25% is typical of the values achieved by the other researchers in this area. However, the fact remains that the phases identified through XPS are all clearly present in the hydrated state. Although the pH of the solution indicates it is slightly acidic (pH=6.3), the reactions given in the literature for MnO_2 in an acidic medium do not seem an appropriate fit to these results. The reactions given for MnO_2 in an alkaline solution, however, do provide a fairly good understanding of the possible reactions that are occurring.

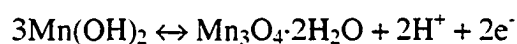
Three groups, Cha and Park²², Gosztola and Weaver⁴² and Messaoudi et al⁴³, give very specific and similar reactions for the oxidation of metallic Mn to MnO₂ in an alkaline medium, which are very similar to this process with the exception of the slightly more acidic solution. Cha and Park²² suggested that the oxidation process proceeds from Mn metal to MnO₂ through a successive production of hydroxides of various valences. While this is a very reasonable supposition, and can address the formation of MnO (Mn(OH)₂) and Mn₂O₃ (MnOOH), it does not adequately address the formation of Mn₃O₄ in our system. Gosztola and Weaver⁴², show an oxidation trace (Figure 5) that is very similar to the traces produced in this thesis (Figure 37). However, they provide only a simplified mechanism whereby metallic Mn is converted to Mn(OH)₂ (hydrated MnO). Mn(OH)₂ is then converted to MnOOH (hydrated Mn₂O₃), which then transforms to MnO₂. These reactions, MnO to Mn₂O₃ to MnO₂ are insufficient to explain the process in Figure 37. Messaoudi et al.⁴³ provide the most complete set of reactions that cover all the transformations from Mn to MnO₂ except that they are for an alkaline medium. It is reasonable to assume, however, that these reactions could occur in a slightly acidic medium with some small modifications. More importantly, however, the reactions that Messaoudi et al. suggest cover all phases that are forming in this particular system.

According to Messaoudi, the oxidation from Mn to Mn(OH)₂ occurs with the elimination of H₃O⁺ and Mn²⁺ according to



The results from the process developed in this thesis suggest that this reaction is likely occurring almost immediately upon immersion of the film in the Na₂SO₄ and at the starting potential of the process (-1.4V), only MnO is present.

The second transformation reaction according to Messaoudi is the transformation of Mn(OH)₂ to Mn₃O₄ according to:



According to the XPS results for this system (Figure 43), this reaction is likely occurring at -1.35 V in the first tens of seconds of the oxidation process where both MnO and Mn₃O₄ simultaneously appear. The large amount of Mn that was detected by AAS in the early oxidation stages (Figure 41) is likely the Mn²⁺ that was released during the initial, and nearly instantaneous, transformation of the Mn to the Mn(OH)₂.

The next transformation is Mn₃O₄ to Mn₂O₃ accompanied by the dissolution of Mn³⁺ according to:



where MnOOH is often considered as the hydrated form of MnO_{1.5} (Mn₂O₃)

Again, according to the XPS data (Figure 43), this reaction occurs at -0.8 V. The dissolution of Mn³⁺ ions is verified by the AAS data, where a fairly substantial amount of Mn is shown in to be in solution and on the surface of the wafer (Figure 41). It is possible that the redox reaction occurs during the plateau region and the subsequent dissolution of Mn³⁺ (which is a chemical reaction) occurs during the transition region between -0.8 V and 0.1 V.

The substantial transformation that occurs at 0.1 V is clearly the most important reaction. MnO₂ forms according to:



By comparison, the major transformation (at constant potential) for Gosztola and Weaver⁴² was identified as a similar transition from MnOOH to Mn(OH)₂, which is not realistic for this particular system. Beyond 0.1 V, there is a region of increasing potential that is not described in other systems found in the literature and then a final plateau at approximately 0.9 V. Again, this plateau is not identified in any other system discussed in the literature. However, the XPS evidence indicates that reaction from MnOOH to $6\text{MnO}_2 \cdot 5\text{H}_2\text{O}$ is occurring between the potentials of 0.1 and 0.9 V. Perhaps, it is

reasonable to assume that the reaction from MnOOH to $6\text{MnO}_2 \cdot 5\text{H}_2\text{O}$ is occurring in two distinct steps, though there is no evidence to support which steps these would be.

Experimentally, it has been noted that beyond 0.9V, the film delaminates and falls off the substrate. It is possible that the reaction beyond 0.9V is described by the final reaction suggested by Messaoudi et al. whereby the MnO_2 converts to MnO_4^- (aq) and MnO_4^{2-} (aq) accompanied by oxygen evolution. There is no direct evidence of this except for the evolution of an unknown gas at potentials beyond 0.9V.

There is still one criterion necessary for high capacitance. The structure needs to be amorphous, to allow for easier proton insertion into the oxide structure. The internal structure of the porous layer and the rest of the film has been studied using the TEM. This hypothesis was tested using the zigzag films, rather than the dense films, as a greater sample volume/thickness was desired to facilitate diffraction work in the TEM.

Again, a current density of 0.1 mA/cm^2 was used for oxidation of the films. One sample was oxidized completely (to 0.9V), and one sample was oxidized only partially. For the thicker zigzag films, complete oxidation occurred in 4750s (to a potential of 0.9V). A second sample was chosen at 1700s representing 36% of total oxidation (a potential of – 0.8V). The FE-SEM images of these two films are shown in Figure 47.

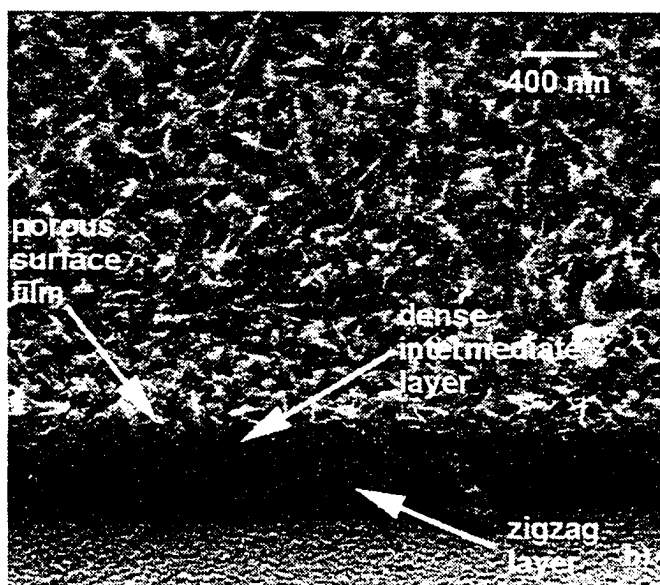
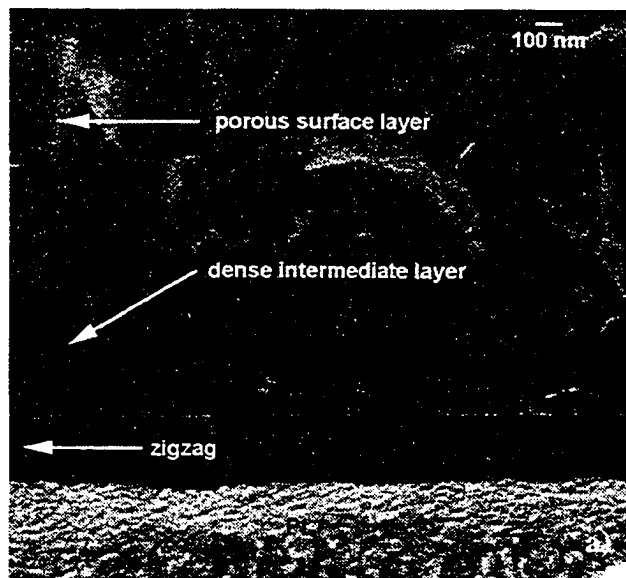


Figure 47. FE-SEM SE images of zigzag films in an oblique view that have been oxidized for a) 1700s, representing 36% of the total oxidation time and b) 4750s, representing 100% of the total oxidation time.

Figure 47 shows FE-SEM images of the oxidation process for the zigzag films and reveals the formation of a similar porous surface layer. The bulk of the zigzag layer

remains intact. While these results are not different from what was seen with the dense samples, the greater thickness of these samples makes identification and visualization of the different layers much easier. The sample oxidized for 1700s reveals that there are, in fact, two layers that form as a result of the oxidation. Directly on the surface of the zigzag is a dense intermediate layer. On top of this layer is a fairly thick, extremely porous layer protruding from the surface. These layers are hereafter referred to as the dense intermediate layer and the porous surface layer, respectively. Although only the porous surface layer is readily visible in the FE-SEM images of the dense films, it is likely that the dense intermediate layer exists in that structure as well, but is simply too thin to be imaged properly in the FE-SEM. Similarly, the FE-SEM image of the film oxidized for 4750s also shows a porous surface layer that was visible in the previous samples, a dense intermediate layer and the zigzag layer.

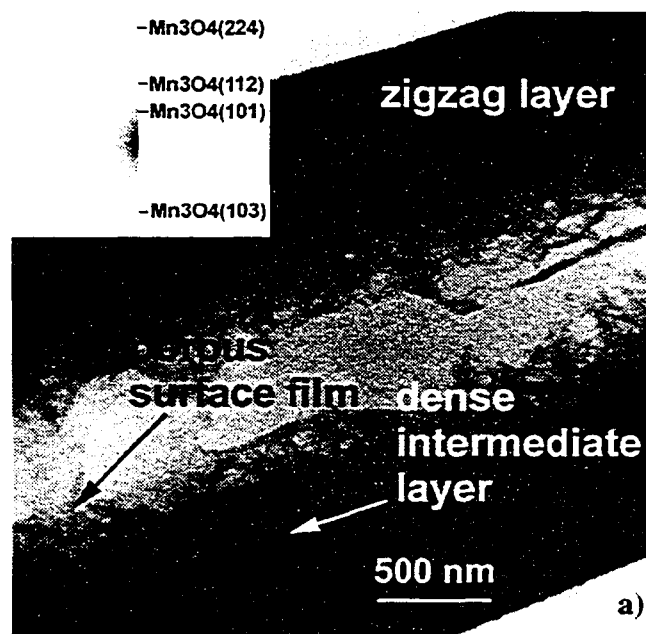
XPS analysis (Mn 3s and O1s) was used to confirm that the chemical structure of the porous layer produced on the zigzag films was the same as those produced on the dense films. The results are shown in Table 10.

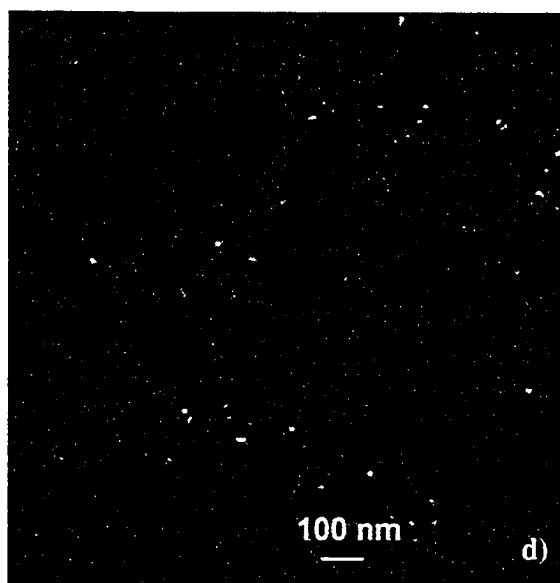
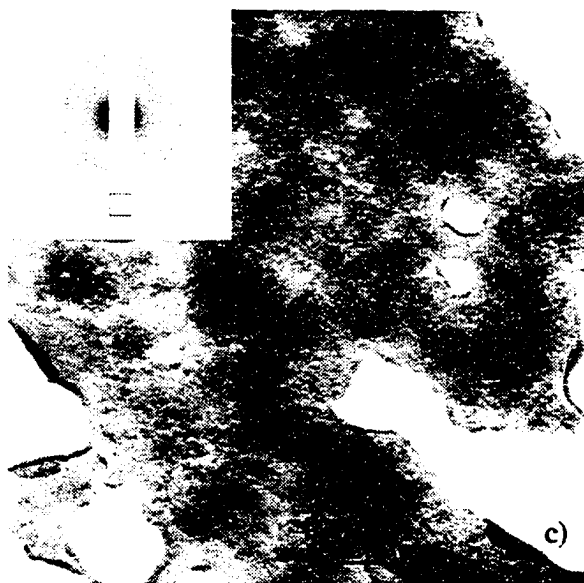
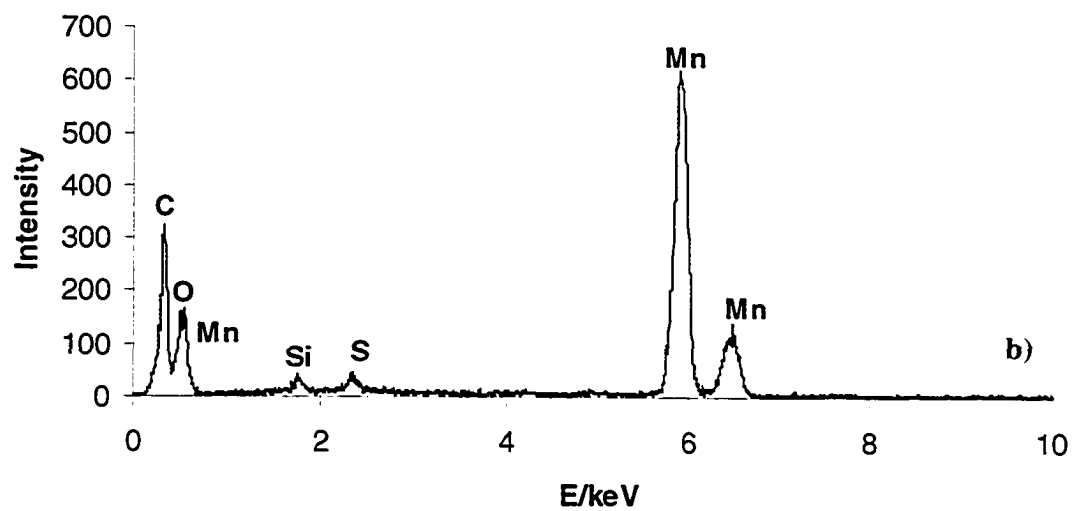
Table 10. XPS data for zigzag films and dense films.

Sample	Splitting Width (eV)	Phase	% Hydration
Zigzag film oxidized to 36%	5.48	Mn ₃ O ₄ & Mn ₂ O ₃	45
Zigzag film oxidized to 100%	4.79	MnO ₂	32
Dense film oxidized to 33%	5.3	Mn ₃ O ₄ & Mn ₂ O ₃	45
Dense film oxidized to 100%	4.7	MnO ₂	25

Table 10 makes it clear that the same phase or phases are forming at the same stage of oxidation regardless of the initial morphology of the evaporated film: zigzag or dense. Additionally, there is a similar trend with respect to the hydration of the porous layer, showing a trend of decreasing hydration as the film reaches complete oxidation.

Since the porous layers of the two different morphologies have been revealed to be identical, it is possible to analyze the TEM results of the zigzag structure and apply them directly and generally to the oxidation of other substrate morphologies. The TEM images for the zigzag films are shown in Figure 48.





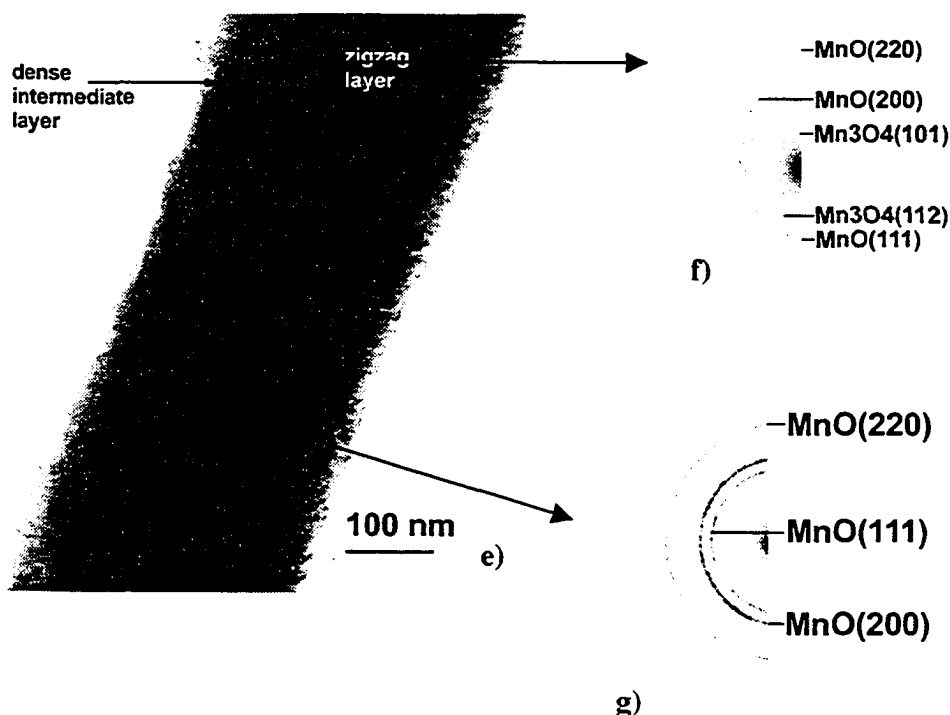


Figure 48. a) TEM BF cross-sectional image of the sample oxidized for 1750 s (36% of total oxidation time) with inset diffraction pattern showing some crystallinity, indexed as single phase Mn₃O₄. b) Representative EDX spectrum from the porous surface layer. c) TEM BF plan view image of porous surface layer with inset diffraction pattern indexed as a mixture of MnO and Mn₃O₄. d) TEM DF plan view image taken from boxed area in diffraction pattern in (c) showing partial crystallinity. e) TEM BF cross-sectional image of zigzag layer from sample electrochemically oxidized for 1750s. f) SAD pattern from the dense intermediate layer indexed as a mixture of MnO and Mn₃O₄. g) SAD pattern from zigzag layer indexed as single phase MnO.

For the sample oxidized to 36%, the cross-sectional TEM image (Figure 48a) clearly shows the porous surface layer on the surface of the denser Mn zigzag layer. EDX analysis from the porous layer (Figure 48b) reveals that it is predominantly manganese-based, indicating a portion of the original zigzag layer has reacted to produce the new layer. The Si in the spectrum is from the surrounding glue, which is Si-based while the S

is likely a contaminant from the Na_2SO_4 solution. The diffraction pattern from the porous surface layer of the sample (inset Figure 48a), with a combination of sharp rings and diffuse rings, indicates partial crystallinity and was indexed as the Mn_3O_4 phase. Despite the weak intensities, there were no MnO rings identified, suggesting the porous surface layer is single phase Mn_3O_4 with mixed crystalline and amorphous content (confirmed as single phase Mn_3O_4 by XPS). However, there is also a possibility that part of the dense intermediate layer is sampled in this diffraction pattern, making it impossible to conclude at this stage if the porous layer is fully amorphous or partially crystalline.

Plan view sections were made in order to attempt to confirm the diffraction analysis in the cross-section. A representative plan view section (Figure 48c) reveals a layer that is partially crystalline in nature but with some amorphous content. However, the morphology presented in the plan section suggests that the images in Figure 48c and d are not of the porous surface layer, but rather, the denser intermediate layer just beneath. The inset diffraction pattern also indicates a mixture of MnO and Mn_3O_4 , rather than single phase Mn_3O_4 that was obtained in cross-section. Although the layer could not be completely characterized in the TEM at this stage, it is suggested that the porous layer is completely amorphous, thereby accounting for the diffuse rings in the inset diffraction pattern in Figure 48a. The crystalline Mn_3O_4 rings are coming from the dense intermediate layer, which has both amorphous and crystalline components.

Unfortunately, in cross-section, it is not possible to image all layers at one time because of preferential sputtering effects during sample preparation. Figure 48e shows a higher magnification image of the layers closest to the Si wafer of the partially oxidized structure with accompanying diffraction patterns. The undisturbed zigzag layer and the dense intermediate layer, visible in Figure 48a, are also visible in Figure 48e. The dense intermediate layer is identified through diffraction as a mixture of MnO and Mn_3O_4 (Figure 48f). Again, the reflections for the MnO phase are extremely weak indicating the bulk of the material is Mn_3O_4 . In addition, the lower portion of the zigzag layer is identified as single phase MnO (Figure 48g) indicating the Mn in the zigzag layer is oxidizing from Mn to MnO . The bulk zigzag film remains crystalline, while the dense

intermediate layer has both amorphous and crystalline components. If the intermediate layer is a mixture of amorphous and crystalline phases, it is reasonable to assume that the porous surface layer is completely amorphous.

Once the oxidation cycle is completed (4750 s), the film exhibits the capacitive tendencies previously reported⁷⁴. Figure 49 a and b show two TEM cross-section views of the film. Figure 49a shows a region where two samples have been glued face-to-face, so that the porous surface layer on each surface is visible. Figure 49b shows the undisturbed zigzag layer with an inset diffraction pattern from the area indexed as single phase Mn_3O_4 .

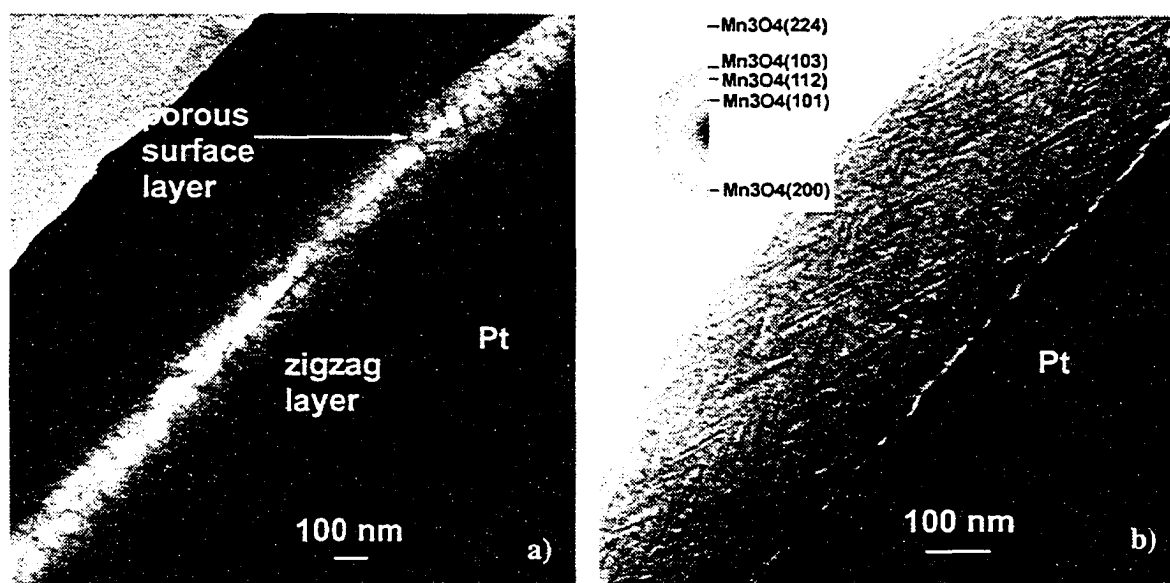


Figure 49 a) TEM BF cross-section image of interface showing growth of the porous surface layer. b) TEM BF cross-section image of zigzag layer only with inset diffraction pattern indexed as single phase Mn_3O_4 .

The continued oxidation of the structure does not destroy the porous layer, it simply further oxidizes the material in the porous surface layer to MnO_2 (Table 10) and the

zigzag material underneath the surface layer from MnO (Figure 48) to Mn₃O₄. Indeed, the plan view (Figure 50), which is truly representative of the outermost surface layer, reveals that the continued oxidation results in the formation of an entirely amorphous layer as previously suggested. Thus, between the potentials of -1.35V and 0.9V, there is an overall oxidation of the under-layer (in this case, the zigzag layer) and the formation of the amorphous porous surface layer.

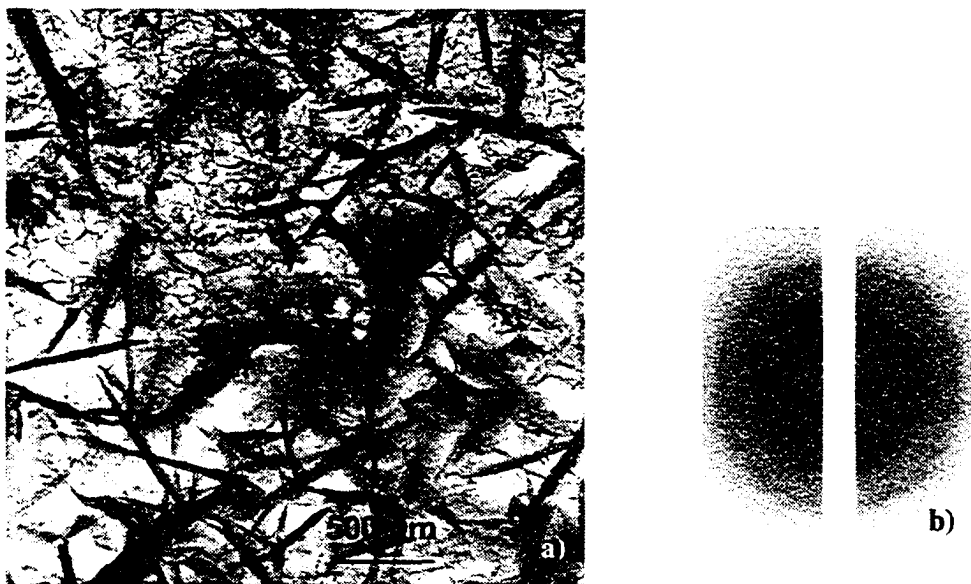
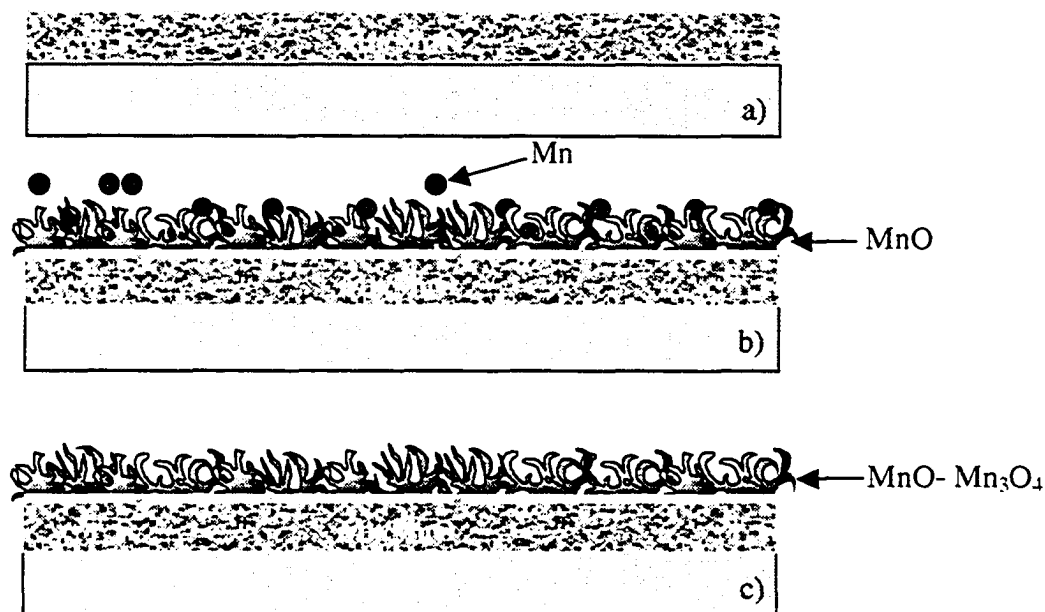


Figure 50. a) TEM BF plan view image of porous surface layer. b) Amorphous SAD pattern from a).

Given the results from the TEM, XPS and FE-SEM, an oxidation process can be postulated that fits with all the results. The oxidation of the Mn in the electrode film occurs almost immediately upon its immersion into the solution (i.e., spontaneously with no applied current) and the porous surface layer forms at this time. The porous layer maintains an approximately constant thickness throughout the oxidation process (-1.35V to 0.1V) until it finally thins just before 0.9V. Thus, it is likely that the porous layer forms in full thickness almost immediately (prior to -1.35V) in the process and is amorphous upon formation. There are two reasons to support the theory that the porous film forms in the amorphous state. The first reason is related to the kinetics of the

process. With the application of an anodic current, the oxidation process is artificially accelerated and thereby occurs fast enough to prevent crystallization. In addition, it is unlikely that a crystalline film would form in the first stages of a process and convert over time to an amorphous state; normally, the opposite is true. The TEM results show that the base electrode film remains crystalline, but the intermediate layer is partly amorphous. Thus, the portion of the Mn that reacts initially to form the porous layer produces an amorphous product, while that material that is not used to form the porous layer remains crystalline (base, undisturbed material). In between these two layers is the intermediate transition layer, i.e., the transition region that has mixed amorphous and crystalline behavior.

When the amorphous porous layer initially forms it has a 2+ valence. As the oxidation process proceeds, the manganese within the porous layer continues to oxidize (eventually reaching the necessary 4+ valence). However, in addition to the continued oxidation of the porous layer, the base layer of undisturbed material continues to oxidize as well, ultimately becoming crystalline Mn_3O_4 . A schematic illustration of the oxidation process is shown in Figure 51.



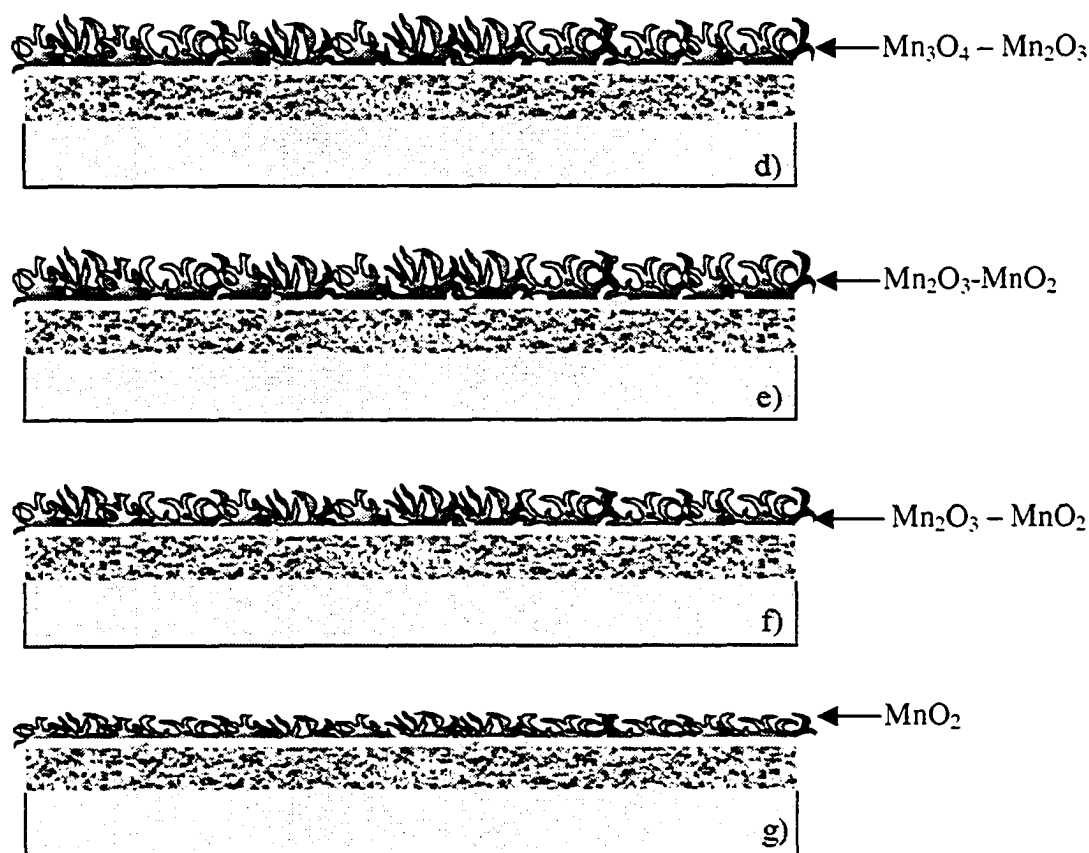


Figure 51. Schematic illustration showing the oxidation process of the porous surface film and the underlying sub-layer through the various stages. a) As-deposited state. b) Immersion into solution showing the immediate dissolution of the manganese and the formation of the porous amorphous surface film (MnO). c) The film during the first plateau at -1.35 V vs. Ag/AgCl , showing the continued oxidation of the porous surface film from MnO to Mn_3O_4 . The sub-layer continues to oxidize from Mn to MnO . d) The film during the second plateau at -0.8 V showing the oxidation of the surface film from Mn_3O_4 to Mn_2O_3 . The sub-layer begins to oxidize from MnO to Mn_3O_4 . e) The film during the third plateau at 0.1 V showing the start of the oxidation of the porous surface layer from Mn_2O_3 to MnO_2 . The sub-layer continues the oxidation process from MnO to Mn_3O_4 . f) The film in the transition region between 0.1 V and 0.9 V showing the continued oxidation of the porous surface film from Mn_2O_3 to MnO_2 . The sub-layer continues the oxidation process from MnO to Mn_3O_4 . The porous surface film begins to become slightly thinner. f) The film at the final potential of 0.9 V showing the formation of a porous surface layer that is entirely composed of MnO_2 . The sub-layer has converted entirely to Mn_3O_4 . In addition, the porous surface film has been significantly reduced in thickness.

The transition from 0.1 to 0.9V shows a significant decrease in hydration and also a loss in the porous surface layer thickness. If this information is combined with the phase results, which show that a significant amount of hydrated MnO_2 forming before 0.1V, it seems more desirable to stop the oxidation process at the end of the plateau at 0.1V where the sample has significant amounts of the desired phase, MnO_2 , with much higher hydration (45at% at 0.1V vs. 25at% at 0.9V) and possibly superior surface area. Only the hydrated lattice sites are said to take part in the capacitive process and therefore higher hydration in the structure means more sites are available to contribute to the overall capacitance of the film⁴⁴. If the capacitance of these films is tested (CV cycling) at various potentials after the plateau at 0.1V, a surprising result is obtained. Figure 52 shows the current vs. potential plots for the various oxidations, which gives a measure of capacitance.

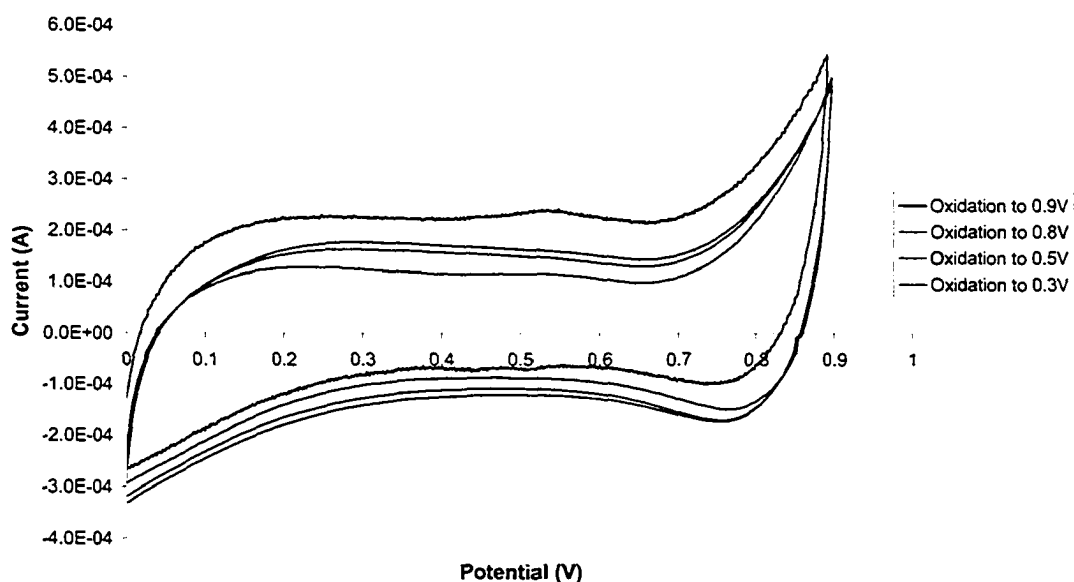


Figure 52. Current vs. potential plots for samples oxidized to various end potentials and then cycled 100 times. The tenth cycle is shown.

If the different amount of charge capacities are compared, it is obvious that a sample oxidized to 0.9V contains the most significant capacitance (11.8 mF/cm^2). However, a

sample oxidized to 0.8V, very close to 0.9V, measures only 7 mF/cm², by far the poorest value of the films tested. The intermediate potentials of 0.3V and 0.5V result in capacitance values between the previous two values, 8 mF/cm² and 8.4 mF/cm², respectively.

Fairly significant capacitance can be developed after oxidation to 0.3V. The capacitance increases slightly as the potential is increased (to 0.5V in this case) and then decreases rather dramatically at the onset of the final plateau (0.8V). There is a very dramatic increase in capacitance once 0.9V has been reached. It is assumed that the reasonable amount of capacitance that can be developed at 0.3V and 0.5V is related to the phase (significant amount of Mn⁴⁺) and the extremely high hydration of the films, giving a substantial number of capacitive (or active) sites. The noticeable decrease in capacitance at 0.8V is suspected to be a result of the dramatic decrease in hydration that occurs between the potentials of 0.5V and 0.9V reducing the number of useable capacitance sites. The oxidation time to reach 0.8V is approximately 760s (Figure 37), which would place the hydration value for the sample oxidized to 0.8V most likely much lower than the value for 0.5V according to the results shown in Figure 46. The sample oxidized to 0.9V has the largest capacitance, but low hydration, and therefore the high capacitance must be related to the effective surface area of the porous film. Although the thickness of the sample is significantly reduced at 0.9V, it likely has a much finer structure resulting in an overall increase in the surface area of the film. Thus, despite the decrease in relative hydration, the dramatically increased surface area actually results in more sites to take part in the capacitance reaction, thereby resulting in the higher capacitance value. In addition, at 0.9V, the film should be 100% MnO₂ which is expected to significantly increase the capacitance.

The microstructure (thinner but possibly with more surface area) can be seen to some degree in the FE-SEM oblique view (Figure 38) where the film is not nearly as thick, but the porosity is much finer in scale and the film likely has a greater overall area exposed to the electrolyte. The refinement of the surface area is likely the transition that is occurring during the plateau leading up to 0.9V. In addition, if the film at 0.8V has the lower

hydration value and does not yet have the very refined structure to provide substantial surface area, it will naturally have a very poor capacitance value. Developing significant capacitance is a balance between the hydration and the available sites for reaction (surface area). Only the hydrated sites are thought to take part in developing capacitance; therefore, for samples of equal surface area, the sample with the greater hydration will develop greater capacitance since there are more hydrated sites present. Likewise, for samples of similar hydration quantity, the sample with the largest surface area will develop the highest capacitance since the greater amount of active (hydrated) sites are present. Thus, it is possible for a sample of seemingly lower hydration (i.e., oxidation to 0.9V) to develop greater capacitance than a sample of much higher hydration (i.e., oxidation to 0.5V) because it has a much greater surface area and therefore a greater overall number of hydrated sites.

Since it is necessary to finish the oxidation at 0.9V in order to maximize the capacitance, it is desirable from a morphological and chemical perspective to reduce the changes that occur during the oxidation between 0.1V and 0.9V in order to maintain higher surface area and hydration. If the sample is oxidized with two separate currents, it may be possible to retain some of the more desirable qualities of the films at 0.1V, even after oxidizing to 0.9V. If the sample is oxidized slowly to 0.1V, there would be ample time to produce a large porous layer and significant hydration. Once 0.1V is reached, the oxidation process is sped up to reduce the amount of time spent in the region between 0.1V and 0.9V where the bulk of the loss of hydration occurs. The film should still be able to fully convert to MnO_2 and refine the structure slightly to increase surface area. This type of oxidation scheme is illustrated in Figure 53, where one of the curves represents complete oxidation at 0.1 mA/cm². The second curve, that is slightly disjointed, represents oxidation at 0.1 mA/cm² until a voltage of 0.3V is reached and then completion of the oxidation process at 0.8 mA/cm². The reason for the slight break in the graph is because of the small time delay that takes place when the potentiostat switches to the second current, although the potential continues to increase on its own.

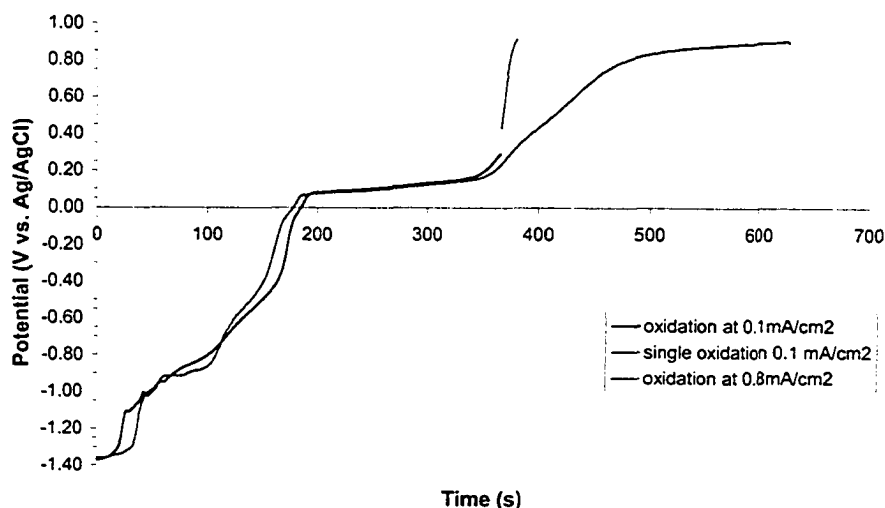


Figure 53. Graph of potential as a function of time for samples oxidized using two different current densities ($0.1/0.8\text{mA}/\text{cm}^2$) compared with a sample oxidized using a single current density ($0.1\text{mA}/\text{cm}^2$).

The sample oxidized at a single current ($0.1\text{ mA}/\text{cm}^2$) completes the oxidation process in 630s, however, approximately 270 s of that oxidation process is spent in the potential range of 0.1-0.9V vs. Ag/AgCl. Although this time is used for the transition to MnO_2 , there are detrimental effects such as loss of hydration. In the other curve, the sample is oxidized at $0.1\text{ mA}/\text{cm}^2$ until a potential of 0.3V is reached (to ensure good hydration). At this point, the oxidizing current is changed to $0.8\text{ mA}/\text{cm}^2$ in order to speed the transition to MnO_2 with a minimal loss in hydration but still refine the structure to provide good surface area. With this type of oxidation, only 30s are spent in the critical region between 0.1 and 0.9V.

The morphology of these two films is shown in the FE-SEM images in Figure 54.

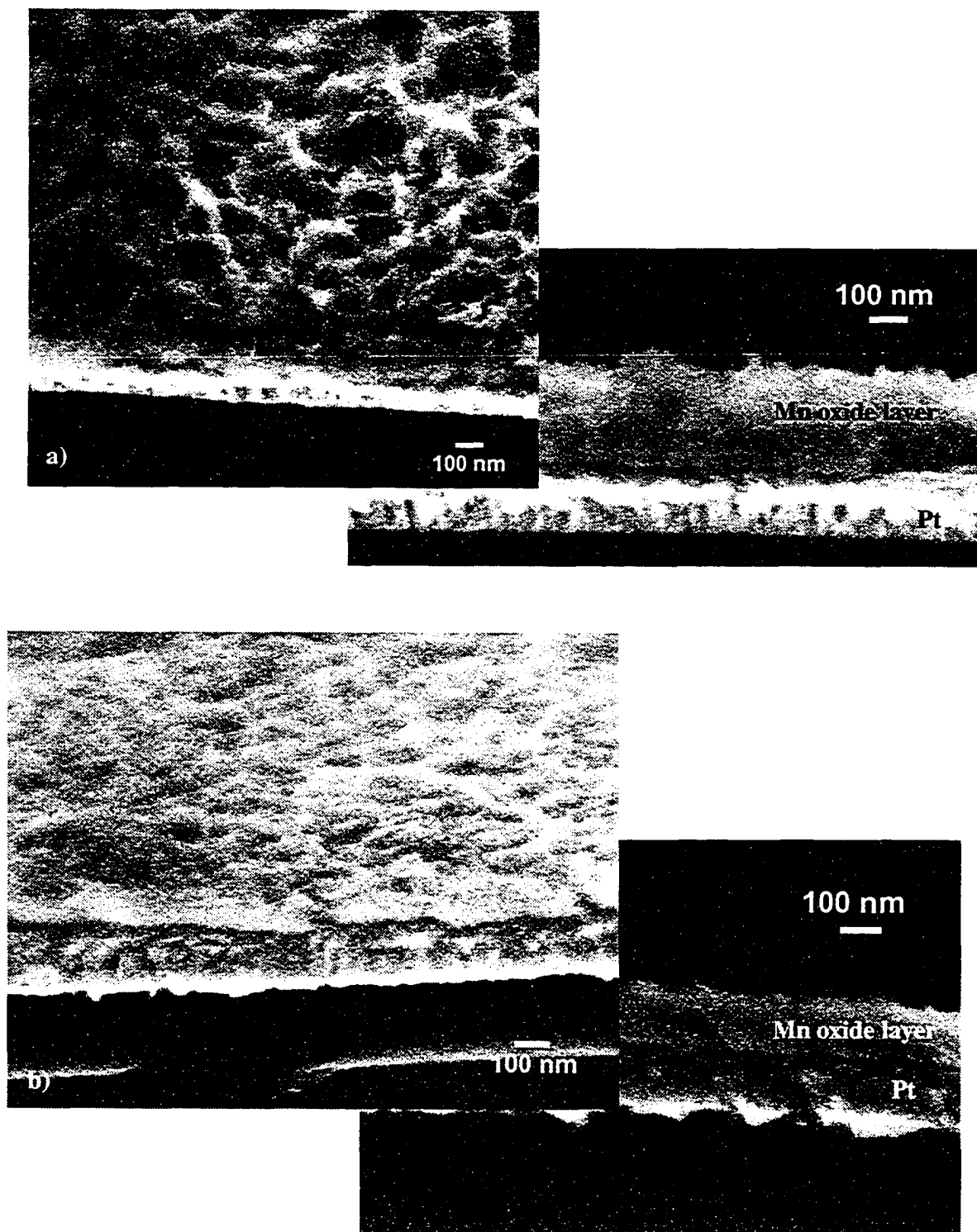


Figure 54. FE-SEM SE images in oblique and cross-section view from films oxidized at a) a single current density (0.1 mA/cm^2) and b) two separate current densities ($0.1/0.8 \text{ mA/cm}^2$).

There is a substantial visible difference in the morphology of these two films. The single current oxidation process (Figure 54a) results in a thicker film with far greater porosity and surface area and therefore, likely superior capacitance. The film oxidized using two different current densities, in contrast, looks quite flat. Figure 55, which is a plot of the current vs. potential behavior for the two films during CV cycling, confirms this hypothesis. The charge storage capability of the single current oxidation film is far superior (greater area under the curve), giving a capacitance of 11.8 mF/cm^2 vs. only 7.7 mF/cm^2 for the dual current oxidation film. This difference is fairly substantial, over 50% more capacitance.

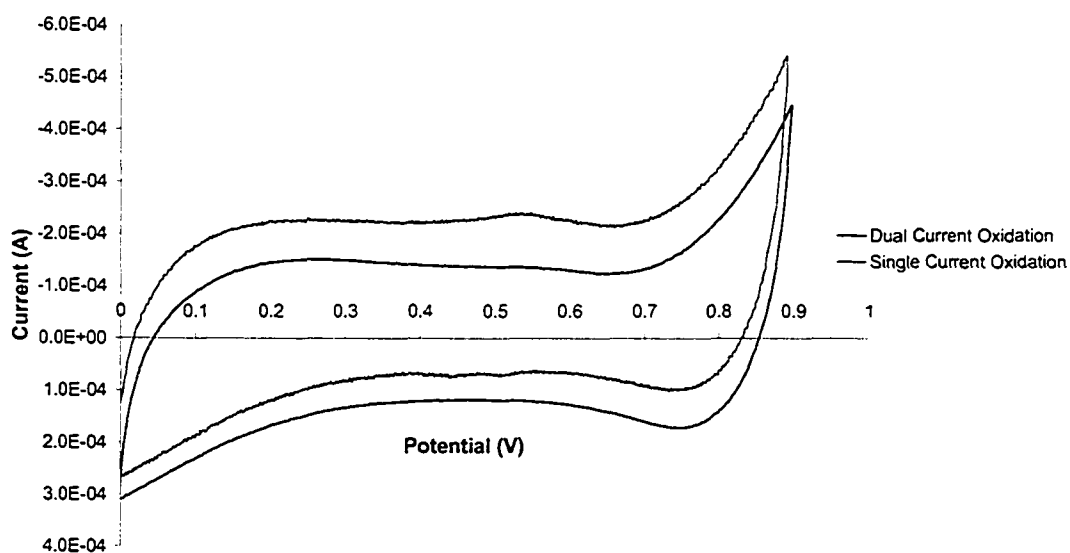


Figure 55. Plot of current vs. potential behavior for the tenth CV cycle for a film oxidized at 0.1 mA/cm^2 and a film oxidized at 0.1 and 0.8 mA/cm^2 .

Although the multiple current oxidation was intended to preserve hydration, this was not the case. XPS analysis of the film oxidized with two current densities gave a final hydration value of 29 at%, which is very close to the 25 at% normally achieved with single current oxidation and a significant decrease from the higher values achievable at

oxidation to 0.5V (>50 at%). In addition, the final oxidation at 0.8 mA/cm² for the last 30s serves to nearly destroy any porosity in the film rather than refining the structure. The higher current density, although accomplishing the oxidation process more quickly, was clearly more destructive to the film. Perhaps this higher current density, and thus faster reaction rate, caused more of the delicate porous layer to be broken off resulting in a thinner film with less porosity. Some support for this hypothesis can be seen in the AAS results (Figure 56).

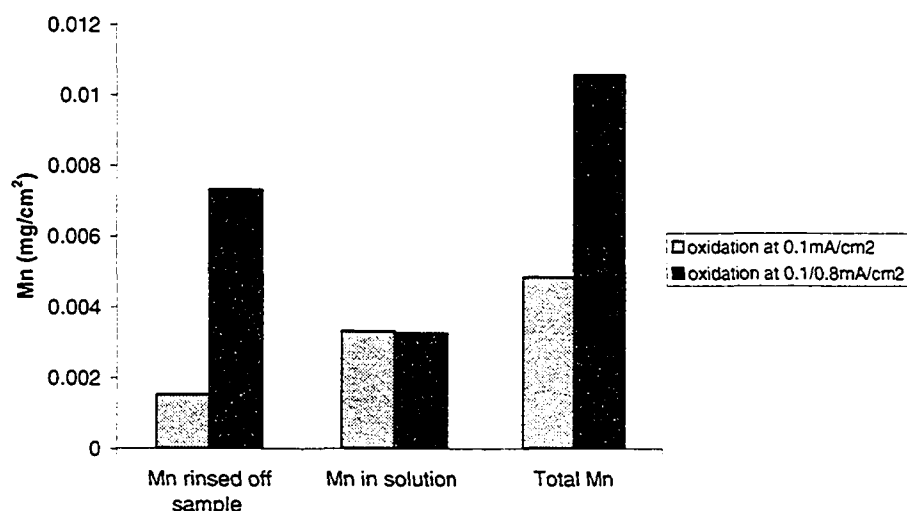


Figure 56. Graph showing the difference between the solubility of Mn during a single current deposition and a bi-current deposition.

Oxidation at a single current results in much less Mn being lost from the structure through rinsing. Although there is roughly the same amount of Mn going in the solution, the rapid and immediate increase in oxidizing current at the end of the process ultimately results in significantly more Mn resting on the surface of the sample than if a single oxidizing current was used. It is felt that the rapid change in current causes spalling of the delicate porous portion of the film leaving behind only the thinner dense under-layer, which is incapable of developing significant capacitance. The large build-up of Mn material on the surface of the film is probably remnants of the porous portion of the film

that has spalled from the film surface. The combination of poorer surface area with essentially unchanged hydration results in the decrease in measured capacitance.

In summary, the electrochemical oxidation process in Na_2SO_4 results in the formation of an extremely porous surface layer. This layer, in morphology, is quite similar to the morphology seen in other films that have been produced by other processes using an electrodeposition technique. Although the underlying zigzag layer is oxidized from Mn/MnO to single phase Mn_3O_4 , the more important result is the formation of the porous surface layer. Electron microscopy has confirmed the porous nature of this film, and selected area diffraction has confirmed its amorphous nature. XPS results indicate that the surface of the film is made up of hydrated manganese oxide in the 4^+ valence state which is the necessary component required for developing good capacitance.

In particular, there is a striking resemblance between the films produced through the electrochemical oxidation step and those produced by Pang and Anderson^{63,66,71} through electrodeposition. Pang and Anderson similarly produced a hydrated film with a $4+$ valence, and with a very similar looking porous surface layer. Unfortunately, their films are shown only in SEM plan view images. While their plan view images are quite similar to those in this work, it is impossible to tell if the films are similarly consistent in the cross-section since none were provided in their work. It should be mentioned as well that, though both types of films were produced by a different method, both involved an electro-oxidation step and it is likely the electro-oxidation is the cause of this unique film morphology.

The most significant difference between the films in this work and those of Pang and Anderson is the scale of the porosity. The porosity is much finer in the films produced by Pang and Anderson than the films that are produced here. Pang and Anderson currently have the superior films (~20% better) and it is worthwhile to be able to reproduce the superior film morphology using a different process. What is also interesting to note is that the films produced by other groups working with electrodeposition processes do not produce films with such a fine-scale porosity in the manner of these two processes.

There is no real reason why the films should not be similar in morphology, but they are not. It is likely related to the currents used for deposition, or the chemical reagents that were employed. Unfortunately, there is insufficient information in the various papers to identify the exact reason for the different morphologies.

It has been shown that the morphology of the underlying substrate is not a factor in electrochemical oxidation as both dense and zigzag films of manganese oxide form the porous, amorphous, hydrated surface film. It is likely that the bulk film does not take part in the charge/discharge process, only the porous surface film does. The dense intermediate layer directly beneath the porous layer may simply be a physical marker of the separation of the active portion of the electrode from the carrier/substrate portion of the electrode. As a result, the thicker zigzag films do not provide a significant advantage over the dense films since there is such a large amount of material that is essentially useless in terms of developing capacitance. Although the dense intermediate and bulk layers are thought to be also present in the dense samples, due to the smaller starting thickness of material, these layers end up being much smaller resulting in a more efficient structure. These ideas will be discussed further in subsequent sections.

The results presented here should greatly simplify the electrode fabrication process. Little attention needs to be paid to the porosity of the starting material as originally thought, since the electrochemical oxidation process produces its own suitably porous surface. This finding eliminates the need to produce the porous amorphous films using the more complicated, multi-step processes of sol-gel or precipitation, since the original surface area/porosity of the electrode is not a significant factor. In addition, this finding surpasses the current electrochemical deposition techniques that deposit the hydrated product directly onto the electrode carrier, since it eliminates the need for carefully controlled MnO_x deposition from a chemical bath. Instead, supercapacitive processing requires only a single solution of Na_2SO_4 and the electrochemical oxidation process can be done in-situ after the capacitor is packaged. In addition, the starting electrode material need not be pure Mn. This process works extremely well using a two-phase mixture of Mn/MnO, which is easily produced in any PVD system since there is no requirement for

low oxide content. The capacitance of the films produced through the PVD/electrochemical oxidation process, reported as 250 F/g⁷⁴, is on par or superior to the majority of the films produced in other laboratories and somewhat below the state of the art value of 720 F/g produced by Pang and Anderson^{63,66,71}.

4.2.4 Effect of CV cycling

4.2.4.1 Microstructure

As mentioned in the previous section, it seems apparent that the only portion of the film developing any usable capacitance is the porous surface layer, and the bulk of the substrate layer is providing only structural support because it is physically and chemically not suitable for capacitance. To confirm this idea, films that were cycled were analyzed in the TEM and by XPS. For this portion of the work, the zigzag films were again studied as they provided a greater volume of material for diffraction work.

A zigzag film cycled as a supercapacitor several hundred times is shown in Figure 57. The three important features in this image are the presence of the porous surface layer, the denser intermediate layer directly below, and the undisturbed base material. All three were seen at the various stages throughout the oxidation. Thus, even after substantial cycling, the three-part structure is not destroyed. However, the porous surface layer does look more fragile and with a finer texture than was seen prior to CV cycling (Figure 47b and Figure 50a). In Figure 58, the zigzag structure is identified through selected area diffraction as single-phase Mn_3O_4 . Presumably, any changes to the zigzag occurring during cycling are reversible as there is no phase change from the pre-cycled condition.

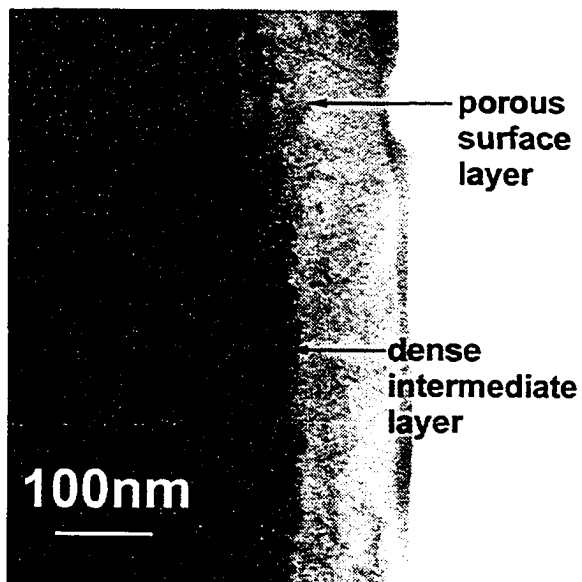
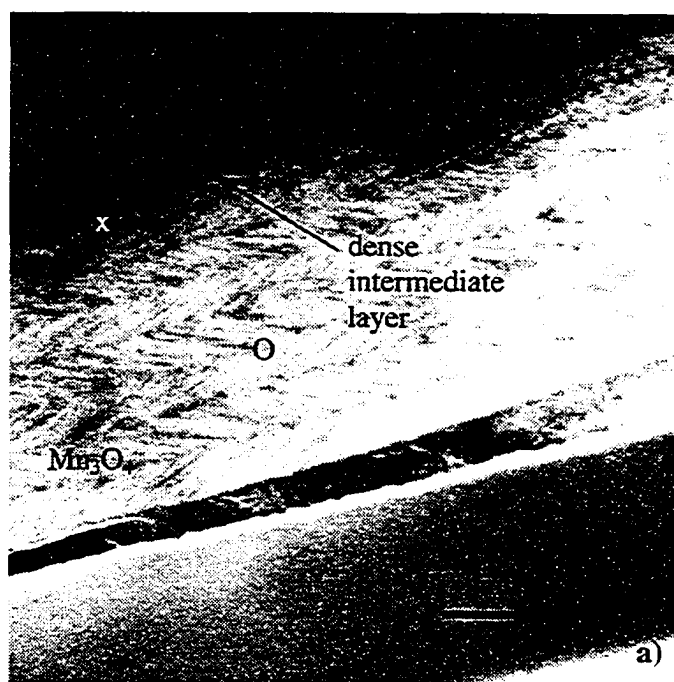


Figure 57. TEM BF cross-section image of a zigzag film that has been electrochemically oxidized and then cycled one hundred times between 0 and 0.9V.



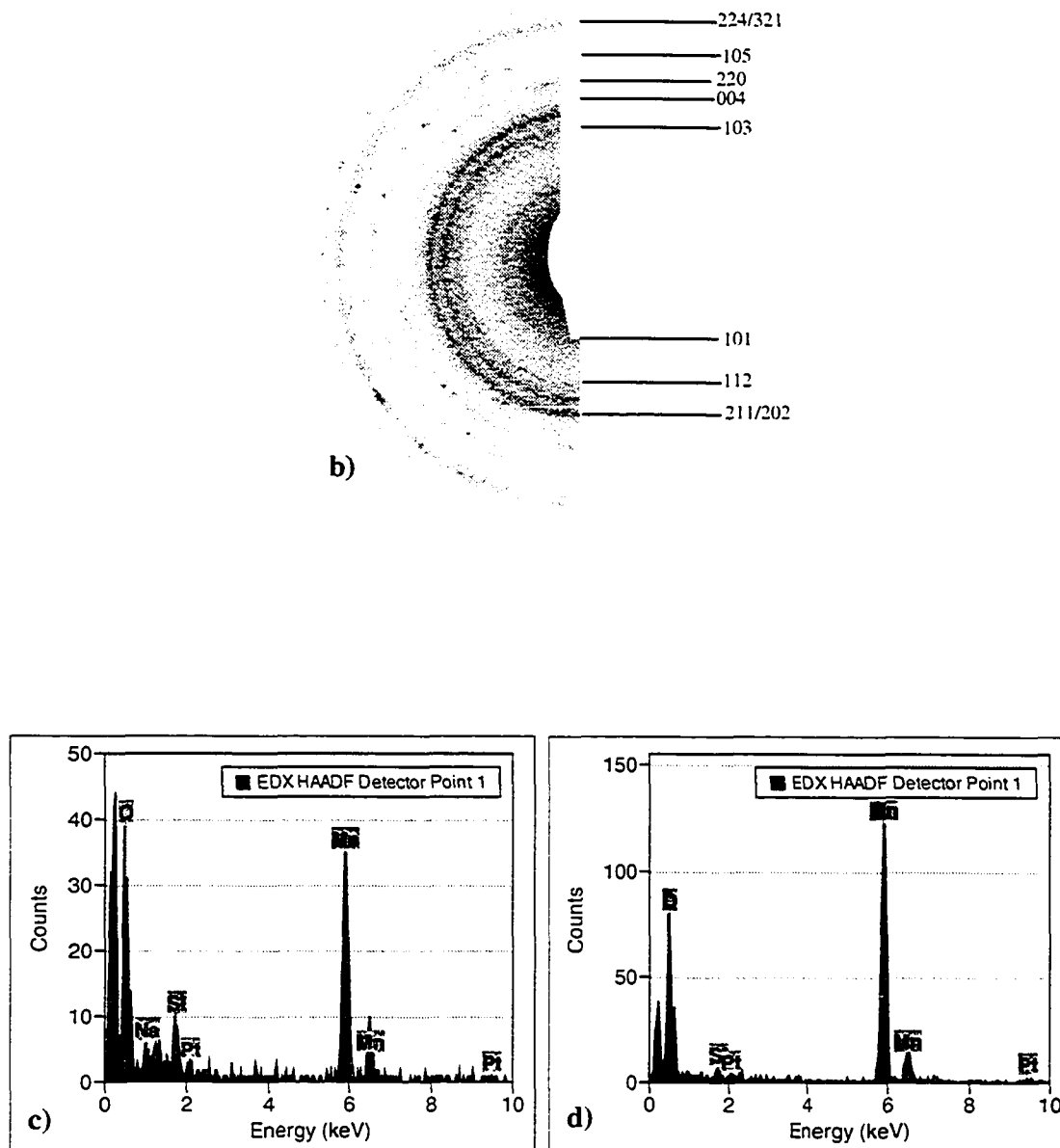


Figure 58 a) STEM annular DF image of the electrochemically oxidized sample. b) SAD pattern taken from zigzag layer indexed as single phase Mn_3O_4 . c) EDX spectrum taken from the thin layer region marked with an X and d) EDX spectrum taken from the bulk sample region marked with an O.

There are conflicting results in the literature as to whether the capacitance is due to a proton insertion mechanism, or the chemisorption of sodium from the electrolyte⁶⁷. The corresponding EDX spectra (Figure 58c,d) from the each area of the film provide some

useful information. The dense intermediate layer that is present on top of the zigzag layer was found, through EDX analysis (Figure 57c), to contain much higher levels of Na relative to the bulk material suggesting the chemisorption mechanism is more likely. Alternatively, the effect may simply be due to ordinary adsorption mechanisms from the electrolyte. Unfortunately, the layer was too thin to be evaluated by convergent beam diffraction. More importantly, the EDX results suggest that the bulk substrate structure, once oxidized from Mn/MnO to Mn_3O_4 is essentially isolated from the electrolyte (no sodium found-Figure 57d), while the porous surface layer and dense intermediate layer clearly have more contact with the electrolyte. This is yet more evidence indicating that *the development of capacitance is restricted to the porous surface layer.*

Again, due to the nature of the porous surface layer, it was analyzed by XPS to glean both the valence of the Mn and the relative hydration of the film. Once the sample has been cycled several hundred times, although there is no change in the bulk substrate layer, there is a definite change in the chemical make-up of the porous surface layer. The Mn 3s data indicates a valence of 2^+ (MnO) (Table 11) for the cycled sample. This result reveals that changes have occurred and a portion of the surface film has been reduced from the 4^+ to the 2^+ and may be indicative of irreversibility in the process where a redox reaction is occurring in conjunction with the pseudocapacitive reaction. The hydrated content of the film (33%) has not changed noticeably from the pre-cycled condition (Figure 46), suggesting that the hydrated structure is not being destroyed through the reduction process. However, the fact that the only changes occurring during the CV cycling process are restricted to the porous surface layer is some evidence that the base substrate structure is not required for developing capacitance, and therefore, thinner films should be used to reduce material waste.

Table 11. XPS results for zigzag sample cycled 100 times.

Sample	Mn 3s Splitting Width (eV)	Phase	at% hydration
Cycled (100 times)	5.79	MnO	33
Un-cycled	4.79	MnO ₂	32

4.2.4.2 Capacitance

Knowing that the valence of the porous surface film is decreasing, it is reasonable to assume that the capacitance would decrease as well. This trend has been revealed for dense films oxidized in a horizontal sample orientation and the current-time curves are shown in Figure 59. These curves provide the total charge storage for the film and when divided by the voltage, give a capacitance value.

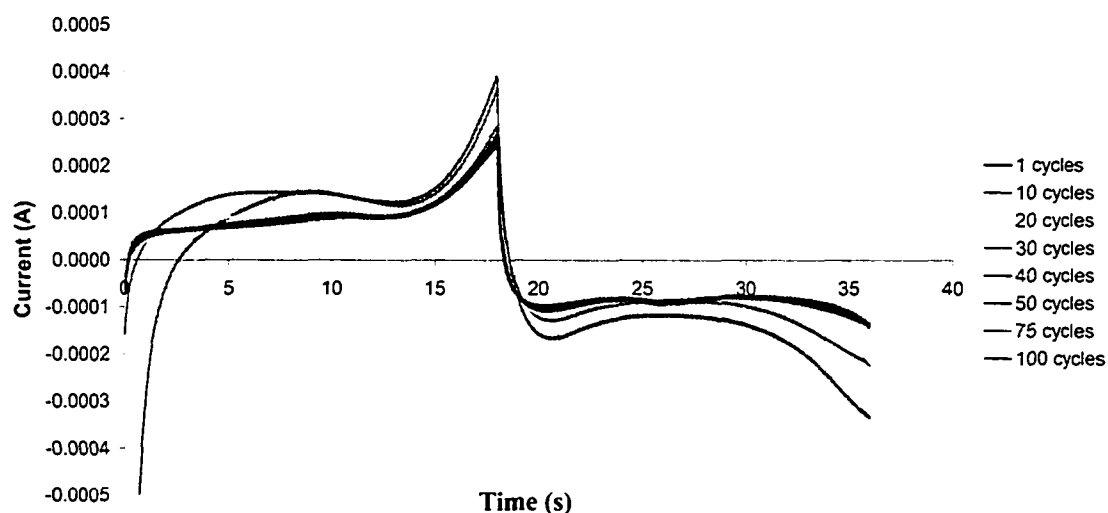


Figure 59. Current vs. Time curves for a dense film oxidized in a horizontal sample orientation at a current density of 0.2mA/cm².

Although the first curve has a somewhat different appearance from the other curves, it is clear that the area under the curve (total charge storage) decreases as the number of cycles increases. For instance, the calculated capacitance for the first cycle is 5.60mF/cm^2 , for the fiftieth cycle it is 4.44mF/cm^2 and for the hundredth cycle it is still 4.44mF/cm^2 . There is a fairly significant decrease ($\sim 21\%$) in the capacitance values between the first and fiftieth cycle showing the detrimental nature of the cycling. However, after the fiftieth cycle, the capacitance stabilizes. The decrease in capacitance can be explained by the previous XPS results (Table 11) where, after 100 cycles, the valence of the manganese was reduced to Mn^{2+} instead of Mn^{4+} . The literature seems to base all its reactions on the Mn^{4+} ion; however, a fairly significant amount of capacitance remains ($\sim 80\%$) and seems to have reached an equilibrium state despite the relatively low valence. It is important to note that there is minimal decrease in the capacitance after 30 cycles suggesting that the bulk of the irreversibility is occurring within the first 30 cycles, after which the film appears to stabilize and maintain a constant capacitance value up to 100 cycles.

In general, the cycling reproducibility of this process is equivalent to anything that has thus far appeared in the literature. In one study, Pang et al⁶⁶ report a 10% decrease in capacitance over the space of 1500 cycles, significantly more than the 100 cycles tested in this thesis. However, in another study⁷¹, a loss of over 20% capacitance is reported over the span of 1500 cycles. Other researchers, Hu and Wang⁷⁶, report a loss of 5% capacitance over 550 cycles. Hong and Kim⁷⁰ report a loss of 7% capacitance after 100 cycles and Jeong and Manithram⁶⁷ report a 5% loss after 200 cycles. Thus, the loss in capacitance recorded by the films made by the PVD/oxidation process are competitive in terms of cyclability. In addition, the results from the literature indicate that a significant decrease in capacitance occurs within the first tens of cycles^{66,68,70,71,76} similar to the PVD/oxidation process, which had a capacitance change of $\sim 20\%$ within the first 30 cycles. After the initial decrease, all films appear to reach a final capacitance value.

In general, the researchers in this area do not report any evidence of a valence change in their films, as is reported in this study. It is possible, however, that the valence of their films is changing during cycling, but none of the publications have closely studied the effect of cycling on the morphology and chemistry of their films. Pang and Anderson⁶⁶ identify, through SEM imaging, some changes to the morphology of the electrodes as a function of repeated CV cycling. They notice a slight degradation in the structure of the electrode films, but because the samples are imaged in plan view, there is not a true sense of the potential damage that may have been inflicted upon their films. In addition, their SEM images are not accompanied by any kind of chemical or phase analysis, so it is difficult to determine the extent of the damage to the films to determine if it is simply a morphological change, or a chemical change as well.

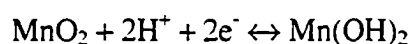
Chigane and Ishikawa^{75,77} on the other hand, have some limited phase analysis of the films as a function of CV cycling. In their particular study, they measured the absorbance of 400nm light and were able to relate it to the chemical state of the film. In order to determine the effects of CV cycling on the film, the absorbance of light was measured as a function of the number of cycles. What was noted was that the absorbance in the oxidized and reduced states increased during the first 1000 cycles. After 1000 cycles the absorbance increased gradually, but the difference in absorbance between the oxidized and reduced state increased by only 7%. They assumed that potential switching (during cycling) produced a repetition of the transient redox state. Thus, the increase in absorbance in the first 1000 cycles and after was attributed to a shifting of the reaction system from $[\text{Mn}^{2+}, \text{Mn}^{3+}/\text{Mn}^{4+}]$ to $[\text{Mn}^{3+}/\text{Mn}^{4+}]$ and finally to $[\text{Mn}^{3+}, \text{Mn}^{4+}/\text{Mn}^{4+}]$. They have reported a gradual oxidation of their system as the cycling continues which is certainly detrimental.

Chigane and Ishikawa's results are slightly contradictory to the results obtained in this study, where it was found that after 100's of cycles, the film has been reduced to Mn^{2+} . Although the starting film consists of amorphous, hydrated Mn^{4+} , many changes may occur during cycling. Looking at the CV curve for the first and tenth cycle (Figure 60), the starting potential is set at 0V vs. E_{ref} ; however, the value of the current at that

potential is vastly different between the two cycles. Note, that the sign convention gives a positive current if it is anodic and a negative current if it is cathodic. During cycling, the film starts a potential of 0V and slowly scans up to 0.9V (top portion of the curve) and then returns from 0.9V to 0V (bottom portion of the curve) to complete the scan. In the first cycle, the starting current is very large and cathodic, indicating some initial reduction from the Mn^{4+} state has occurred. As the progress of the cycle continues, the current eventually becomes oxidizing signaling an oxidation. Once 0.9V is reached, and the reverse trace starts, the current almost immediately becomes negative (cathodic) signaling a reduction process (Figure 61) down to a starting potential of 0V. During the tenth cycle, as the potential increases, the current becomes oxidizing right away and exhibits a rectangular shape that is typical of pseudocapacitance. Thus, the first cycle seems to indicate an initial reduction of the film is required before true pseudocapacitive cycling can begin. This is logical if it is considered that a film in the 4+ state will not be able to oxidize further. In addition, the cycling tests are always stopped at 0V, which is the reduced form of the film. In light of this, and the results presented by Chigane and Isikawa⁷⁵, it is reasonable to assume that our PVD/electrochem system is the in $[Mn^{2+}, Mn^{3+}/Mn^{4+}]$ reduction couple that they discuss. Thus, a reasonable pseudocapacitive mechanism for our film is



based on the work of Chigane and Ishikawa⁷⁵. For our particular system, a possible reaction could have $x=2=y$. If this is the case, the reaction reduces to



In the oxidized state, the manganese has a valence of 4+ and in the reduced state the manganese has a valence of 2+, which corresponds to the XPS results. This pseudocapacitive reaction is considered to be the most favorable for this system since it fits the experimental data quite well.

If the reaction proposed by Pang and Anderson⁶³ is considered (seen below) it is possible to have a 4+ valence, but impossible to obtain the 2+ valence that appears in our system

unless no charge is passed. The difference arises because Pang and Anderson deal only with partial charge transfer while Chigane and Isikawa do not make that limitation.

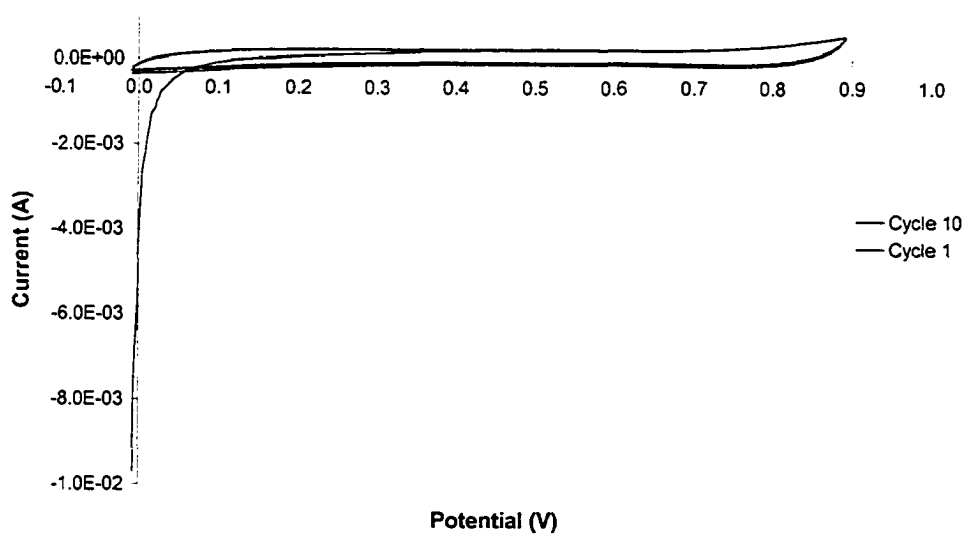


Figure 60. CV curves for the first and tenth cycle.

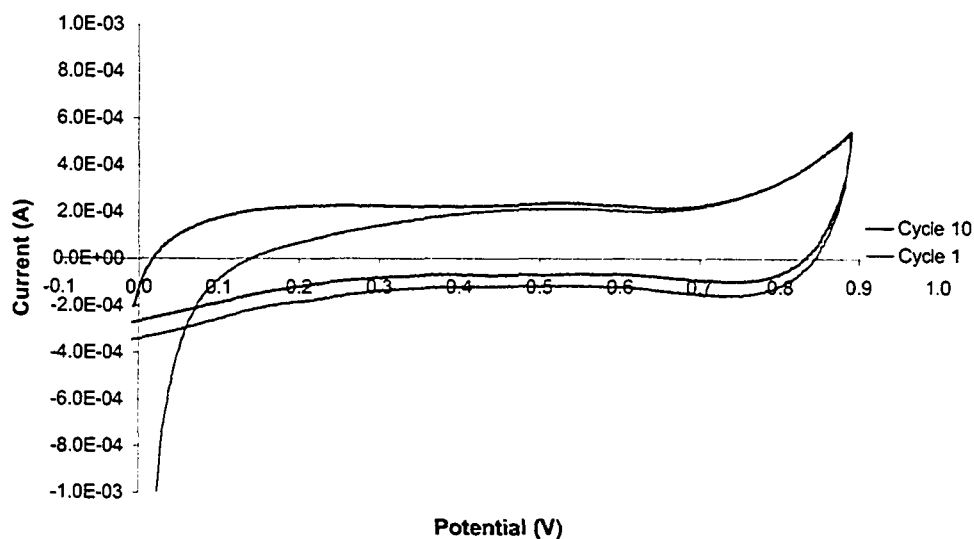


Figure 61. CV curves for the first and tenth cycle.

4.2.5 Effect of sample orientation on the oxidation process and production of a porous surface layer

The results of the previous sections have identified the crucial role played by the porous surface layer in the development of significant capacitance. Thus, the manipulation and improvement of this layer will ultimately increase the capacitance of these films. One of the important factors influencing the morphology and chemistry of this layer is the sample orientation during the oxidation process. The previous results were all achieved using the horizontal cell configuration seen in Figure 14. If the cell configuration is changed, such that the sample is held vertically (Figure 13) rather than horizontally, there are some changes in the oxidation process and the resulting films (Figure 62 and Figure 63).

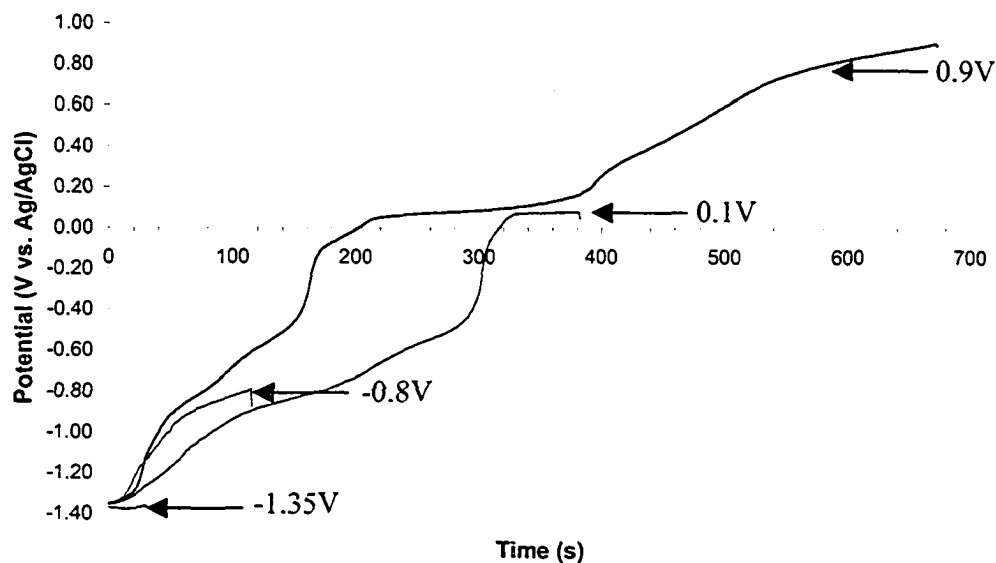
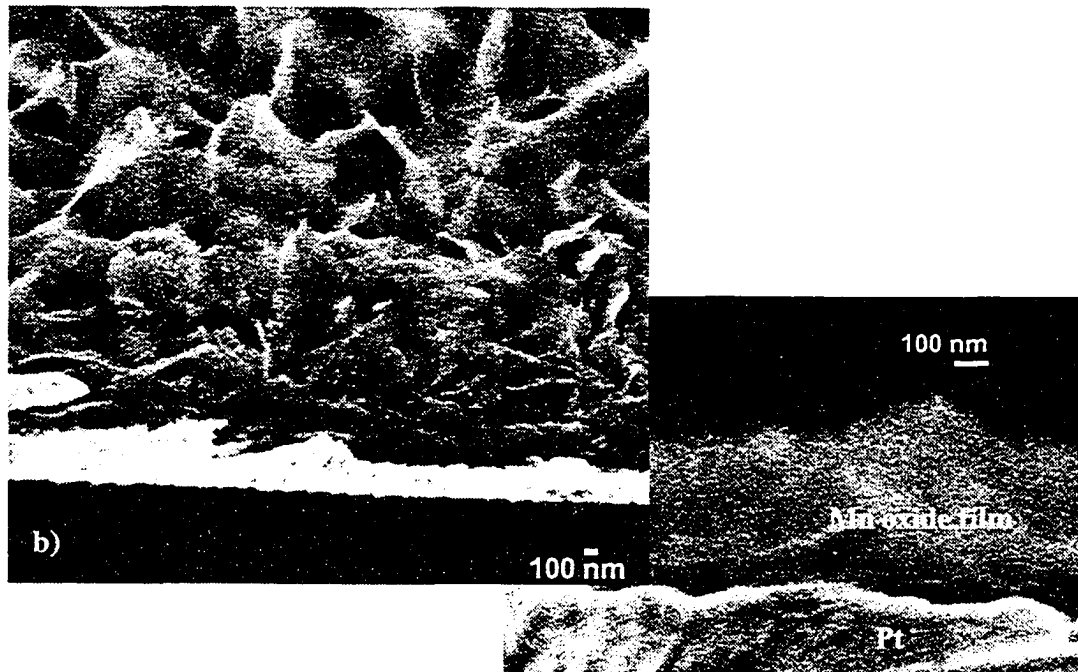
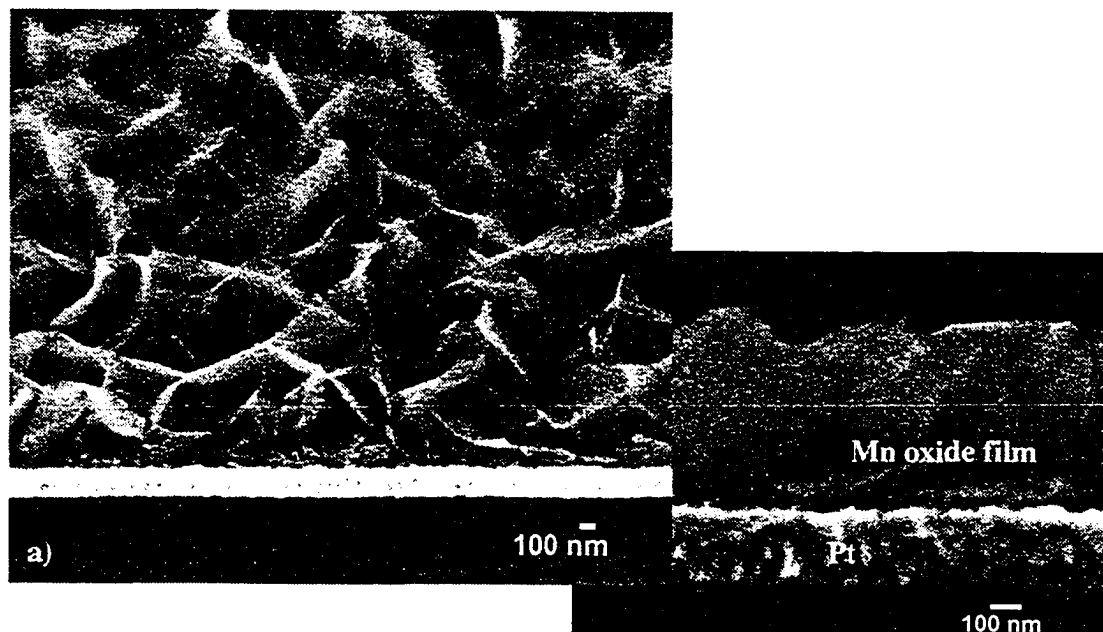


Figure 62. Graph of oxidation process stopped during the various stages indicated by the legend for the sample in a vertical orientation.

Comparing the results for a vertical sample orientation to the results for the horizontal sample orientation (Figure 37), it can be seen that the plateaus all occur at the same voltage and there is the same type of scatter for the oxidation rates even within the same wafer. Again, this is due to minute differences in surface quality and Mn layer thickness. It is worth noting that the overall oxidation time for the sample with the vertical orientation is slightly less than the time required for oxidation with a horizontal orientation. It is difficult to say if this difference is due to different surface qualities and part of the data scatter. The oxidation for both sample orientations was carried out at a current density of 0.1mA/cm^2 . The differences in the oxidation process appear quite minor, and the differences in film morphology appear similarly minor (Figure 63).



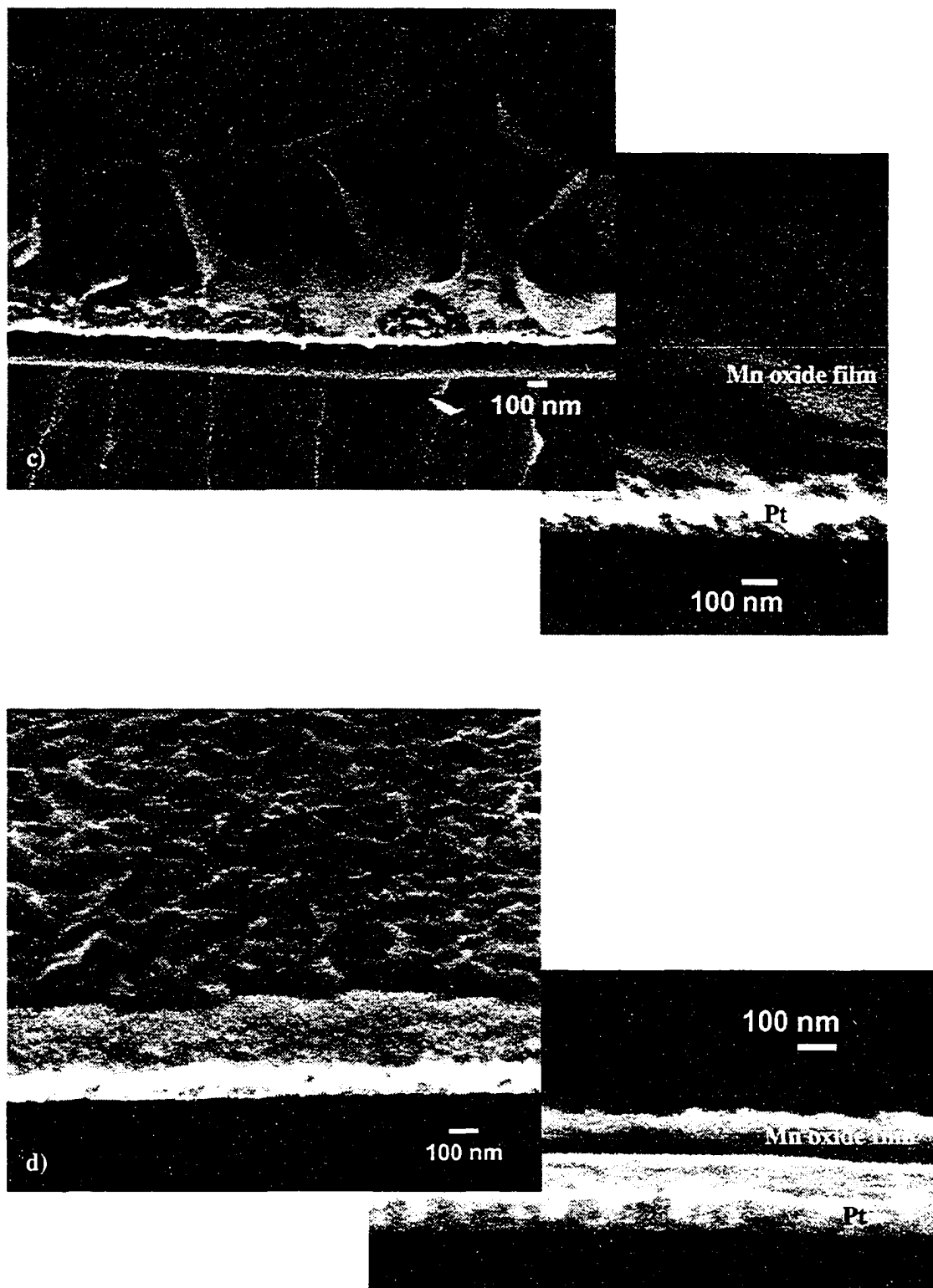


Figure 63. FE-SEM SE images of the various stages of oxidation in both oblique and cross-section views for samples oxidized with a vertical sample orientation to a final potential of a) -1.35V, b) -0.8V, c) 0.1V and d) 0.9V.

Immediately obvious from the FE-SEM images is that the same type of porous surface layer forms as for the films produced using a horizontal sample orientation. A major difference in the films, as Figure 64 shows, is the thickness of the overall porous surface layer. As well, the morphology of the film at 0.9V (the critical stage) appears to be less porous than the film produced using a horizontal sample orientation. Ultimately, this is not a desirable outcome as the surface area of the layer may be significantly reduced.

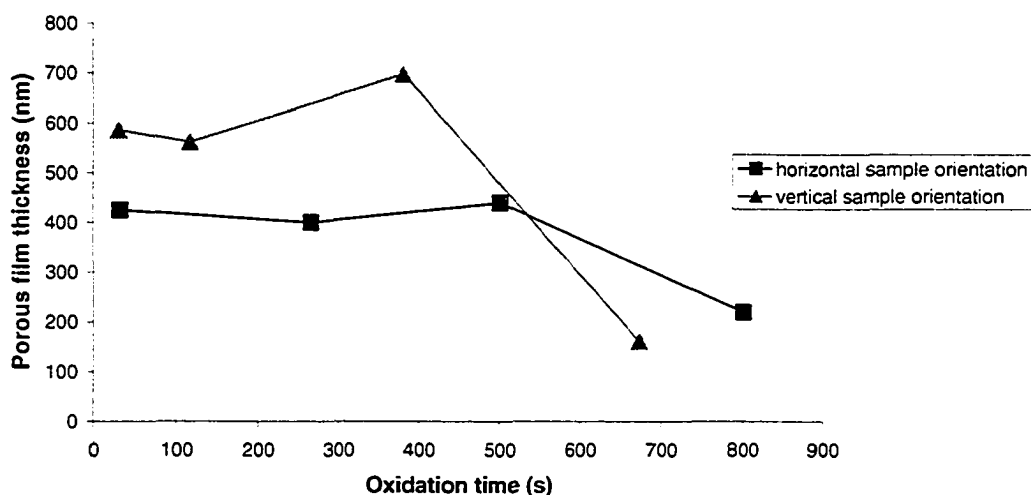


Figure 64. Graph of porous film thickness as a function of oxidation time and sample orientation.

Since the thickness of the porous layer does not aid in sorting out the growth mechanism of the film: the mass of the film as a function of oxidation time must be considered (Figure 65).

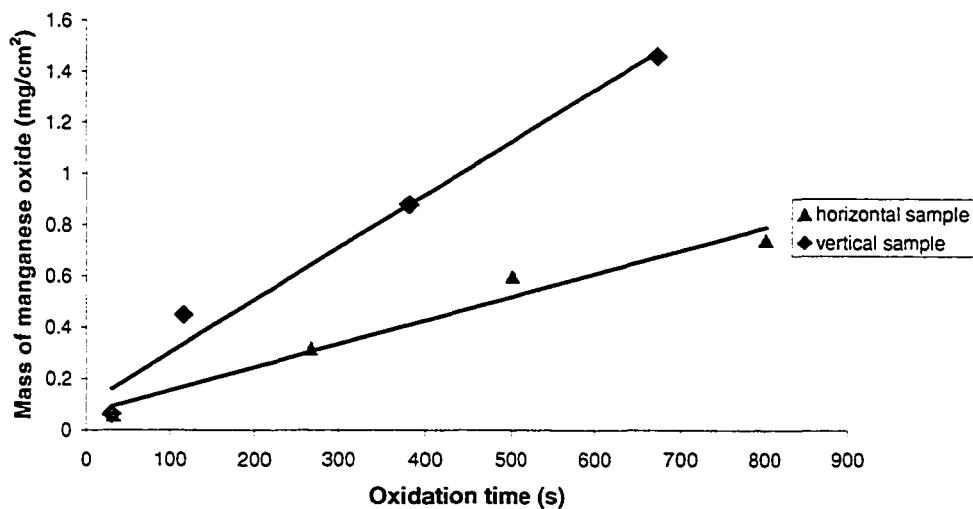


Figure 65. Graph of film mass as a function of oxidation time.

The trend for each sample orientation is linear which is expected since the same type of oxidation curve is produced in each case with a similar type of porous film resulting. However, there is significantly more mass gained with the vertical sample orientation than for the horizontal sample orientation. The best explanation is that the increased access of solution to the sample surface in the set-up for the vertical sample allows the reaction to occur more quickly than in the set-up with the horizontal sample, thus resulting in a greater film mass. This hypothesis will be discussed in the following pages.

The amount of Mn that is lost during the oxidation process was analyzed using the AAS. The amount of Mn going into the solution during the vertical oxidation process is compared with the horizontal configuration in Figure 66.

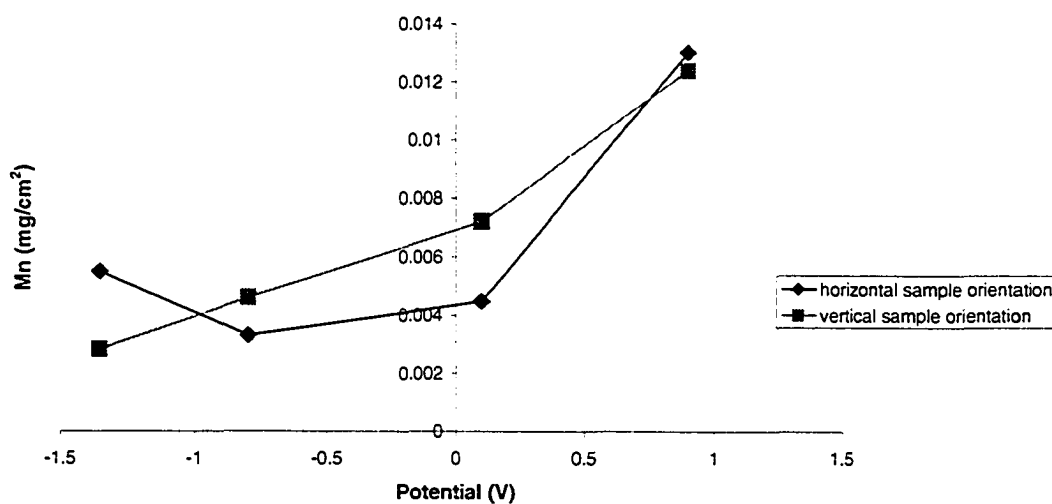


Figure 66. Graph showing the amount of total Mn lost during oxidation as a function of the oxidation potential and sample orientation.

At the end of the oxidation process (0.9V), there is approximately the same total amount of Mn being removed from the sample. These values represent both the Mn in the solution and the Mn that is rinsed off the surface of the wafer. In the vertical sample orientation, the total rate of Mn loss is fairly constant. The amount of Mn lost in the horizontal sample orientation is fairly constant up to a transition between the potentials of 0.1 and 0.9V when a more significant amount of the Mn is dissolved into solution.

The major difference in the sample orientations, however, is revealed in Figure 67, which considers the Mn lost from near the surface of the sample.

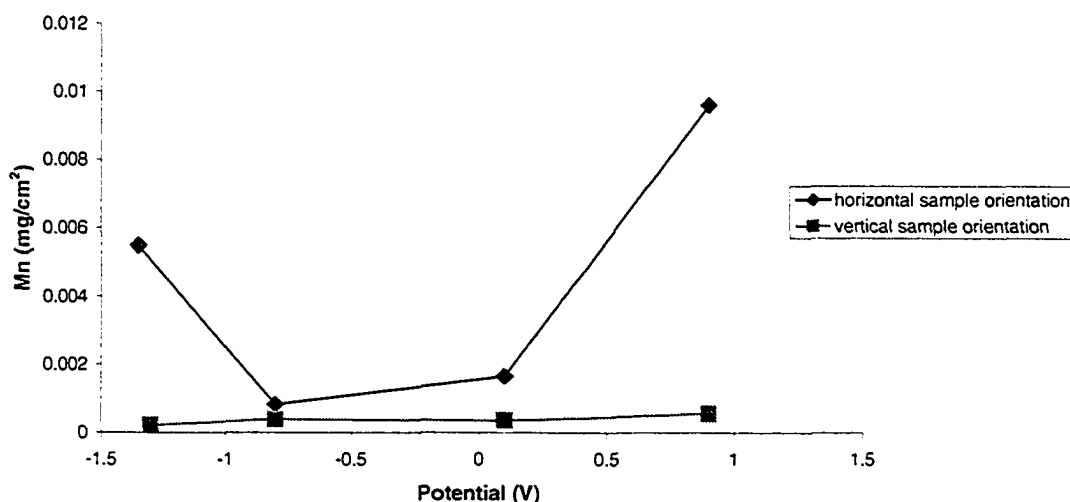
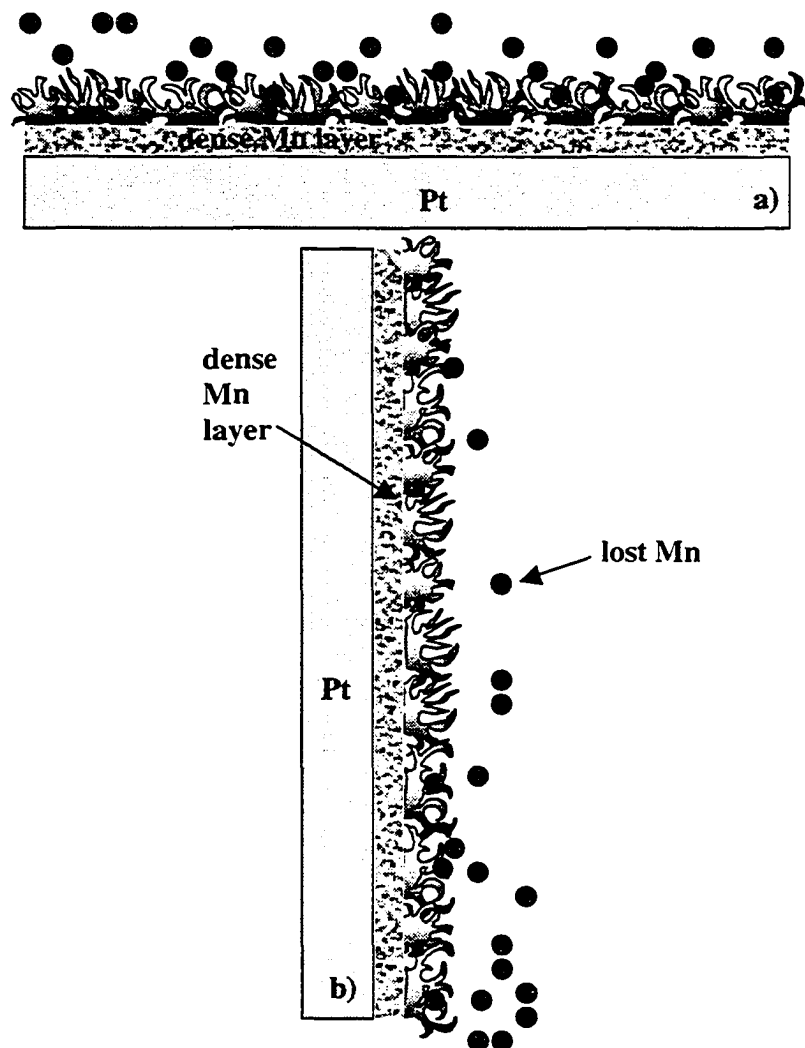


Figure 67. Graph of amount of Mn rinsed off the sample during the oxidation process.

There is consistently more Mn rinsed off the horizontal sample than the vertical sample. The amount of Mn rinsed from the vertical sample is the same at each potential and is quite small. Thus, most of the Mn lost from the vertical sample goes straight into solution. On the other hand, a significant quantity of the Mn lost during oxidation of a horizontally orientated sample actually remains on the surface of the sample, especially at -1.35V and 0.9V where this accounts for the majority of the total Mn. This results in the U-shaped curve that is seen in Figure 67, which was explained previously in Section 4.2.3 and is illustrated in Table 12, which specifies the location of the Mn after a complete oxidation cycle (0.9V). The same amount of Mn is lost during the oxidation process regardless of the orientation of the sample. However, in the vertical test there is no detectable Mn on the surface of the sample as it has all gone into solution. On the other hand, in the horizontal cell, three times as much Mn remains loosely resting on the surface of the sample such that it is easily removed with a gentle rinse in de-ionized water. This difference can be easily understood if the schematics of sample orientation are considered (Figure 68)

Table 12. AAS results for complete oxidation for the two different sample orientations.

Cell set-up	Mn in solution rinsed off wafer (mg/cm ²)	Mn in bulk solution after oxidation (mg/cm ²)	Total Mn in rinse and solution (mg/cm ²)
Electrodeposition Cell (vertical)	0	0.0128	0.0128
Testing cell (horizontal)	0.0096	0.0034	0.0130

**Figure 68.** a) A schematic of oxidation process with a horizontal sample orientation showing the location of the lost Mn . b) A schematic of the oxidation process with a vertical sample orientation showing the location of the lost Mn.

When the oxidation occurs on a sample oriented horizontally (Figure 68a) any Mn that leaves the layer during oxidation (either ionic or in the oxide form) is likely to remain near the surface of the growing porous layer due to gravitational effects. However, with the vertical sample orientation (Figure 68b) most of the Mn leaving the sample during oxidation will slip off the surface of the growing layer due to the gravitational effects, resulting in less Mn on or near the surface of the sample, and more in the solution as compared with the horizontal sample orientation. These schematics can also help to explain why the growth rate of the vertical sample was larger than the horizontal sample. Consider the effects of concentration on the potential of an electrochemical reaction as described by the Nernst equation.

$$E = E_s + \frac{RT}{nF} \log C$$

where E is the potential, E_s is the standard potential, R is the universal gas constant, T is the temperature of the system, n is the number of electrons transferred during the reaction, F is Faraday's constant and C is the concentration of the ions.

As the concentration of the Mn ions increases in the diffusion layer, the potential of the electrode will become more and more positive, making oxidation less likely. However, if the Mn ion concentration is quite low in the diffusion layer, the electrode potential becomes more negative resulting in a greater tendency for oxidation. Thus, in the vertical sample orientation, as the Mn is more easily removed from the vicinity of the sample, the Mn concentration near the surface is relatively low, resulting in a more negative potential, and quicker oxidation. In the horizontal sample orientation, the Mn ions can easily remain near or on the surface of the sample and thus the Mn concentration is relatively high near the surface, which serves to slow the oxidation process and result in relatively less mass gain. Thus, it is beneficial to oxidize vertically, as a greater mass of film can be produced (hence more active sites); however, if the surface area is not as great as the surface area produced through horizontal oxidation, then fewer active sites will be exposed to the electrolyte.

The chemical make-up of the porous films, produced using the vertical orientation, was evaluated using XPS and the results are presented in Figure 69 and Figure 70. Note that the trend of oxidation is the same for the vertical sample as for the horizontal sample with the same transformations occurring in the same plateau regions for each film regardless of orientation: $\text{MnO} \rightarrow \text{Mn}_3\text{O}_4$ in the first plateau, $\text{Mn}_3\text{O}_4 \rightarrow \text{Mn}_2\text{O}_3$ in the second plateau, $\text{Mn}_2\text{O}_3 \rightarrow \text{MnO}_2$ in the third and fourth plateaus and a thinning of the film at the end of the fourth plateau. As well, the hydration of the film follows the same trend regardless of sample orientation except that the absolute value of the hydration is greater for the vertical sample orientation during the initial stages of oxidation. However, both types of samples ultimately achieve the same hydration value in the end, so there is no gain in hydration by oxidizing using a vertical sample orientation.

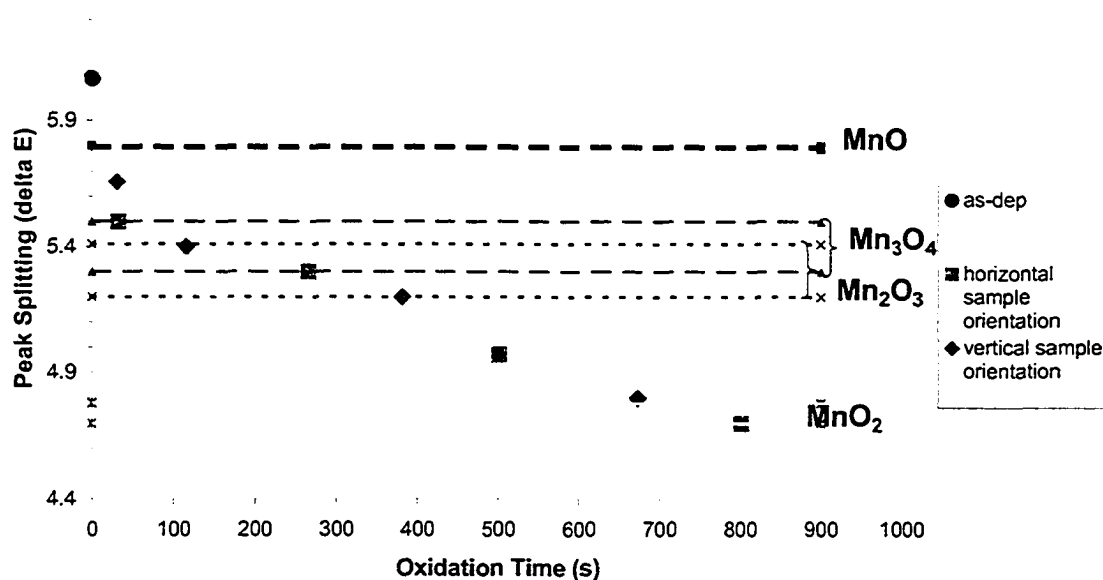


Figure 69. Plot of Mn 3s splitting width from XPS as a function of oxidation time.

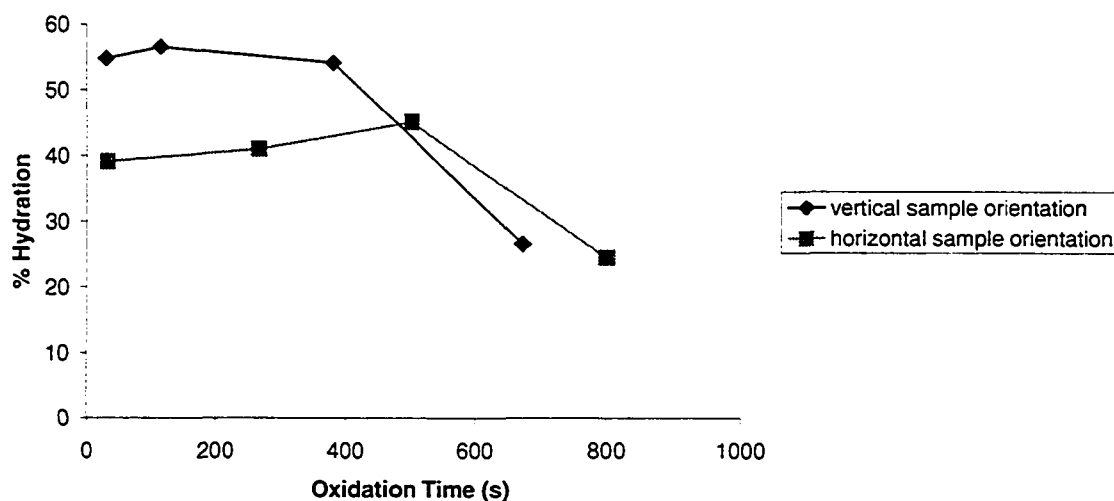


Figure 70. Plot of hydration of the porous film as a function of oxidation time.

Although the vertical sample orientation results in more film (i.e., greater mass) and therefore, more active sites (Figure 65), it also appears less porous (Figure 63) resulting in fewer active sites being exposed to the electrolyte. The ultimate result is significantly less capacitance for the films oxidized vertically. This can be seen in the graph of current vs. time, which give the total charge of the films per square centimeter of wafer surface (Figure 71). It is obvious that there is significantly less charge per cm^2 for the vertical sample, with the actual values of $0.0032\text{C}/\text{cm}^2$ for the vertical sample as compared with $0.0068\text{C}/\text{cm}^2$ for the horizontal sample. This is a doubling of the charge storage for the samples produced horizontally. If this value is converted to a capacitance (dividing by the voltage range) the capacitance values are $3.6\text{mF}/\text{cm}^2$ for the vertical sample compared with $7.6\text{mF}/\text{cm}^2$ for the horizontal sample. Thus, the films produced horizontally are vastly superior to those produced vertically.

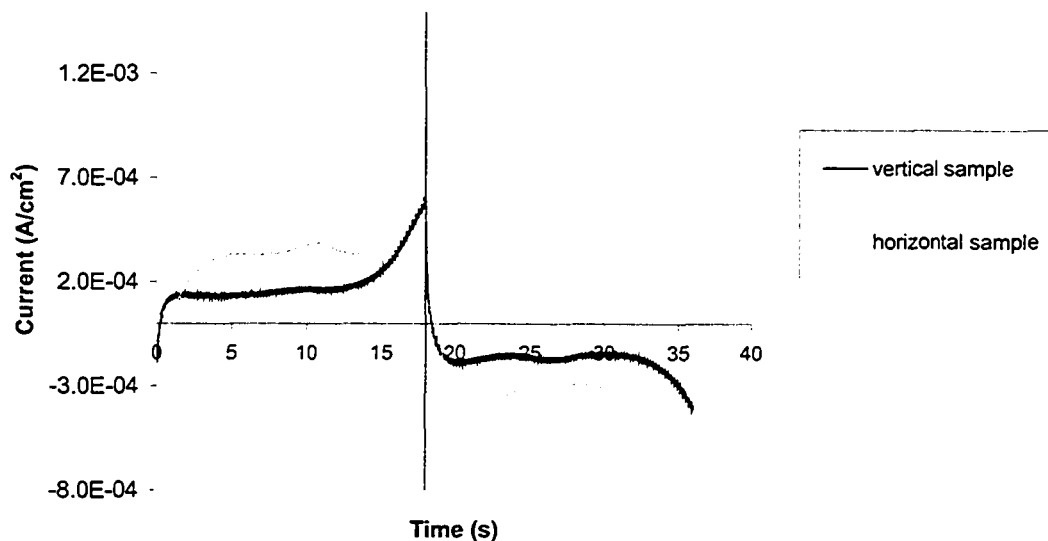


Figure 71. Plot of current vs. time for cyclic voltammetry scans.

What is not clear is the cause of the large difference in surface area between the films produced horizontally and vertically. Those samples produced vertically obviously differ in sample orientation, but in addition, the solution volume that is exposed to the sample (Figure 14) is significantly smaller than the solution volume in the vertical cell set-up (Figure 13). The main cause of this is the narrow neck (Figure 14), which does not allow the solution above to easily penetrate the area sitting near the sample surface, restricting the usable sample volume to approximately 1mL. This is a much smaller volume as compared with the approximately 45mL that are used during oxidation of the vertically orientated sample.

To help determine the cause of the film differences, the sample set-up in Figure 13 was reconfigured to produce a film with a horizontal orientation rather than a vertical orientation to see if there was a noticeable change in the nature of the film. As the solution volume was held constant, the effects of gravity could be tested independently of solution volume. In addition, a sample was produced (horizontally) using a similar cell

set-up as Figure 14, but with an increase in solution volume in order to test the effects of solution volume on the production of the porous layer independently of the effect of gravity. In the cell shown in Figure 14, a total solution volume of 25mL is ordinarily used. In order to test the effect of solution volume, double the volume (50mL) is used for the testing. However, the actual increase in solution volume may be far greater. Examining the geometry of Figure 14 more closely, the small neck diameter effectively limits the amount of solution that can realistically contact the sample surface. If this geometrical constraint is considered, then the volume is increasing by a factor of 50 as there is only 1mL of solution within the neck region of the cell. The results of these experiments are shown in Figure 72. The vertical and horizontal control samples were prepared in the standard manner using the oxidation cells seen in Figure 13 and Figure 14. The effect of gravity was tested by using the vertical oxidation cell (Figure 13) but positioning the sample horizontally. The counter electrode remained in its position on the other side of the cell, with the reference electrode held close to the side of the sample as was done with the vertical sample orientation. The effect of solution volume was tested using the vertical oxidation cell again with a horizontally orientated sample. The difference from the previous test was that the counter electrode and reference electrode were suspended directly above the surface of the sample as they were in the horizontal test cell (Figure 14).

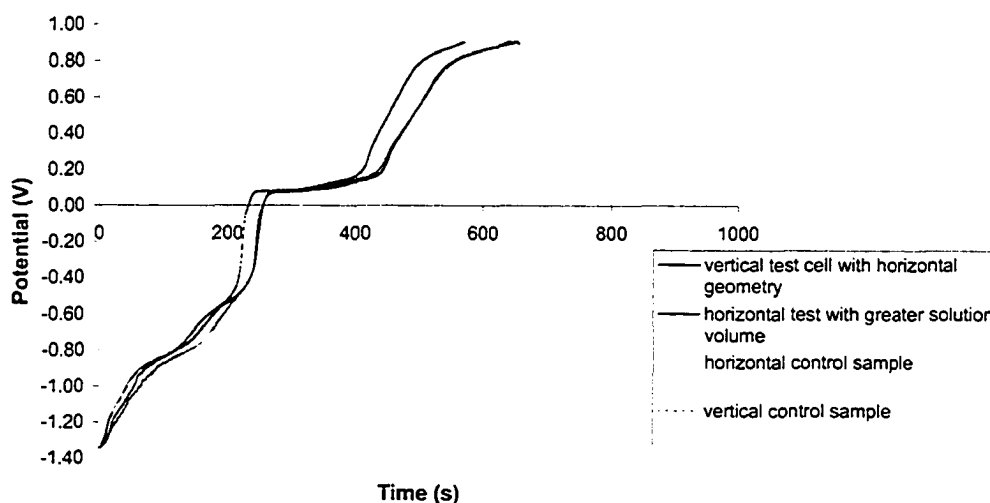
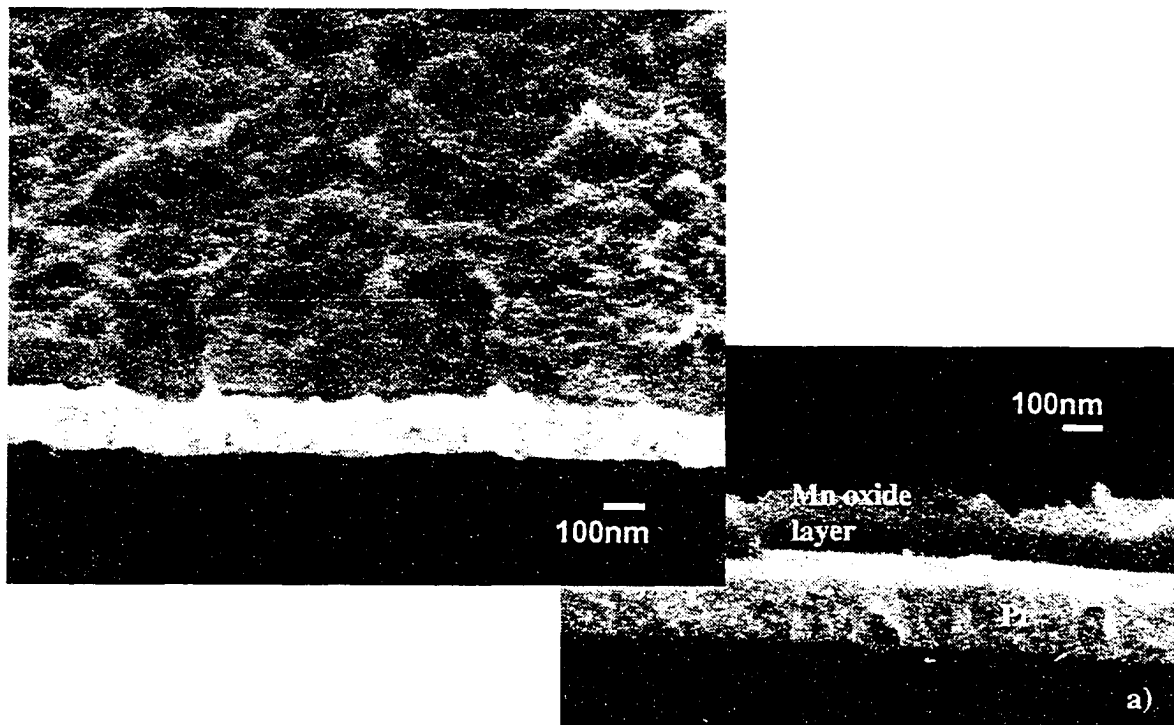


Figure 72. Graph of oxidation process at a constant current of 0.1 mA/cm^2 under different geometrical constraints.

Considering the two control samples from Figure 72, the horizontal orientation takes a longer time to complete the oxidation than the vertical sample, which was previously explained in terms of concentration of ions near the surface of the growing layer. In addition, the two oxidation traces for the samples made to study the effects of gravity and sample volume exhibit identical traces. This confirms that the oxidation process is independent of the location of the counter electrode. This is an expected result since a well-designed oxidation cell should not be sensitive to the location of the counter electrode.

The effects of sample orientation (or gravity) can be understood by comparing the vertical control sample oxidation in the vertical testing cell with horizontal geometry oxidation. The oxidation with a horizontal geometry, instead of a vertical geometry, takes longer to reach a final oxidation state. This result suggests a reduction in the rate of oxidation for the horizontal sample that is likely due to a local increase in the Mn ion concentration next to the surface of the growing porous layer. Thus, the porous surface

layers for these two samples should look different. A comparison of the morphology of the two films is shown in Figure 73.



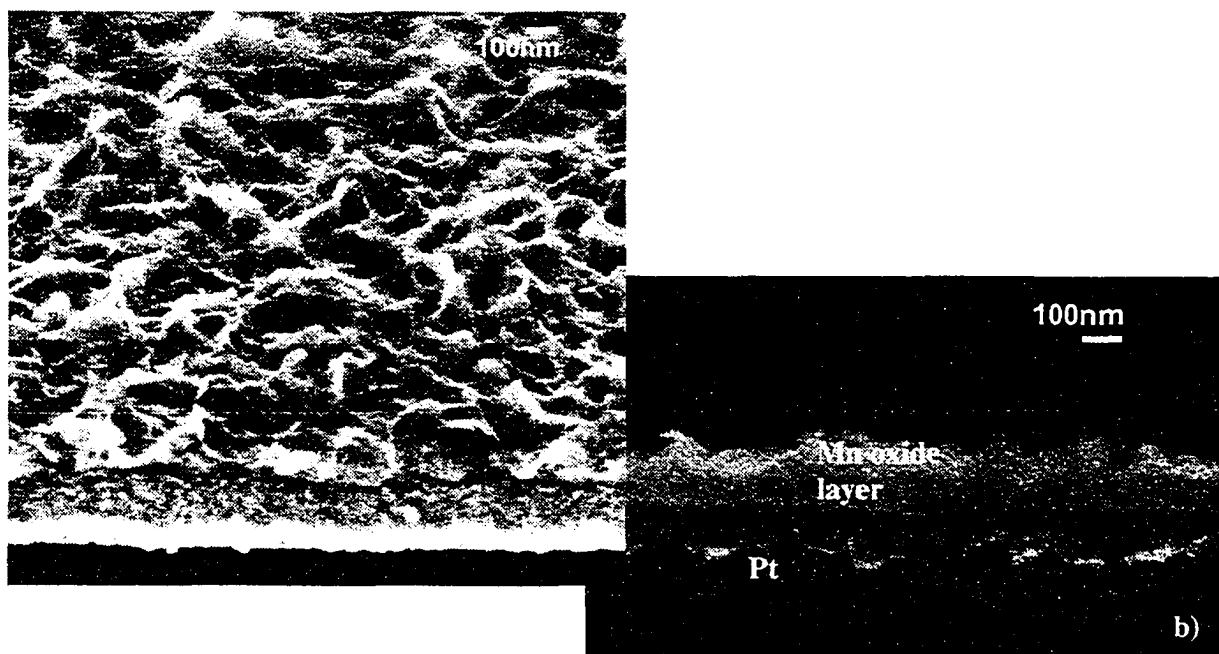


Figure 73. FE-SEM SE oblique and cross-section images of films produced using a) a normal vertical sample orientation and b) a horizontal sample in the vertical sample cell. The oxidation current for both samples was $0.1\text{mA}/\text{cm}^2$.

The difference in surface texture is immediately apparent between the sample held vertically and the sample held horizontally. The sample held horizontally has far more porosity that extends more deeply into the film than the sample held vertically. This is also mirrored in the thickness of the layers. For the vertical sample, the thickness was measured as 200 nm while the thickness of the horizontal sample was also 200 nm. There is essentially no difference between the two. Additionally, the horizontal film has a similar morphology to the film produced using the standard horizontal sample cell (Figure 14), with the exception that it is slightly thinner than the standard horizontal sample: 200nm vs. 230nm (Figure 38).

The AAS results offer more insight into this process. Figure 74 clearly shows that there is no Mn in the rinse solution for either the horizontal or vertical sample. It is expected from previous results that the vertical sample would have no Mn in the rinse solution: however, it is also expected that the horizontal sample would have a significant quantity

of Mn in the rinse solution (Table 12). Instead, for both samples, all the Mn lost during the oxidation process is going into solution. This suggests that the reason for the increased Mn concentration near the surface of the film during horizontal oxidation is not entirely due to gravity, but may be due to the restricted solution volume as well. However, gravity still has some effect as evidenced by the FE-SEM images and the oxidation trace.

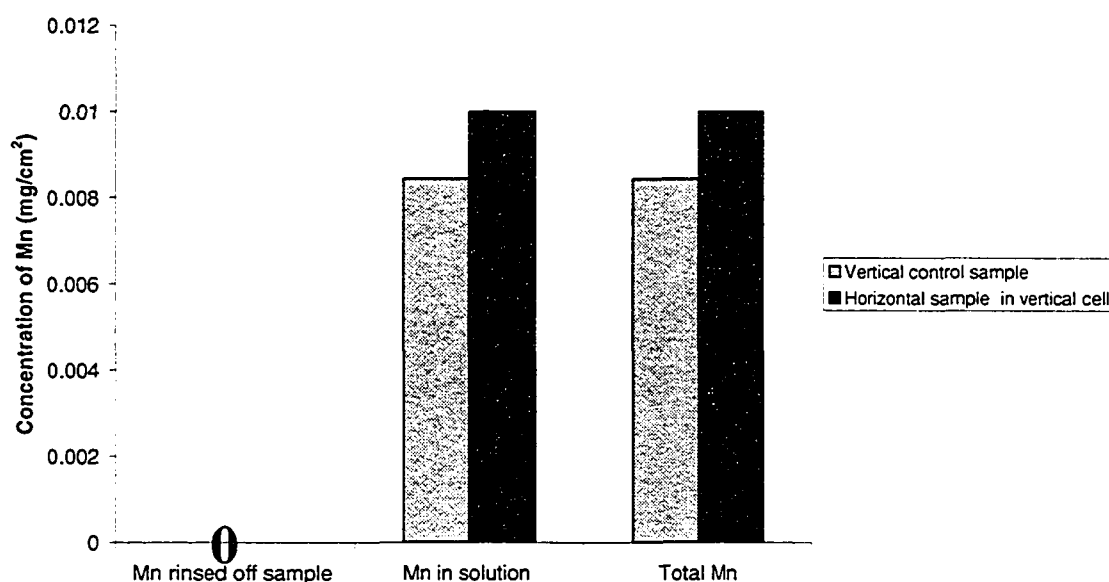


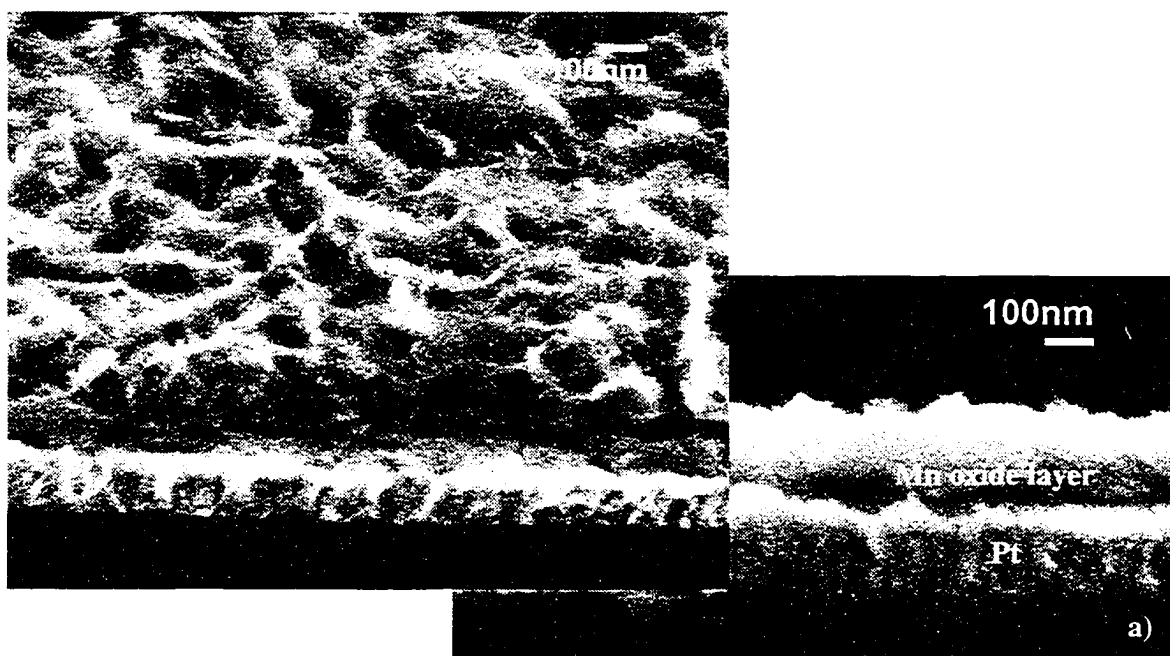
Figure 74. AAS results comparing the control sample, with a vertical orientation, to a sample with a horizontal orientation in the vertical oxidation cell to identify the location and amount of Mn lost during the oxidation process.

The XPS results from the porous surface film (Table 13) show that all other properties of the films are the same. Thus, the only difference is the relative amount of surface area, indicating that the horizontal oxidation geometry does result in a superior film.

Table 13. XPS results from the Mn 3s splitting data and the O1s peak de-convolution for the different geometries. Each sample was oxidized to 0.9V.

Sample	Mn 3s Splitting Width (eV)	Phase	at% hydration
Vertical control	4.9	MnO ₂ with trace Mn ₂ O ₃	20
Horizontal film in vertical cell	4.65	MnO ₂	17

To consider the effects of solution volume independent of the effects of gravity, the data for the horizontal test cell must be compared to the data for the horizontal test cell with greater solution volume. Figure 72 clearly shows that the horizontal test cell, with the increase in solution volume, completes the oxidation process much more quickly than the horizontal solution with the small volume (654s vs. 916s). This quicker oxidation indicates that there is likely less buildup of Mn ions near the growing oxide film as compared with the test sample. These results are confirmed by the morphology of the film as seen in the FE-SEM images in Figure 75.



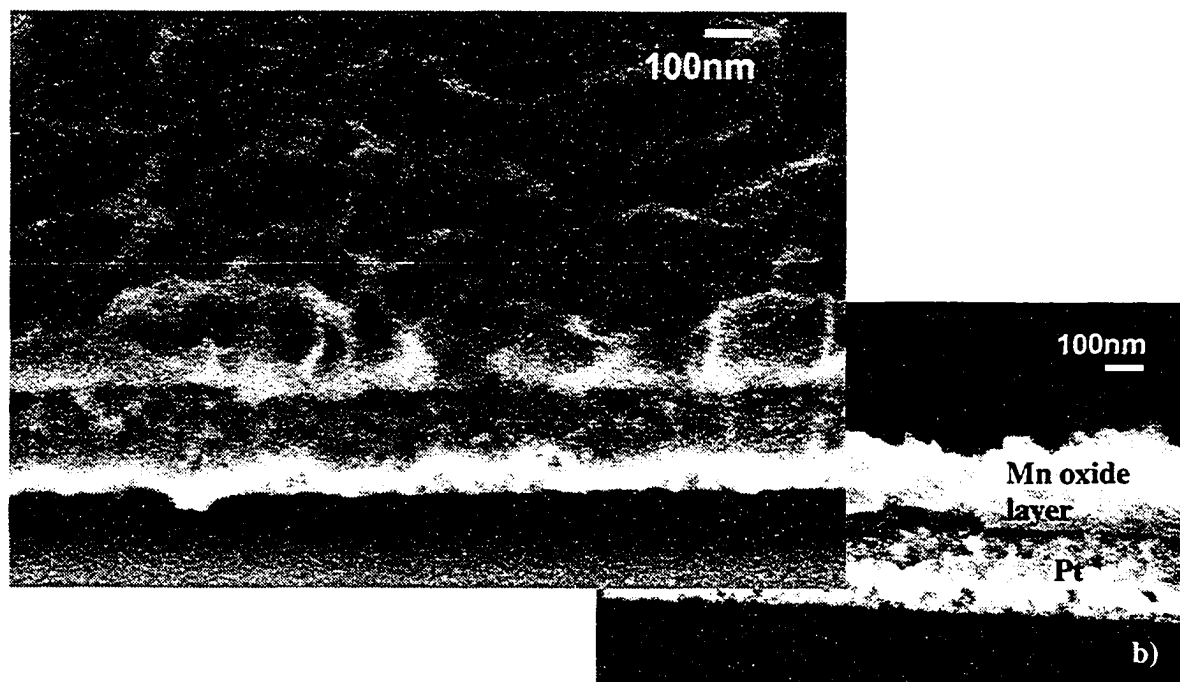


Figure 75. Oblique and cross-sectional FE-SEM, SE images for a) horizontal test sample and b) horizontal sample with greater solution volume. Both samples were oxidized at 0.1 mA/cm^2 .

The difference in film morphology between the two samples is quite subtle. However, the horizontal test sample (smaller volume) has a greater amount of porous film and greater texture, which ultimately leads to a greater surface area. The thickness of these films is also different. The test film has a thickness of approximately 300nm, while the thickness of the film produced with a greater solution volume has a thickness of only 200nm. Since the effect of gravity is not an issue with this set of films, it is clear that the limited solution volume in the control test results in a superior film in terms of morphology and hence capacitance.

The AAS results (Figure 76) confirm this idea. The horizontal control sample has a significant quantity of Mn remaining loose on the surface of the sample as a percentage of the total amount of Mn lost during the oxidation process. On the other hand, the horizontal oxidation carried out with a greater solution volume has virtually no Mn left on the solution of the film, with all the lost Mn in the bulk of the solution. These results suggests that the greater amount of solution volume allows for better movement of the Mn ions away from the oxide layer interface and thus a faster oxidation process and a film with a decreased surface area (and hence capacitance).

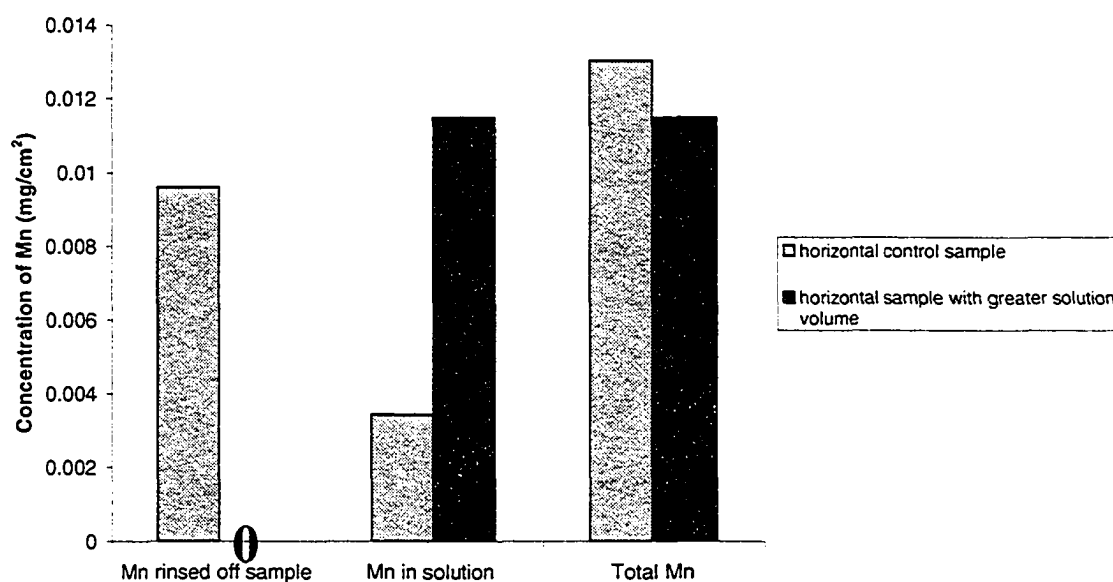


Figure 76. AAS results comparing the amount and location of Mn lost during the oxidation process for the horizontal control sample and the horizontal sample with greater solution volume.

The chemical structure of the films was evaluated again using XPS (Table 14).

Table 14. XPS Mn 3s peak splitting results and O 1s de-convolution results for different solution volumes

Sample	Mn 3s Splitting Width (eV)	Phase	at% hydration
Horizontal control	4.6	MnO ₂	27
Horizontal film with greater solution volume	4.9	MnO ₂ with trace Mn ₂ O ₃	16

While the valence of the films is nearly the same, there is a rather significant difference in the relative hydration: 27% for the control sample vs. 16% for the greater solution volume. These results confirm that the control sample clearly produces a superior film for capacitive purposes, although there is no explanation as to why the hydration should be reduced for the sample produced in a greater solution volume. Similarly, there is no reasonable explanation as to why a trace amount of Mn₂O₃ remains in the porous surface film.

The above suppositions are supported by the capacitance data shown in Figure 77. The horizontally produced control sample, as expected from its morphology and hydration, produces the highest charge capacity and capacitance at 10mF/cm². The film made with a horizontal geometry, but with greater solution volume has a much lower capacitance value (3.6mF/cm²) as a result of its poorer morphology and lower hydration. Finally, the vertically produced film displays the poorest capacitance (3mF/cm²) due largely to its poor morphology since its hydration is fairly similar to that for the horizontal control sample. What is interesting to note is that changing the sample geometry has little effect compared with changing the solution volume, in terms of how much capacitance can be developed. Thus, it can be concluded that the most critical variable to creating maximum capacitance is restricting the volume of the solution to impose a diffusion limiting situation.

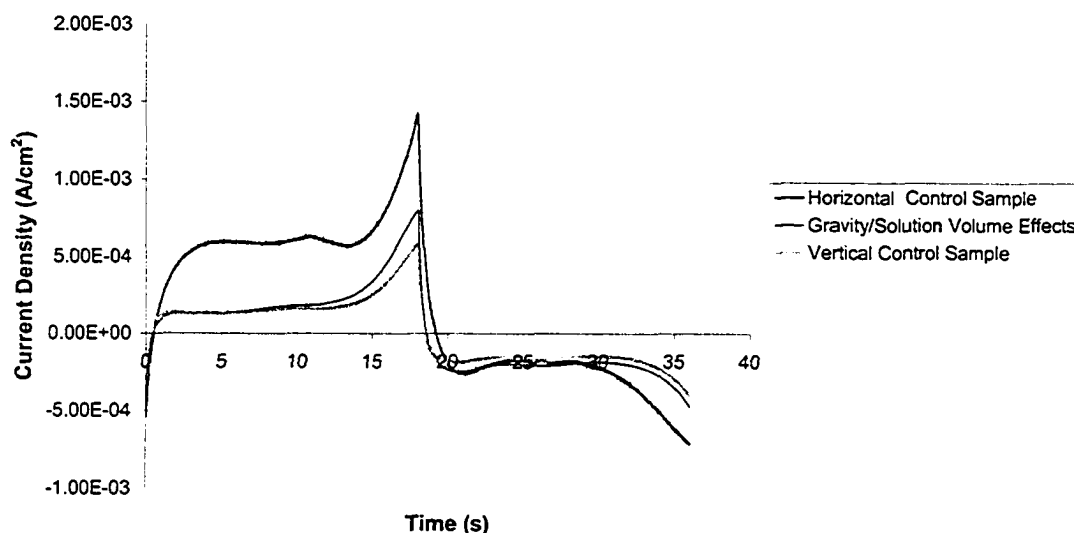


Figure 77. Current vs. time curves for films of differing geometry.

In order to produce a highly capacitive film, two things are required during the oxidation process. The first is a horizontal sample orientation, which provides the benefit of increased Mn ion concentration near the surface of the growing film resulting in a more porous film. The second necessity is a small solution volume. The result again is to confine the lost Mn ions near to the surface of the growing film to again produce an increase in porosity, likely due to greater incorporation of Mn, and an increase in hydration of the film. Both qualities are essential for high capacitance. An unfortunate by-product of these results is that this process may be very difficult to scale up. It could be challenging to restrict the solution volume in the scaled-up experimental set-up without exactly reproducing the geometry of Figure 14 (or at least the neck portion), which could be difficult to work with in an industrial setting.

4.2.6 Effect of current density on porous layer formation

With the intention of producing the best possible porous surface layer, and therefore, the highest possible capacitance, the effect of the oxidizing current density on the formation

of the porous layer was studied for the two different morphologies of deposited layer: zigzag and dense.

4.2.6.1 Zigzag films

Samples oxidized using different current densities were studied in an attempt to determine which produces the superior porous surface layer on the surface of the zigzag structure. The experimental details of the samples are listed in Table 15.

Table 15. Sample descriptions for oxidation of zigzag films at different oxidizing currents.

Oxidation Current Density (mA/cm ²)	Oxidation Time to 0.9V (s)
0.2	2950
0.4	1650
0.8	460
1	300

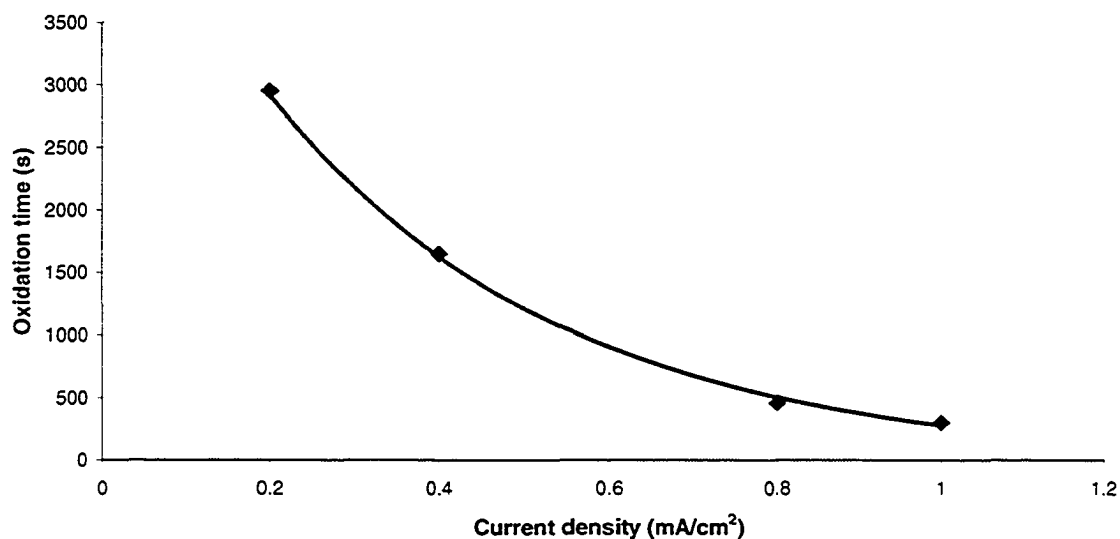


Figure 78. Plot of the oxidation time to 0.9V for the zigzag samples as a function of applied oxidation current density.

The graph in Figure 78 shows an exponential decay in the amount of time required for the oxidation (to 0.9V) with respect to applied current density. The negative trend is not unexpected as a higher current density is essentially a higher reaction rate and therefore the oxidation will occur more quickly.

Figure 79 shows the trend of the porous layer thickness as a function of the applied current density. Porous layer thickness decreases linearly with an increase in oxidizing current density, which is not an unexpected result. The increase in current density gives a faster reaction rate resulting in less time for the oxidation process and thus a thinner layer. This trend is very visible in the corresponding FE-SEM images of these films in Figure 80.

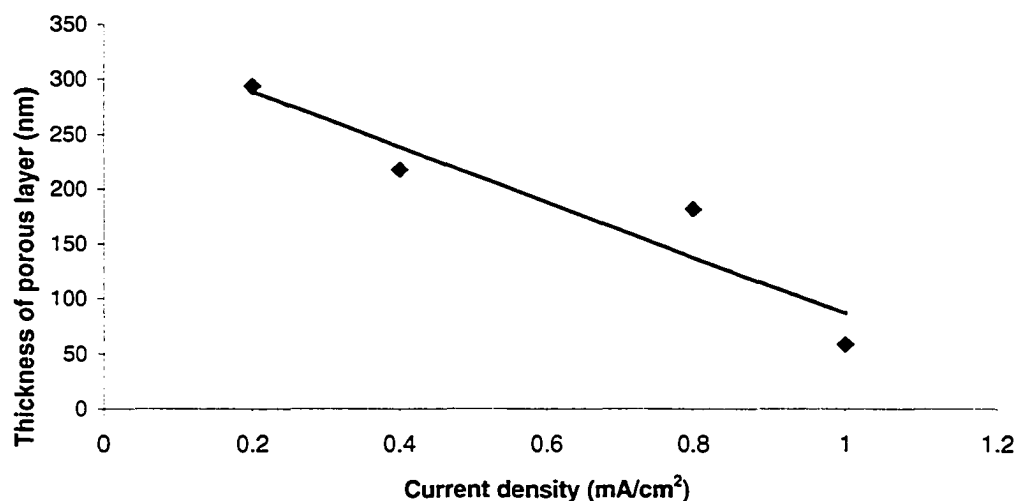
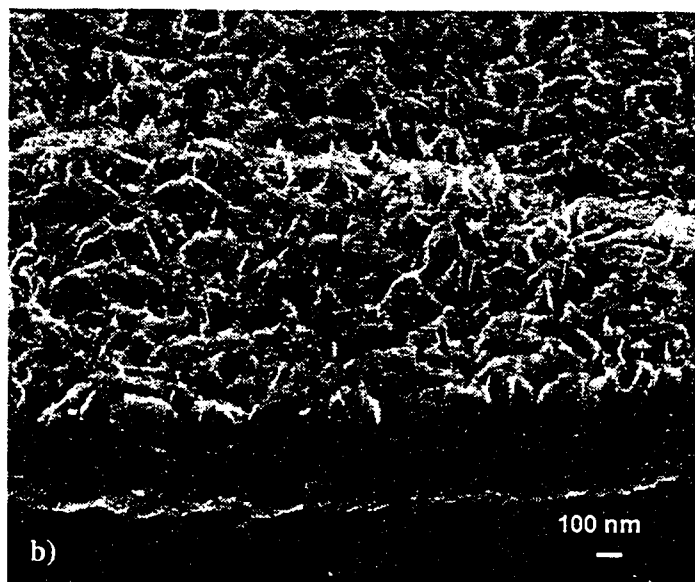
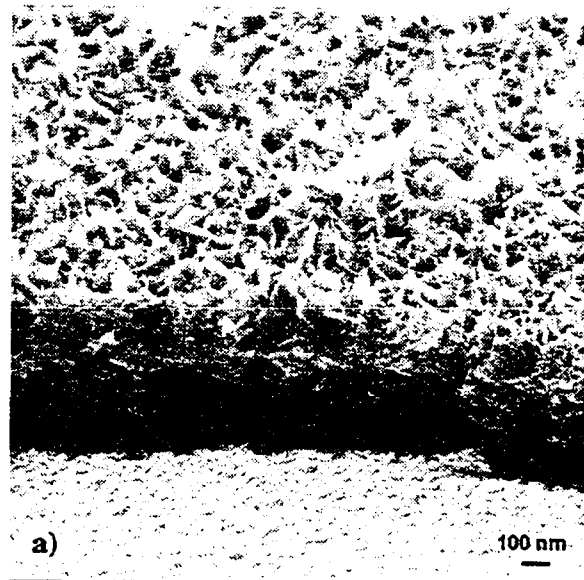


Figure 79. Plot of the thickness of the porous layer as a function of the applied current density.



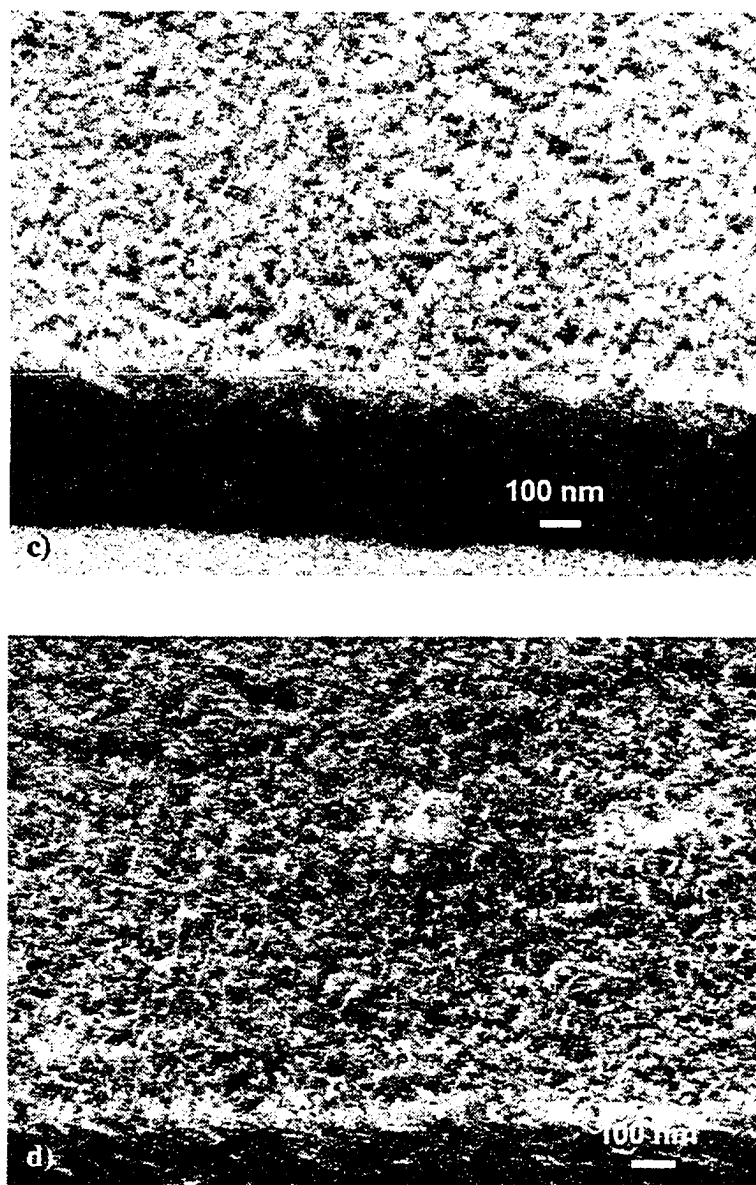
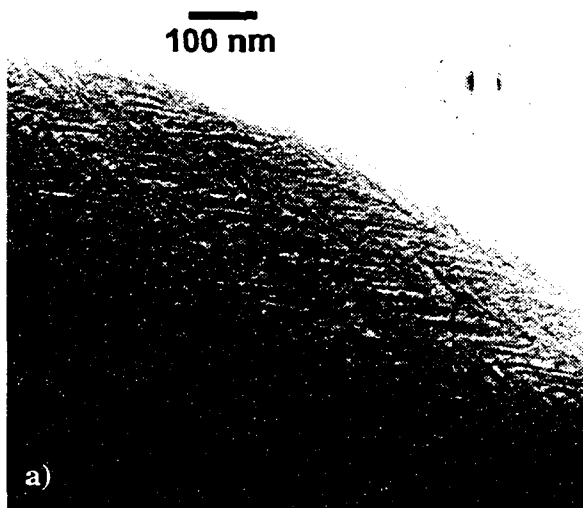


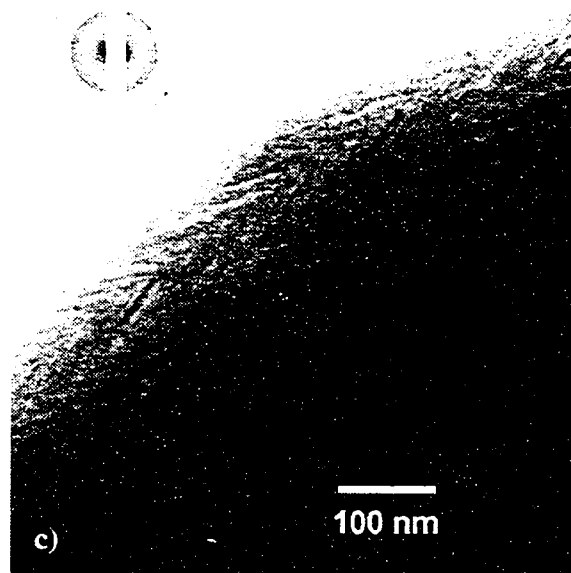
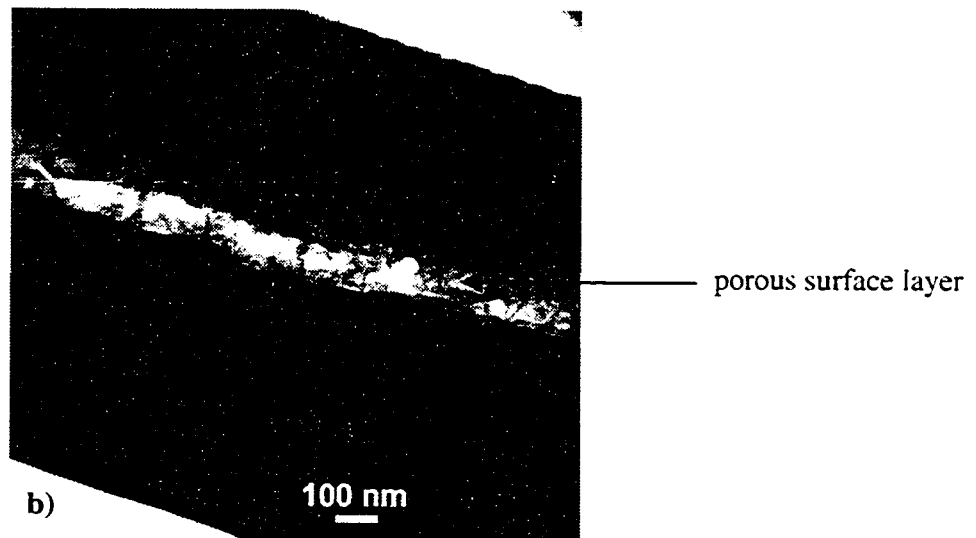
Figure 80. FE-SEM SE images of the zigzag films oxidized at various current densities a) 0.2 mA/cm^2 , b) 0.4 mA/cm^2 , c) 0.8 mA/cm^2 and d) 1 mA/cm^2 .

Without doing any quantitative work, it is still possible to note the trend of decreasing surface layer thickness with increasing current density. In fact, at current densities of 8×10^{-4} and $1 \times 10^{-3} \text{ A/cm}^2$, the porous surface layer is so fine that it is often difficult to resolve in the FE-SEM. Where it is visible, the structure is not nearly as coarse as for the lower current densities (Figure 80 a and b). Intuitively this makes sense, as higher

current densities impose a faster reaction rate resulting in limited growth and maximum nucleation, and hence a finer structure. At the lower current densities, however, the reaction rate is slowed enough to allow for continual growth of the structure. In addition, because the oxidation process takes longer for the lower current densities, there is more time to produce a thicker layer. In contrast, the faster times for oxidation at a higher current density do not provide enough time to grow a substantial layer. Because the porous layers that are produced at the higher current densities are thin and very fine in structure, their surface area may be small relative to the porous layers produced at lower currents.

In order to further analyze the structure of the porous surface layers, the samples were studied in the TEM. The samples oxidized at 2×10^{-4} and 1×10^{-3} A/cm² have been analyzed. The TEM cross-sectional images are shown in Figure 81 for both samples and the difference in film morphology is quite apparent.





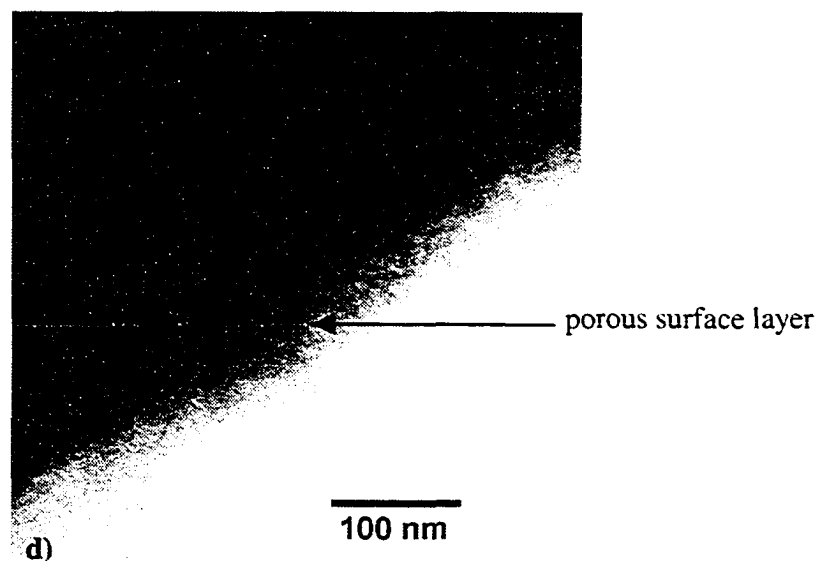


Figure 81. a) TEM BF cross-sectional image of a zigzag sample oxidized at $2 \times 10^{-4} \text{ A/cm}^2$ with inset diffraction pattern identifying the phase of the zigzag as Mn_3O_4 . b) TEM BF cross-sectional image of sample oxidized at $2 \times 10^{-4} \text{ A/cm}^2$ showing porous structure. c) TEM BF cross-sectional image of sample oxidized at $1 \times 10^{-3} \text{ A/cm}^2$ with inset diffraction pattern identifying the phase of the zigzag as MnO and Mn_3O_4 . d) TEM BF cross-sectional image of sample oxidized at $1 \times 10^{-3} \text{ A/cm}^2$ showing detail of the porous surface layer.

Of particular note is the smaller amount of surface film produced for the sample oxidized at the higher current density. The maximum thickness of the layer is approximately 50 nm at 1 mA/cm^2 as compared with a maximum thickness of approximately 150 nm for the sample oxidized at 0.2 mA/cm^2 . Also of note is that the bulk zigzag structure of the sample was converted entirely to Mn_3O_4 at the lower current density, but remains a two-phase mixture of MnO and Mn_3O_4 for the higher current density. This is likely a direct result of the time required for oxidation. At the higher current density, 300s is clearly not enough time to completely oxidize the bulk structure. However, the ultimate phases present in the base zigzag layer are considered unimportant, since the phases do not take part in the capacitive reaction but are simply by-products of the oxidation process.

The porous surface layer has been shown to be amorphous earlier in this thesis and therefore XPS was used to identify the structure of the surface layer. The results for all four samples are presented in Table 16.

Table 16 XPS results giving valence of the samples.

Oxidation current density (mA/cm ²)	Splitting width (eV)	Valence
0.2	4.7	4
0.4	4.9	3.4
0.8	5.10	3.4
1	5.12	3.4

All four samples are fairly close in value, although there are some minor differences. All samples were oxidized to the same end point (0.9V vs. Ag/AgCl); however, the samples oxidized at the higher current densities have a higher splitting width indicating incomplete conversion to MnO₂. The most probable explanation for this is that the oxidation rate is too quick to complete the oxidation prior to reaching 0.9V. Previous results (Figure 44) indicate that for low current densities (0.1 mA/cm²) some Mn₂O₃ is still present in the film at 0.5V when most of the oxidation has already occurred. Therefore oxidations at higher current densities may occur too quickly to complete the oxidation to MnO₂ before 0.9V is reached. However, given the values of the splitting width, there is clearly far more MnO₂ than Mn₂O₃ in the porous layer of samples oxidized at the higher current densities.

The amount of hydration in the porous layer, can be gleaned from the O 1s peaks, as shown in Figure 82.

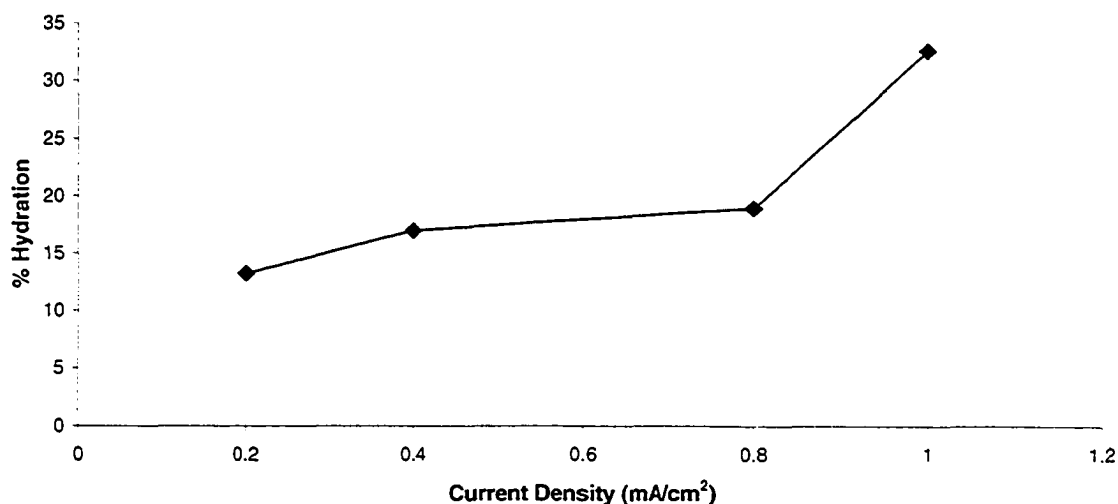


Figure 82. Graph showing hydration of the film as a function of the oxidizing current density.

The hydration amount of the porous film increases with increasing current density. Typically a large amount of hydration results in better capacitance; however, in this case, the high hydration could be counterbalanced by the finer structure (and possible reduction in surface area) that is produced at the higher current densities. In addition, it is difficult to infer which will make the greater contribution to capacitance, hydration or surface area. Given the relatively small amount of porous layer produced from such a significant amount of starting material, the zigzag films were not considered to be very effective substrate materials and the focus returned to the dense starting materials.

4.2.6.2 Dense films

Dense films oxidized using different current densities were studied in an attempt to determine if trends similar to those seen with the zigzag morphologies would be produced. The experimental details of the samples are listed in Table 17.

Table 17 Sample descriptions for oxidation of dense films at different oxidizing currents.

Oxidizing Current (mA/cm ²)	Oxidizing Time to 0.9V (s)
0.2	447
0.4	206
0.8	89
1	73

The trend regarding oxidation time (to 0.9V) is similar to that seen for the zigzag films, following a similar exponential decay trend of decreasing oxidation time required for an increase in current density (Figure 83). Of note is that the overall oxidation times at a particular current density (e.g., 0.2mA/cm²) are significantly less for the dense film than for the zigzag film (e.g., 447 s vs. 2950 s). The full explanation for this phenomenon can be found in Section, 4.2.7, but it is essentially related to the amount of material (i.e., thickness) to be oxidized.

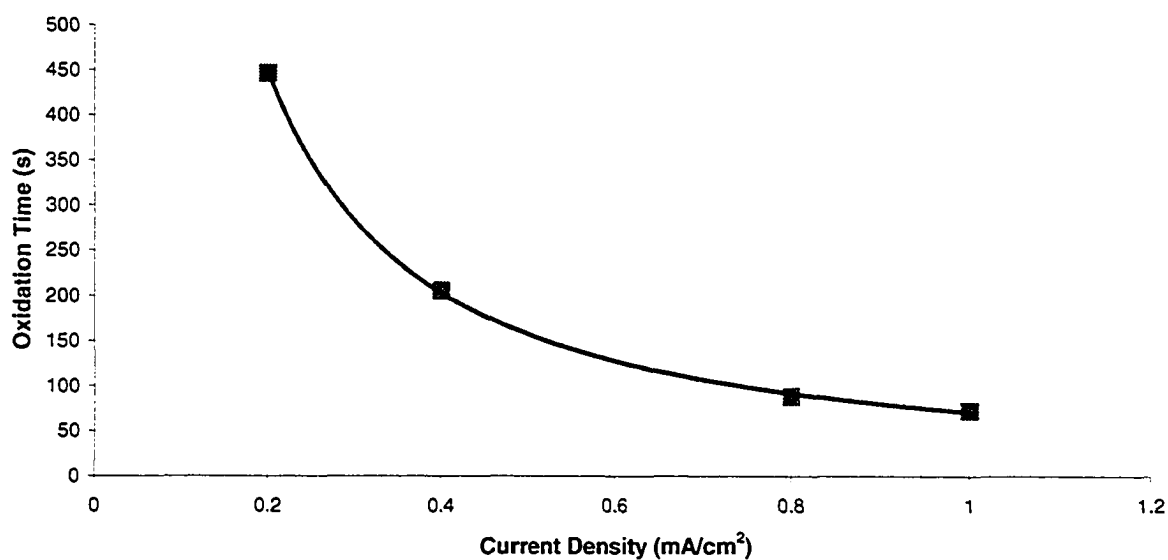
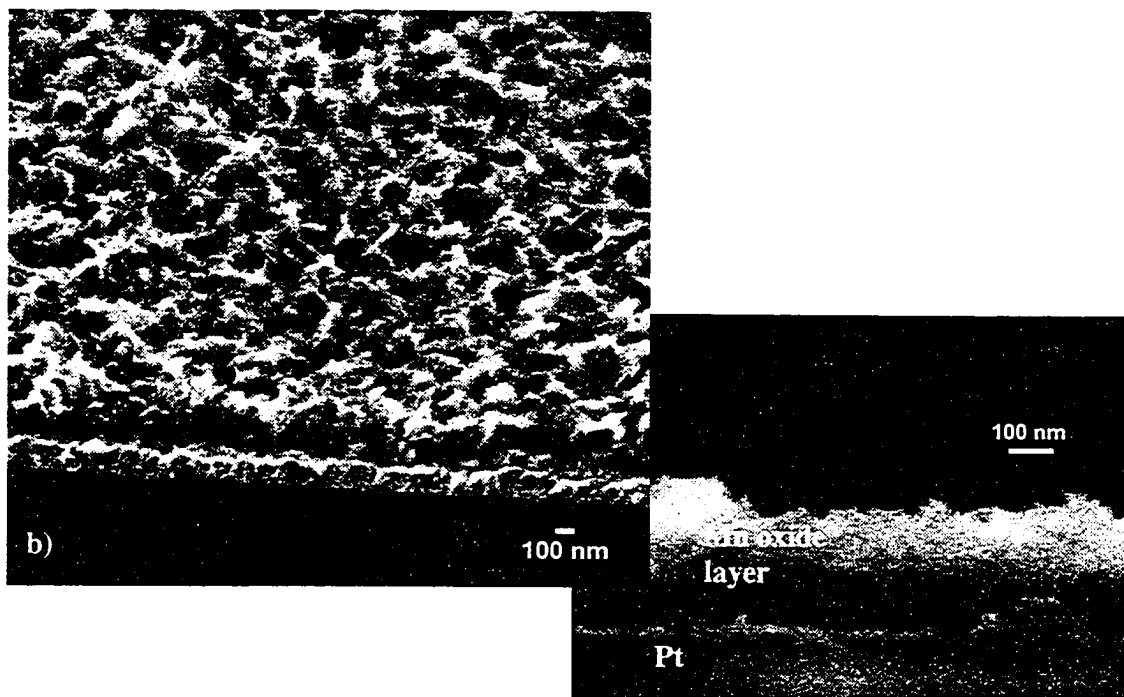
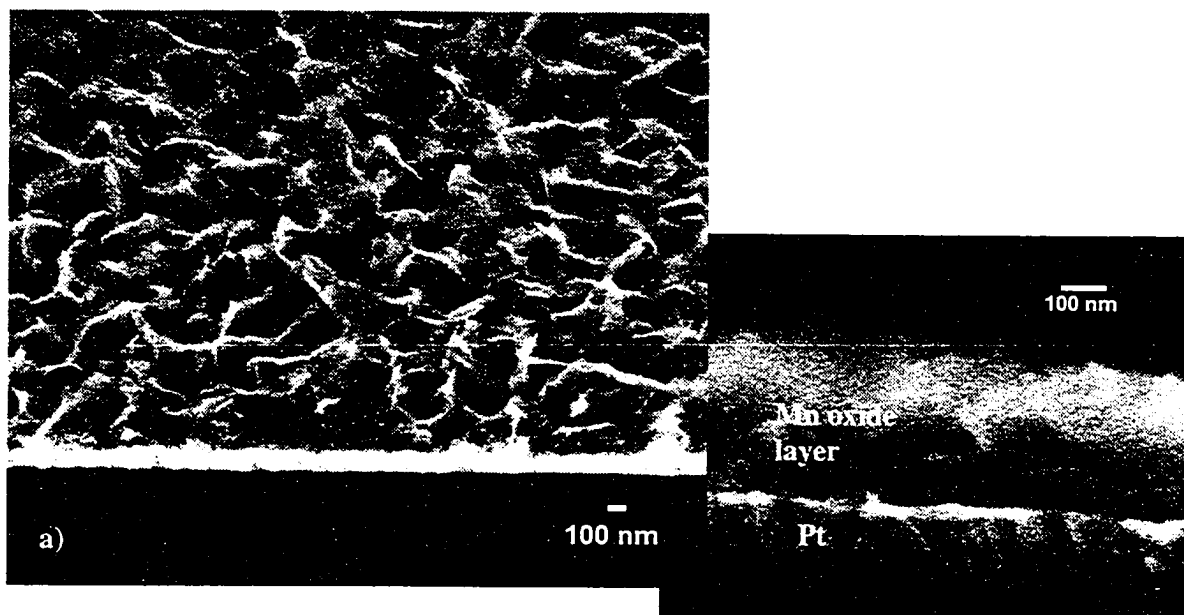


Figure 83. Oxidation time to 0.9V as a function of current density for the dense films.

In a general sense, the dense films and the zigzag films produce a similar looking porous surface layer, although they have a different starting morphology. Ultimately, the higher current densities produce an oxidized layer that is very fine and much thinner for both zigzag and dense morphologies. The morphology of the dense films is shown in Figure 84.



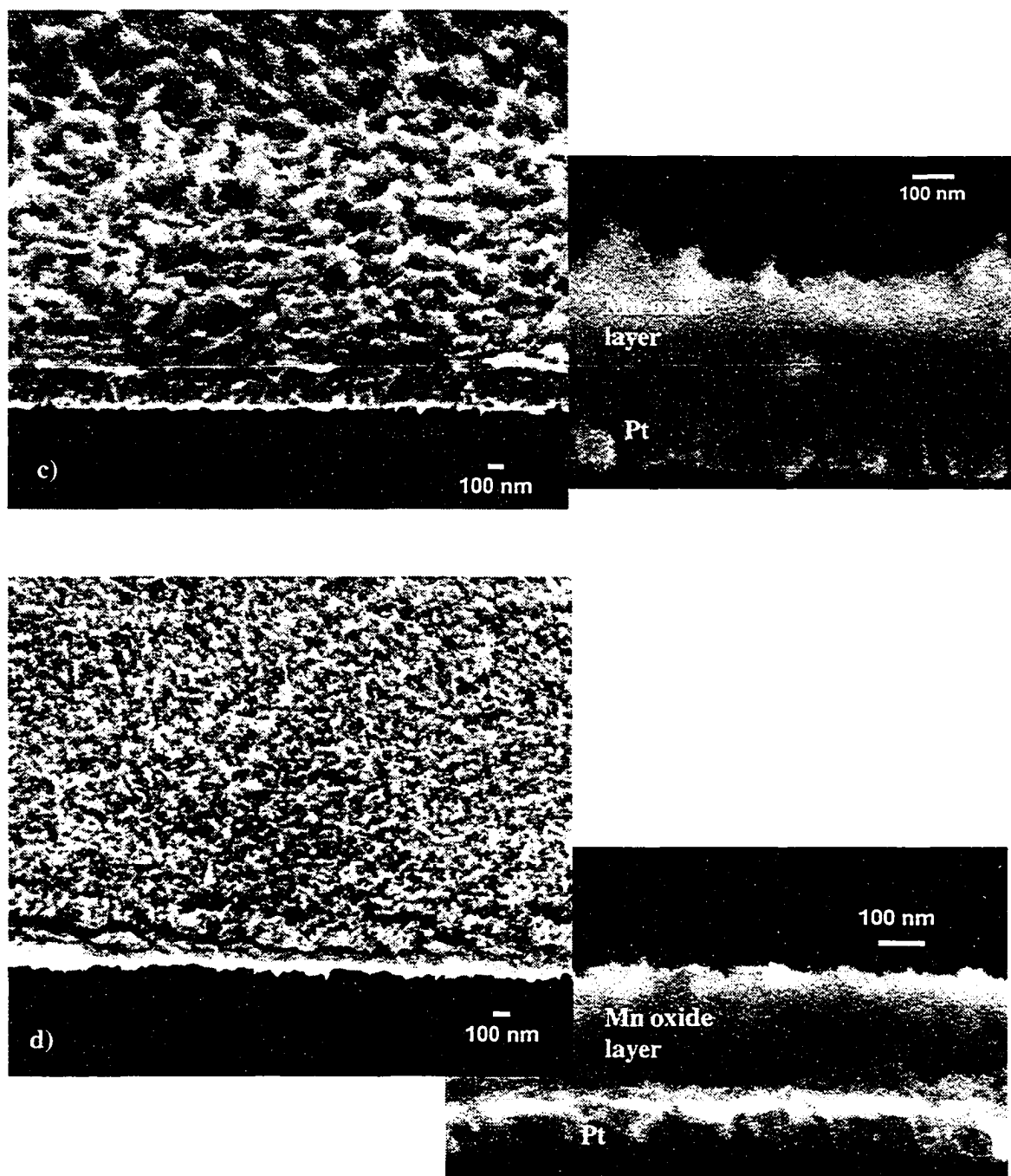


Figure 84. FE-SEM SE images of the films produced at various oxidizing currents in oblique view and cross-sectional view. a) $0.2\text{mA}/\text{cm}^2$, b) $0.4\text{mA}/\text{cm}^2$, c) $0.8\text{mA}/\text{cm}^2$, and d) $1\text{mA}/\text{cm}^2$.

A similar linear trend for layer thickness as a function of current density is obtained for both zigzag and dense films. The layer thickness decreases as the current density

increases. The dense film produces a slightly thicker porous layer than the zigzag film, although the difference is not extremely large (Figure 85). However, if the amount of porous film produced relative to the amount of starting film is considered (Figure 86), then the trend becomes far more pronounced. Again, this phenomenon is explained more clearly in the following section.

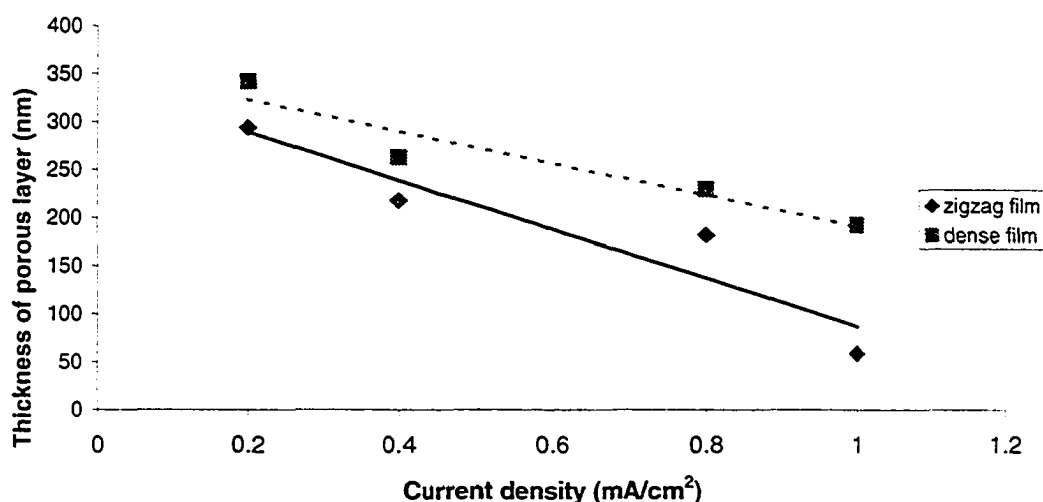


Figure 85. Plot of porous layer thickness as a function of oxidizing current density for both dense and zigzag films.

The trend in Figure 86 can also be inferred from the FE-SEM images (Figure 80 and Figure 84), where it is clear that most of the dense film has transformed into a porous film during the oxidation. The bulk of the zigzag film remains morphologically untouched with only the surface region transforming into a usable porous surface layer.

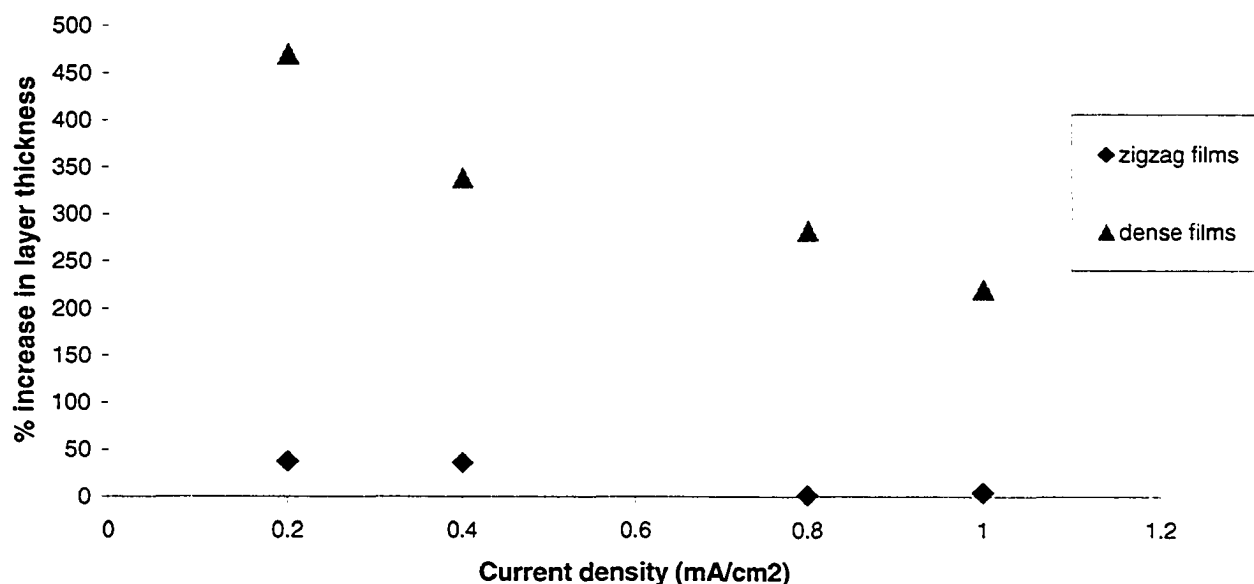


Figure 86. Plot of percent increase in the total layer thickness (porous surface and dense under-layer) as a function of the oxidizing current density for both zigzag and dense films.

The XPS results for the dense films are again similar to the results obtained for the zigzag films and are shown below in Table 18 and Figure 87.

Table 18 XPS Mn 3s splitting width results giving valence of the samples.

Oxidation current density (mA/cm ²)	Splitting width (eV)		Valence	
	Dense films	Zigzag films	Dense films	Zigzag films
0.2	4.7	4.7	4	4
0.4	4.7	4.9	4	3.4
0.8	4.7	5.10	4	3.4
1	4.9	5.12	3.4	3.4

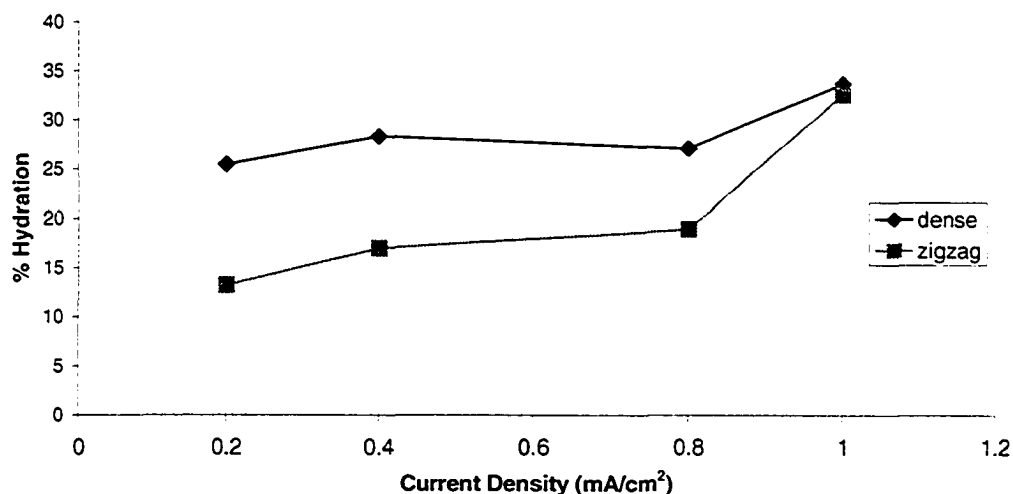


Figure 87. Graph showing the hydration of the dense film as a function of the oxidizing current density.

At the highest current density, there is incomplete oxidation resulting in a two-phase mix of MnO_2 and Mn_2O_3 , although the amount of Mn_2O_3 is miniscule (Table 18). The difference between the zigzag films and the dense films is that there were more instances of incomplete oxidation of the porous surface layer with the zigzag films than with the dense films. It is possible that this phenomenon is related to the overall thickness of the deposited layer. The zigzag films are much thicker (500nm as opposed to 50nm), resulting in a longer oxidation time since a greater volume of material must oxidize. In addition, because of the increase in the volume of material to oxidize there are more instances of incomplete oxidation for zigzag films where the entire porous surface layer is not able to convert to MnO_2 . While the porous surface layer is oxidizing, the dense sub-layer is also oxidizing. Because of the greater thickness of zigzag material, there may be issues with conductivity through the dense layer to the porous surface that affect the ability of the porous surface layer to oxidize completely in the time allowed.

The variation in the hydration of the film as a function of the oxidizing current density follows a fairly similar trend as the zigzag film, i.e., there is an overall increase in the hydration of the film with an increase in the oxidizing current density. Again, this results in two competing mechanisms: film hydration increases with increasing current density, but there is a simultaneous reduction in the thickness of the film and possibly the surface area as well. The actual change in hydration with current density is far more pronounced for the zigzag films than for the dense films, although, they ultimately both achieve a similar amount of hydration (~35%). The dense films have nearly constant hydration content until $0.8\text{mA}/\text{cm}^2$ is reached after which the increase in hydration is more substantial. For instance, the hydration varies between 25% and 35% over the range of current densities tested for the dense films and between 10% and 35% for the zigzag films.

4.2.6.3 Capacitance

Given the relatively small amount of porous layer produced from such a significant amount of starting material, the zigzag films were not considered to be very effective substrate materials for electrochemical capacitors, and were therefore not tested for capacitive qualities. The effect of oxidizing current on the final capacitance of the dense films, however, was studied and the results are shown below (Figure 88). By overlapping the various CV curves it is seen that the films oxidized at a higher current density exhibit a CV curve that encloses a greater area and thus have larger capacitance values. The relationship between capacitance and oxidizing current density is shown in Figure 89. Although the trend is not extremely strong, within errors, planar capacitance increases with increasing current density.

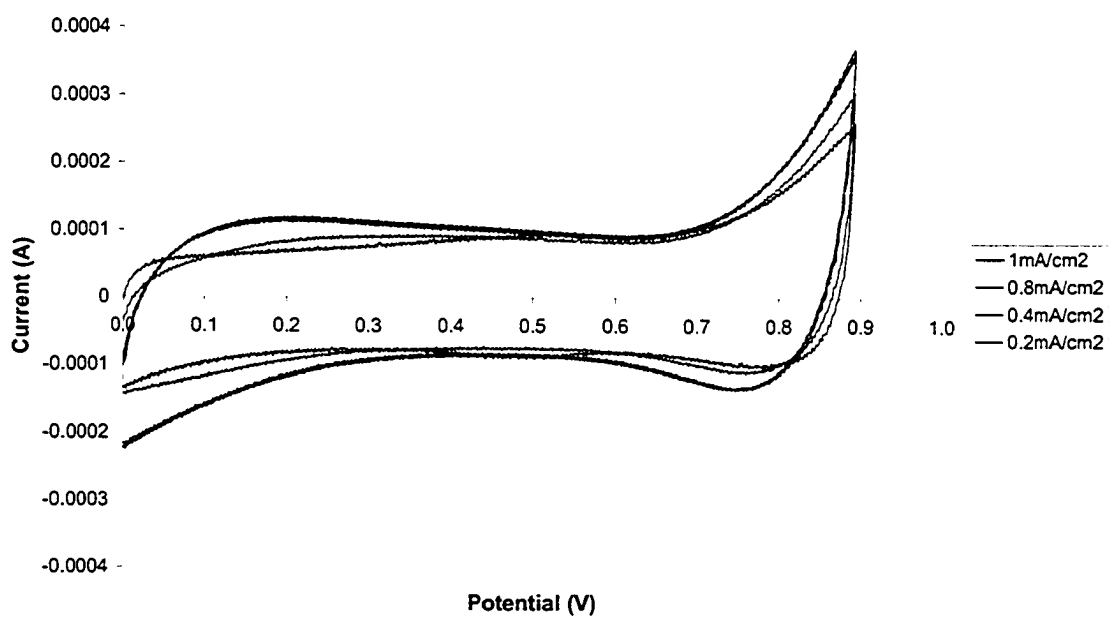


Figure 88. Current-Voltage curves for the dense samples oxidized at various oxidizing current densities.

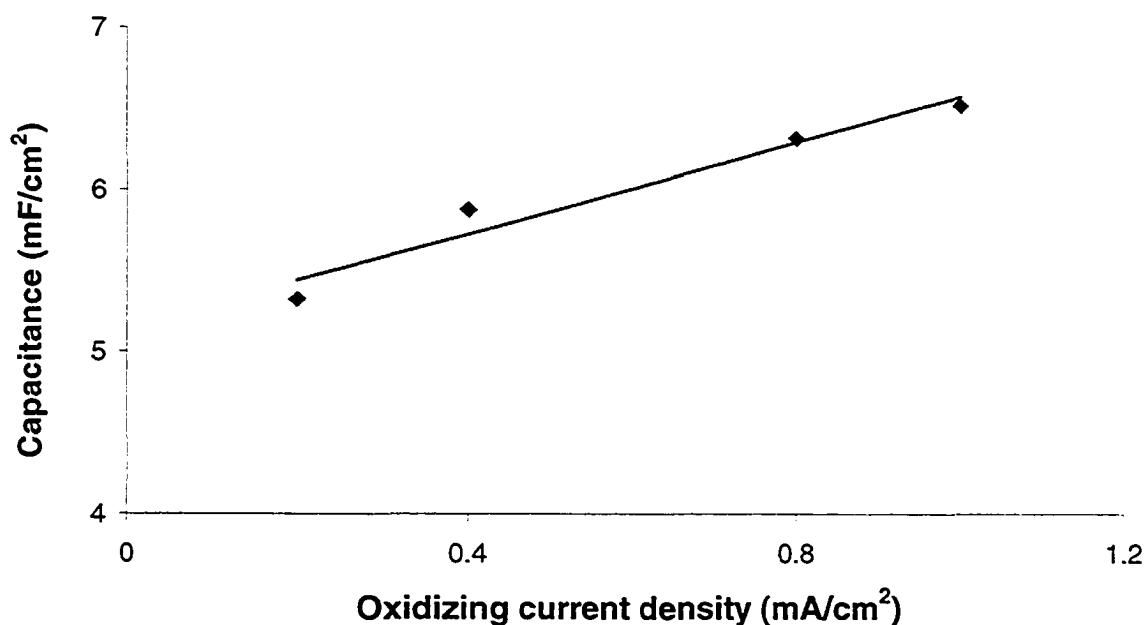


Figure 89. Plot of planar capacitance for the dense samples as a function of the oxidizing current density.

The increase in capacitance with increasing oxidizing current density is partly due to the increased hydration of the films. However, there may be more to the increased capacitance than just an increase in the hydration of the sample. Although both the hydration and the capacitance increase with increasing current density, there does not appear to be a direct correlation. The hydration increases 40% over the range of current densities tested while the capacitance increases only 25%. It is reasonable to assume that the films produced at higher current densities have less overall surface area due to the fine structure that is produced. If the decrease in surface area is not as significant as the increase in hydration, then the overall effect will be a reduction in the positive trend between current density and capacitance (Figure 89), as compared with the positive trend between hydration and current density.

The solution from each oxidation was analyzed using AAS to determine the amount of Mn present in the solution. The results, for the total amount of Mn left in the solution are shown in Figure 90.

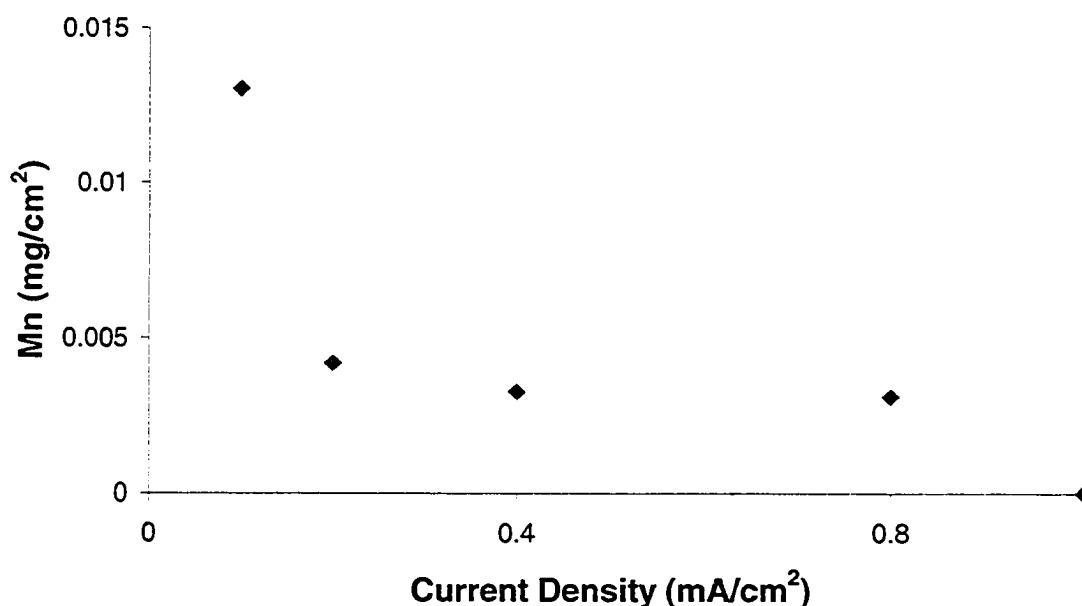


Figure 90. Graph showing the amount of Mn left in solution following an oxidation at a particular current density.

As the oxidizing current density increases, the amount of Mn left in the solution is minimal (near zero). The initial decrease in Mn in the solution is quite substantial (0.1 to 0.2mA/cm²) but remains constant from 0.2-0.8mA/cm² and then drops to 0 at 1mA/cm². Thus, since the samples oxidized with the higher current densities lose less Mn, they have more Mn in the structure to provide more active sites to develop capacitance and hence higher capacitance values. This effect is likely related to the amount of time required for the oxidation. At the higher current densities, the oxidation occurs faster and thus there is less time/opportunity for the soluble Mn to make its way into the solution. This effect, combined with the higher hydration amount clearly compensates for the thinner layers produced at the higher current densities.

The effect of current density on the morphology of the porous surface layer is quite pronounced in both the zigzag and dense layers. In both films, a higher current density results in a much thinner, finer porous layer. In addition, the increased current density results in a film with greater relative hydration. The result is a slight increase in capacitance with increasing current density. However, this increase is not overly pronounced, suggesting that the competing variables of hydration and film surface area are fairly balanced in these situations. From a manufacturing perspective, it is advantageous to oxidize with a higher current density since it will not only produce marginally better capacitance, but it will also significantly reduce the manufacturing time.

Although other researchers have explored the use of galvanostatic deposition (Hu and Wang⁷⁶), they have used only a single deposition current and have not studied the effects of the deposition current on the quality of their films. As a result, it is difficult to compare this section of the thesis with work currently being done in the literature. In addition, the current applied to the films in this study is done purely to oxidize the manganese that has already been deposited on the electrode substrate. In the literature, galvanostatic deposition is used to deposit a manganese oxide film directly from a plating bath, and thus, it is unlikely that these results can be applied to other galvanostatic systems unless they were also oxidizing a previously deposited manganese film.

4.2.7 Effect of starting layer thickness on porous layer formation

4.2.7.1 Dense Films

Many of the differences (hydration, valence) between the zigzag films and the dense films have been attributed to differences in thickness. Because of this effect, it was important to determine more precisely the effects of starting layer thickness on the porous layer. Samples of different deposited Mn layer thickness were therefore oxidized using a constant current. Each sample was oxidized to a potential of 0.9V vs. the Ag/AgCl reference electrode. The experimental details of the samples are listed in Table 19.

Table 19 Sample descriptions for dense films of different deposited thicknesses.

Starting film thickness (nm)	Oxidation Current Density (mA/cm²)	Complete Oxidation Time (s)
25	0.1	250
60	0.1	520
110	0.1	1350
230	0.1	3100

Figure 91 reveals that the time required for complete oxidation is linear with the thickness of the starting layer. The results in Figure 91 are intuitively obvious. A thicker film has more material that needs to be oxidized and therefore more time will be required to complete the oxidation. In addition to the greater time required for oxidation, the final total film thickness is a linear function of the starting layer thickness (Figure 92) which is clearly visible in the corresponding FE-SEM images (Figure 93). The results in Figure 92 are also intuitively obvious. If the starting layer is quite thick prior to oxidation, it is expected to become even thicker after the oxidation.

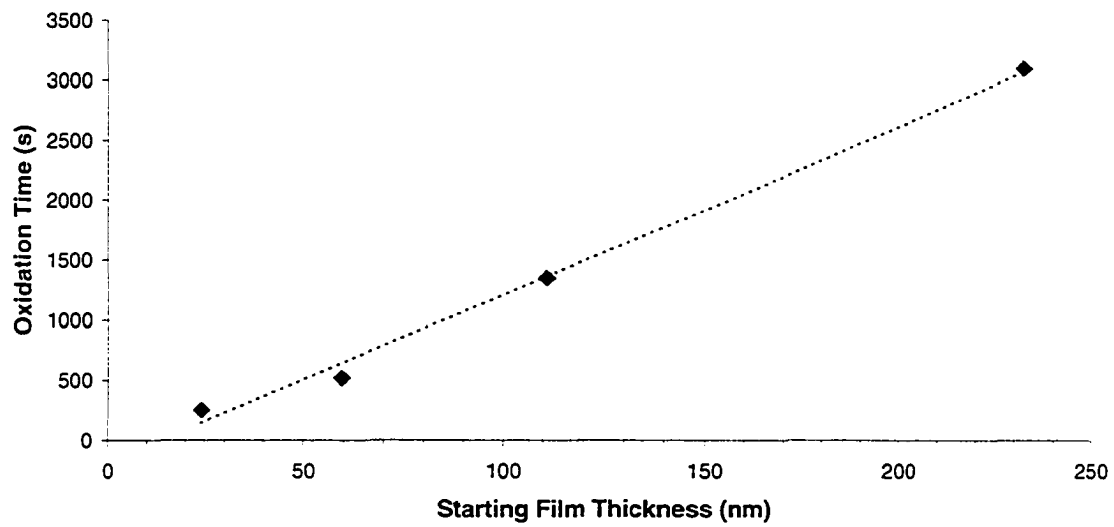


Figure 91. Plot of the total oxidation time as a function of the starting film thickness.

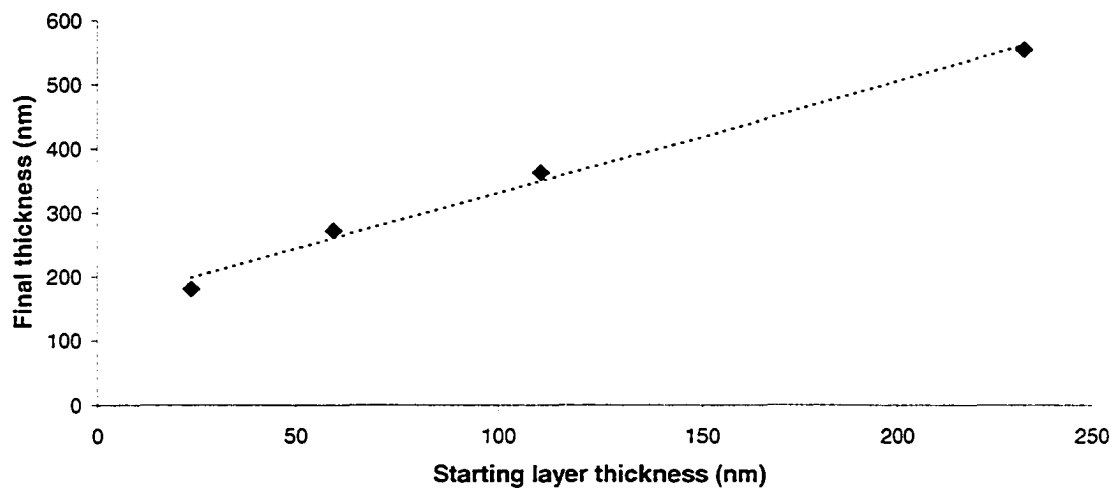
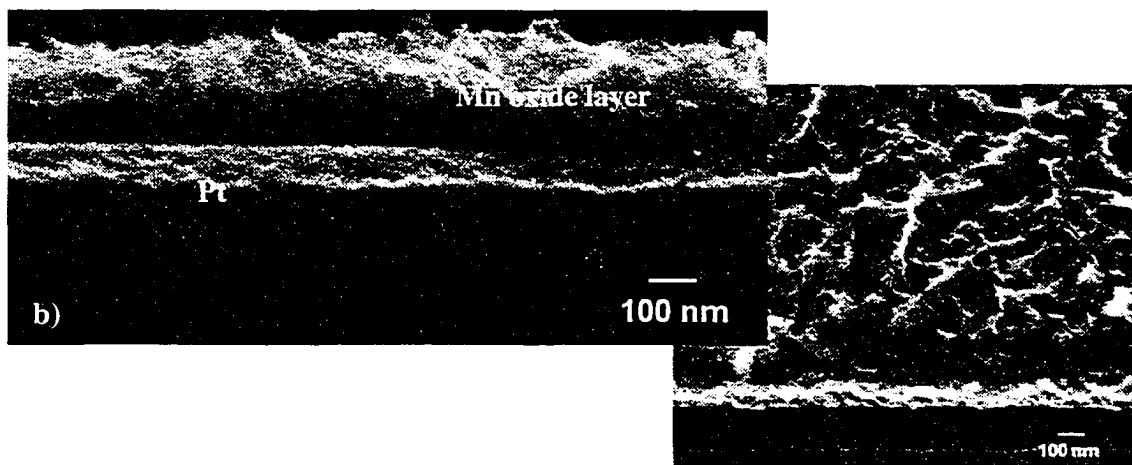
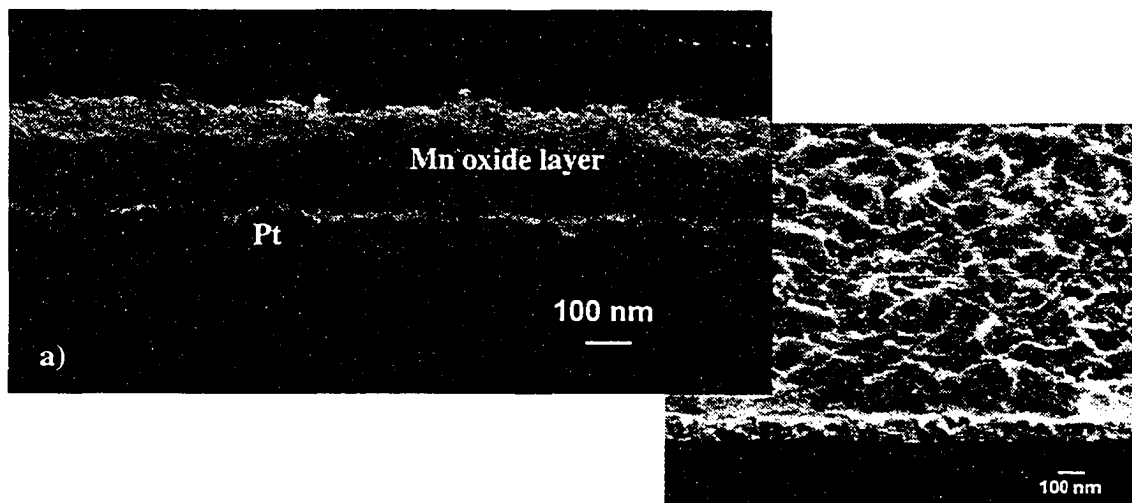


Figure 92. Effect of starting layer thickness on the thickness of the final layer.



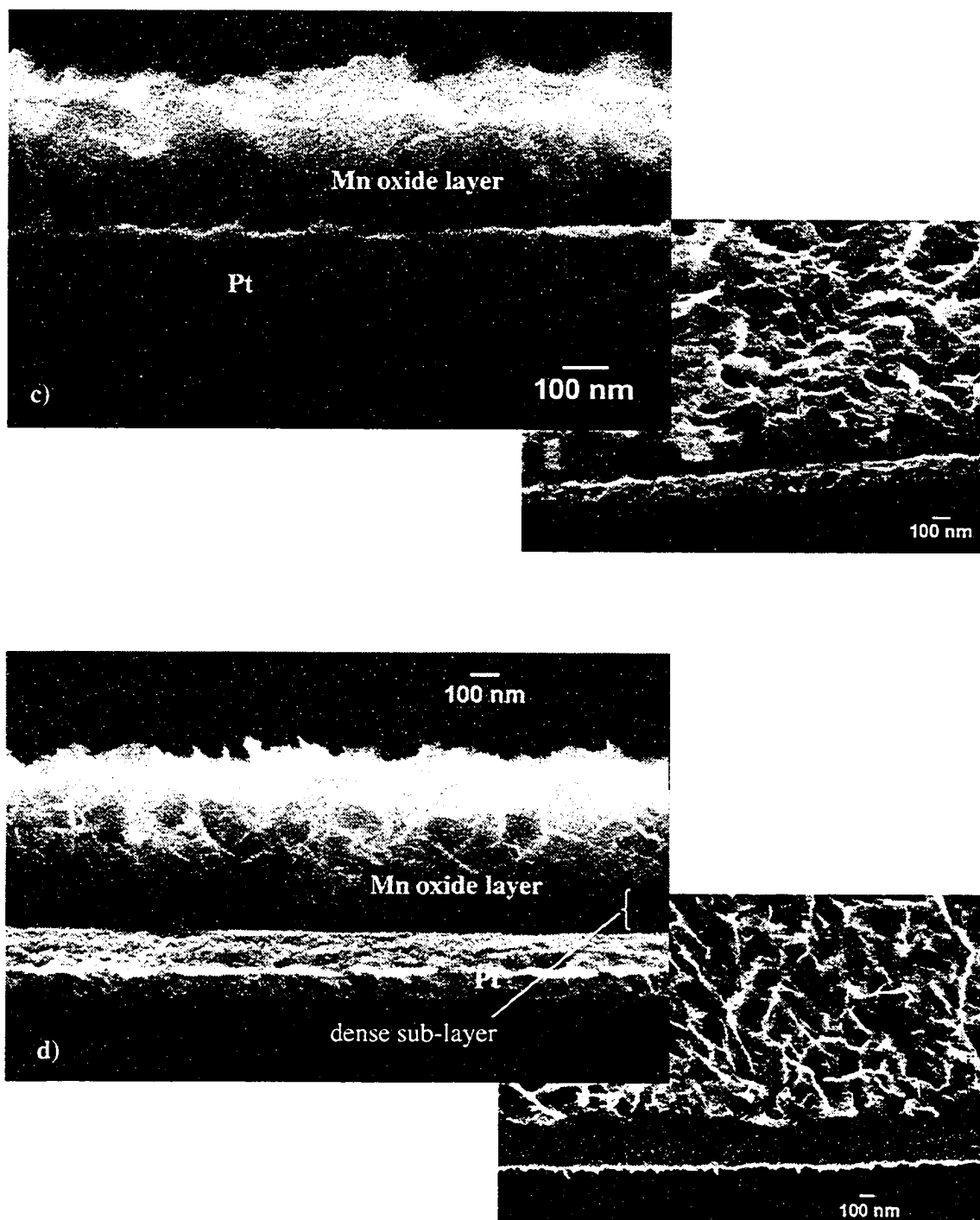


Figure 93. FE-SEM SE images in the oblique and cross-sectional views for samples different starting film thickness. a) 25nm, b) 60nm, c) 110nm, and d) 230nm.

From the images in Figure 93 it is clear that films with a greater starting thickness produce thicker final layers. However, looking closely at the cross-section of these films, it is apparent that the entire film thickness is not a porous layer. Like the zigzag films that were studied previously, during the oxidation process, only a certain portion of the film transforms into the porous hydrated structure. A portion of the film remains, morphologically, the same as before the oxidation step (although there is a phase change from Mn/MnO to Mn_3O_4). This effect can be seen most clearly in Figure 93d, where the bottom 200nm of the deposited film has retained its dense structure during the oxidation process. Therefore, the final film thickness includes both the porous surface layer (active layer) and a dense layer that makes up the substructure.

If the final thickness of the porous layer is plotted against the starting layer thickness, the linear relationship in Figure 94 is revealed. However, although there is a relationship between the two quantities, it is not a one to one correlation: i.e. the porous film thickness is not consistently four times the size of the starting film thickness. The film with a starting film thickness of only 25 nm produced a porous surface film of 100nm, four times the size of the starting film. However, a film with a starting film thickness of 230 nm, produces a porous film with a thickness of only 350 nm or approximately 1.5 times the original thickness of the film. The reason for the drop in the proportion of porous film that can be produced is related to the thickness of the film. The thicker films, by nature, will experience more problems with electronic conductivity through the bulk of the layer that may serve to slow the oxidation process and overall, result in a proportionally thinner porous layer being produced.

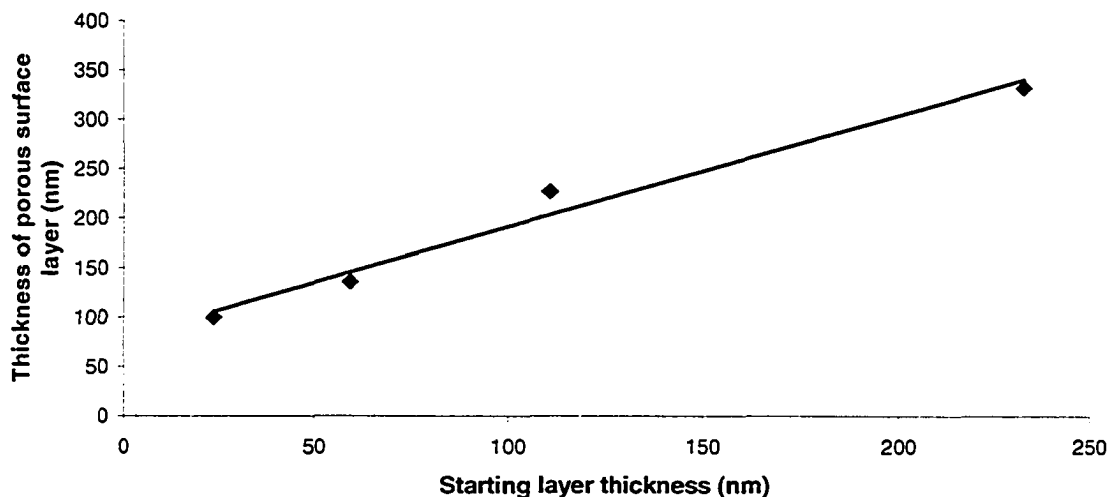


Figure 94. Effect of the starting layer thickness on the thickness of the porous surface layer produced.

A similar trend is occurring with respect to the dense under-layer. If the final thickness of the dense sub-layer is graphed versus the starting layer thickness, the linear relationship in Figure 95 is revealed. Again, although the relationship is linear, there is no one to one correlation between the two quantities. For instance, the dense under-layer measures 75 nm in the film with 25 nm starting thickness (three times the original value). However, in the film with 230 nm starting thickness, the dense under-layer measures approximately 230nm. Thus, there is proportionally less dense material being produced as the thickness of the starting layer is increasing. Although it may at first seem counter-intuitive to have 75 nm of dense material present after the oxidation of a layer that was only 25 nm of dense material to start, it is a combination of volume expansion during the phase change from Mn/MnO to Mn_3O_4 and the production of a layer with less than bulk density. As a benchmark, the greatest volume change would occur if a film of dense Mn ($7.2g/cm^3$) transformed to a film of dense Mn_3O_4 ($4.8g/cm^3$). In this case, the original 25 nm Mn layer would become a 50 nm layer of Mn_3O_4 . Since the starting layer is actually

a mixture of Mn and MnO (5.4g/cm^3) rather than pure Mn, its initial density would be significantly less than 7.2g/cm^3 and therefore the volume change associated with the transformation of Mn/MnO to Mn_3O_4 would be less than the change associated with the transformation of Mn to Mn_3O_4 . Experimentally, the layer thickness increases from 25nm to 75 nm, a change too large to be accounted for by volume expansion alone. Therefore, the thickness change must be a result of volume expansion during the transformation and the production of a layer with a density significantly less than bulk density.

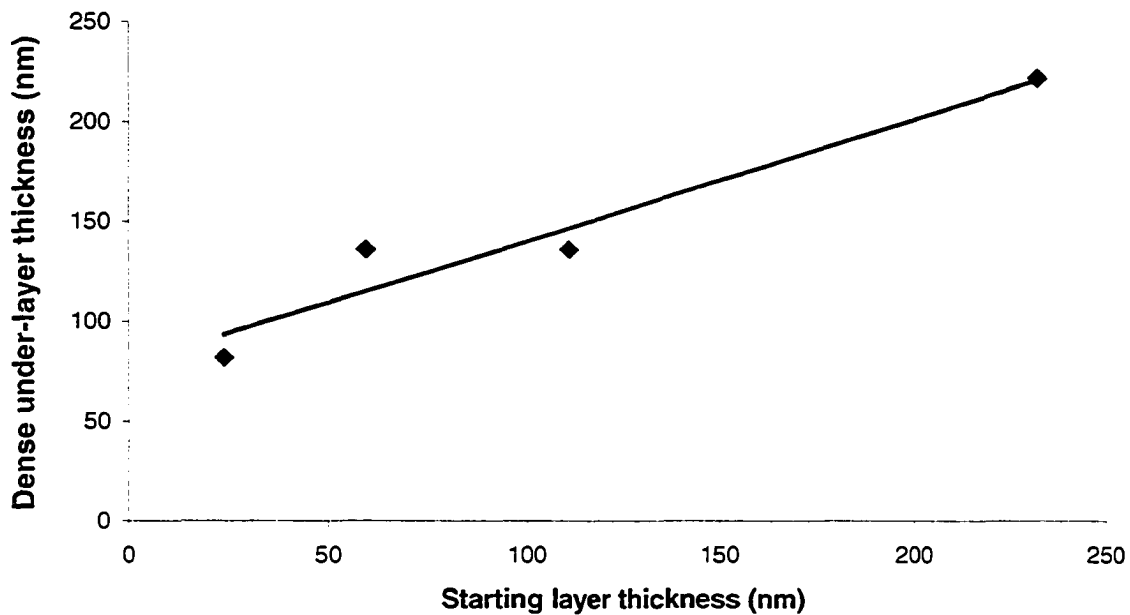


Figure 95. The effect of starting layer thickness on the thickness of the dense under-layer.

The relationships in Figure 94 and Figure 95 are both linear, though the slope is not the same for the two graphs. The slope is twice as great for the porous surface layer graph, indicating the starting film thickness has a more pronounced effect on the final thickness of the porous layer than on the dense layer beneath. This is an advantage for this process since the focus is on obtaining the largest porous layer. From the standpoint of

developing capacitance, thicker films, which have greater porous surface area, should produce greater capacitance.

There is no clear explanation for why a thicker starting layer should result in a thicker porous surface film. There is obviously some kind of balance established between the amount of material that can oxidize into the porous layer and the amount of material that will remain intact as the dense sub-layer. Thus, the greater amount of starting material (i.e., thicker layer) allows more film to be oxidized, resulting in a thicker porous surface layer.

Surface area is not the only important factor in developing capacitance. The valence and relative hydration of the films were examined using XPS and the results are shown in Table 20 and Figure 96.

Table 20 XPS Mn 3s peak splitting results giving valence of the samples.

Starting film thickness (nm)	Splitting width (eV)	Valence
25	4.6	4
60	4.5	4
110	4.7	4
230	4.6	4

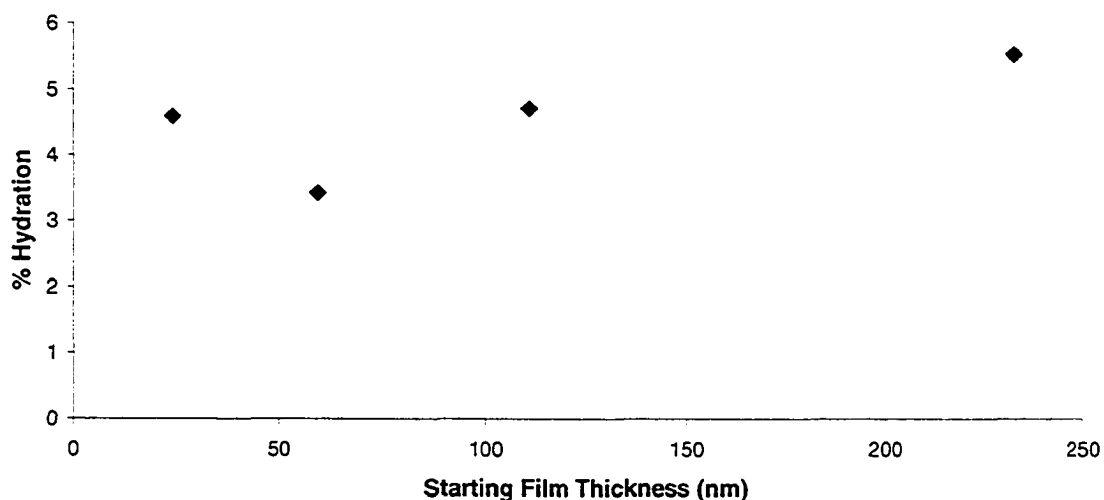


Figure 96. Graph of relative hydration of films as a function of the starting film thickness.

Changing the thickness of the starting film has no impact on the final valence of the film as they all produce MnO_2 . However, this was not the case with respect to the zigzag films. In previous sections, it was seen that the zigzag films tended to have more trace Mn_2O_3 in the porous surface layer than the thinner dense films. This effect was attributed to the difference in thickness between the two films. Although the dense films do not show a tendency to form Mn_2O_3 as the thickness of the starting film increases, it must be mentioned that the zigzag films have a thickness of 500nm (substantially greater than the 230 nm tested with the dense films) which would compromise electronic conductance even more and the inherent porosity in the zigzag structure itself is certainly disruptive to conductance. All dense films were oxidized at 0.1 mA/cm^2 , a current density at which the zigzag films also exhibited complete conversion to MnO_2 . If higher current densities were used, it is speculated that thicker dense films would experience an inability to oxidize completely (i.e. some trace Mn_2O_3 found in the porous surface layer).

Given the errors of the XPS technique, the % hydration remains constant despite the starting film thickness. Thus, based on previous work, the amount of hydration in the

sample is a function of the current density used for oxidation rather than the thickness of the film. This is an expected result since the starting film thickness should not affect the final chemistry of the film, just the final size of the film. Considering that the hydration is independent of the starting film thickness, it is suggested that a thicker film would give better capacitance per planar area due to the increase in thickness of the porous layer that provides more active sites for capacitance.

4.2.7.2 Capacitance

The effect of starting film thickness on the capacitance of the films was studied for the four different dense film thicknesses. The results for the planar capacitance are shown in Figure 97. The trend is obviously one of increasing planar capacitance with an increase in starting layer thickness. This result was expected from the analysis of the porous layer done in the previous section. The thicker films produce more of the porous surface layer, with the same amount of hydration as the other starting film thicknesses and thus, are expected to develop greater capacitance. The capacitance appears to tail off at the larger starting film thicknesses suggesting the possibility of reaching a maximum value. However, with the data collected thus far, there is no way to determine what that maximum value would be or if there is a maximum value.

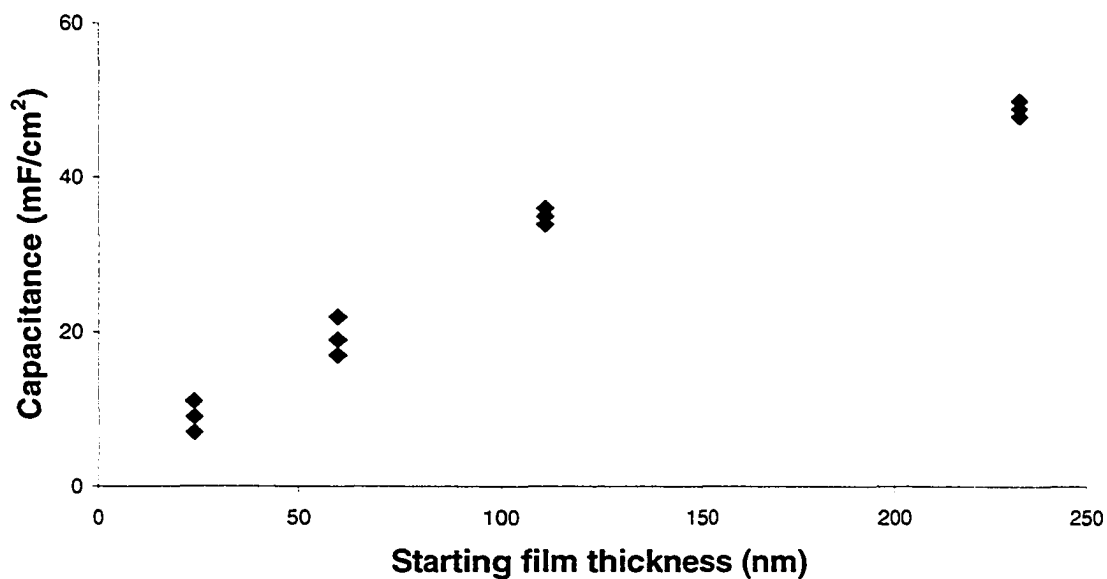


Figure 97. Effect of starting film thickness on the planar capacitance of the films.⁸⁰

One must also consider, however, not just the final amount of porous layer that can be produced, but also the proportion of the original film that is converted to porous film. Referring to Figure 93, the thicker starting films, although they produce larger porous layers, also leave significantly more “unused” material. Figure 98 reveals that the relative % of porous layer produced is the greatest for the thinnest layers, and slowly drops off. Thus, from a manufacturing perspective, the thinner starting layers result in the most efficient use of material. This trend concerning efficient material use is also reflected in the specific capacitance (F/g) of the film (Figure 99). The specific capacitance is calculated with respect to the total mass of manganese oxide film (including both the porous surface layer and the dense underlayer). Although there is some error in the weight measurements (± 1 microgram for a film that is hundreds of micrograms), the scatter in the capacitance data (Figure 99) is much greater than this measurement error. Therefore, error bars are not shown since the error is encompassed in the scatter. Within errors, the specific capacitance is independent of the starting film thickness. This effect is quite simple to explain. While the capacitance increases with the starting layer thickness, the amount of material is also increasing. Therefore, the

amount of capacitance developed per gram of manganese oxide material is the same as for the thinner films, which develop less capacitance but also have significantly less mass. The significant scatter is a direct result of the difficulty in obtaining accurate mass measurements when working with such small amounts of material (micrograms).

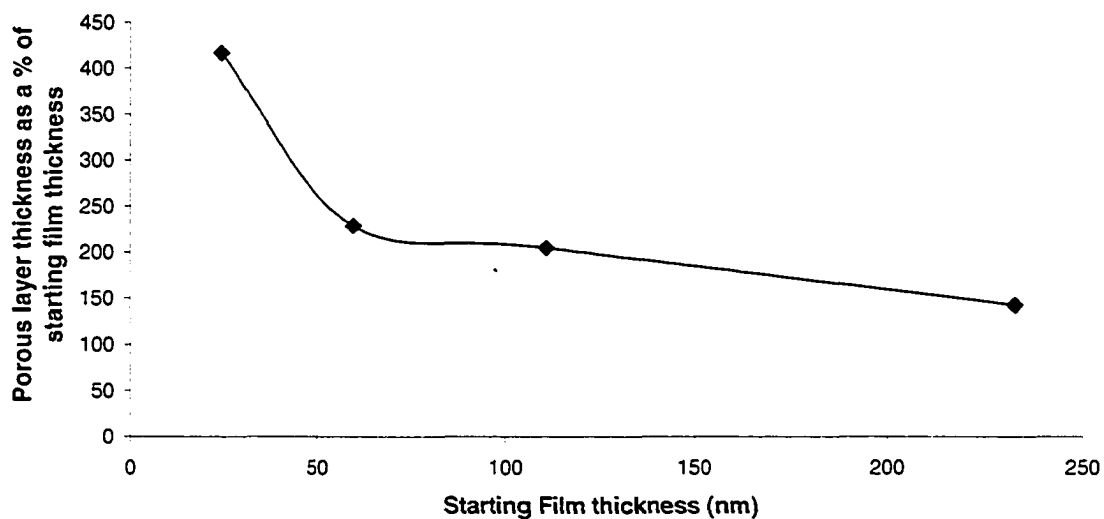


Figure 98 Graph of the porous film thickness as a fraction of the original film thickness.

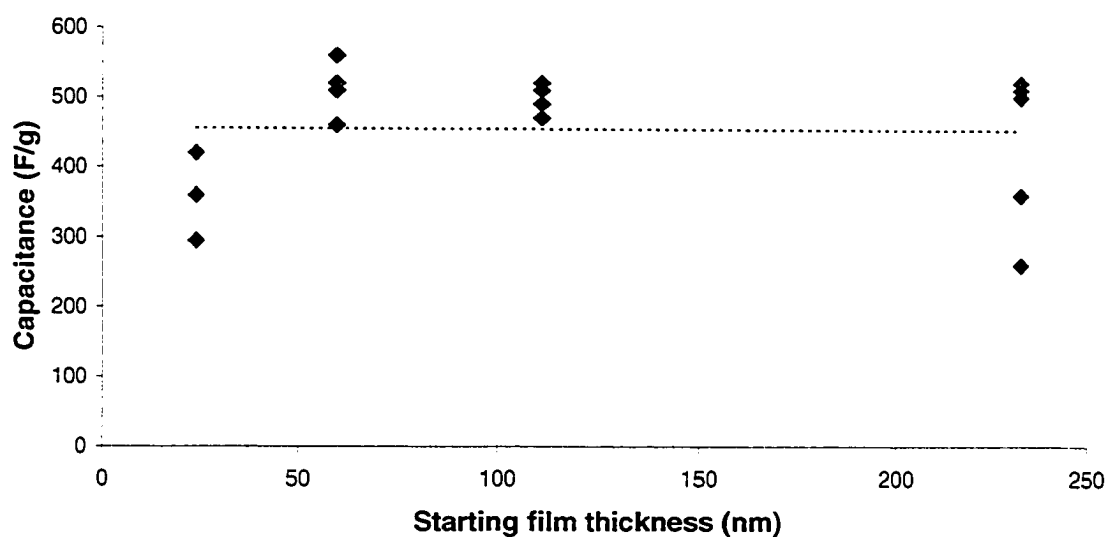


Figure 99. Graph of the specific capacitance of the film as a function of the starting film thickness⁸⁰.

The effect of the deposited layer thickness on the quality of the porous layer produced through electrochemical oxidation is quite pronounced. As the thickness of the originally deposited layer increases, so does the thickness of the porous layer that is produced during the electrochemical oxidation. The result is a significant increase in the surface area of the layer. The oxidation occurs at a single current density and, as a result, the relative hydration of the film does not change noticeably as the thickness of the deposited layer is increased. The ultimate effect of increasing the deposited layer thickness is the production of a porous surface layer that increases in thickness, but with a constant amount of hydration. The combination of variables results in a significant increase in the areal capacitance of the film with increasing deposited layer thickness. The specific capacitance remains relatively unchanged because, although the capacitance for the thinner deposited films is much less, the mass of porous material is much less, resulting in a similar value for specific capacitance.

It is difficult to compare these results to those found in literature since the processing is quite different. However, several groups^{66,63} have reported the effects of electrodeposited layer thickness on the subsequent capacitance. Since Pang and Anderson's group makes use of a sol-gel process, they have correlated the thickness of the electrode (number of dip-processes) with the value of capacitance for the film. As a general trend, an increase in the thickness of the film was shown to greatly increase the capacitance of the films, though this is accompanied by a subsequent loss of stability upon cycling. In addition, the capacitance increases linearly with the thickness of the films (though no reason is given). However, the excessively thicker films also have significantly reduced cycle lives, which were suggested to be due to a higher rate of dissolution during charging and discharging resulting in greater changes to the electrode film. This is similar to the results from this thesis, where a dramatic increase in areal capacitance was seen with increasing deposited layer thickness.

In general, the specific capacitance that can be generated by these films (~500F/g) is superior to many groups working in this field who produce values of approximately 250F/g^{62,65,67,70,76}, but less than the current state-of-the-art of 720F/g⁷¹ produced from an ultra-thin film. Overall, this process is near the top of the field for producing good capacitance values and should, therefore, be considered a viable manufacturing process.

It can be misleading to compare specific capacitance results to each other. For instance, in this thesis, it was necessary to include the dense sub-layer in the overall mass used to calculate specific capacitance since the two layers (porous surface layer and dense sub-layer) could not be separated. However, if a specific capacitance were calculated based on just the mass of the porous surface film, the values would naturally be much higher. From a manufacturing perspective, therefore, areal capacitance (F/cm² of projected area) is felt to be a more meaningful measure of the capacitance since it gives an idea of the size of device required to develop a particular capacitance. Considering the current trend in reduction of packaging size, a capacitor that can develop high capacitance in a small geometric area (F/cm² of projected area) is obviously more meaningful than a capacitance developed per gram of material where the geometry is unknown. Although it is desirable

to reduce the weight of devices for portable applications (cell phones, laptops) the weight of the capacitive film will be insignificant compared with the overall weight of the packaging materials. Thus, it is felt that reporting capacitance per gram of material is a less meaningful number than reporting capacitance per geometric area. With respect to this project, the thicker dense films are clearly superior since they produce greater capacitance per area. The additional thickness (230 nm vs. 25 nm) and the additional weight (several milligrams) of the capacitive film are not felt to be significant considering the weight and thickness of the total package. Unfortunately, much of the work being done by other researchers to-date focuses on specific capacitance.

5 Conclusions

There are several new and important conclusions that have resulted from this study for both the general growth of GLAD films and for the use of MnO_2 materials for electrochemical capacitor applications. For convenience, they will be broken up into two sections to deal with the two sections of work dealt with in this thesis.

5.1 General GLAD structure

1. While the macrostructure (morphology) of the film can be easily predicted from process variables (T_s/T_m), it is more difficult to predict microstructure from these variables. In many instances, the crystal structure of the material is more important for determining the final microstructure than the process variables.
2. Annealing of GLAD structures was found to induce crystallinity and significantly reduce the surface area of the film; however, the annealing does not alter the overall morphology of the structures at lower temperatures.
3. Rotation speed has a very significant effect on the macroporosity (morphology) of the films that are produced, but a limited effect on the microstructure as seen in the TEM pictures.

5.2 Manganese oxide electrochemical capacitor materials

1. The PVD process that produces both the zigzag and dense films results in a two-phase layer. The Mn and MnO are evenly distributed throughout the film and the grains of one are indistinguishable from the other. The entire structure is crystalline in the as-deposited state. The zigzag exhibits only limited macroporosity, while the dense films exhibit a columnar structure free from porosity.
2. Thermal annealing of the zigzag films at a temperature of 300°C results in the growth of a dense capping layer on the surface of the zigzag material. This capping layer grows linearly with time, ultimately converting entirely to Mn_3O_4 . Because this oxidation occurs thermally, there is no hydration (Mn-O-H) in the structure at all. As a result, this film does not develop any capacitance at all. When the structure is immersed into the electrolyte, and a current is impressed, rather than continuing the oxidation process, the current destroys the film making

it useless for capacitance. The annealing step must therefore be done after the electrochemical oxidation in order to obtain the benefits.

3. Electrochemical oxidation is shown to be the critical step in the process. It is this step alone that is responsible for the production of the porous, hydrated, amorphous layer that has a 4+ valence.
4. The porous layer is produced almost immediately during the oxidation process. The plateau at -1.35V corresponds to the transition from MnO to Mn_3O_4 . The plateau at -0.8 corresponds to the transition from Mn_3O_4 to Mn_2O_3 . The larger plateau at 0.1V corresponds to the transition from Mn_2O_3 to MnO_2 . It is unclear what step is occurring during the final plateau at 0.8V . During the transition from 0.1 to 0.9V , there is a significant reduction in film thickness and a fairly significant reduction in hydration.
5. The maximum capacitance occurs once the film is oxidized to 0.9V .
6. The position of the film during oxidation is also quite important. Horizontally oriented films produce more capacitance than vertically oriented films. The horizontally produced films have superior film surface area. In addition, the volume of solution used during the oxidation plays an important role in the quality of the film produced. Films oxidized with a very limited amount of solution ultimately produce thicker layers with greater surface area and better capacitance.
7. Current density has a very significant effect on the morphology of the film, but a more limited effect on the actual value of the capacitance. As the current density used for the oxidation is increased, the thickness of the layer is reduced, but becomes finer. However, the hydration of the film increases with the increasing current density. The result is a slight increase in the capacitance of the film as the oxidizing current density is increased. This is true for both the zigzag and dense films.
8. The effect of the thickness of the starting layer on the production of the porous layer is more significant. As the thickness of the starting layer is increased, the thickness of the final porous layer is also increased in a linear fashion. Because the current density remains constant, there is little change in the hydration of the

film. The overall result is a dramatic increase in the areal capacitance of the film as a function of the starting film thickness. The increased starting layer thickness results in a thicker porous layer, and thus greater areal capacitance. However, the thicker films result in more material remaining on the electrode and thus the overall specific capacitance (F/g) does not change significantly as the thickness of the starting layer is increased.

6 Further Recommendations

There are a number of recommendations for further study that can be made regarding this project.

6.1 General GLAD structure

1. The study clearly needs to be extended to include more materials, and more processing variables. In order to accomplish this, it is necessary to be able to measure substrate temperature very accurately. This type of study would also require a deposition system that is very consistent in terms of the quality of film fabricated to eliminate some unexpected differences in the films (oxygen content, thickness, etc.).

6.2 Manganese oxide electrochemical materials

1. The true mechanism causing pseudocapacitance needs to be identified. This is an important step, since it may help give a better understanding of how the process can be controlled. In order to study this effectively, in-situ experimentation will be required. There are systems in place for in-situ Raman spectroscopy and in-situ-XRD that would allow for the identification of the phase (XRD) and the chemical make-up of the film (Raman). With this type of in-situ study, it may be possible to determine if the mechanism is related to proton insertion or electrolyte ion insertion.
2. The cause of irreversibility during extended cycling needs to be identified. The results show that in addition to the pseudocapacitive reaction, there must also be a redox reaction occurring since the valence of the film is changing over a number of cycles. It is imperative that the cause of this irreversibility be determined since it limits the viability of this process for industrial applications. It is likely that an extended study will be required, perhaps making use of in-situ techniques to determine, first of all, which reaction is occurring and secondly, the reason for this alternate reaction. It is imperative that this issue be solved before the process can be considered a reasonably viable technology.

3. There was no advantage to using the zigzag structure due to insufficient porosity to make a true difference. For instance, the electrolyte was not able to penetrate through the pores in the zigzag to oxidize the material down the sides of the zigzag structure. However, if a structure were made in which the posts are situated farther apart, it would be possible for the entire structure to be oxidized, thereby maximizing the surface area available for capacitance (Figure 100). With the posts far enough apart, it would be possible to oxidize all sides of them as well as the material between the posts, which should significantly increase the amount of porous layer that can be produced. Producing this post structure has already been perfected by Brett's group in Department of Electrical and Computer Engineering through a combination of lithography and GLAD deposition. In addition, it would be quite simple to produce this patterned structure using electrochemical deposition onto a wafer patterned using standard lithography techniques, which may be a more inexpensive option.

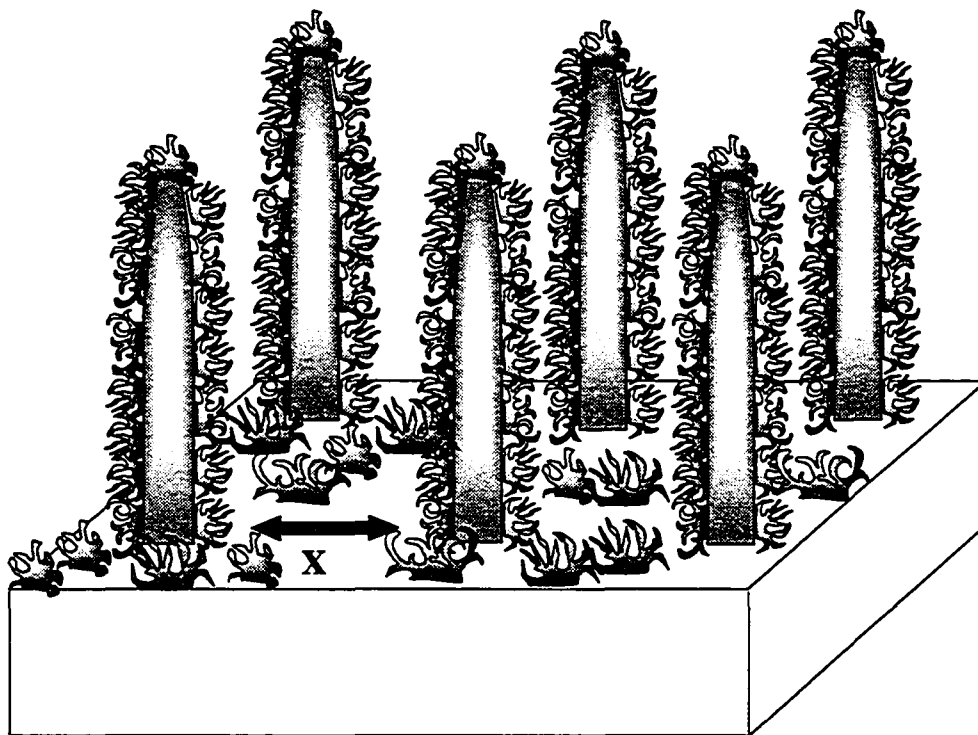


Figure 100. Schematic illustration of modified post structure.

4. A recommendation for the future direction of the research would be to look at the hybrid capacitors. This is the new direction being explored for research in this field. A hybrid capacitor involves not only hybrid materials (i.e., MnO_x with carbon in the same electrode), but also electrodes of two different materials (i.e., MnO_x electrode coupled with a polymer electrode). The advantage of these systems is increased power capacity and increased voltage range over which they are stable, ultimately making them more attractive to the industrial market.

5. There is also the possibility that this process could be used in photocapacitor cells⁸¹. A photocapacitor combines both a solar cell and a capacitor device on a single chip in order to simplify the storage of the energy developed by the solar cell. Current technology makes use of an activated carbon layer to store the charge in the double layer; however, it is reasonable to assume that this process for MnO_x could be used in this capacity and thereby increase the efficiency of the device.

7 References

- ¹ Robbie, K., L.J. Friedrich, S.K. Dew, T. Smy, and M.J. Brett. "Fabrication of thin films with highly porous microstructures". *J. Vac. Sci. Technol. A.* **12**(3) 1032-1035, 1995.
- ² Robbie, K., M.J. Brett, and A. Lakhtakia. "First thin film realization of a helicoidal bianisotropic medium". *J. Vac. Sci. Technol. A.* **13**(6) 2991-2993, 1995.
- ³ Robbie, K. and M.J. Brett. "Sculptured thin films and glancing angle deposition: Growth mechanics and applications". *J. Vac. Sci. Technol. A.* **15**(3), 1460-1465, 1997.
- ⁴ Robbie, K., J.C. Sit, and M.J. Brett. "Advanced techniques for glancing angle deposition". *J. Vac. Sci. Technol. B.* **16**(3), 1115-1122, 1998.
- ⁵ Malac, R. F. Egerton, M.J. Brett, and B. Dick. "Fabrication of submicrometer regular arrays of pillars and helices". *J. Vac. Sci. and Technol. B.* **17**(6), 2671-2674, 1999.
- ⁶ Malac and R.F. Egerton. "Observations of the microscopic growth mechanism of pillars and helices formed by glancing angle thin film deposition". *J. Vac. Sci. Technol. A.* **19**, 158-166, 2001.
- ⁷ Malac and R.F. Egerton. "Thin-film regular-array structures with 10-100 nm repeat distance". *Nanotechnology* **12**, 11-13, 2001.
- ⁸ Dick, B and M.J. Brett. "Investigation of substrate rotation at glancing incidence on thin-film morphology." *J. Vac. Sci. Technol. B.* **21**(6), 2569-2575, 2003.
- ⁹ Liu, F., Umlor, T., Weston, J., Eads, W., Barnard, J.A., and Mankey, GJ. "The growth of nanoscale structured iron films by glancing angle deposition". *J. Appl Phys* **85**, 5486-5488, 1999.
- ¹⁰ Vick, D., YY Tsui, MJ Brett, and R., Fedosejevs. "Production of porous carbon thin films by pulsed laser deposition". *Thin Solid Films* **350**, 49-52, 1999.
- ¹¹ Vick, D., LJ., Friedrich, SK Dew, MJ Brett, K Robbie, M Seto, and T. Smy. "Self-shadowing and surface diffusion effects in obliquely deposited thin films". *Thin Solid Films* **339**, 88-94, 1999.
- ¹² Bales, GS., R., Bruinsma, EA Eklund, RPU Karunasiri, J., Rudnick, and A., Zangwill. "Growth and erosion of thin solid films". *Science*, **249**, 264-268, 1990.
- ¹³ Messier, R., T., Gehrke, C., Frankel, VC., Venogopal, W., Otano, and A., Lakhatia. "Engineered sculptured nematic thin films". *J. Vac. Sci. Technol. A* **15**(4), 2148-2152, 1997.

-
- ¹⁴ ASM Handbook. Volume 3 Phase Diagrams. ASM Int.: Materials Park, OH, 1993.
- ¹⁵ Fritsch, S. and A. Navrotsky. "Thermodynamic properties of manganese oxides". *J. Am. Ceram. Soc.*, **79**(7), 1761-1768, 1996.
- ¹⁶ International Tables for X-ray Crystallography. Vol. 1 Symmetry Groups. Ed. Norman F.M. Henry and Kathleen Lonsdale. Kynoch Press: Birmingham, England, 1952.
- ¹⁷ Fernandes, J.B., B.D. Desai, and V.N. Kamat Dalal. "Manganese dioxide-A review of a battery chemical Part I: Chemical synthesis and x-ray diffraction studies of manganese dioxides". *Journal of Power Sources*, **15**, 209-237, 1985.
- ¹⁸ Malati, M.A. "The solid state properties of manganese dioxides". *Chemistry and Industry*, **17**, 446-452, 1971.
- ¹⁹ Turner, S. and P.R. Buseck. "Manganese oxide tunnel structure and their intergrowths". *Science*, **203**(4379), 456-458, 1979.
- ²⁰ De Wolff, P.M. "Interpretation of some γ -MnO₂ diffraction patterns". *Acta Cryst.* **12**, 341-345, 1959.
- ²¹ Buseck, P.R., B. Miner, and S. Turner. "High-resolution transmission electron microscopy of lithiated manganese oxides". *Proceedings of the symposium on Manganese dioxide electrode theory and practice for electrochemical applications*. Ed. B. Schumm, Jr., M.P. Grotheer, R.L. Middaugh, and J.C. Hunter. The Electrochemical Society Inc.: USA, 1985.
- ²² Cha, D.K., and S-M Park. "Electrochemical Oxidation of Mn(OH)₂ in Alkaline Media". *J. Electrochem. Soc.*, **144**(8), 2573-2580, 1997.
- ²³ Liang, C.C. in *Encyclopedia of Electrochemistry of the Elements Vol 1*. Ed. Allen J Bard. Marcel Dekker Inc: New York, 1973.
- ²⁴ Moussard, A., J. Brenet, F. Jolas, M. Pourbaix, and J. Van Muylder in *Atlas of electrochemical equilibria in aqueous solutions*. Ed. M. Pourbaix. Pergamon Press: New York, 1966.
- ²⁵ Zordan, T.A. and L.G. Hepler. "Thermochemistry and oxidation potentials of manganese and its components". *Chem. Rev.*, **68**, 737, 1968.
- ²⁶ Cahoon, N.C., R.S. Johnson, and M.P. Korver. "Cathode reactions in the Leclanche dry cell". *J. Electrochem. Soc.* **105**, 296-298, 1958.
- ²⁷ Cahoon, N.C. "An electrochemical evaluation of manganese dioxide for dry battery use". *J. Electrochem. Soc.* **99**, 343-348, 1952.

-
- ²⁸ Vosburgh, W.C. "The manganese dioxide electrode". *J. Electrochem. Soc.*, **106**, 839-845, 1959.
- ²⁹ Vosburgh, W.C. and P.S. Lou. "Experiments on the discharge mechanism of the manganese dioxide electrode". *J. Electrochem. Soc.*, **108**, 485-490, 1961.
- ³⁰ Yu, P. and T.J. O'Keefe. "Evaluation of Lead Anode Reactions in Acid Sulfate Electrolytes. Part II: Manganese Reactions". *J. Electrochem. Soc.*, **149**(5), A558-A569, 2002.
- ³¹ Nijjer, S., J. Thonstad, and G.M. Haarberg. "Oxidation of manganese(II) and reduction of manganese dioxide in sulphuric acid". *Electrochimica Acta*, **46**, 395-399, 2000.
- ³² Rodrigues, S. N. Munichndraiah, and A.K. Shukla. "A cyclic voltammetric study of the kinetics and mechanism of electrodeposition of manganese dioxide". *J. Appl. Electrochem.* **28**, 1235-1241, 1998.
- ³³ Petitpierre, J.Ph., Ch. Comninellis, and E. Plattner. "Oxydation Du MnSO₄ en dioxyde de manganese dans H₂SO₄ 30% ". *Electrochim. Acta.* **35**, 281-287, 1990.
- ³⁴ Kao, W.H., and V.J. Weibel. "Electrochemical oxidation of manganese (II) at a platinum electrode". *J. Appl. Electrochem.* **22**, 21-27, 1992.
- ³⁵ Bodoardo, S., J. Brenet, M Maja, and Spinelli. "Electrochemical behaviour of MnO₂ in sulphuric acid solutions". *Electrochim. Acta.* **39**, 1999-2004, 1994.
- ³⁶ Lee, J.A., W.C. Maskell, and F.L. Tye. "Electrochemical reduction of manganese dioxide in acidic solutions-1". *J. Electroanal. Chem.* **79**, 79-104, 1977.
- ³⁷ Lee, J.A., W.C. Maskell, and F.L. Tye. "Electrochemical reduction of manganese dioxide in acidic solutions-3". *J. Electroanal. Chem.* **110**, 145-158, 1980.
- ³⁸ Bell, G.S. and R. Huber. "On the cathodic reduction of manganese dioxide in alkaline electrolyte". *J. Electrochem Soc.* **111**, 1-6, 1964.
- ³⁹ Bard, Allen and Larry Faulkner. *Electrochemical Methods: Fundamentals and Applications*. John Wiley and Sons: Toronto, 1980.
- ⁴⁰ Kozawa, A. and J.F. Yeager. "The cathodic reduction mechanism of electrolytic manganese dioxide in alkaline electrolyte ". *J. Electrochem. Soc.* **112**, 959-963, 1965.
- ⁴¹ Kozawa, A. and T. Kalnoki-Kis. "Solubilities of Mn (II) and Mn(III) ions in concentrated alkaline solutions ". *J. Electrochem. Soc.*, **113**, 405-409, 1966.

-
- ⁴² Gosztola, D., and M.J. Weaver. "Electroinduced structural changes in manganese dioxide and manganese hydroxide films as characterized by real-time surface-enhanced Raman spectroscopy". *J. Electroanal. Chem.*, **271**, 141-154, 1989.
- ⁴³ Messaoudi, B., S. Joiret, M. Keddou, H. Takenouti. "Anodic behaviour of manganese in alkaline medium". *Electrochimica Acta*, **46**, 2487-2498, 2001.
- ⁴⁴ Conway, B.E. "Electrochemical Supercapacitors: Scientific Fundamentals and Technological Applications". Kluwer/Plenum Publishing: New York, 1999.
- ⁴⁵ Kotz, R., and M. Carlen. "Principles and applications of electrochemical capacitors". *Electrochimica Acta*, **45**, 2438-2498, 2000.
- ⁴⁶ Clavilier et al. "Electrochemical monitoring of the thermal reordering of platinum single-crystal surfaces after metallographic polishing from the early stage to the equilibrium surfaces". *J. Electroanal. Chem.*, **295**, 333-356, 1990.
- ⁴⁷ Engelsman et al. "Underpotential deposition of lead on polycrystalline and single-crystal gold surfaces." *J. Electroanal. Chem.*, **114**, 1-10, 1980.
- ⁴⁸ Conway, B.E. "Two-dimensional and quasi-two-dimensional isotherms for Li intercalation and UPD processes at surfaces". *Electrochimica Acta*, **38**, 1249-1258, 1993.
- ⁴⁹ Ren, X., S. Gottesfeld, J.P. Ferraris, in: F.M. Delnick, M. Tomkiewicz (Eds.), "Electrochemical Capacitors: Proceedings". The Electrochemical Society: Pennington, NJ: p. 138, 1996.
- ⁵⁰ Arbizzani, C., M. Mastragostino, L. Meneghello. "Polymer-based redox supercapacitors: A comparative study". *Electrochim. Acta*, **41**, 21-26, 1996.
- ⁵¹ Hadzi-Jordanov, S., H.A. Kozłowska, M. Vukovic, and B.E. Conway. "Reversibility and growth behaviour of surface oxide films at ruthenium electrodes". *J. Electrochem. Soc.* **125**, 1473-1480, 1978.
- ⁵² Hadzi-Jordanov, S., H.A. Kozłowska, and B.E. Conway. "Surface oxidation and H deposition at ruthenium electrodes-resolution of component processes in potential-sweep experiments". *J. Electroanal Chem.* **60**, 359-362, 1973.
- ⁵³ Birss, V., R. Myers, and B.E. Conway. "Electron microscopy study of formation of thick oxide films on IR and RU electrodes". *J. Electrochem. Soc.* **131**, 1502-1510, 1984.
- ⁵⁴ Trasatti, S., and G. Lodi. *Conductive Metal Oxides*, S. Trasatti, ed., vol.A, p. 338, Elsevier, Amsterdam, 1980.
- ⁵⁵ Mitchell, D., D.A.J. Rand, R. Woods. "A study of ruthenium electrodes by cyclic voltammetry and x-ray emission spectroscopy". *J. Electroanal. Chem.*, **89**, 11-27, 1978.

-
- ⁵⁶ Galizzioli, D., F. Tantardini, and S. Trasatti. "Ruthenium dioxide: a new electrode material. I. Behaviour in acid solutions of inert electrolytes". *J. Appl. Electrochem.*, **4**, 57-67, 1974.
- ⁵⁷ Zheng, J.P., T.R. Jow. "A new charge storage mechanism for electrochemical capacitors". *J. Electrochem. Soc.*, **142**, L6-L8, 1995.
- ⁵⁸ Zheng, J.P., P.J. Cygan, and T. R. Jow. "Hydrous ruthenium oxide as an electrode material for electrochemical capacitors". *J. Electrochem. Soc.*, **142(8)**, 2695-2698, 1995.
- ⁵⁹ Kleijn, J.M., J. Lyklema. "The electrical double layer on oxides: specific adsorption of chloride and methylviologen on ruthenium dioxide". *J. Coll. Interface.* **120**, 511-522, 1987.
- ⁶⁰ Jiang, J and Kucernak, A. "Electrochemical supercapacitor material based on manganese oxide: preparation and characterization". *Electrochimica Acta*, **47(15)**, 2381-2386, 2002.
- ⁶¹ Hu, C.C., and Y-T Wu. "Electrochemical and textural characterization of manganese oxide-based electrodes for electrochemical supercapacitors". American Electrochemical Society Annual Meeting, Hawaii, October, 2004.
- ⁶² Toupin, M., T. Brousse, D. Belanger. "Influence of microstructure on the charge storage properties of chemically synthesized manganese dioxide". *Chem. Mater.* **14**, 3946-3952, 2002.
- ⁶³ Pang, S., M.A. Anderson, T.W. Chapman. "Novel electrode materials for thin-film ultracapacitors: Comparison of electrochemical properties of sol-gel-derived and electrodeposited manganese dioxide". *J. Electrochem. Soc.* **147(2)**, 444-450, 2000.
- ⁶⁴ Hu, C., T. Tsou. "Capacitive and textural characteristics of hydrous manganese oxide prepared by anodic deposition". *Electrochimica Acta.* **47**, 3523-3532, 2002.
- ⁶⁵ Lee, H.Y., S.W. Kim, H.Y. Lee. "Expansion of active site area and improvement of kinetic reversibility in electrochemical pseudocapacitor electrode". *Electrochemical and Solid State Letters.* **4(3)**, A19-A22, 2001.
- ⁶⁶ Pang, S-C., and M.A. Anderson. "Novel electrode materials for electrochemical capacitors: Part II. Material characterization of sol-gel-derived and electrodeposited manganese dioxide thin films". *J. Mater. Res.*, **15(10)**, 2096-2106, 2000.
- ⁶⁷ Jeong, Y.U. and A. Manthiram. "Nanocrystalline Manganese Oxides for Electrochemical Capacitors with Neutral Electrolytes". *Journal of the Electrochemical Society.* **149(11)** A1419-A1422, 2002.

-
- ⁶⁸ Tsang, C., J. Kim, and A. Manthiram. "Synthesis of Manganese Oxides by Reduction of KMnO_4 with KBH_4 in Aqueous Solutions". *Journal of Solid State Chemistry*, **137**, 28-32, 1998.
- ⁶⁹ Shao-Horn, R., S.A. Hackney, C.S. Johnson, and M.M. Thackeray. "Microstructural features of MnO_2 electrodes for lithium batteries". *J. Electrochem. Soc.*, **145(2)**, 582-589, 1998.
- ⁷⁰ Hong, M.S., S.H. Lee, and S.W. Kim. "Use of KCl aqueous electrolyte for 2V manganese oxide/activated carbon hybrid capacitor". *Electrochemical and Solid State Letters*, **5(10)**, A227-A230, 2002.
- ⁷¹ Chin, S-F., Pang, S-C., and M. A. Anderson. "Material and Electrochemical Characterization of Tetrapropylammonium Manganese Oxide Thin Films as Novel Electrode Materials for Electrochemical Capacitors". *Journal of the Electrochemical Society*, **149(4)**, A379-A384, 2002.
- ⁷² H. Lee and J.B. Goodenough. "Supercapacitor behaviour with KCl electrolyte". *J.S.S. Chemistry*, **144(1)**, 220-223, 1999.
- ⁷³ Seike, T., and Junichi Nagai. "Electrochromism of 3d transition metal oxides". *Solar Energy Materials*, **22**, 107-117, 1991.
- ⁷⁴ Broughton, J.N., and M.J. Brett. "Electrochemical Capacitance in Manganese Thin Films with Chevron Microstructure". *Electrochemical and Solid State Letters*, **5(12)**, A279-A282, 2002.
- ⁷⁵ Chigane, M., and M. Ishikawa. "Manganese Oxide Thin Film Preparation by Potentiostatic Electrolyses and Electrochromism". *Journal Electrochem. Soc.*, **147(6)**, 2246-2251, 2000.
- ⁷⁶ Hu, C-C., and C-C Wang. "Nanostructures and capacitive characteristics of hydrous manganese oxide prepared by electrochemical deposition". *Journal Electrochem. Soc.*, **150(8)**, A1079-A1084, 2003.
- ⁷⁷ Chigane, M., M. Ishikawa, and M. Izaki. "Preparation of manganese oxide thin films by electrolysis/chemical deposition and electrochromism". *Journal Electrochem. Soc.*, **148(7)**, D96-D101, 2001.
- ⁷⁸ Oku, M., K. Hirokawa, and S. Ikeda. "X-Ray photoelectron spectroscopy of manganese-oxygen systems". *Journal of electron spectroscopy and related phenomena*, **7**, 465-473, 1975.
- ⁷⁹ Colgan, M., B. Djurfors, D.G. Ivey, and M.J. Brett. "Effects of annealing on titanium dioxide structured films". *Thin Solid Films*, **466 (1-2)**, 92-96, 2004.
- ⁸⁰ Broughton, J.N. and M.J. Brett. "Investigation of thin sputtered Mn films for electrochemical capacitors." *Electrochimica Acta*, **49**, 4439-4446, 2004.

⁸¹ Miyasaka, T., and T. Murakami. "The photocapacitor: An efficient self-charging capacitor for direct storage of solar energy". *Applied Physics Letters*. **85(17)**, 3932-3934, 2004.